Solid Electrolytes Derived From Precursors and Liquid-Feed Flame Spray Pyrolysis Nano-Powders Enabling Assembly of All-Solid-State-Batteries

by

Eleni Temeche

A dissertation submitted in partial fulfillment
of the requirements for the degree of
Doctor of Philosophy
(Materials Science and Engineering)
in the University of Michigan
2021

Doctoral Committee:

Professor Richard M.Laine, Chair
Professor John Kieffer
Professor Pierre F. Poudeu-Poudeu
Professor Nirala Singh

Eleni Temeche

elenite@umich.edu

ORCID iD: 0000-0002-7546-0541

Dedication

To my parents, family, and friends.
In the memory of Prof. Dr. Andreas Hintennach

Acknowledgements

First, I would like to thank my advisor, Professor Richard M. Laine, for his mentorship, encouragement, and guidance during my graduate studies. I would also like to acknowledge my committee members, Professors John Kieffer, Nirala Singh, and Pierre F. Poudeu-Poudeu for their insightful feedback.

I would like to extend special thanks to my colleagues in the Laine group: Xinyu Zhang, Mengjie Yi, Taylor Brandt, Philyong Kim, Jun Guan, and Dr. Eongyu Yi. I must acknowledge contributions from undergraduate researcher colleagues, especially Kayla Byrd, Dhruv Tatke, and Dylan Edleman for their support and contributions. I would also like to thank professor Sylvio Indris and Elizaveta Buch for their help with characterization as well as collaborative work.

I must acknowledge my fellow soldiers in HHB 119th FA unit. I would also like to thank my parents, family, and friends. This journey was only possible with their support.

Finally, I would like to acknowledge the financial support from Department of Energy, National Science Foundation, Mercedes-Benz Research & Development North America, and Rackham Merit Fellowship. I especially like to thank Mr. Tobias Glossmann and for his continuing encouragement.

Table of Contents

List of Tables

List of Figures

List of Schemes

Abstract

Solid electrolytes enable several next-generation energy storage systems (designs) including solid oxide fuel cells, super capacitors, and batteries. State-of-the-art battery technologies depend highly on the discovery of electrically insulating solids with high ionic mobilities. Current Li-ion batteries (LIBs), using traditional organic liquid electrolytes, suffer from poor electrochemical and thermal stabilities, leakage and flammability. Hence, replacing liquids with solid electrolytes offers multiple possibilities for developing new battery chemistries and designs. Solid electrolytes enhanced thermal stabilities provide opportunities to design new architectures that simplify battery configurations and reduce the peripheral mass of traditional LIBs. For example, the battery pack can be redesigned to minimize thermal management systems and overpressure vents are typically installed to overcome the challenges of using flammable liquid electrolytes. Furthermore, solid electrolytes facilitate adoption of newer battery chemistries. The development of state-of-the-art Li-S and Li-air batteries will benefit greatly from the use of solid electrolytes.

In this dissertation, we investigate the design, synthesis, characterization, and performance of polymer and inorganic solid electrolytes to enable the assembly of all-solid-state batteries (ASSBs). Key properties that determine the utility of solid electrolyte include high ionic conductivity (>10^{-6} S/cm), high transference number (≈ 1), low electrical conductivity (>10^{-8} S/cm), wide electrochemical stability window (0-5 V vs Li/Li^+), good chemical and thermal stability, excellent mechanical properties, low cost, ease of fabrication, eco-friendliness, and simple device integration.

Our first study is to develop polymer precursor electrolytes that offer properties anticipated to be similar or superior to (lithium phosphorous oxynitride, LiPON) glasses. Such precursors offer the potential to be used to process LiPON-like thin glass/ceramic coatings for use in ASSBs. LiPON glasses provide a design basis for the synthesis of sets of oligomers/polymers by lithiation of $OP(NH_2)_{3-x}(NH)_x$ [from $OP(NH)_3$], $OP(NH_2)_{3-x}(NHSiMe_3)_x$ and $[P{=}N]_3(NHSiMe_3)_{6-x}(NH)_x$. Treatment with selected amounts of $LiNH_2$ provides varying degrees of lithiation and Li^+ conducting properties commensurate with Li^+ content. Polymer electrolytes impregnated in/on Celgard exhibit Li^+ conductivities up to ~1×10^{-5} S cm^{-1} at room

temperature and are thermally stable to ≈150 °C. A Li-S battery assembled using a Li_6SiPON composition polymer electrolyte exhibits an initial reversible capacity of 1500 mAh g_{sulfur}^{-1} and excellent cycle performance at 0.25 and 0.5 C rate over 120 cycles at room temperature.

We then show the versality of co-dissolution of poly(ethylene oxide) (PEO, M_n 900k) with Li_xPON and Li_xSiPON polymer systems at ratios of approximately 3:2 followed by casting provides transparent, solid solution films 25-50 μm thick, lowering PEO crystallinity, and providing measured impedance values of 0.1-2.8 mS/cm at ambient. These values are much higher than simple PEO/Li^+ salt systems. These solid solution polymer electrolytes (PEs) are: (1) thermally stable to 100 °C; (2) offer activation energies of 0.2-0.5 eV; (3) suppress dendrite formation and (4) enable the use of lithium anodes at current densities as high as 3.5 mAh/cm^2. Galvanostatic charge/discharge cycling of SPAN/PEs/Li cell (SPAN = sulfurized, carbonized polyacrylonitrile) shows discharge capacities of 1000 mAh/g_{sulfur} at 0.25 C and 800 mAh/g_{sulfur} at 1 C with high columbic efficiency over 100 cycles.

We have also investigated another promising inorganic solid electrolyte, γ-$LiAlO_2$. Following series of studies explore the use of flame made nanopowders (NPs) in processing Li^+ conducting membranes. We exhibit an effective method of processing $LiAlO_2$ membranes (< 50 μm) using NPs produced via liquid-feed flame spray pyrolysis (LF-FSP). Membranes consisting of selected mixtures of lithium aluminate polymorphs and Li contents were processed using conventional tape casting of NPs followed by thermo-compression of the green films (100 °C/10 kpsi/10 min). The sintered green films (1100 °C/2 h/air) present a mixture of $LiAlO_2$ (~ 72 wt.%) and $LiAl_5O_8$(~ 27 wt.%) phases, offering ionic conductivities (>10^{-6} Scm^{-1}) at ambient with an activation energy of 0.5 eV, greatly increasing their potential utility as ceramic electrolytes for ASSBs that could simplify battery designs, significantly reduce costs, and increase their safety. A solid-state Li/$Li_{3.1}AlO_2$/Li symmetric cell was assembled and tested successfully exhibiting a transference number ≈ 1.

The electrochemical and mechanical stability of anode/cathode materials during extensive charge/discharge cycles is crucial to enable the assembly of practical ASSBs. Thus, we have investigated $Li_4Ti_5O_{12}$ (LTO) as an alternate anode material for high power density batteries for large scale applications. Our study demonstrates a facile synthesis of LTO NPs using LF-FSP which provides high surface area (~38 m^2/g) spinel structure LTO NPs with average particle sizes (APSs) of 45 ± 0.3 nm. Pristine LTO-Li half-cells exhibit reversible capacity of 70 mAh/g at 10 C. In this study, we show that mixing $LiAlO_2$ NPs (5 wt.%) and Li_6SiON polymer precursor (10 wt.%) with pristine LTO via ball-milling and ultrasonication followed by tape casting enhances the LTO rate performance providing reversible capacity of ~ 217 mAh/g at 5 C over 500 cycles. The Li_6SiON polymer electrolyte is synthesized from rice hull ash (RHA), an agricultural waste, providing a green synthetic approach to electrode coating materials.

The assembly of ASSB highly rely on the fabrication and material cost of solid electrolyte and electrodes. RHA produced during combustion of rice hulls to generate electricity consists (following dilute acid leaching) of high surface area SiO_2 (80-90 wt. %) and 10-20 wt. % carbon (80 m^2/g total). RHA SiO_2 is easily extracted by distillation (spirosiloxane) producing SDRHA (50-65 wt. % SiO_2), which offers an opportunity to develop "green" hybrid lithium-ion capacitor (LICs) electrodes.

Chapter 1

Introduction

Progress in the energy storage technologies plays an important role in the reduction of carbon emissions and global warming.[1] Lithium-ion batteries (LIBs) have demonstrated multiple advantages since their commercialization in 1990s because of their high energy and power densities, and long cycle life.[2,3] It is well known that the electrochemical performance of a battery depends to a large extent on electrolyte properties. Conventional LIBs have critical safety issues primarily because they require highly flammable organic liquid electrolytes.[4] Although, liquid electrolytes offer high ionic conductivity (> 10^{-3} S/cm) and excellent wetting of electrode surfaces, they often suffer from low thermal stability, low flash point, and inadequate electrochemical stability sufficient for assembling next generation energy storage devices ($Li\text{-}O_2$).[4]

Solid electrolytes, intrinsically, are more thermally stable than liquids. Solid electrolytes enable the development of new generations of LIBs, e.g. Li-S and Li-air devices.[5] ASSB performance, in turn, requires development of electrically insulating solids with high ionic mobilities.[6] In principle, solid electrolytes can offer distinct advantages including resistance to corrosion during operation, low rates of oxidation (non-flammable), inability to leak and resistance to internal shorting when designed carefully.[7] The most significant properties sought in developing solid electrolytes for ASSBs include chemical stability with the electrode materials, thermal stability during extensive cycling, wide electrochemical windows (0-5 V), high superionic conductivity (> 10^{-3} S/cm), and negligible electrical conductivity (<10^{-8} S/cm).[8]

Despite their advantages, solid electrolytes have not been widely used in battery applications because they are mostly limited by their relatively low ionic conductivity at room temperature. There has been tremendous effort to synthesize promising solid electrolytes with competitive ionic conductivities to those of liquid electrolytes.[9] However, the integration of solid electrolytes with high ionic conductivities into the current battery structures is still challenging mainly due to high resistivity at the electrode/SE interfaces.

1.1 Brief history of solid electrolytes

The transport of electrical charge by diffusion of ions in solids has been studied for almost two centuries. The history of solid-state ionic conductors dates back to the 1830s, with a report by Michael Faraday on ionic conduction in heated solids (Ag_2S and PbF_2).[10] A ZrO_2/Y_2O_3 composite was used as a glowing rod in a device known as the *Nernst glower* in 1900s.[11] This composite conducts electrical charge via defect diffusion through the oxide lattice at high temperatures. The discovery of Ag^+ and Na^+ conductors with ionic conductivities comparable to liquid electrolytes led to a renewed interest in the development of solid electrolytes in 1960s.[12,13]

Most common alkali halides exhibit low ionic conductivity and high activation energies, in which the electrical charge transport proceeds through temperature dependent motion of vacancies in the crystal structure.[14] However, the discovery of silver and copper halides with high ionic conductivities and low activation enthalpies wherein ionic conductivity is via motion of interstitial species resulted in a breakthrough in the field of superionic conductors.[12]

To date, a huge family of solid electrolytes has been developed that offer high ionic conductivities (> 10^{-4} S/cm) at ambient conditions, low activation energies (< 0.4 eV), thermal stability (> 200 °C), and wide electrochemical stability windows (5 V).[9,15] The discovery of ionic transport in poly(ethylene oxide) (PEO) in 1973, broadened the scope of solid electrolytes from inorganic materials to solid polymer materials.[16] The Figure **1.1** timeline illustrates key developments in solid electrolyte batteries. Solid electrolytes with different crystallographic or amorphous morphologies provide several specific advantages. Solid electrolytes can be divided into inorganic solid electrolytes (ISEs) and polymer electrolytes (PEs).

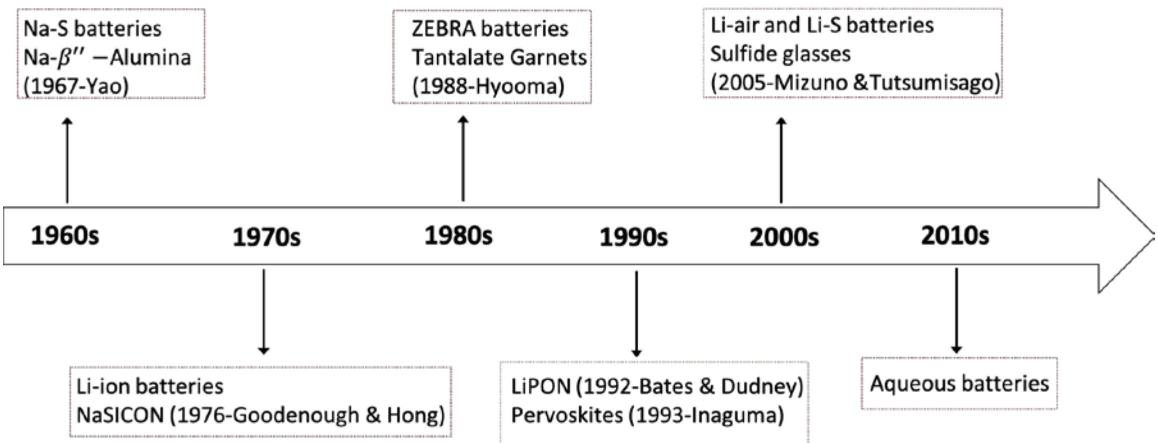

Figure 1.1. Historical outline of progress in solid electrolytes.

1.2 Ionic transport in inorganic solid electrolytes (ISEs)

In liquid electrolytes, ionic transport generally relies on the migration of the solvated Li^+-ions in the solvent medium.[8] The ionic conductivity of liquid electrolytes can be enhanced by increasing the dissociation of salt/ion by using solvents with high dielectric constants.[8] In addition, the mobility of the solvated ions can be enhanced by lowering the viscosity of solvents. Typically, it is difficult to find one solvent that can meet all the desired properties (i.e. high dielectric constant, low viscosity, low melting point, and low vapor pressure) to promote fast Li^+ ion transport.[17] Thus, liquid electrolytes are composed of two or more solvents.

In contrast, the ionic transport in crystalline materials generally depends on the concentration and distribution of defects.[8] Typically, the ion diffusion mechanism is based on Schottky and Frenkel point defects, which relies on the available interstitials, vacancies, and interstices sites.[10] There are three main ion migration mechanisms in crystalline solids: (1) vacancy diffusion in which the ion migrates into a neighboring vacant site (Figure **1.2a)**, (2) direct interstitial mechanism between sites not fully occupied (Figure **1.2b)**, and (3) knock-off mechanism, where the migrating interstitial ion displaces a neighboring lattice ion into the adjacent site (Figure **1.2c)**.[9]

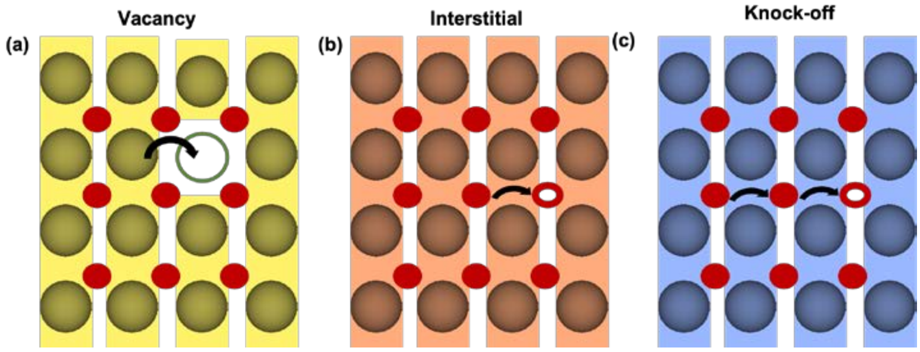

Figure 1.2. Ion migration mechanisms in crystalline solids via a. vacancy, b. direct interstitial, and c. knock-off.

This defect formation energy (E_f) is one of the key factors in determining the ionic mobilities of crystalline solids. The Li^+-ion conductivity in ISEs can be enhanced by increasing the concentration of mobile lithium ions by aliovalent substitutions to create vacancies or interstitial sites.[8] However, there is a decrease in the ionic conductivity past the optimal aliovalent doping, which is ascribed to the increase in the migration energy associated with the local structure distortion.[8]

The ionic conductivity of ISEs is dependent up on the periodic bottleneck points, which define the migration energy barrier (E_m), where low migration energies leads to high ionic conductivity.[8] One of the main factors in regulating the intrinsic Li^+-ion migration of ISEs is the topology of the particular anion arrangements.[18] ISEs with body-centered cubic (bcc) anion sublattice are known to exhibit the lowest E_m and highest ionic conductivities.[18]

In addition, the most favorable and stable Li^+-ion site in ISEs is usually a tetrahedral or octahedral site connected to the other polyhedral sites through shared anion triangles. Most ISE materials rely on solid state diffusion through well-defined crystallographic structures wherein the ionic framework permits fast ion mobility via vacant and/or interstitial sites. Mostly ISE crystal structures consist of a stationary, polyhedral metal oxide framework matrix with open channels that allow diffusion of mobile ions.[8] Mobile ions include H^+, Li^+, Na^+, K^+, Ag^+, Cu^+, Mg^{2+}, F^-, Cl^-, and O^{2-}. A number of framework metals and nonmetals can form polyhedral networks with the latter typically coming from elements in groups VA, VIA, and VIIA .[10] Ionic conductivity in ISEs can be tuned (enhanced) via selective doping. To do this effectively requires an extensive understanding of their crystal chemistries. Fundamental criteria that have been used to (greatly) improve fast ionic conduction in ISEs include:

1. The number of sites that mobile ions can occupy should be larger than the number of mobile species.
2. The mobile ion should fit through the smallest cross-sectional area of the conduction channel (bottleneck).
3. The concentration of vacant and interstitial sites should be optimal to minimize the migration energy.
4. The interaction forces between mobile ions and main framework should be weak.
5. The available sites for mobile ions to occupy should be interconnected to allow continuous diffusion pathways.
6. The framework moieties should consist of stable ions with different coordination numbers to minimize the activation energy.

1.3 Ionic transport in polymer electrolytes (PEs)

PEs offer several advantages over ISEs such as enhanced resistance to variations in electrode volumes during cycling, excellent flexibility, and low-cost processability. In addition, Li metal dendrite growth may be suppressed in solvent-free PEs under certain conditions.[19] A large number of PEs have been prepared and characterized since their discovery in 1973.[16] Substantial efforts have targeted elucidation of Li-ion transport mechanisms, and the physical and chemical properties of new PEs.[20]

PEs comprised of polymer matrices and lithium salts are classified as dry solid polymer electrolytes (dry-SPEs).[21] Lithium salts are dissolved in a polymer matrix to provide ionic conductivity.[22] Polyethers dissolve Li-salts by complexation of the Li^+ via binding interaction with ether oxygens.[23] Thus, polyethylene oxide (PEO)-based solid electrolytes have received considerable attention because of their superior ability to solvate Li^+, combined with excellent segmental motion allowing rapid Li^+ transport but typically near their T_g of 65 °C as well as their excellent commercial availability in relatively pure states with different molecular weights and at reasonable costs.[21]

Dry-SPEs usually exhibit low ionic conductivity at ambient (10^{-7}-10^{-6} S/cm), which represent a significant barrier to practical applications.[24] The ionic conduction mechanism is affected by two factors: one is the fraction of the amorphous material in the polymer matrix, and the other is *Tg*. It is generally accepted that Li^+ transport (diffusion) occurs preferentially in amorphous regions of solid PEO.[21] Significant efforts to improve ionic conductivities of dry-SPEs have focused in reducing crystallinity. Such efforts include, modifying the polymer matrix by copolymerization, crosslinking, and blending, increasing the salt concentrations, and immobilizing the anions as pendant groups.[21]

Another method to increase the ionic conductivity of dry-SPE is to increase the salt concentration.[25] Polymer-in-salt electrolytes require that the salt should have low *Tg* to ensure the formation of rubbery electrolyte.[26] Rubbery electrolytes possess the combined qualities of polymer electrolytes (good mechanical properties) and glass electrolytes (fast ion conduction).[27] Polyacrylonitrile (PAN) based rubbery electrolytes have been extensively studied because of the interaction between Li^+ ions and the nitrile groups, which results in the stabilization of highly conducting amorphous ionic clusters.[25,28]

Efforts have been made to explain the ion conduction mechanism in PE systems.[20] The efficient mechanism of ion transport is associated with a high degree of ion aggregation in the polymer-in-salt electrolytes.[29,30] The increase in ionic conductivity of these systems is attributed to the formation of a percolation path in the polymer matrix associated with the increase salt concentration.[25] The high ionic conductivity of polymer-in-salt electrolyte is associated with the critical cluster concentration, in which all the separate single clusters came into contact with each other to form infinite cluster which promotes fast ion mobility.[31] Even though polymer-in-salt systems have a higher ionic conductivity than dry-SPEs, they suffer from poor mechanic property due to the increase salt concentration. Networked polymer electrolytes have been developed to overcome this challenge.[32] The polyethylene glycol (PEG) network with highest Li salt loading (EO/Li = 1:1) exhibits rubbery-like characteristic and high ionic conductivity of 6.7×10^{-4} S/cm at 30 °C.[32]

In general, Dry-SPEs are bi-ionic conductors, in which cations bind to polar groups of the polymer matrix and anions contribute the electrical conductivity of the electrolyte.[25] In the bi-ionic conductors, both the cations and anions are mobile species resulting in a decrease in the transference numbers, which is generally < 0.5 due to the electro-polarization from anion buildup.[33]

The electro-polarization leads to a decrease in the overall electrochemical performance of the electrolyte due to high internal resistance, voltage losses, and dendritic growth.[25] In order to minimize the polarization and increase the Li^+ transference number, the mobility of anions have to be reduced either by anchoring the anions to the polymer backbone or by adding anion receptor that preferentially interact with anions.[25]

Many efforts have been devoted to synthesizing single-ion conductors based on polymeric Li salts and various anionic structures.[34–36] The immobilization of anions is the most common approach to fabricate single-ion conductor. Lithium poly(2-acrylamido-2 methylpropanesulfonic acid), (LiPAMPS) is one example of single-ion conductor electrolyte.[35] The structural of this electrolyte contains sulfonic acid group and double bond, which gives the AMPS ability to polymerize radically with itself or with other monomers. The polymer electrolyte has a high dissociation ability to yield mobile cations as a result of the sulfonic acid group which is chemically attached to the polymer back bone after polymerization. The LiPAMPS single ion conductor exhibits ionic conductivity of ~2 x 10^{-5} S/cm at 20 °C, and good electrochemical stability (4.4 V vs. Li/Li^+).[35]

An alternative method to enhance the ionic conductivity and improve the transference number is through the introduction of anion receptors.[25] In these systems, the anion receptors trap the anions and the interaction between them promotes the further dissociation of Li salts, increasing both the ionic conductivity and the Li^+ transference number.[37] The effect of an anion receptor on the PEs depends on the coordinating property of the anion.[38]

Significant attempts to improve the ionic conductivities of PEs are reported in the literature through the addition of ceramic fillers that interfere with crystallization and the choice of Li^+ salt.[39–41] The first approach, introducing ceramic fillers also been explored in some detail with inert (Al_2O_3, TiO_2, SiO_2, and ZrO_2)[42] active Li^+ conducting fillers (LATP, $LiAlO_2$, and LLZO).[43,44] Inactive fillers improve Li^+ conductivity by reducing PEO crystallization. Active fillers contribute to Li^+ conductivity by both reducing PEO crystallinity and by promoting surface Li^+ transport at PEO-nanofiller interfaces.[41,45]

1.4 Lithium phosphorus oxynitride (LiPON)

Some solid electrolyte materials exhibit poor Li^+ conductivities ($<10^{-6}$ S/cm), which can be compensated by using pinhole-free, dense, and thin film formats. Thin-film solid electrolytes were first developed in the 1980s using $Li_4P_2S_7$, $Li_{12}Si_3P_2O_{20}$, and Li_3PO_4 as starting materials.[46] In 1990s, Oak Ridge National Laboratory described LiPON-based thin-film solid electrolytes. Since their discovery, LiPON-based electrolytes have received wide attention owing to their broad electrochemical stability window (0-5 V vs Li^+/Li), high critical current density (>10 mA/cm^2), and negligible electronic conductivity (10^{-7} μS cm^{-1}).[47] Typically, ultra-thin solid electrolytes are synthesized via gas-phase deposition techniques. The main limitation to gas-phase deposition methods centers on their low deposition rates limiting their use for processing large surface area substrates or multiple substrates simultaneously.[48] Hence, ultra-thin-film electrolytes are typically used for micro-battery applications.

Glassy $Li_{2.9}PO_{3.3}N_{0.5}$ electrolyte is synthesized by sputtering Li_3PO_4 targets in N_2 .[49] This electrolyte exhibits an ionic conductivity of 3.3 μS/cm and an electrochemical window of 5.5V.[49] The ionic conductivity is determined by product of charge density and mobility. Hence, there are two ways to increase Li^+ conductivity of LiPON thin film electrolytes. One is to increase the Li^+ content to increase charge carrier densities and the other is to change the inherent organization of the elements in the electrolyte to increase Li^+ mobility (i.e. increasing the N/P ratio).[48] The positive correlation between ionic conductivity and the N/P ratio can be attributed to the decrease in electrostatic energy as adding more P-N$<_P^P$ crosslink structural units apparently increases Li^+ mobility.[48] Thus, controlling the nitridation process is key to achieving higher conductivity.

Aliovalent substitution of P^{5+} by Si^{4+} in Li_3PO_4 to create compositions (Li_4SiO_4-Li_3PO_4) promotes and improves Li^+ conduction by shortening the distance between Li^+ binding sites.[48] Thus, silicon-containing LiPON has attracted attention due to its increased ionic conductivity (10^{-5} S/cm).[47] This implies that introducing nitrogen to Li_2O-SiO_2-P_2O_5 systems increases Li^+ mobility presumably via reduced electrostatic interactions. Another series of thin-film solid electrolytes include $Li_xAl_2O_3$, $Li_xSi_yAl_2O_3$, and $Li_2B_4O_7$.[46] All these thin films have several advantages for the development of micro-batteries, which are typically used in ultra-thin watches, computer memory chips, and micro sensors.

1.5 Advantages of polymer electrolytes

A well-established problem with cycling LIBs with any type of electrolyte is that during recharging, Li deposition can be non-uniform causing metal dendrites to grow more rapidly at the expense of uniform coverage such that they can penetrate the electrolyte layer bridging to the cathode.[1-3] Bridging causes a short circuit that can lead to catastrophic failure.[4,5] Consequently, tremendous efforts have been directed to solve this problem.

In part, these efforts led to the development of ceramic electrolytes originally thought to offer a mechanical solution by blocking dendrite growth, including for example LATP [$Li_{1.3}Al_{0.3}Ti_{1.7}(PO_4)_3$] and c-LLZO ($Li_7La_3Zr_2O_{12}$).[6-11]

However, these materials were found to suffer from other problems that render them less than completely practical for battery applications. Thus, LATP undergoes irreversible reduction during cycling.[11] C-LLZO is susceptible to dendrite penetration along grain boundaries again leading to short-circuiting.[12] Thus, other solutions were sought to resolve all of these problems. To this end, a set of materials has been identified that appears to be resistant to dendrite penetration, also wets with Li metal, and offers sufficient ionic conductivity ($>10^{-3}$ $mScm^{-1}$) to permit use as interfaces with LATP and LLZO. These materials include the family of LiPON glasses, Li_xAlO_y, and Li_xZnO_y among others.[1,13]

However, a key problem with these materials is that their Li^+ conductivities are much lower ($2\text{-}10\times10^{-3}$ mS cm^{-1}) than those of LATP (2-6 $mScm^{-1}$[,7-9]) or c-LLZO (0.2-2 $mScm^{-1}$ Al vs Ga doping[10-14]) such that they must be introduced as interface materials at thicknesses of 50-200 nm to offer practical Li^+ cycling. This requirement, to-date, has mandated their application via gas phase deposition methods that include a variety of sputtering methods (e.g. magnetron), chemical vapor as well as atomic layer deposition (CVD/ALD).[1,15] Unfortunately, these methods all require specialized apparatus to control deposition atmospheres, rates, film properties and control of coating uniformity. As such, they represent an expensive and not easily scaled step in the fabrication of ASSBs for large scale commercial applications.

In contrast, polymeric ceramic precursor systems that melt or are soluble offer a facile, low cost alternative for the application of thin ceramic films. Polymer precursor methods of processing ceramics have been the subject of multiple reviews.[15,16] However, to our knowledge, no one has sought to apply this approach to the synthesis of thin LiPON coatings/interfaces for battery applications. This then represents the motivation for the work reported here: to develop and optimize scalable precursors to Li_xPON-like materials that overcome the abovementioned obstacles. A further advantage to the use of polymer precursors is that because they can be applied in a liquid format, the precursors can also be used to coat particles to be used in formulation/processing of anode and cathode components thereby serving as a non-fugitive binder during processing to dense or almost dense components. Alternately, these same precursors can be used to infiltrate porous green or intermediately sintered bodies including electrolytes, anodes and cathodes to both strengthen the component and/or introduce continuous cation conducting phases within the initially porous ceramic such that they can act as a second ion conducting phase plus introducing additional, useful mechanical properties.

Finally, the objective of processing ASSBs has some inherent assembly problems. One can envision sintering anode, cathode and electrolyte thin films in one step starting from green ceramic powder filled polymer thin films that are themselves assembled and thereafter thermally compressed followed by binder burnout and co-sintering all the green layers together at one time. Several problems arise from this approach: (1) not each layer needs the same processing conditions to reach full density with optimal properties but not each layer will sinter correctly under the harshest conditions needed to optimize the performance of the most difficult to sinter layer. (2) On heating, components (ions) in one layer may diffuse into the other layers changing both the phases, chemistries, electrochemistries and even mechanical properties in an unwanted fashion; and (3) binder burnout in the intermediate treatment may lead to pores or other unwanted defects (e.g., chemical reactions) in other layers such that optimization of all global properties is prevented. Consequently, it seems likely that in some cases assembly of ASBs may best be conducted by forming the individual layers first and then assembling them which must involve uniform mating of surfaces.

The problem therein is that the surface roughness (smoothness) is not the same for all thin films needed to produce intimate and/or uniform mating of the two or even three or more components. One solution to this is to formulate a coating that can be a liquid or, a meltable or malleable solid such that a uniform mating of the two surfaces in question is possible. It is advantageous when on heating this coating not only transforms into an ion conducting interface but also acts to uniformly bond one surface to the other. Different surfaces may require different coatings and as such first coatings may be overlaid with second precursor coatings to ensure wetting of all components. It is further advantageous if the precursor coating system can be transformed into a ceramic (glass) interface at temperatures below those needed to sinter the original films such that minimal chemical reactions take place unless desirable. One can envision an instance where the precursor that serves as an “adhesive or bonding” interface also penetrates to some extent the porous substrate to extend, on conversion to ceramic or glass the conducting layer into the substrate some distance while also improving mechanical properties in the substrate and between bonded components.

This is the motivation for the work presented in this dissertation. We have developed polymer precursors to LiPON-like glasses based on design principles discussed below and learned to use them to make protective coatings/interfaces on selected ceramic electrolytes.

1.6 General criteria to design/synthesize polymer precursors

In the following sections, we briefly discuss the design principles that guided our original efforts to prepare superior precursors.[50] Relevant concerns are:

Rheology. For thin films and fiber-forming; processing from solution or melt places some constraints on what is considered useful polymer rheology. In general, the precursor should exhibit thixotropic (non-Newtonian) viscoelastic behavior such that, during extrusion/coating, it flows readily without necking. The viscosity should be sufficiently high at zero shear so that the formed coating or fiber retains its new shape and for fibers are self-supporting. An added mandate for coating is that surface wetting must be uniform.

Latent Reactivity Precursor fibers must be self-supporting, as extruded, whereas substrates provide mechanical support for coatings. However, both must not melt, creep or de-wet during thermal conversion to glass/ceramic. Thus, precursor coatings/fibers must retain some chemical reactivity so they can be rendered infusible before or during heating. Infusibility is commonly obtained through reactions that provide extensive crosslinking. These include free radical, condensation, oxidatively or thermally induced molecular rearrangements.

Pyrolytic Degradation. Most precursors contain extraneous moieties added to aid processability or provide latent reactivity. During pyrolysis these moieties must be eliminated as gases. The decomposition rates and mechanisms require close monitoring to ensure conversion to the correct ceramic material, to avoid retention of impurities or creation of gas-generated flaws (e.g. pores). The processes involved are like binder burnout in ceramic powder compacts.[51,52]

In principle, this criterion is best served if hydrogen is the only extraneous ligand required for stability and/or processability. Indeed, there is often a trade-off between precursor stability or processability and ceramic product purity that mandates processing with a less stable precursor to obtain higher quality ceramic products. In this instance, quality is equated with purity.

High ceramic yield. This criterion, which is product rather than precursor-property driven, is critical to the design and synthesis of new precursors. The need for high ceramic yields arises because of excessive volume changes associated with pyrolytic conversion to ceramic materials. Typical precursor polymers have densities of $\approx$ 1 g/cc whereas typical ceramics have densities > 3.0 g/cc. Thus, a 100 % conversion still leads to volume changes > 66 %. If mass is lost during thermolysis then the volume changes can easily be 90 %.[28] In ceramic fibers, most volume changes occur symmetrically so fiber diameters and lengths shrinks. For thin films, shrinkage for thin (< 1 μm) films typically occurs perpendicular to the substrate with the substrate constraining lateral shrinkage. For thicker films, this may not happen, and shrinkage can lead to mud cracking; highly undesirable for achieving uniform coatings.

Phase and chemical purity. Careful design of precursor chemistry can limit the number of extraneous ligands needed for processability. However, even with small added chemical moiety, impurities can form in the final ceramic. In some instances, heat treating in air or hydrogen can reduce impurity contents to near zero allowing optimization of composition and phase purity. In some instances, some impurities act as sintering aids. For example, most of the thin film electrolytes we have made previously have excess Li as carbonate impurities purposely introduced to compensate for Li_2O loss on sintering.[53,54] The carbonates act as sintering aids promoting densification at lower temperatures as they melt as they decompose with loss of CO_2.[52]

Control of Microstructure and Densification. Dense final products provide optimal mechanical properties. Unfortunately, heating a precursor to high temperatures to convert it to phase pure materials frequently does not lead to dense materials.

As a final comment on criteria for the design, synthesis and processing of precursors, if the precursor targeted is for coatings only, where the substrate provides most of the mechanical properties, a few additional criteria must be considered. First, the precursor must wet the substrate effectively to form uniform, adherent coatings. Some reaction with the substrate may/may not be desirable as a means of achieving either chemical or/and mechanical adhesion.

Additionally, to process flaw (pore and crack) free ceramic coatings using dip, spin on or spray coating processes, it is generally necessary to limit coating thicknesses to < 2 μm. This is because mismatches in coefficients of thermal expansion and the overall densification process lead to compressive stresses in the films. These stresses can provide improved coating adhesion and abrasion resistance; however, at higher thicknesses the compressive/tensile stresses cause mud cracking, unless a ceramic powder filler is used to offset dimensional changes. In addition, for precursors used as non-fugitive binders/adhesives for other ceramic components, control of off-gassing of extraneous organic moieties must be a concern because these are often pore generating species. Slow heating and or the use of pressure can mitigate pore formation.

These general criteria provide a basis for selecting candidate precursors potentially useful for processing both oxide and nonoxide ceramics. For specific materials, additional criteria can also play a role including ease of synthesis, purification and stability toward air and moisture.

One critical criterion is cost. Costly syntheses reduce the utility of a given precursor. However, in ceramic fiber and coating applications, the pyrolytic conversion and post-processing heat treatments designed to provide optimal properties may be more costly than the chemistry.

To date and based on the above criteria, we have developed three LiPON-like precursors (Scheme **1.1**) and coated them on dense, 10-50 µm thick ceramic substrates. We have developed a low cost, minimal step syntheses from commercially available $OP(NH_2)_3$, (can be made from $OPCl_3$ and x's NH_3) having only those elements needed to produce LiPON. A second precursor incorporates Si and C components based on a literature report that introduction of Si and C can give rise to fast Li^+ ion conduction,[37] providing motivation for this selection. A third precursor was synthesized from chlorophosphazene $[Cl_2P{=}N]_3$ and eliminates all oxygen while also incorporating Si and C. Given that most processing will introduce adventitious oxygen, we assume that some nitrogen rich form of LiPON glass is likely to form.

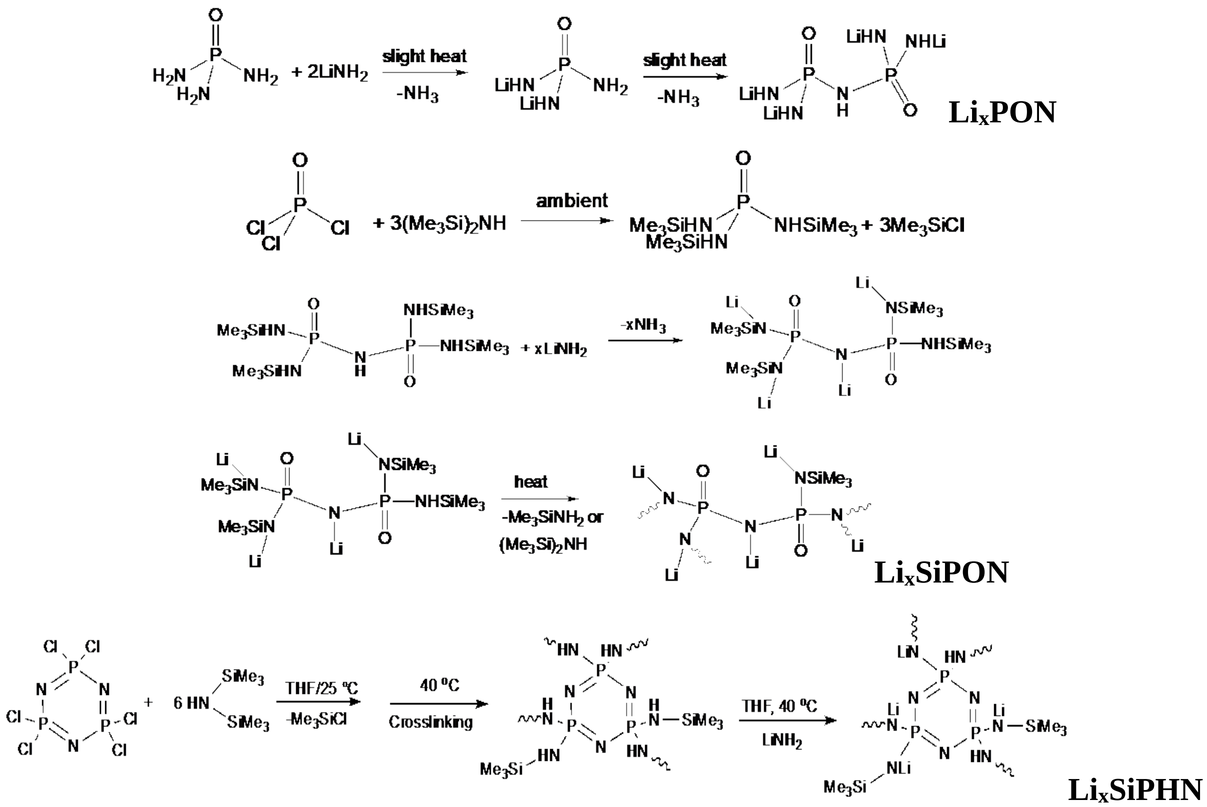

Scheme 1.1. General syntheses of Li_xPON, Li_xSiPON and LiSiPHN precursors.

1.7 Scope of dissertation

As discussed above, solid electrolytes are the key components in enabling the assembly of ASSBs that outperform conventional LIBs as well as offer inherent safety by removing flammable liquid electrolyte. Hence, identifying polymer electrolytes with similar/better electrochemical performance as liquid counterpart is the main focus of the work presented here.

Chapter 2 provides relevant experimental information about the design and synthesis of polymer and inorganic solid electrolytes, as well as descriptions of characterization methods, including X-ray diffraction, scanning electron microscopy, surface area analysis, thermogravimetric analysis, X-ray photoelectron spectroscopy, and electrochemical studies.

Chapter 3 describes the synthesis of a set of polymers that emulate LiPON chemistries and that allow simple and extensive control of composition, degree of lithiation and incorporation of silicon as well as exclusion of oxygen and understand their effects on the ionic conductivity. In depth characterization of LiPON/LiSiON polymer electrolytes to enable the assembly of Li-S batteries is also discussed.

Chapter 4 present a comparative evaluation of different types of polymer precursors (Li_xPON, Li_xSiPHN, and Li_xSiPON) on PEO derived composite films. These active fillers were synthesized via a novel polymer precursor route with controlled lithiation, resulting in a remarkable enhancement on the cation transport. The increase in Li^+ ion concentration and the addition of secondary phase (PON) resulted in decrease in activation energy for PEO/Li_xPON films, indicating a high dissociation ability to yield mobile cations.

Chapter 5 provides the utility of synthesized polymer precursors as a coating material on inorganic solid electrolyte thin films. It is important to have a set of substrates qualified to be used to test the efficacy of the coatings and processing conditions explored. Given that we want to optimize ion conductivity in the resulting ceramized precursors, we also need well-defined substrates that offer: (1) no Li^+ (Al_2O_3) conductivity; (2) minimal Li^+ conductivity ($LiAlO_2$) or (3) good Li^+ conductivity (LATSP). Efforts to optimize the ionic conductivity of coated thin films are presented by electrochemical impedance measurements.

Chapter 6 presents an effective alternate of processing $LiAlO_2$ membranes (< 50 µm) using high surface area, flame made NPs produced via LF-FSP. We also demonstrate optimization of Li^+ conductivity in $LiAlO_2$ membranes through careful engineering of grain boundary properties by introducing a second phase ($LiAl_5O_8$) and modifying sintering conditions to minimize grain boundary resistance.

Chapter 7 describes the synthesis and electrochemical performance of high surface area, phase pure LTO NPs via LF-FSP. Pristine LTO was mixed with $LiAlO_2$ and Li_6SiON electrolytes to improve the ionic and electronic conductivity by simple ball-milling and ultrasonication methods. Detailed electrochemical analysis about the LTO-anolytes is discussed in this chapter.

Chapter 8 discuss about the use of silica derived rice hull ash (SDRHA), derived from a renewable bio-source, RHA, as a potential electrode material for hybrid LICs without any chemical activation. The high surface area and the microstructure of the SDRHA results in high Li-ion mobility and increase surface charge absorption/desorption when assembled in both half and full-cell configurations.

Chapter 9 presents detailed electrochemical performance of the Li_xSiON polymer electrolyte, derived from RHA, an agriculture waste product. XRD studies show the amorphous nature of Li_xSiON polymer electrolyte dried at ambient. The amorphous nature coupled with the high Li content and nitridation resulted in optimal conductivity of the Li_6SiON electrolyte.

Chapter 10 presents an effective method of producing nearly fully dense, single phase, and transparent C12A7 thin films (< 50 μm) by processing LF-FSP derived NPs into green films by tape-casting, thermo-compression and then sintering to 1300℃/3 h/O_2. Subsequent heat treatments in 20/80 H_2/N_2 replaces cage trapped O^{2-} ions forming C12A7:H^- followed by UV irradiation to generate C12A7:e^- with electrical conductivities of 35 mS cm^{-1}.

Chapter 11 provides general conclusions of the work presented in this dissertation as well as recommendations for future work.

References

(1) Chan, C. C. The State of the Art of Electric, Hybrid, and Fuel Cell Vehicles. *Proc. IEEE* **2007**. https://doi.org/10.1109/JPROC.2007.892489.

(2) Albertus, P.; Babinec, S.; Litzelman, S.; Newman, A. Status and Challenges in Enabling the Lithium Metal Electrode for High-Energy and Low-Cost Rechargeable Batteries. *Nat. Energy* **2018**, *3* (1), 16. https://doi.org/10.1038/s41560-017-0047-2.

(3) Väyrynen, A.; Salminen, J. Lithium Ion Battery Production. *J. Chem. Thermodyn.* **2012**. https://doi.org/10.1016/j.jct.2011.09.005.

(4) Goodenough, J. B.; Kim, Y. Challenges for Rechargeable Batteries. *J. Power Sources* **2011**. https://doi.org/10.1016/j.jpowsour.2010.11.074.

(5) Wang, H. C.; Cao, X.; Liu, W.; Sun, X. Research Progress of the Solid State Lithium-Sulfur Batteries. *Front. Energy Res.* **2019**, *7* (October), 1–20. https://doi.org/10.3389/fenrg.2019.00112.

(6) Albertus, P.; Babinec, S.; Litzelman, S.; Newman, A. Status and Challenges in Enabling the Lithium Metal Electrode for High-Energy and Low-Cost Rechargeable Batteries. *Nat. Energy* **2018**. https://doi.org/10.1038/s41560-017-0047-2.

(7) Tarascon, J. M.; Armand, M. Issues and Challenges Facing Rechargeable Lithium Batteries. In *Materials for Sustainable Energy: A Collection of Peer-Reviewed Research and Review Articles from Nature Publishing Group*; 2010. https://doi.org/10.1142/9789814317665_0024.

(8) Bachman, J. C.; Muy, S.; Grimaud, A.; Chang, H. H.; Pour, N.; Lux, S. F.; Paschos, O.; Maglia, F.; Lupart, S.; Lamp, P.; Giordano, L.; Shao-Horn, Y. Inorganic Solid-State Electrolytes for Lithium Batteries: Mechanisms and Properties Governing Ion Conduction. *Chemical Reviews*. 2016. https://doi.org/10.1021/acs.chemrev.5b00563.

(9) Famprikis, T.; Canepa, P.; Dawson, J. A.; Islam, M. S.; Masquelier, C. Fundamentals of Inorganic Solid-State Electrolytes for Batteries. *Nature Materials*. 2019. https://doi.org/10.1038/s41563-019-0431-3.

(10) Manthiram, A.; Yu, X.; Wang, S. Lithium Battery Chemistries Enabled by Solid-State Electrolytes. *Nature Reviews Materials*. 2017. https://doi.org/10.1038/natrevmats.2016.103.

(11) Kilner, J. A. Feel the Strain. *Nat. Mater.* **2008**. https://doi.org/10.1038/nmat2314.

(12) Bradley, J. N.; Greene, P. D. Solids with High Ionic Conductivity in Group 1 Halide Systems. *Trans. Faraday Soc.* **1967**. https://doi.org/10.1039/tf9676300424.

(13) Goodenough, J. B.; Hong, H. Y. P.; Kafalas, J. A. Fast Na+-Ion Transport in Skeleton Structures. *Mater. Res. Bull.* **1976**. https://doi.org/10.1016/0025-5408(76)90077-5.

(14) Jacobs, P. W. M. IONIC CONDUCTIVITY. In *NATO ASI Series, Series B: Physics*; 1983.

(15) Fergus, J. W. Ceramic and Polymeric Solid Electrolytes for Lithium-Ion Batteries. *Journal of Power Sources*. 2010. https://doi.org/10.1016/j.jpowsour.2010.01.076.

(16) Fenton, D. E.; Parker, J. M.; Wright, P. V. Complexes of Alkali Metal Ions with Poly(Ethylene Oxide). *Polymer (Guildf).* **1973**. https://doi.org/10.1016/0032-3861(73)90146-8.

(17) Hu, L.; Zhang, S. S.; Zhang, Z. Electrolytes for Lithium and Lithium-Ion Batteries. *Green Energy Technol.* **2015**. https://doi.org/10.1007/978-3-319-15458-9_8.

(18) He, X.; Zhu, Y.; Mo, Y. Origin of Fast Ion Diffusion in Super-Ionic Conductors. *Nat.*

Commun. **2017**. https://doi.org/10.1038/ncomms15893.
(19) Judez, X.; Zhang, H.; Li, C.; Eshetu, G. G.; Zhang, Y.; González-Marcos, J. A.; Armand, M.; Rodriguez-Martinez, L. M. Polymer-Rich Composite Electrolytes for All-Solid-State Li-S Cells. *J. Phys. Chem. Lett.* **2017**. https://doi.org/10.1021/acs.jpclett.7b01321.
(20) Zheng, Y.; Yao, Y.; Ou, J.; Li, M.; Luo, D.; Dou, H.; Li, Z.; Amine, K.; Yu, A.; Chen, Z. A Review of Composite Solid-State Electrolytes for Lithium Batteries: Fundamentals, Key Materials and Advanced Structures. *Chemical Society Reviews*. 2020. https://doi.org/10.1039/d0cs00305k.
(21) Long, L.; Wang, S.; Xiao, M.; Meng, Y. Polymer Electrolytes for Lithium Polymer Batteries. *Journal of Materials Chemistry A*. 2016. https://doi.org/10.1039/c6ta02621d.
(22) Manuel Stephan, A.; Nahm, K. S. Review on Composite Polymer Electrolytes for Lithium Batteries. *Polymer*. 2006. https://doi.org/10.1016/j.polymer.2006.05.069.
(23) Shriver, D. F.; Papke, B. L.; Ratner, M. A.; Dupon, R.; Wong, T.; Brodwin, M. Structure and Ion Transport in Polymer-Salt Complexes. *Solid State Ionics* **1981**. https://doi.org/10.1016/0167-2738(81)90199-5.
(24) Zhao, Y.; Zhang, Y.; Gosselink, D.; Doan, T. N. L.; Sadhu, M.; Cheang, H. J.; Chen, P. Polymer Electrolytes for Lithium/Sulfur Batteries. *Membranes*. 2012. https://doi.org/10.3390/membranes2030553.
(25) Long, L.; Wang, S.; Xiao, M.; Meng, Y. Polymer Electrolytes for Lithium Polymer Batteries. *Journal of Materials Chemistry A*. 2016. https://doi.org/10.1039/c6ta02621d.
(26) Angell, C. A.; Liu, C.; Sanchez, E. Rubbery Solid Electrolytes with Dominant Cationic Transport and High Ambient Conductivity. *Nature* **1993**. https://doi.org/10.1038/362137a0.
(27) Agrawal, R. C.; Pandey, G. P. Solid Polymer Electrolytes: Materials Designing and All-Solid-State Battery Applications: An Overview. *J. Phys. D. Appl. Phys.* **2008**. https://doi.org/10.1088/0022-3727/41/22/223001.
(28) Chen-Yang, Y. W.; Chen, H. C.; Lin, F. J.; Chen, C. C. Polyacrylonitrile Electrolytes: 1. A Novel High-Conductivity Composite Polymer Electrolyte Based on PAN, LiClO4 and α-Al2O3. *Solid State Ionics* **2002**. https://doi.org/10.1016/S0167-2738(02)00457-5.
(29) Forsyth, M.; Jiazeng, S.; MacFarlane, D. R. Novel High Salt Content Polymer Electrolytes Based on High Tg Polymers. *Electrochim. Acta* **2000**. https://doi.org/10.1016/S0013-4686(99)00328-X.
(30) Mishra, R.; Baskaran, N.; Ramakrishnan, P. A.; Rao, K. J. Lithium Ion Conduction in Extreme Polymer in Salt Regime. *Solid State Ionics* **1998**. https://doi.org/10.1016/s0167-2738(98)00209-4.
(31) Bushkova, O. V.; Zhukovsky, V. M.; Lirova, B. I.; Kruglyashov, A. L. Fast Ionic Transport in Solid Polymer Electrolytes Based on Acrylonitrile Copolymers. *Solid State Ionics* **1999**. https://doi.org/10.1016/S0167-2738(98)00506-2.
(32) Walker, C. N.; Versek, C.; Touminen, M.; Tew, G. N. Tunable Networks from Thiolene Chemistry for Lithium Ion Conduction. *ACS Macro Lett.* **2012**. https://doi.org/10.1021/mz300090m.
(33) Guhathakurta, S.; Min, K. Lithium Sulfonate Promoted Compatibilization in Single Ion Conducting Solid Polymer Electrolytes Based on Lithium Salt of Sulfonated Polysulfone and Polyether Epoxy. *Polymer (Guildf).* **2010**. https://doi.org/10.1016/j.polymer.2009.07.047.
(34) Marzantowicz, M.; Pozyczka, K.; Brzozowski, M.; Dygas, J. R.; Krok, F.; Florjańczyk, Z.; Lapienis, G. From Polymer to Polyelectrolyte: Studies of Star-Branched Poly(Ethylene Oxide) with Lithium Functional Groups. *Electrochim. Acta*

2014. https://doi.org/10.1016/j.electacta.2013.09.167.
(35) Cui, W. W.; Tang, D. Y. Electrospun Poly(Lithium 2-Acrylamido-2-Methylpropanesulfonic Acid) Fiber-Based Polymer Electrolytes for Lithium-Ion Batteries. *J. Appl. Polym. Sci.* **2012**. https://doi.org/10.1002/app.36804.
(36) Sadoway, D. R. Block and Graft Copolymer Electrolytes for High-Performance, Solid-State, Lithium Batteries. In *Journal of Power Sources*; 2004. https://doi.org/10.1016/j.jpowsour.2003.11.016.
(37) Mehta, M. A.; Fujinami, T.; Inoue, T. Boroxine Ring Containing Polymer Electrolytes. *J. Power Sources* **1999**. https://doi.org/10.1016/S0378-7753(99)00151-2.
(38) Mehta, M. A.; Fujinami, T. Novel Inorganic-Organic Polymer Electrolytes - Preparation and Properties. *Solid State Ionics* **1998**. https://doi.org/10.1016/s0167-2738(98)00285-9.
(39) Osińska, M.; Walkowiak, M.; Zalewska, A.; Jesionowski, T. Study of the Role of Ceramic Filler in Composite Gel Electrolytes Based on Microporous Polymer Membranes. *J. Memb. Sci.* **2009**. https://doi.org/10.1016/j.memsci.2008.10.036.
(40) Wu, X.; Wen, Z.; Xu, X.; Liu, Y. Fabrication of Li4SiO4 Pebbles by a Sol-Gel Technique. *Fusion Eng. Des.* **2010**, *85* (2), 222–226. https://doi.org/10.1016/j.fusengdes.2010.01.018.
(41) Wang, W.; Yi, E.; Fici, A. J.; Laine, R. M.; Kieffer, J. Lithium Ion Conducting Poly(Ethylene Oxide)-Based Solid Electrolytes Containing Active or Passive Ceramic Nanoparticles. *J. Phys. Chem. C* **2017**. https://doi.org/10.1021/acs.jpcc.6b11136.
(42) Ahn, J. H.; Wang, G. X.; Liu, H. K.; Dou, S. X. Nanoparticle-Dispersed PEO Polymer Electrolytes for Li Batteries. In *Journal of Power Sources*; 2003. https://doi.org/10.1016/S0378-7753(03)00264-7.
(43) Li, Z.; Huang, H. M.; Zhu, J. K.; Wu, J. F.; Yang, H.; Wei, L.; Guo, X. Ionic Conduction in Composite Polymer Electrolytes: Case of PEO:Ga-LLZO Composites. *ACS Appl. Mater. Interfaces* **2019**. https://doi.org/10.1021/acsami.8b17279.
(44) Masoud, E. M.; El-Bellihi, A. A.; Bayoumy, W. A.; Mousa, M. A. Effect of LiAlO2 Nanoparticle Filler Concentration on the Electrical Properties of PEO-LiClO4 Composite. *Mater. Res. Bull.* **2013**. https://doi.org/10.1016/j.materresbull.2012.12.012.
(45) Temeche, E.; Zhang, X.; Richard, M. L. *Solid Electrolytes for Li-S Batteries. Solid Solutions of Polyethylene Oxide with LixPON and LixSiPON Based Polymers*; 2020.
(46) Manthiram, A.; Yu, X.; Wang, S. Lithium Battery Chemistries Enabled by Solid-State Electrolytes. *Nat. Rev. Mater.* **2017**, *2* (4), 16103. https://doi.org/10.1038/natrevmats.2016.103.
(47) Zhang, X.; Temeche, E.; Richard, M. L. *Design, Synthesis and Characterization of Chemical Precursors to LixPON and LixSiPON Glasses. Materials That Enable All Solid-State Batteries.*; 2020.
(48) Temeche, E.; Zhang, X.; Laine, R. M. Polymer Precursor Derived LiXPON Electrolytes: Toward Li-S Batteries. *ACS Appl. Mater. Interfaces* **2020**. https://doi.org/10.1021/acsami.0c03341.
(49) Chen, R.; Qu, W.; Guo, X.; Li, L.; Wu, F. The Pursuit of Solid-State Electrolytes for Lithium Batteries: From Comprehensive Insight to Emerging Horizons. *Materials Horizons*. 2016. https://doi.org/10.1039/C6MH00218H.
(50) Laine, R. M.; Babonneau, F. Preceramic Polymer Routes to Silicon Carbide. *Chem. Mater.* **1993**, *5* (3), 260–279. https://doi.org/10.1021/cm00027a007.
(51) Yi, E.; Temeche, E.; Laine, R. M. Superionically Conducting B″-Al2O3thin Films Processed Using Flame Synthesized Nanopowders. *J. Mater. Chem. A* **2018**. https://doi.org/10.1039/c8ta02907e.
(52) Yi, E.; Wang, W.; Kieffer, J.; Laine, R. M. Key Parameters Governing the

Densification of Cubic-Li7La3Zr2O12 Li+ Conductors. *J. Power Sources* **2017**. https://doi.org/10.1016/j.jpowsour.2017.03.126.

(53) Yi, E.; Wang, W.; Mohanty, S.; Kieffer, J.; Tamaki, R.; Laine, R. M. Materials That Can Replace Liquid Electrolytes in Li Batteries: Superionic Conductivities in Li1.7Al0.3Ti1.7Si 0.4P2.6O12. Processing Combustion Synthesized Nanopowders to Free Standing Thin Films. *J. Power Sources* **2014**, *269*, 577–588. https://doi.org/10.1016/j.jpowsour.2014.07.029.

(54) Yi, E.; Wang, W.; Kieffer, J.; Laine, R. M. Flame Made Nanoparticles Permit Processing of Dense, Flexible, Li^{+} Conducting Ceramic Electrolyte Thin Films of Cubic-$Li_{7}La_{3}Zr_{2}O_{12}$ (c-LLZO). *J. Mater. Chem. A* **2016**, *4* (33), 12947–12954. https://doi.org/10.1039/C6TA04492A.

Chapter 2

Experimental

2.1 Introduction

This chapter discuss about the experimental methods and characterization tools used in the course of this dissertation. Detailed experimental techniques can be found in each chapter.

2.2 Polymer electrolyte syntheses

The polymer precursors are synthesized in two steps. The first step is to substitute the -Cl in the phosphorus source ($OPCl_3$ or $Cl_6N_3P_3$) with $-NH_2$ (from $NaNH_2$) or $-NHSiMe_3$ [from $NH(SiMe_3)_2$] producing byproduct NaCl or Me_3SiCl (Table **2.1**). It is followed by lithiation from the lithium source $LiNH_2$. Table **2.2** lists $LiNH_2$ amounts and properties of as-synthesized precursors. Distilled Tetrahydrofuran (THF) is used as the solvent. All syntheses are done under N_2 in Schlenk flasks.

Table 2.1. P, N source and the stoichiometry of the first step synthesis of polymer precursors.

Polymer precursor (unlithiated)	P source	N source	Byproduct	Stoichiometry
PON	$OPCl_3$	$NaNH_2$	NaCl	Na/Cl = 1.1
SiPON	$OPCl_3$	$NH(SiMe_3)_2$	Me_3SiCl	$SiMe_3$/Cl = 1.2
SiPHN	$Cl_6N_3P_3$	$NH(SiMe_3)_2$	Me_3SiCl	NH/Cl = 1.1

Table 2.2. Lithiation of the polymer precursors.

Polymer precursor	$LiNH_2$/-NH[a]	Appearance[b]	Typical yield[c], %
Li_3PON	1	Light-yellow suspension	50-70
Li_6PON	2	Light-yellow suspension	50-70
Li_2SiPHN	1	Orange solution	80-90
Li_3SiPON	1	Yellow solution	≥90
Li_6SiPON	2	Orange solution	≥90

[a] The molar ratio of $LiNH_2$ to the -NH in the unlithiated precursors. [b] The appearance of the centrifuged precursor supernatants. [c] The obtained yield divided by the theoretical yield.

Based on precursor design criteria described previously,[22,39] three LiPON-like precursors were synthesized. The simplest approach uses oligomeric $OP(NH_2)_3$ which, following lithiation, has only those elements needed to produce LiPON. A second precursor incorporates Si for the reasons noted above[6,27–29]

The third precursor was synthesized from the chlorophosphazene $[Cl_2P{=}N]_3$ eliminating all oxygen but also incorporating Si.

2.2.1 Synthesis of PON and Li_xPON precurors

The simplest synthetic approach is ammonolysis of $OPCl_3$ forming phosphoramide $OP(NH_2)_3$ as shown in Scheme **2.1**:

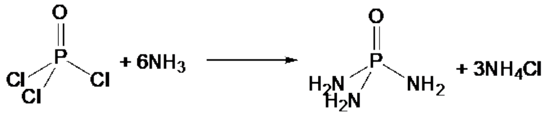

Scheme 2.1. Ammonolysis of $OPCl_3$.

However, depending on solvent, byproduct NH_4Cl is difficult to remove/interferes with purification. An alternative uses $NaNH_2$ as shown in Scheme **2.2**:

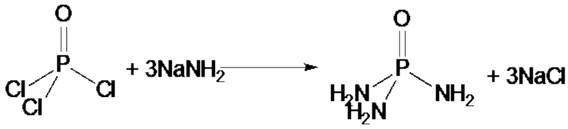

Scheme 2.2. Reaction of $OPCl_3$ with $NaNH_2$.

$NaNH_2$ rather than $LiNH_2$ is used because LiCl is more soluble in polar solvents than NaCl and may not precipitate as easily and thus, $NaNH_2$ is preferable.

Thereafter, there are two options for producing LiPON precursors. The first is to promote oligomerization/polymerization following reactions shown as stepwise condensation reactions presented in Scheme **2.3**:

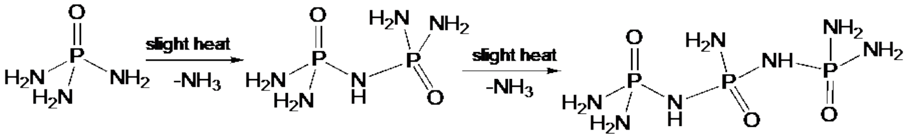

Scheme 2.3. Linear oligomerization/polymerization of $OP(NH_2)_3$ forming PON precursor.

In a 200 ml round bottom Schlenk flask, $NaNH_2$ (7.0 g, 0.179 mol) was first added to 80 mL of distilled THF, then $OPCl_3$ (5.0 ml, 53.6 mmol) was added with a graduated pipette. All was done in an ice bath under N_2. The ice bath was removed after 1 d of reaction and the reaction kept running at room temperature under N_2 for 1 week. The reaction mixture remained cloudy due to insoluble NaCl byproduct.

Thereafter, the soluble and insoluble parts in the reaction mixture were separated by centrifugation. This results into 50 ml of transparent solution. To obtain the yield of the reaction, a small sample (3 ml) was taken from the solution and vacuum dried at 60 °C on a Schlenk line. The product is a yellow solid with a yield of 0.28 g, the total yield would be ~4.5 g, which is about 90 % of theoretical yield.

As shown in Scheme **2.4**, only linear oligomers are formed. However, it is highly likely that both branched and cyclomeric products arise coincidentally:

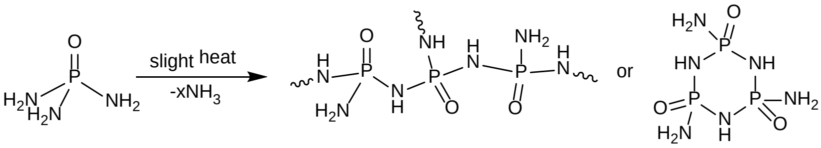

Scheme 2.4. Branched or cyclomeric products on heating of $OP(NH_2)_3$.

Following the synthesis of PON precursor, $LiNH_2$ (3.6 g, 0.160 mol, equivalent amount of -NH in the PON precursor) was added to the PON precursor solution under N_2 in an ice bath. The reaction mixture stayed cloudy due to the low solubility of $LiNH_2$. The ice bath was removed after 1 d reaction. The reaction kept running at room temperature for 1-2 weeks or kept warming at 40 °C for 1 week. Thereafter, the reaction mixture of Li_3PON precursor was centrifuged to separate the liquid and solid parts. This results into 30 ml of yellow stable suspension. The yield is ~5 g (about 80 % of theoretical yield).

The volatile system might offer a novel method for chemical vapor deposition. At this juncture, it is possible to now add Li as shown in Scheme **2.5**:

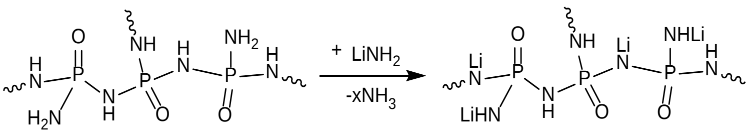

Scheme 2.5. Lithiation of PON.

As an alternative, our preferred choice is to do this right after the first step. This may not be optimal, but it appears to be the easiest approach as shown in Scheme **2.6**:

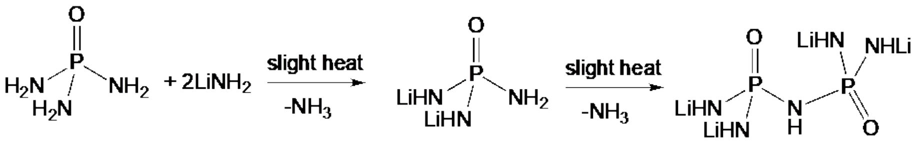

Scheme 2.6. Lithiation of $OP(NH_2)_3$ followed by oligomerization/polymerization, forming LiPON precursor.

The Li content can be controlled by the degree of initial lithiation. One can also envision promoting a condensation reaction as suggested in a simple fashion above. The condensation process is likely more complex than shown. However, one can use these intermediates as precursors to make LiPON thin films, binders or bonding agents by using traditional precursor processing techniques.[22,39] In some instances, the intermediates will be liquids and in others, they will be meltable or soluble solids. As demonstrated below it is possible to make Li_3PON and Li_6PON precursors simply by choosing the amount of $LiNH_2$ to add.

2.2.2 Polymer precursors to Li_xSiPON

As noted above, a few reports describe silicon containing LiPON or LiSiPON.[6,27–29] To our knowledge, LiSiPON precursors have not been synthesized via the route shown in Scheme **2.7**,which takes advantage of the affinity of Si for Cl:

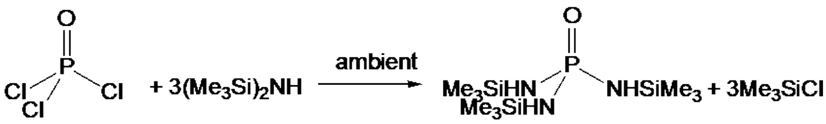

Scheme 2.7. Reaction of $OPCl_3$ with $(Me_3Si)_2NH$ (mole ratio = 1:3).

In a 200 ml round bottom Schlenk flask, 80 ml of distilled THF was first collected, $(Me_3Si)_2NH$ (20.1 ml, 96.6 mmol) and $OPCl_3$ (5.0 ml, 53.6 mmol) were then added via graduated pipettes. All was done in an ice bath under N_2. Initially, the reaction mixture was transparent, 5-10 min after stirring, insoluble solid started to form from the reaction and the mixture became cloudy. The ice bath was removed after 1 d of reaction and the reaction kept running at room temperature under N_2 for 1 week. Thereafter, the reaction mixture of SiPON precursor was centrifuged to separate the liquid and solid parts. This results into 60 ml of transparent solution. A small sample (3 ml) was taken from the solution and vacuum dried at 60 °C on a Schlenk line. The product is a yellow viscous liquid with a yield of 0.15 g, the total yield would be ~3 g, which is ~80 % of theoretical yield.

A modified route uses (Scheme **2.8**) less than 2.5 $(Me_3Si)_2NH$ or:

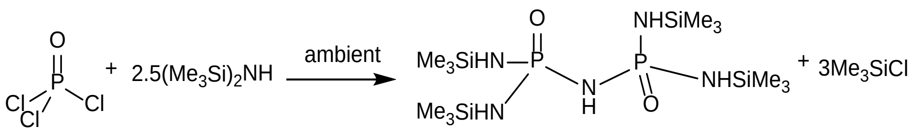

Scheme 2.8. Reaction of $OPCl_3$ with $(Me_3Si)_2NH$ (mole ratio = 1:2.5).

One can envision promoting polymerization using less $(Me_3Si)_2NH$ (≥1.5), forming SiPON precursor. At this stage, one can lithiate as shown in Scheme **2.9**:

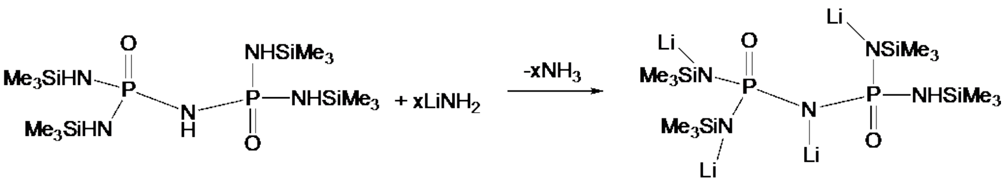

Scheme 2.9. Lithiation of SiPON.

and then warm as suggested below, which is not likely the only reaction pathway as presented in Scheme **2.10**:

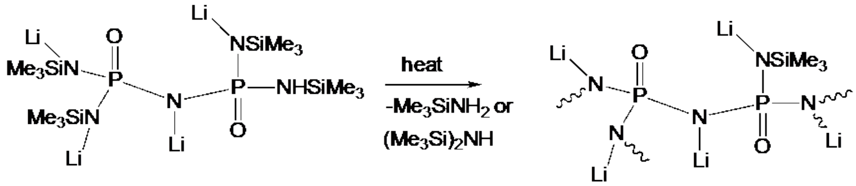

Scheme 2.10. Oligomerization/polymerization forming LiSiPON precursor.

Following the synthesis of SiPON precursor, $LiNH_2$ (1.8 g, 77.3 mol, equivalent amount of -NH in the SiPON precursor) was then added to the SiPON precursor solution under N_2 in an ice bath. The reaction mixture stayed cloudy due to the low solubility of $LiNH_2$. The ice bath was removed after 1 d reaction. The reaction kept running at room temperature for 1-2 weeks or kept warming at 40 °C for 1 week.

Thereafter, the reaction mixture of Li_3SiPON precursor was centrifuged to separate the liquid and solid parts. This results into 50 ml of yellow transparent solution. The yield is ~3 g (about 70 % of theoretical yield). The resulting material compositions will depend on the amount of $LiNH_2$ and method of processing. The conductivity will be determined by this as well.

2.2.3 SiPHN and Li_xSiPHN systems

To investigate the use of a polymer solely based on phosphorus and nitrogen, one can envision starting from the commercial cyclomer: $[Cl_2P{=}N]_3$, replacing Cl with NH via the Si-Cl exchange process, followed by lithiation with $LiNH_2$ as demonstrated in Scheme **2.11**:

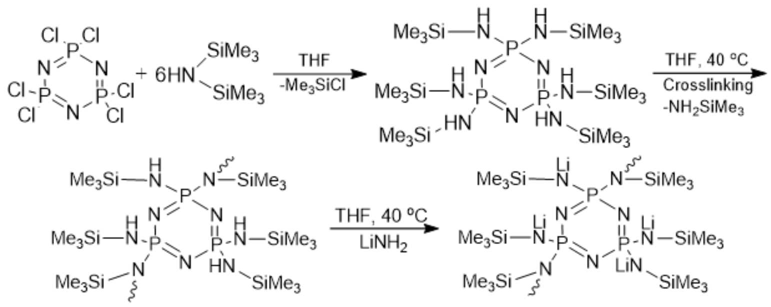

Scheme 2.11. Synthesis of LiSiPHN precursor.

As detailed in the experimental, we followed this approach in formulating systems as illustrated, targeting processable polymers by using non-stoichiometric amounts of $(Me_3Si)_2NH$.

In this work, “x” in Li_xPON, Li_xSiPHN and Li_xSiPON stands for the Li content, which is based on the theoretical Li/P ratios of the corresponding precursor.

2.3 Nanopowder (NP) synthesis

Typically, nanoparticles (< 100 nm) show physical and chemical properties different from their bulk form attributed to the high fraction of atoms at or near the surface.

$LiAlO_2$, Li_4TiO_2, and $Ca_{24}Al_{28}O_{64}$ NPs were synthesized by using LF-FSP method. Sections 2.3.1 and 2.3.2 describes the precursor synthesis and NP production methods.

2.3.1 Precursor synthesis

In this dissertation, two types of precursors are mainly used as a starting material for producing nanoparticles. The first is metal carboxylates, synthesized by reacting metal hydroxides, oxides, or carbonated with excess carboxylic acid. The second is metal-atrane compounds, synthesized by reacting metal hydroxides or alkoxides with triethanolamine at selected molar ratios. The representative examples are briefly discussed below.

Lithium propionate. [$LiOH{\cdot}H_2O$, 113 g, 2.7 mol] was reacted with excess propionic acid (500 ml, 6.8 mol] in a 1 L flask equipped with a still head at 130 °C for 2 h in N_2 with coincident distillation of byproduct water. During the reaction, the solution was magnetically stirred until a transparent liquid was obtained. On cooling to room temperature, [$LiO_2CCH_2CH_3$] crystallizes and can be filtered off.

Alumatrane. Al[$OCH(CH_3)CH_2CH_3$, 200 ml, 0.8 mol] was reacted with [$N(CH_2CH_2OH)_3$, 194 ml, 0.96 mol] at a molar ratio of 1 to 1.2, in a 1 L round bottom flask under N_2 flow. [$N(CH_2CH_2OH)_3$] was added slowly via addition funnel while the mixture was magnetically stirred constantly over a 4 h period. The product alumatrane, dissolved in byproduct butanol, was analyzed by TGA giving a ceramic yield of 7.5%.

2.1.1. Liquid flame spray pyrolysis (LF-FSP)

The metalloorganic precursors are mixed at selected molar ratios and are dissolved in anhydrous ethanol to give a 3 wt. % ceramic yield solution. The precursor solution is aerosolized with oxygen into a chamber where it is ignited via methane/oxygen pilot torches and combusted in an oxygen rich environment. The resulting NPs are collected down-stream in rod-in-tube electrostatic precipitators (ESP) operated at 10 kV. The schematic of the LF-FSP apparent is displayed in Figure **2.1**.

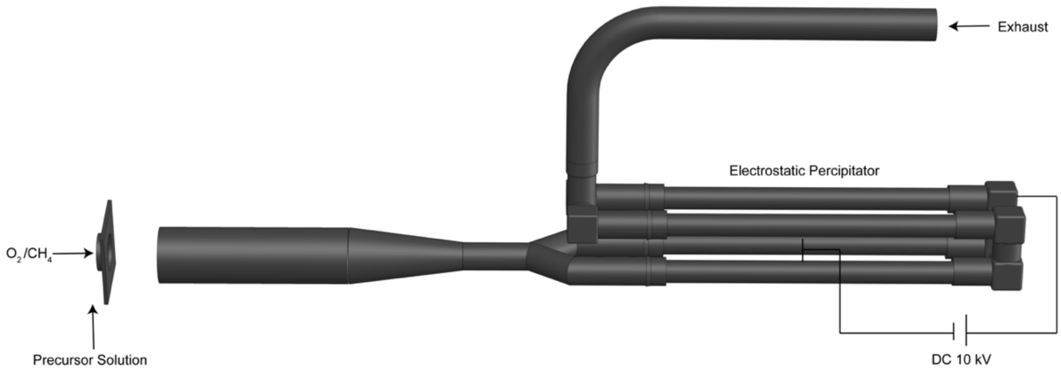

Figure 2.1. Schematics of LF-FSP apparatus

2.3.2 Thin film processing

As-produced NPs (10-20g) were first dispersed in anhydrous ethanol (300-500 ml) with selected dispersant polyacrylic acid or bicine (1-4 wt.%), using an ultrasonic horn at 100 W for 10 min. The suspension was left to settle for overnight to allow larger particles to settle. Supernatant was decanted and the recovered solution was poured into a clean beaker and left to dry overnight in the oven (60 °C). The dried powders were ground in an alumina mortar and pestle.

Ceramic-polymer composite slurries were processed by mixing the cleaned NPs (0.7-1 g), benzyl butyl phthalate (0.1-0.15 g) as a plasticizer, poly acrylic acid (0.01g) as a dispersant, polyvinyl butyral (0.1-0.15 g) as a binder dissolved in selected polar solvent (1.5 -2 ml). The mixture was placed in a 20 ml vial and milled with spherical alumina beads (6 g) with 3 mm diameter media overnight to homogenize the suspension. Suspension was cast using a wire wound rod coater (Automatic Film Applicator 1137, Sheen Instrument, Ltd). After solvent evaporation, dried green films were uniaxially pressed in between stainless-steel dies at 100 °C with a pressure of 50–70 MPa for 5 min using a heated bench (Carver, Inc) top press to improve packing density.

2.4 Characterization

GPC analyses were done on a Waters 440 system equipped with Waters Styragel columns (7.8 × 300, HT 0.5, 2, 3, 4) with RI detection using an Optilab DSP interferometric refractometer and THF as solvent. The system was calibrated using polystyrene standards. Analyses were performed using Empower 3 Chromatography Data Software (Waters, Corp., Milford, MA).

MALDI-TOF was done on a Micromass TofSpec-2E equipped with a 337 nm nitrogen laser in negative-ion reflectron mode, trihydroxyanthracene was used as the matrix.

Samples were prepared by mixing solutions of the matrix (10 mg mL^{-1} in THF) and polymer precursor sample (1 mg mL^{-1} in THF), 1:1 volumetric ratio, and blotting the mixture on the target plate. The calculation of polymer precursor structures based on MALDI was done by a Python program written by Andrew J. Alexander.

FTIR Spectra analyses were run on Nicolet 6700 Series FTIR spectrometer (Thermo Fisher Scientific, Inc.) was used to measure FTIR spectra. 1 wt. % of the samples were mixed with KBr (International Crystal Laboratories); the mixtures were ground rigorously with an alumina mortal pestle; and the dilute samples were packed in the sample holder to be analyzed. Prior to data acquisition in the range of 4000-400 cm^{-1}, the sample chamber was purged with N_2.

TGA and differential thermal analysis (DTA) were performed on an SDT Q600 simultaneous TGA/DTA (TA instrument, Inc.). Samples (15-25 mg), hand pressed in a 3- mm dual action die, were placed in alumina pans and heated to 800 °C at 10 °C min^{-1} under constant N_2 flow (60 mL min^{-1}).

XRD. were characterized using Rigaku Rotating Anode Goniometer (Rigaku Denki., LTD., Tokyo, Japan). Cu Kα (λ = 1.54 Å) radiation operating at working voltage of 40 kV and current of 100 mA was used. Scans were continuous from 10 to 80° 2θ using a scan rate of 3-5 min^{-1} in 0.01 increments. The presence of crystallographic phases was determined by using Jade program 2010 (Version 1.1.5 from Materials Data, Inc.)

AC Impedance data were collected with broadband dielectric spectrometer (Biologics). "EIS spectrum analyser" software was used for extracting total resistance. The total conductivity (σ_t) was calculated using the equation (σ_t= t(A*R)), where t is the thickness of the sample, A is the active area of the electrode and R is the total resistivity obtained from the Nyquist plots. The constant current cycling experiments were carried out using Biologics SP300 potentiostat/galvanostat.

XPS experiments were carried out on a Kratos Axis Ultra XPS system at room temperature under 3.1×10^{-8} Pa using monochromatic Al source (14 kV and 8 mA). Binding energies of all the elements were calibrated relative to the gold with Au $4f_{7/2}$ at 84 eV. All the data were analyzed by CASAXPS software.

Specific Surface Area (SSA) Analyses Micromeritics ASAP 2020 sorption analyzer was used to obtain SSA data. Samples (400 mg) were degassed at 300 ℃/5 h, and each analysis was run at −196 ℃ (77 K) with nitrogen gas. BET multipoint method using ten data points with relative pressures of 0.05–0.30 was used to determine SSAs.

SEM micrographs of as-produced and sintered thin films were taken using JSM-IT300HR In Touch Scope SEM (JEOL USA, Inc.) For imaging purpose, thin films were fractured, and powders were used as is. SPI sputter coater (SPI Supplies, Inc.) was used to sputter coat all the samples with gold and palladium.

UV Treatment. SUNRAY 400 SM (Uvitron International, Inc.) was used as a source of UV-light. Films were illuminated by UV-light for 1 h before measuring electronic conductivity.

Electronic conductivity measurements AC impedance data was collected using (Novocontrol technologies, Hundsangen, Germany) in a frequency range of 10 MHz to 1 Hz at -20° to 85 °C. Film surfaces were coated with Au/Pd electrodes, 1 mm in diameter, using a SPI sputter coater. Nyquist plots were obtained using EIS spectrum analyzer software to estimate the total resistance of the films.

Chapter 3

Polymer Precursor Derived Li_XPON Electrolytes

3.1 Introduction

Traditional Li^+ batteries employ molecular electrolytes dissolved in organic solvents imposing battery design and size restrictions that have inherent safety risks and constrain service temperatures.[1,2] In contrast, solid-state electrolytes offer potential to reduce overall battery footprints thereby increasing energy densities coincident with improved safety.[3–5] However, most solid electrolytes suffer from low ionic conductivities or limited stability windows. Lithium phosphorus oxynitride glass (LiPON) is a commonly used solid-state electrolyte. Since its discovery in the early '90s by Bates *et al.*,[6,7] the material has received increasing attention due to its broad electrochemical stability window (0-5 V vs Li^+/Li),[8–10] reasonable conductivity (10^{-6} S cm^{-1}),[8–11] and negligible electronic conductivity (10^{-7} μS cm^{-1}).[1,10]

LiPON solid electrolytes enable ASB thin film batteries.[1] LiPON thin films are typically processed by radio frequency magnetron sputtering (RFMS) deposition of lithium silicates and lithium phosphate in Ar or N_2 atmospheres.[8,12] Other synthesis methods include pulse laser deposition (PLD),[13] electron-beam (EB) evaporation,[14] ion beam assisted deposition (IBAD),[15] plasma-assisted direct vapor deposition (PA-DVD),[16] ion beam sputtering (IBS),[17] and plasma-enhanced metalloorganic chemical vapor deposition (MOCVD).[18] Table **3.1**. summarizes the properties of a variety of LiPON materials produced by vacuum deposition.

Table 3.1. Examples of LiPON thin coating processes and properties.

Composition	N/P ratio	Synthesis method	Thickness	Conductivity[a] (S/cm)	Ref.
$Li_{3.3}PO_{3.8}N_{0.24}$ to $Li_{3.6}PO_{3.3}N_{0.69}$	0.24-0.69	RFMS of a Li_3PO_4 target in N_2	1 μm	2 (±1) × 10^{-6}	[8]
$Li_{3.3}PO_{2.1}N_{1.4}$	1.4	RFMS of a Li_3PO_4 target in N_2	1 μm	1.8 × 10^{-6}	[12]
LiPON	N/A	PLD	1-3 μm	1.6 × 10^{-6}	[13]
LiPON	N/A	EB evaporation of Li_3PO_4	N/A	6.0 × 10^{-7}	[14]
LiPON (Y290, Y301)	N/A	IBAD of thermally evaporated Li_3PO_4	1.05 μm	Y290: 1.3 × 10^{-6} Y301: 9.0 × 10^{-7}	[15]
LiPON	0.39-1.49	PA-DVD	0.3-2 μm	10^{-7}-10^{-8}	[16]
Ultra-thin LiPON	N/A	IBS	≥12 nm	1-2 × 10^{-7}	[17]
$Li_{2.9}PO_{4.5}N_{0.42}$ to $Li_{3.1}PO_{4.1}N_{0.42}$	0.42	MOCVD	N/A	2.75-2.95 × 10^{-7}	[18]

[a] Conductivity at room temperature

The main limitation to gas phase deposition methods centers on their low deposition rates limiting their utility for fabricating large surface area targets or multiple targets simultaneously. For example, RFMS deposition rates are often <3.0 nm min^{-1},[12,16,19] PLD films deposition rates range 13.3-50 nm min^{-1},[13,16] while those processed using IBAD can approach 70 nm min^{-1}.[15,16] Additionally, controlling the extent and uniformity of Li_3PO_4 nitridation can be challenging. Sputtering is also limited to depositing high quality films on 3D geometries.[20] To overcome these obstacles, researchers have been developing alternative deposition techniques, *i.e*. atomic layer deposition (ALD) for fabrication of uniform, thin, and conformal LiPON films.[21] Unfortunately, these methods all require specialized apparatus to control deposition atmospheres, rates, film properties and coating uniformity. As such, they represent an expensive step in fabricating ASBs which makes it challenging for commodity applications.

In contrast, polymer precursors that melt or are soluble offer a facile, low cost alternative as they permit application in liquid format; easy to control and scale. Polymer precursor methods of processing ceramics are the subject of multiple reviews.[22–26] However, to our knowledge, no one has sought to apply this approach to processing thin Li_xPON films for battery applications. This then represents the motivation for the work reported here: to develop and optimize scalable precursors to Li_xPON-like materials that overcome the abovementioned obstacles.

Additionally, studies have shown that doping Li_xPON with Si improves ionic conductivity.[6,27–29] Lee *et al.*[27,28] report that introducing Si lowers activation energies increasing conductivities up to 10^{-5} S cm^{-1}. Su *et al.*[29] prepared Li_xSiPON with different compositions by RFMS. The highest conductivity found at ambient was $\approx 1 \times 10^{-5}$ S cm^{-1} with an activation energy ≈ 0.41 eV at Si:P = 1:1. This provides the impetus to include Li_xSiPON precursors in our repertoire as presented below.

Furthermore, if we assume that oxygens with two lone electron pairs and higher electronegativity may bind Li^+ more tightly than nitrogen with only one electron pair and a lower electronegativity, then it seems logical to explore using a polymer based solely on phosphorus and nitrogen leading to our studies on Li_xSiPHN precursors.

Thus, LiPON glasses provide a design basis for synthesizing sets of oligomers/polymers by lithiation of $OP(NH_2)_{3-x}(NH)_x$ [from $OP(NH)_3$], $OP(NH_2)_{3-x}(NHSiMe_3)_x$ and $[P{=}N]_3(NHSiMe_3)_{6-x}(NH)_x$. The resulting systems have degrees of polymerization of 5-20. Treatment with selected amounts of $LiNH_2$ provides varying degrees of lithiation and Li^+ conducting properties commensurate with Li^+ content.

The objective here was to characterize the electrochemical and physical properties of the polymers through electrochemical impedance (EIS), thermogravimetric analysis (TGA), X-ray powder diffraction (XRD), FTIR, matrix-assisted laser desorption/ionization (MALDI), NMR, and X-ray photoelectron spectroscopy (XPS).

Coincidentally we explored using these Li_xPON emulating oligomers/polymers as Li^+ electrolytes and as stable interface between Li and a sulfur-based cathode (SPAN).[30] The theoretical energy density of Li-S systems (~2600 Wh kg^{-1})[31] is 5× higher than traditional Li-ion systems.[32–34] The combination of abundant, inexpensive, nontoxic, and environmentally attractive features makes Li/S a promising next-generation energy storage technology.[35–37] The stability of the Li-S cell at high c-rates (0.5C) and over long cycle times (>120) appears to arise, at least in part due to the electrochemical stability of the Li_xSiPON emulating polymer electrolyte.

3.2 Cell fabrication

Celgard separator (25 µm × 12 mm diameter) substrates were dip-coated for 1 min in Li_3PON (0.05 g ml^{-1}), Li_6PON (0.05 g ml^{-1}), Li_2SiPHN (0.08 g ml^{-1}), Li_3SiPON (0.1 g ml^{-1}), and Li_6SiPON (0.1 g ml^{-1}) solutions. Celgard separator were purchased from (MTI, Richmond, CA). These experiments were conducted to measure coating impedances without heat treatments; similar to measuring the impedance of conventional liquid electrolyte-soaked separators. The total conductivity [$\sigma_t = T/(A \times R)$], where T is the thickness of the Celgard, A is the contact area between the Celgard and the stainless steel (SS) disk (diameter = 16 mm), and R is the total resistivity obtained from the straight line of the real axes from the Nyquist plot.[40]

3.2.1 Electrochemical characterization

The electrochemical compatibility of the polymer precursor solutions in THF (20 µl) was investigated using EIS of the stainless steel (SS)/Celgard+polymer precursor/SS with a potential amplitude of 10 mV from 0.1 to 100 kHz**.** The electrochemical stability of the polymer precursor was investigated by linear sweep voltammograms, which was obtained on Biologics instrument at a scanning rate of 1 mV s^{-1}, where the polymer precursor coated Celgard was sandwiched between lithium anode and SS.

To further assess polymer electrochemical properties, symmetric cells were assembled to study the effects of current density on the stability and kinetics of the Li/ polymer electrolyte interface. Before cell assembly, the metallic Li (~2 cm^2) was scraped exposing a clean surface. Symmetric and half coin cells were constructed using the standard procedure and compressed at ~0.015 psi using digital pressure controlled electric crimper (MTI, Richmond, CA).

The Celgard was dip-coated for 1 min in Li_3PON (0.05 g ml^{-1}), Li_6PON (0.05 g ml^{-1}), Li_2SiPHN (0.08 g ml^{-1}), Li_3SiPON (0.1 g ml^{-1}), and Li_6SiPON (0.1 g ml^{-1}) polymer precursor solutions and heated to 90 °C/12 h/vacuum prior to half and symmetric cell assembly. Furthermore, polymer precursors in THF solution (20 µl) were also used as an additional electrolyte to wet the surface of the electrodes. The Li/Celgard+polymer precursor/Li symmetric cells were cycled at room temperature at the desired current densities of (±0.1-7.5 mA) with a rest period of 10 min between each current step. The Li metal, polymer electrolytes, Celgard, and SPAN were stored in an argon filled glove box (MBRAUN) with an average H_2O and O_2 content below 0.1 ppm.

The SPAN electrode was prepared by coating 70:15:15 wt.% mixture of SPAN: C65: PVDF in NMP on carbon coated Al foil.[30] The cathode was then vacuum dried at 60 °C. After drying the electrode, 14 mm in diameter SPAN were punched out and transferred to coin cells. The SPAN /Li_6SiPON/Li half-cell was charged and discharged to the cutoff voltages of 1-3 V using 0.5 C rate. Specific capacities were calculated based on the mass of sulfur in the cathode (1C = 1672 mAh g^{-1}).

3.3 Results and discussions

In the following section, we briefly explain characterizations of the polymer precursors, a more detailed description is available elsewhere.[38] We first monitored compositional and structural changes caused by the degree of lithiation and by the addition of silicon. The extent of lithiation and nitrogen content and its effect on the structure are discussed.

3.3.1 Characterization of polymer precursors

GPC, MALDI-ToF and TGA-DTA (800 °C N_2 $^{-1}$) studies of polymer precursors are discussed in detail elsewhere.[38] Table **3.2** compares the MWs, ceramic yields (CYs) and likely structural components of the polymers based on GPC, MALDI and TGA-DTA studies. All the polymers have similar CYs of 45-65 wt. %. In general, CYs improve with increases in MWs.

Table 3.2. MWs, CYs and estimated compositions of polymer precursors.

Polymer precursor	MW[a], kDa	#monomer units[b]	CY[c], %	T_d(5%)[d], °C	T_m[e], °C	Likely monomer structures[f]
Li_3PON	0.6-1.4	5-15	50-60	150-180	560-580	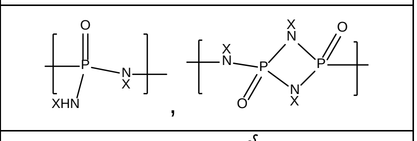
Li_6PON	0.6-1.9	5-20	50-60	150-180	570-590	
Li_2SiPHN	0.7-1.5	2-4	45-55	140-160	≈600	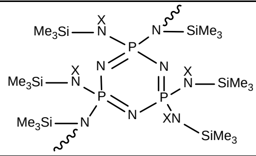

Li_3SiPON	0.5-1.2	5-13	45-60	150-200	≈600	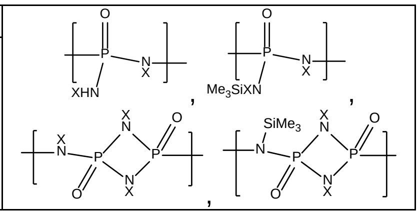
Li_6SiPON	0.7-1.5	6-15	50-65	150-170	≈600	

[a] MW = molecular weight. [b] Number monomer units calculated based on MALDI. [c] CY = ceramic yield in TGA (800 °C/N_2). [d] T_d (5%) = 5 % mass loss temp. in TGA (N_2/10°C/min). [e] T_m = endotherm with no associated mass loss in DTA (N_2/10 °C/min). [f] X = H or Li

Figure **3.1(a)** shows the FTIR of representative as-synthesized precursors. Table **3.3** summarizes literature reported FTIRs of LiPON glasses. Typically, the precursors exhibit νN-H (~3000 cm^{-1}, ~1500 cm^{-1}), νP=O (1150-1300 cm^{-1}), νP-O^- (1000-1150 cm^{-1}), νP-N=P (800-900 cm^{-1}) and νP-O-P (1150, 780-680 cm^{-1}) absorptions.[18,41–46] A small peak at ~2200 cm^{-1} is also observed for all the precursors; suggested by Pichonat *et al.*[45] and Stallworth *et al.*[46], to arise from P-N$<^P_P$ or P-N=P bonds. Additionally, Si-containing precursors exhibit νC-H at ~2950 cm^{-1} from $SiMe_3$ groups. Precursor FTIR often present νO-H at ~3400 cm^{-1}, likely from unreacted $LiNH_2$ that reacts with trace moisture forming LiOH. FTIR spectra recorded with stringent control of atmosphere during sample preparation show reduced νO-H intensities.

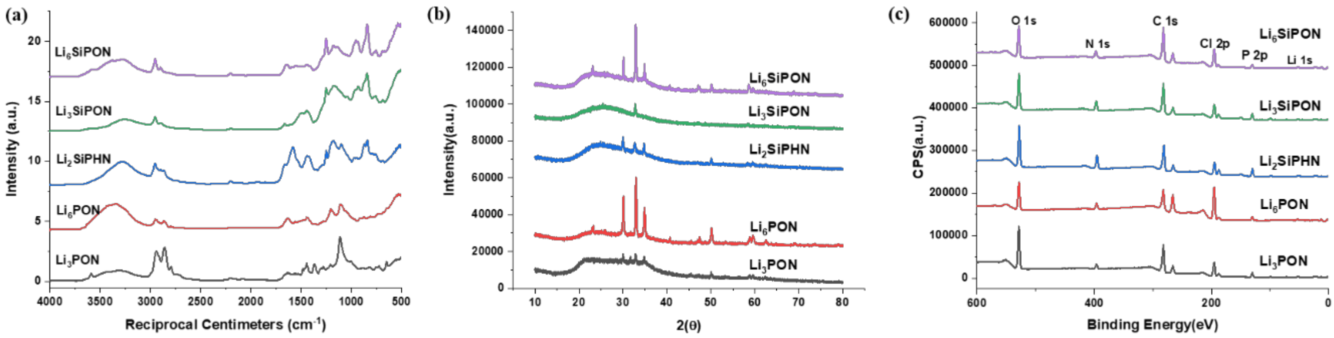

Figure 3.1. (a) FTIR spectra, (b). XRD. (C). and XPS of Li_xPON, Li_xSiPHN, and Li_xSiPON precursors.

Table 3.3. Reported FTIR of LiPON glasses.

IR bands	Wavenumber, cm^{-1}	Reference
P=O	1150-1300	1-5
P-O^-	950-1150	
P-O-P	1150, 780-680	
P-N=P	800-900	
P-N=P or P-N$<^P_P$	2200-2100	5, 6
-NH_2/-NH	~3400	1
Li-O-P	450-550, 850-925, 1450-1500	2

The Li_3PON, Li_6PON, Li_2SiPHN, Li_3SiPON, and Li_6SiPON precursors were heated to 60 °C/Vacuum to remove solvent. Dried powders (1 g) were pelletized (3 mm diameter die). Pellets were heated between alumina plates to 100 °C/2 h/1 °C min^{-1}/120 ml min^{-1} N_2.

XRDs of Li_3PON, Li_2SiPHN, and Li_3SiPON show low intensity peaks ~30°, 33°, and 35° 2θ dominated by a broad amorphous hump centered ≈ 22 ° 2θ. The Li_6PON and Li_6SiPON pellets also show three peaks at 30°, 33°, and 35° 2θ indexed to partially crystalline $Li_{2.88}PN_{0.14}O_{3.73}$.[47] High Li^+ content pellets seem to have higher intensity peaks compared to the pellets with lower Li^+ concentrations as shown in Figure **3.1(b)**.

The absence of significant amounts of crystalline phases means XRD cannot be used to quantify phase compositions. Thus, XPS analyses were run on Li_xPON, LixSiPHN, Li_xSiPON pellets, Figure **3.1(c)** reveals signature Li, P, O, Si, N peaks and minor peaks for C and Cl; the latter from residual NaCl. The carbon likely arises from brief air exposure forming Li_2CO_3.

Table 3.4. Atomic ratios based on XPS analyses for Li_xPON, Li_xSiPHN, and Li_xSiPON.

Ratio	Li_3PON	Li_6PON	Li_2SiPHN	Li_3SiPON	Li_6SiPON
O/P	6	4.5	3.15	3.56	5.54
N/P	1.25	1.66	1.84	1.9	2.4
Li/N	2.68	3.5	1.33	1.43	1.68

Table **3.4** summarizes the XPS data. Li_3PON and Li_6PON conform to XPS data reported previously.[9,45,48] XPS analyses also provide information about elemental bonding environments. The O 1s peak is attributed to Li-O-P, P-O-P, and P=O bonding environments as shown by the core-level spectrum presented in Figure **3.2**. The Li/N ratios increase from ~2.7 to 3.5 as more $LiNH_2$ is added to the PON precursor. The experimental synthesis used had an N/P ratio of 3, the lower ratio found in the XPS suggests polymerization by loss of nitrogen. Quite important is the fact that the N/P ratio (1.25-1.66) is higher than the highest values reported for gas phase deposition techniques (0.92).[45] XPS further confirms that the Li_3PON and Li_6PON pellets have 4.7 and 5.35 at. % N, higher than atom % for Li_xPON films deposited by PE-MOCVD and RF magnetron sputtering (4 at. %).[49]

The data indicate that the Li/N ratio increases from ~1.43 for Li_3SiPON to 1.68 for the Li_6SiPON precursor as more $LiNH_2$ is used. However, the ratio is smaller than calculated for Li_3PON (2.86) and Li_6PON (3.5) pellets, likely due to the silicon introduced. However, the N atom % for Li_3SiPON and Li_6SiPON are 8.5 and 6.7% respectively. The N/P ratio (1.9-2.4) is still higher than found above for Li_3PON and Li_6PON. The presence of oxygen in the Li_2SiPHN precursor might be from brief air exposure during pellet pressing forming Li_2CO_3. The calculated atomic composition shows a Li/N ratio of 1.33 similar to Li_3SiPON in Table **3.4**. However, this ratio is smaller than that introduced experimentally for Li_2SiPHN, likely a consequence of polymerization.

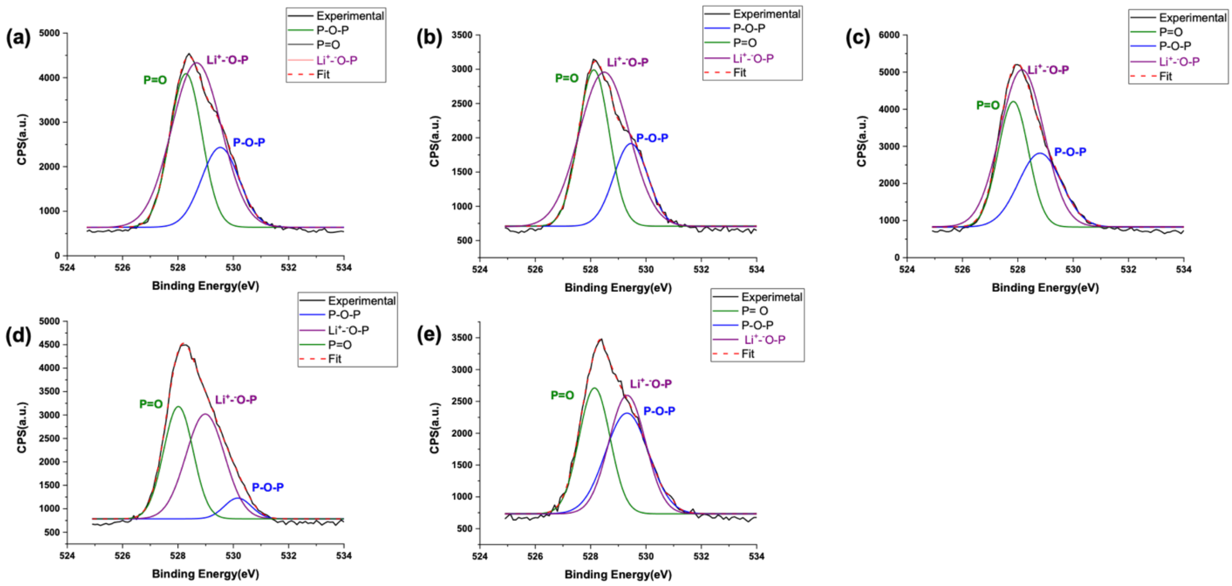

Figure 3.2. O 1s core-level spectrum of (a) Li_3PON, (b) Li_6PON, (c) Li_2SiPHN, (d) Li_3SiPON, and (e) Li_6SiPON polymer precursor pellets heated to 100 °C.

3.3.2 Ionic conductivity of polymer electrolytes

Table **3.5** summarizes the total ambient conductivities of SS/Celgard+Li_3PON, Li_6PON, Li_2SiPHN, Li_3SiPON, and Li_6SiPON/SS. The polymers showed optimal Li^+ diffusivity through the separator. The wet conductivities of electrolyte + Celgard are Li_3PON <<Li_6PON<<Li_2SiPHN<<Li_3SiPON<<Li_6SiPON. The incorporation of silicon into Li_xPON improves ionic conductivity (~1×10^{-5} S cm^{-1}) in good agreement with literature reports for Li_xSiPON thin films as shown in Figure 3.3**(a)**.[27,28]

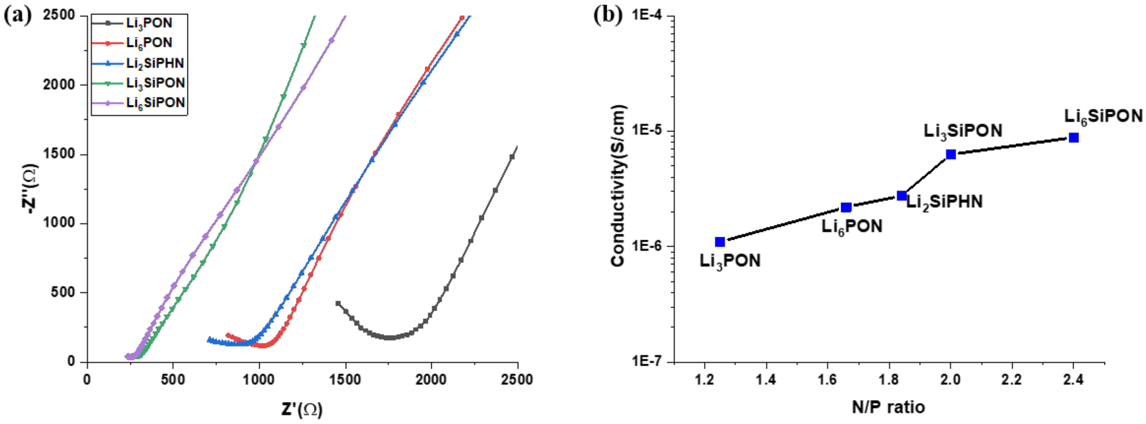

Figure 3.3. (a)Nyquist plots of SS/Celgard + Li_xPON, Li_xSiPHN, and Li_xSiPON/SS at room temperature, (b) N/P ratio vs. conductivity.

According to Roh et al 1999,[48] ionic conductivity is determined by the product of charge density and mobility. Hence, there are two ways to increase the Li^+ ionic conductivity of Li_xPON emulated polymer electrolytes.

One is to increase the Li^+ content to increase charge carrier densities (i.e. Li_3PON to Li_6PON). This is difficult to achieve using gas phase deposition methods as Li content is nearly constant irrespective of the deposition technique (i.e. rf power).[50] However, our synthesis route permits control of Li^+ contents by varying $LiNH_2$ amounts.

Table 3.5. Total room temperature conductivity of polymer precursors.

Celgard+polymer	Conductivity (S/cm)
Li_3PON	$1.1 \pm 0.3 \times 10^{-6}$
Li_6PON	$2.2 \pm 0.6 \times 10^{-6}$
Li_2SiPHN	$2.7 \pm 0.4 \times 10^{-6}$
Li_3SiPON	$6.3 \pm 0.1 \times 10^{-6}$
Li_6SiPON	$8.8 \pm 0.4 \times 10^{-6}$

The other is to change the inherent organization of the elements in the polymer to increase Li^+ mobility (i.e. increasing the N/P ratio), again something difficult to do in gas phase approaches. Figure 3.3**(b)** shows the correlation of N/P ratio with polymer ionic conductivities. The increase in the N/P ratio results in a linear increase in conductivity for coated Celgard. A maximum conductivity of 8.8×10^{-6} S cm^{-1} is achieved for the Li_6SiPON+Celgard polymer electrolyte with an N/P ratio of 2.4. Our N/P ratio is very high compared to traditional gas-phase techniques resulting in enhanced ionic conductivity.[45,50] The positive correlation between ionic conductivity and the N/P ratio can be attributed to the decrease in electrostatic energy as adding more P-N$<^{P}_{P}$ crosslink structural units apparently increases Li^+ mobility.[27,50]

In addition, aliovalent substitution of P^{5+} by Si^{4+} in Li_XPO_4 has been reported to create compositions that promote fast Li^+ conduction by shortening the distance between Li^+ binding sites promoting superior ionic conductivity.[51] The ionic conductivity of the LiSiPON has been reported to be superior to lithium silicophosphate, suggesting that introducing nitrogen to Li_2O-SiO_2-P_2O_5 systems increases Li^+ mobility presumably via reduced electrostatic interactions.[27] Here we find that increasing the Si/P ratio also results in linear increases in conductivity deduced from the XPS at.% and EIS measurements for Li_xSiPHN and Li_xSiPON electrolytes, Figure **3.4** and Table **3.6**. The Li_6SiPON polymer electrolyte with a Si/P ratio of ~0.5 resulted in an ionic conductivity of 8.8×10^{-6} S cm^{-1}.

Table 3.6. Atomic ratios based on XPS analyses for Li_xSiPHN and Li_xSiPON.

Ratio	Li_2SiPHN	Li_3SiPON	Li_6SiPON
Si/P	0.17	0.32	0.5

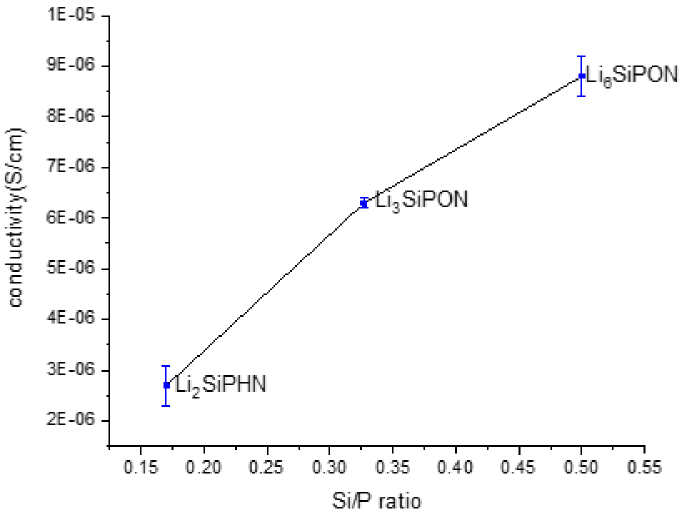

Figure 3.4. Correlation of conductivity and Si/P ratio.

3.3.3 Morphology and electrochemical stability of polymer electrolytes

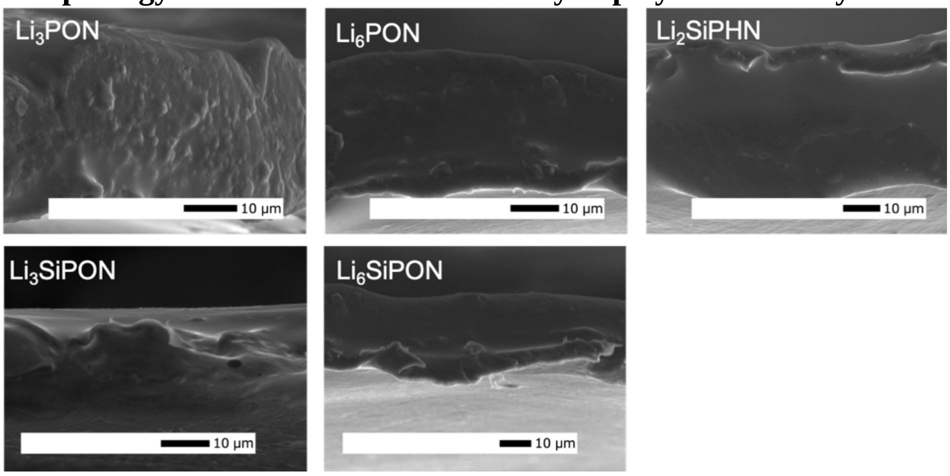

Figure 3.5. SEM fracture surface images Celgard + polymer precursors heated to 90 °C/12 h/Vacuum.

Figure **3.5** shows SEM fracture surface images of Celgard coated with polymer precursors. Celgard coated with polymer precursors did show interfaces. The coatings are optimal with average coating thicknesses of 5 - 10 µm, see Table **3.7**. The fracture surface images of the coatings reveal a uniform, smooth, and dense microstructure.

Tolerance to high potential is very crucial for polymer electrolytes especially for development of long-life cycle ASBs with high energy densities. To obtain further insight concerning the electrochemical stability of the polymer electrolytes dissolved in THF, the linear sweep voltammograms were carried out at a scanning rate of 1 mV s^{-1}.

Table 3.7. List of Celgard coated with polymer precursors and heated to 90 °C/12 h/vac**.**

Sample	Coating mass (mg)	Coating thickness (µm)
Li_3PON	11±0.3	5±0.5
Li_6PON	15±1.2	9±0.4
Li_2SiPHN	14±0.5	7±0.5
Li_3SiPON	8±2.2	8±0.1
Li_6SiPON	11±0.6	8±0.3

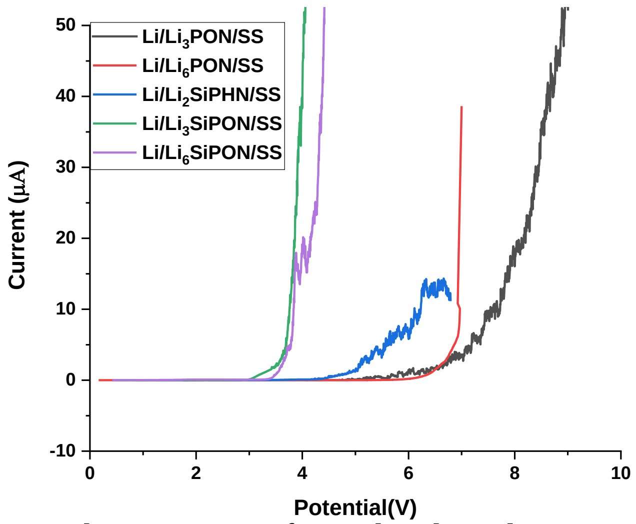

Figure 3.6. Linear sweep voltammograms of Li/Celgard + polymer precursor electrolytes/SS.

Figure 3.6 shows linear sweep voltammograms obtained for the Li/Celgard + polymer electrolytes/SS from 0 to 9 V. The current increases dramatically when voltage exceeds 7 and 6 V for Li_3PON and Li_6PON polymer electrolytes respectively, indicating the decomposition potential of Li_xPON electrolyte in contact with Li. These values are higher than what is reported for gas phase deposited LiPON (0-5.0 V vs Li/Li^+).[52] These quite wide electrochemical stability windows appear suitable for Li ASBs with the high-potential cathode materials.[53]

Comparatively, Li_2SiPHN shows a decomposition potential ~5 V, indicative of good oxidative stability for a polymer electrolyte based solely on phosphorus and nitrogen compared to the Li_xSiPON materials. Li_3SiPON and Li_6SiPON are only stable to 4 V which suggests a different decomposition potential perhaps due to the presence of Si. Thus, while incorporating Si enhances ionic conductivity by increasing the N/P ratio; it has a limited operating voltage window compared to the Li_xPON electrolytes. The origin of the significant voltage difference depends on the electronegativity of the framework,[54] which weakens or strengths the covalency of the Li-N bonds. The introduction of Si in the polymer precursors decreases the covalency of Li-N framework, which decreases the energy of the antibonding states. Hence, the difference in voltage stability between the Li^+/Li couples in SiPON and PON framework.

3.3.4 Electrochemical performance of polymer electrolytes

EIS was used to study the individual resistive elements that comprise the total Li/Celgard + polymer electrolyte/Li cell resistance. The symmetric cells were cycled at room temperature using DC cycling to determine the critical current densities.

Figure 3.7 **(a)** shows the Li/Celgard+Li_3PON/Li cell galvanostatically cycled at room temperature.

The cell was tested for charge/discharge using a DC steady state method with a constant current density (±0.05 $mAcm^{-2}$). A stable potential of (±0.007 V) was measured over the extended cycles. The Li/polymer precursor electrolyte interface stability was characterized vs. current density. The potential vs capacity plot in Figure 3.7**(b)** shows that the Li_3PON electrolyte is stable to 0.5 $mAhcm^{-2}$.

Figure 3.7 **(c)** shows a Li/Celgard+Li_3SiPON/Li cell galvanostatically cycled at ambient. The cell was tested for charge/discharge using a constant current (±0.15-0.75 mA). The symmetric cell shows a stable voltage response (0.04 V) when a high current density of 0.75 mA is used. The potential vs capacity plot in Figure 3.7 **(d)** also shows that the electrolyte is stable to 0.375 mAh cm^{-2} without showing any voltage fluctuation or polarization.

Figures 3.7 **(e)** and **(d)** show the selected overpotential profiles of subsequent lithium plating/stripping process on the working electrode in the Li/Li symmetrical cells with Celgard+ Li_3SiPON as the electrolyte. At current density (j = 0.1 mA/cm^2), there is a heterogeneous lithium dissolution region on/at the lithium metal anode. The overall dissolution process in Figure 3.7 **(e-d)** is divided into four parts (a, b, c, and d). In the first part (a), the lithium dissolution process starts with an immediate steeply increase in the potential to (0.1 V at j = 0.1 mA/cm^2) which is the maximum overpotential in the whole experiment, whereas the second part shows a decrease of the overpotential (b), followed by a fast drop to 0.03 V (c). The dissolution process shows further decreases in potential to 0.02V (d).

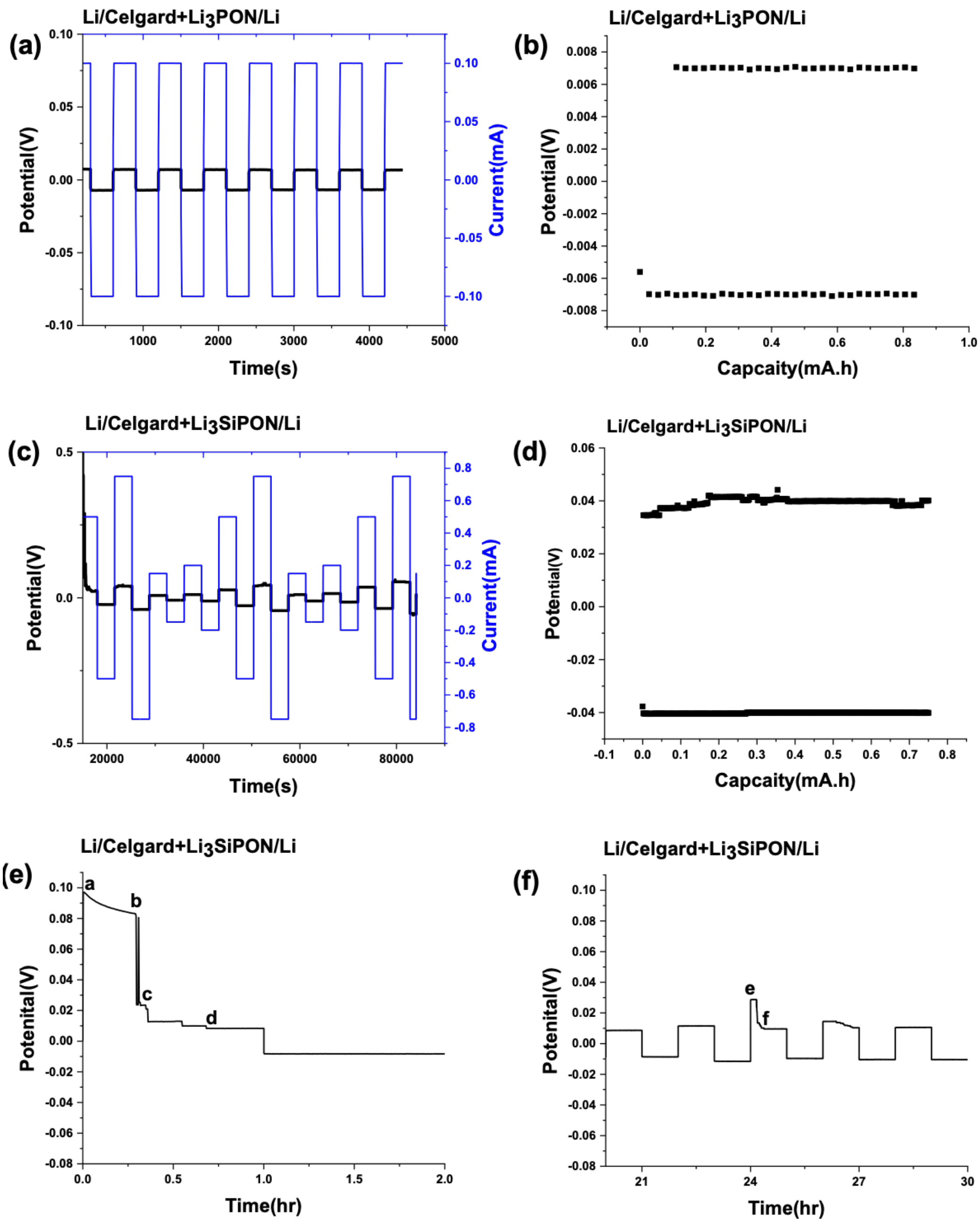

Figure 3.7. Galvanostatic cycling of Li/Celgard+Li_3PON (a-b) and Li_3SiPON (c-d) /Li symmetric cell at the current density of ±0.1 mA. Selected overpotential profiles of Li/Celgard+Li_3SiPON/Li symmetric cell at the current densities of ±0.13 mA/cm^2 (e) and 0.66 mA/cm^2 (f).

The rapid increase of the overpotential indicates the end of the corresponding dissolution process. The overpotential is high in region (a) because the process primarily takes place on the pristine, smooth and low surface area Li substrate. The decrease of the overpotential after the first cycle confirms that the corresponding lithium dissolution mostly takes place form an already roughened Li surface.[55] Similar to dendrite formation, Li plating and stripping also change the surface morphology of the electrode.

The increase in current distribution (j = 0.6 mA/cm^2) might lead to the crack of the SEI and increase in the electrode surface area and decrease of the SEI resistance (e). As the local roughness makes spots that are preferable for Li stripping and deposition, continuous cycling will result in a decrease in overpotential (f) for the rest of the cycle.

Higher current densities (>0.1 mA) seem to result in higher interfacial impedance as seen by the increases in voltage response to 1 V. However, the symmetric cell shows a stable voltage response (0.25 V) when at 0.075 mA, Figure **3.8(a)**. The potential vs capacity plot in Figure **3.8(b)** shows that the electrolyte is stable to 0.375 mAhcm^{-2}.

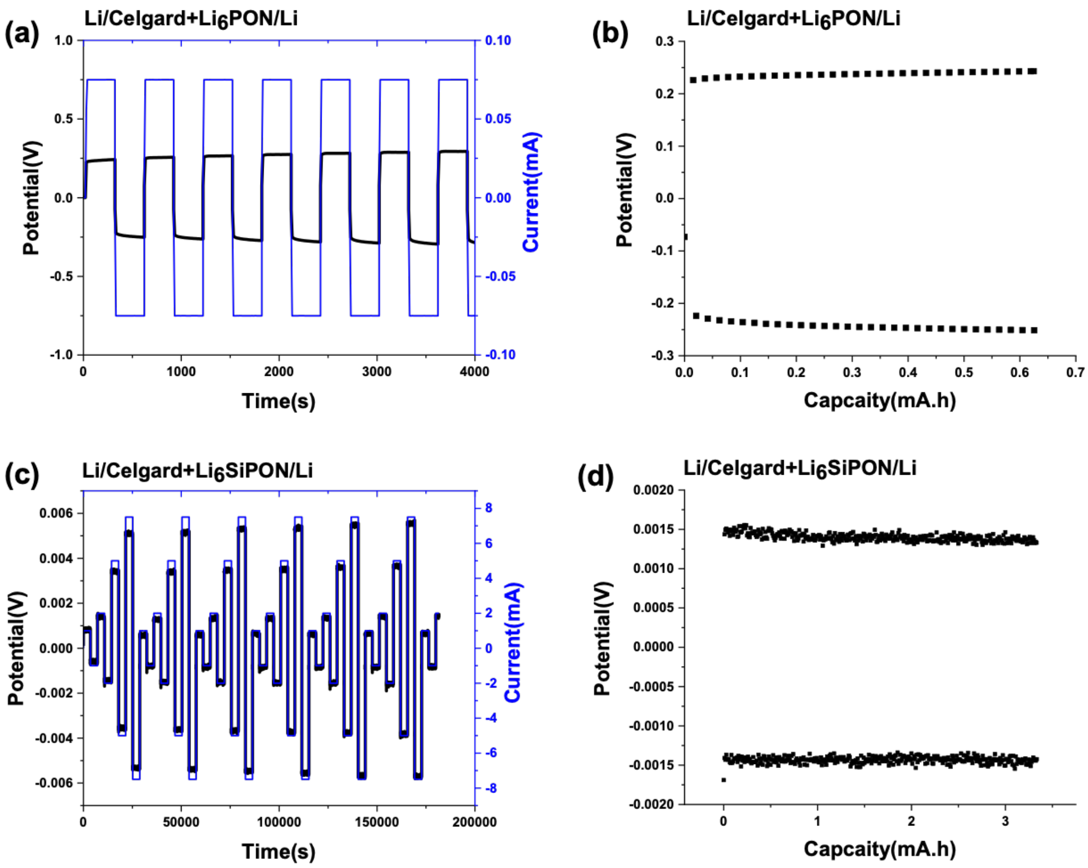

Figure 3.8. Galvanostatic cycling of Li/Celgard+Li_6PON (a-b) and Li_6SiPON (c-d)/Li symmetric cell at the current densities of ±0.1-7.5 mA. The blue line corresponds to the constant current and the black line is the voltage response.

Celgard coated with Li_6SiPON shows an ideal voltage response suggesting that there was a minimum interfacial impedance throughout the galvanostatic cycling at room temperature as shown in Figure **3.8 (c)**. This is revealed by a low voltage response at higher current densities (±1.5-7.5 mA). The interfacial impedance is nearly constant when the current density increases to (±7.5 mA) demonstrating by the voltage response and confirmed per Ohms' law (R = V/I). The potential vs capacity plot shows that the electrolyte is stable to 3.5 mAhcm^{-2}.

These high current densities are attributed to the stability of the Li_6SiPON polymer electrolyte against Li metal with very low ohmic resistivity of ~1 Ω. In addition, the high critical current density of the polymer electrolyte matches rate performances of state-of-art Li^+ at 1-3 mA cm^{-2}.[56]

Figure **3.9(a)** shows Li/ Celgard+Li_2SiPHN/Li cells galvanostatically cycled at room temperature. The cell was tested for charge and discharge using a DC steady-state method in which a constant current (±7.5 mA) was used. The symmetric cell shows a voltage response (0.02 V) for the first 20 hours at a constant current density of 7.5 mA. The overpotential gradually increases to ~0.025 V after the first 10 cycles. This indicates a general increase in the overall resistance vs. lithium deposition. Long-term cycling shows that the overpotential (~0.03 V) profile becomes constant after the first 20 initial cycles. The potential vs capacity plot also shows that the Li_2SiPHN electrolyte is stable up to 3.75 $mAhcm^{-2}$ as shown in Figure **3.9 (b)**.

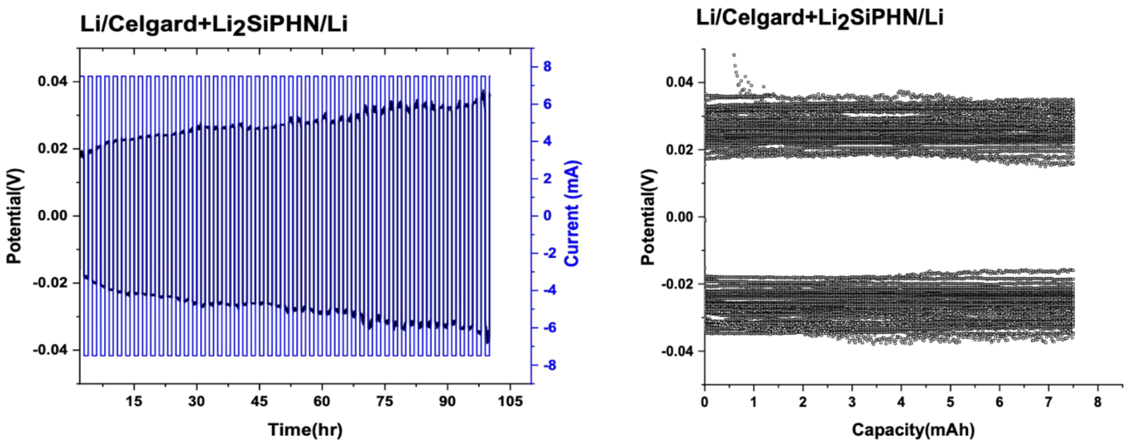

Figure 3.9. Galvanostatic cycling of Li/Celgard + Li2SiPHN/Li symmetric cell at ±7.5 mA.

The equivalent circuit is shown in Figure **3.10**. The R_1 and R_2 corresponds to the Ohmic resistance of the polymer electrolyte and the electrode surface resistance referred as (R_{SEI}). The R_3 in the insert of Figure **3.10** refers to charge transfer resistance.

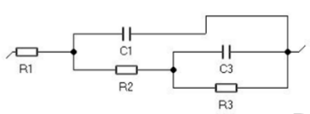

$$z(f) = R_1 + \frac{R_3 + R_2(1 + i2\pi f C_3 R_3)}{1 + i2\pi f C_3 R_3 + i2\pi f\, C_1(R_3 + R_2(1 + i2\pi f C_3 R_3))}$$

Figure 3.10. Z fit for the Li/Celgard +polymer electrolytes/Li symmetric cells.

Figure **3.11** shows the Nyquist plots of Li/Celgard + polymer precursor/Li symmetric cells at room temperature before cycling. EIS measurements compare the impedance differences of the symmetric cells using the different polymer electrolytes. In general, the high-frequency semicircle relates to Li^+ migration through the polymer electrolyte interface resistance, and the lower frequency semicircle relates to charge transfer resistance (R_{ct}). The low frequency semicircle diameter was divided by a factor of two to determine the R_{ct} as the cell employed two Li metals of equal area. At room temperature, a R_{ct} of ~50 Ω cm^2 was measured for Li_2SiPHN polymer electrolyte. This R_{ct} value is similar to state-of-art Li^+ liquid electrolytes typically tens of Ω cm^2.[57] The Nyquist plots mainly show high resistance at the electrode surface, suggesting that the overpotential of Li stripping and plating processes are dominated by the nature of SEI at the Li/electrolyte interface.[56]

Lithium transference number (t_{Li^+}) was determined following the procedure and equation suggested by Bruce et al.[61] Symmetrical cells using (Li/polymer coated Celgard electrolytes/Li) were monitored under chronoamperometry until a steady-state current was reached. The initial (I_0) and steady-state (I_{SS}) currents in addition to the initial (Z_0) and steady-state (Z_{SS}) resistances were obtained from the chronoamperometry and EIS measurements. Transference number (t_{Li^+}) was calculated by the following equation:

$$t_{Li^+} = I_{SS}(DV\text{-}Z_0 \times I_0)/I_0(DV\text{-}Z_{SS} \times I_{SS})$$

The stability of polymer electrolyte against Li was evaluated by monitoring the electrochemical impedance spectra of Li/ polymer coated Celgard electrolytes/Li symmetrical cell before and after chronoamperometry measurements under open circuit conditions at ambient.

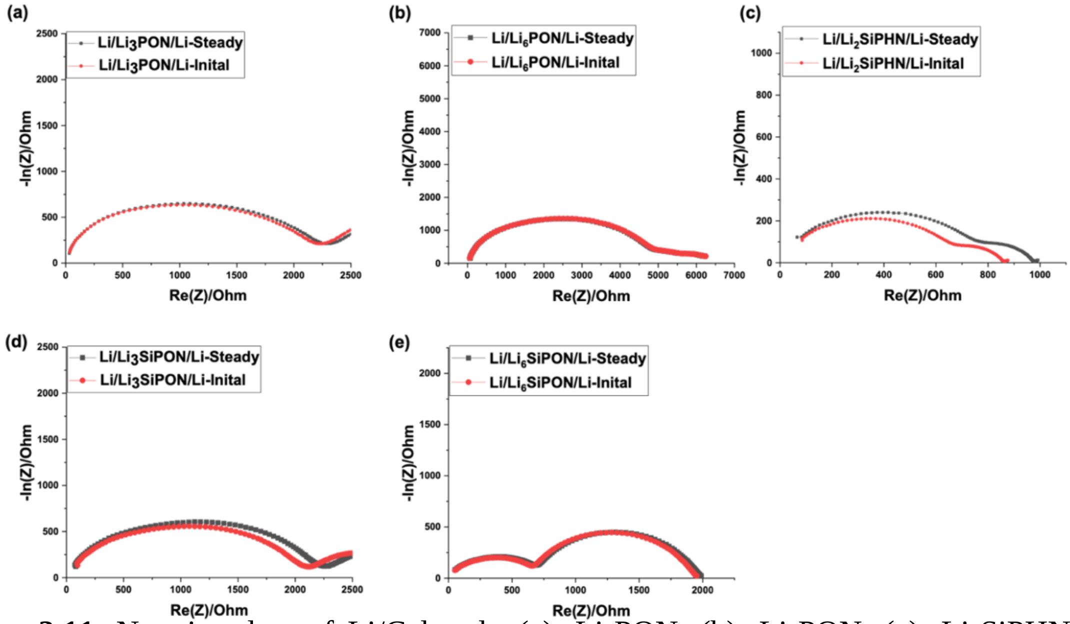

Figure 3.11. Nyquist plots of Li/Celgard+ (a). Li_3PON, (b). Li_6PON, (c). Li_2SiPHN, (d). Li_3SiPON, (e). Li_6SiPON /Li cells.

Figure **3.11** shows Nyquist plots of symmetric cells assembled with polymer precursor coated Celgard electrolytes. The Nyquist plots for cells assembled with Li_6PON and Li_6SiPON electrolytes show that the impedance is stable before and after steady-state current. However, the impedance increased after steady-state current is achieved for cells assembled with Li_2SiPHN and Li_3SiPON polymer electrolytes. The spectra start with the Ohmic resistance and then show a semicircle at lower frequencies. The Ohmic part of the cell resistance is determined by the ionic conductivity of the polymer electrolytes, the following semicircle consequently corresponds to the capacitive properties, SEI, and charge-transfer resistance at the Li electrodes. Since both plots start at the same high frequency (Ohmic part), the ionic conductivity of the Li_2SiPHN and Li_9SiPON precursors are the same before and after steady-state current measurement, hence the increment in impedance has to be related to the formation of SEI and charge-transfer resistance at the Li electrodes.

Interfacial resistance (Z_0 and Z_{ss}) values were obtained by analyzing the real resistances of the semicircle of EIS Nyquist plots. After 1 hr., a steady-state current was achieved. Figure **3.12** shows Chronoamperometry plots of symmetric cells assembled with polymer precursor coated Celgard electrolytes. The increase in the transference number for the polymer electrolyte is indicative of a chemical interaction between Li and PON and SiPON, that in turn afforded high Li^+ mobility.

It is noteworthy that since the interfacial resistances were higher than the electrolyte resistance, this steady-state method is now considered less of a quantitative and more of a qualitative comparison of the increase in tLi^{+}.

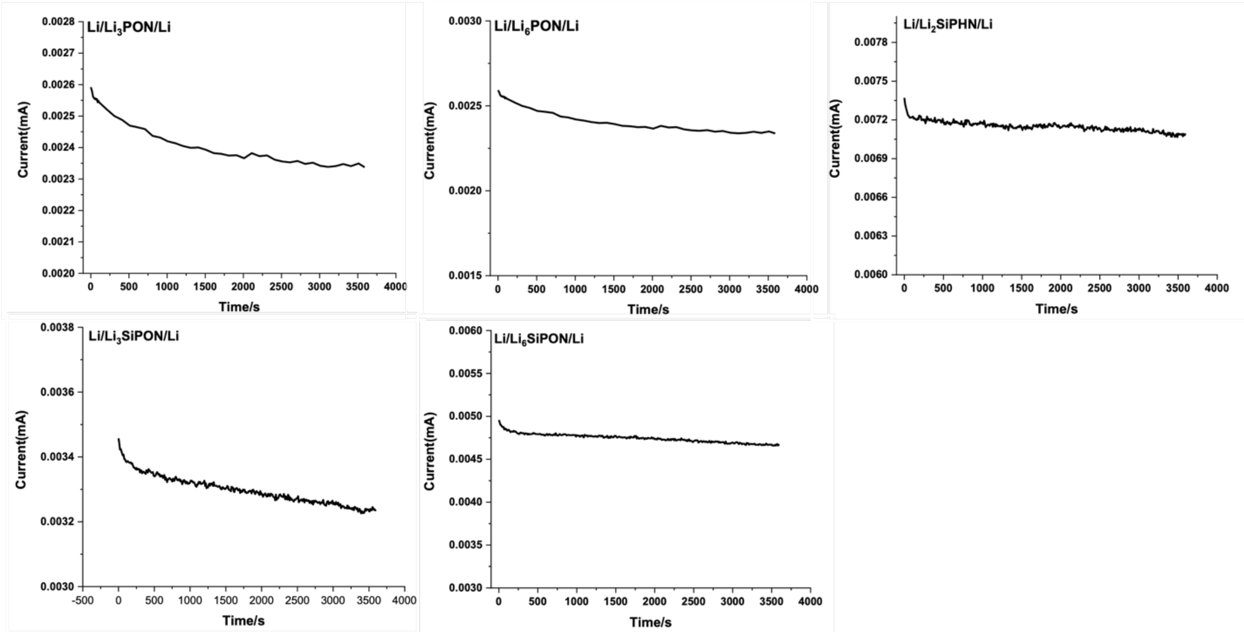

Figure 3.12. Chronoamperometry plots of the symmetric cells using Celgard coated polymer precursors.

Table **3.8** lists the average transference numbers of polymer precursor coated celgards assembled in symmetric cell configuration. The Li_2SiPHN precursor showed an ideal transference number of ~0.9 comparable to solid-state electrolytes.

From these preliminary results, the transference number is in the order of $Li_6SiPON \ll Li_3PON \ll Li_3SiPON \ll Li_6PON \ll Li_2SiPHN$.

Table 3.8. Calculated Li^+ transfer numbers of polymer precursor coated Celgard electrolytes.

Electrolyte	$tLi^{+}avg$
Li_3PON	0.8±0.02
Li_6PON	0.8±0.06
Li_2SiPHN	0.9±0.02
Li_3SiPON	0.8±0.03
Li_6SiPON	0.7±0.06

The electronic conductivity of the polymer electrolytes was determined by DC measurements of the current under potential polarization using Bio-Logic SP 300 potentiostat with low current functions (current resolution < 1nA). The potential was ramped in the ranges of - 0.03 to + 0.03 V with a step of 10 mV and was held at each step for up to 1 hr. The stabilized current at each step was used to determine the electronic conductivity. The electronic conductivity is deduced from the stabilized current (*Iss*) using the relation:

$$\sigma_e = (t \times Iss)/(A \times U)$$

where t is the thickness of the Celgard (25 µm), A is the area of the Li electrode (radius = 8 mm), and U is the applied voltage.

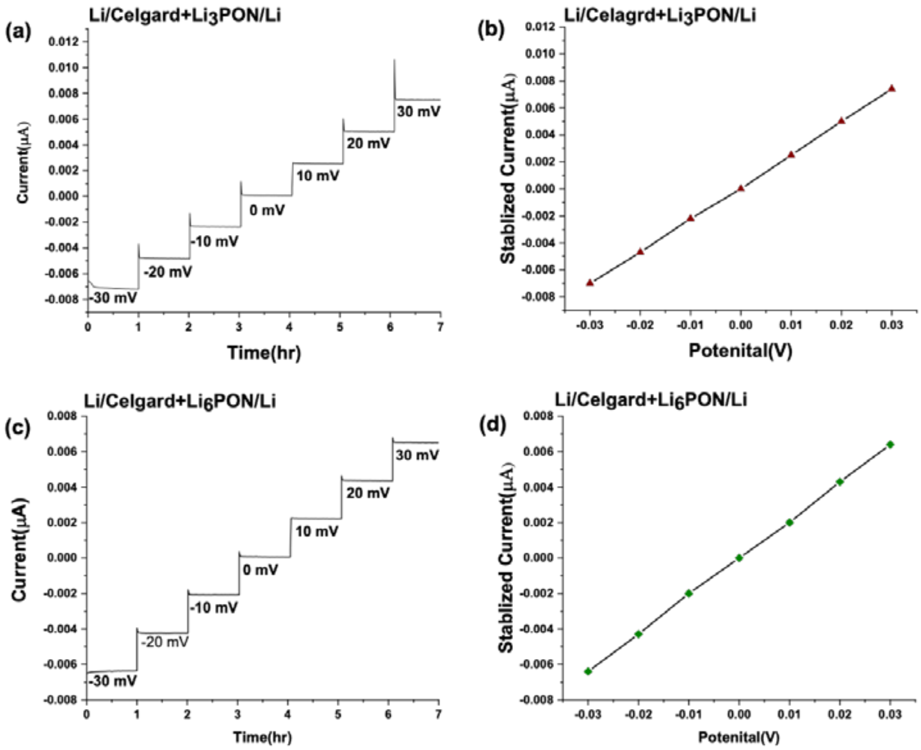

Figure 3.13. Time dependence of current during step voltages (a and c). Stabilized current-voltage relations of Li/Li_xPON/Li cells (b and d).

The electronic conductivities of Celgards coated with Li_xPON polymer precursors are measured by DC polarization experiments and is summarized in Table **3.9**. Representative current-voltage plots of Li_3PON and Li_6PON are shown in Figures **3.13 (a-b)** and **(c-d)** respectively. The stabilized current- shows a linear increase with the step increase of voltage as expected from Ohms law (V = IR). The Li_3PON and Li_6PON polymer electrolytes showed an average electrical conductivity of ~3×10^{-10} and 2.6×10^{-10} S/cm respectively. These values are higher than what is reported for Li_xPON systems (10^{-15}-10^{-12} S/cm).[58,59] However, the reported electrical conductivities are much lower than LLZO (10^{-8}-10^{-7} S/cm)[60] and Li_2S-P_2S_5 (10^{-9}-10^{-8} S/cm)[61] solid electrolytes. It is also worth to note that the electrical conductivity measurements are done on the polymer precursor coated separators, the precursor by itself might have lower electronic conductivity.

Table 3.9. List of electrical conductivities for Li/Celgard + polymer precursor/Li cell obtained by DC measurements.

Potential(mV)	Li_3PON σ_e (S/cm)	Li_6PON σ_e (S/cm)	Li_2SiPHN σ_e (S/cm)	Li_3SiPON σ_e (S/cm)	Li_6SiPON σ_e (S/cm)
-30	2.9×10^{-10}	2.6×10^{-10}	2.5×10^{-9}	6.2×10^{-10}	1.9×10^{-10}
-20	2.9×10^{-10}	2.7×10^{-10}	2.5×10^{-9}	6.2×10^{-10}	1.9×10^{-10}

-10	2.7×10^{-10}	2.5×10^{-10}	2.5×10^{-9}	6.2×10^{-10}	1.9×10^{-10}
10	3.1×10^{-10}	2.5×10^{-10}	2.5×10^{-9}	6.2×10^{-10}	1.7×10^{-10}
20	3.1×10^{-10}	2.7×10^{-10}	3.0×10^{-9}	6.2×10^{-10}	1.7×10^{-10}
30	3.0×10^{-10}	2.6×10^{-10}	3.3×10^{-9}	6.2×10^{-10}	1.7×10^{-10}

The electronic conductivities of Li_xSiPON and Li_2SiPHN polymer precursors coated Celgards are measured by DC polarization experiments and are summarized in Table **3.9**. Representative current-voltage plots of Li_2SiPHN and Li_xSiPON are shown in Figures **3.14** and **3.15**, respectively. The Li_2SiPHN polymer electrolytes showed an average electrical conductivity of ~2.7×10^{-9} S/cm. Whereas, the Li_3SiPON and Li_6SiPON polymer electrolytes showed lower average electronic conductivities of ~6.2×10^{-10} and 1.8×10^{-10} S/cm, respectively. The increase in Li^+ concentration from Li_3SiPON to Li_6SiPON seems to decrease the electrical conductivity in Li_6SiPON polymer coated Celgard electrolytes. Further studies about the space charge region and heterojunction between the Li metal and the polymer precursor electrolytes are needed to understand the electrical conductivity of the electrolyte.

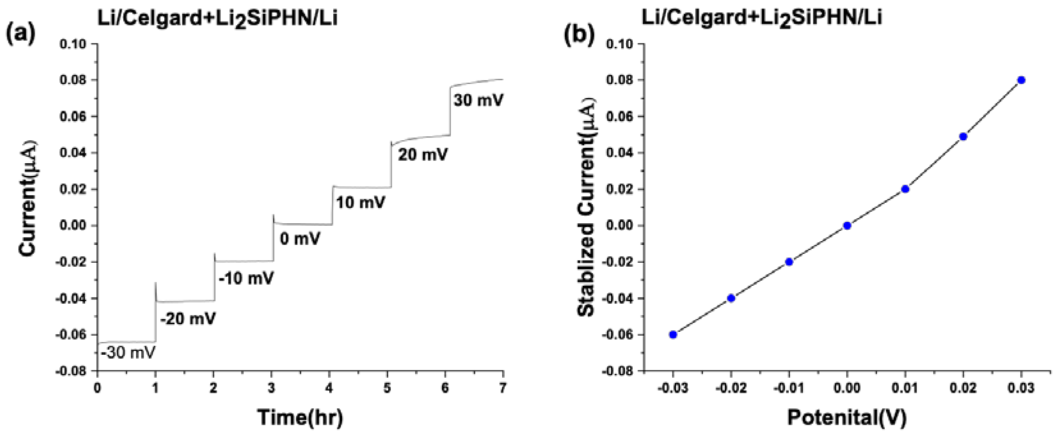

Figure 3.14. Time dependence of current during step voltages (a) and stabilized current-voltage relations (b) of $Li/Li_2SiPHN/Li$ cell.

Interestingly, the Celgard coated with Li_6SiPON polymer precursor showed the lowest electrical conductivity when compared to the other polymer electrolytes. This electrolyte also showed the highest ionic conductivity and high critical current density (3.75 $mAcm^{-2}$). All of these properties ensured that Li_6SiPON has a similar dendrite suppression capability to that of Li_xPON. The Li_6SiPON polymer precursor electrolyte was used to assemble a half cell with Li metal and SPAN cathode. Detail synthesis and performance of SPAN cathodes can be found elsewhere.[30]

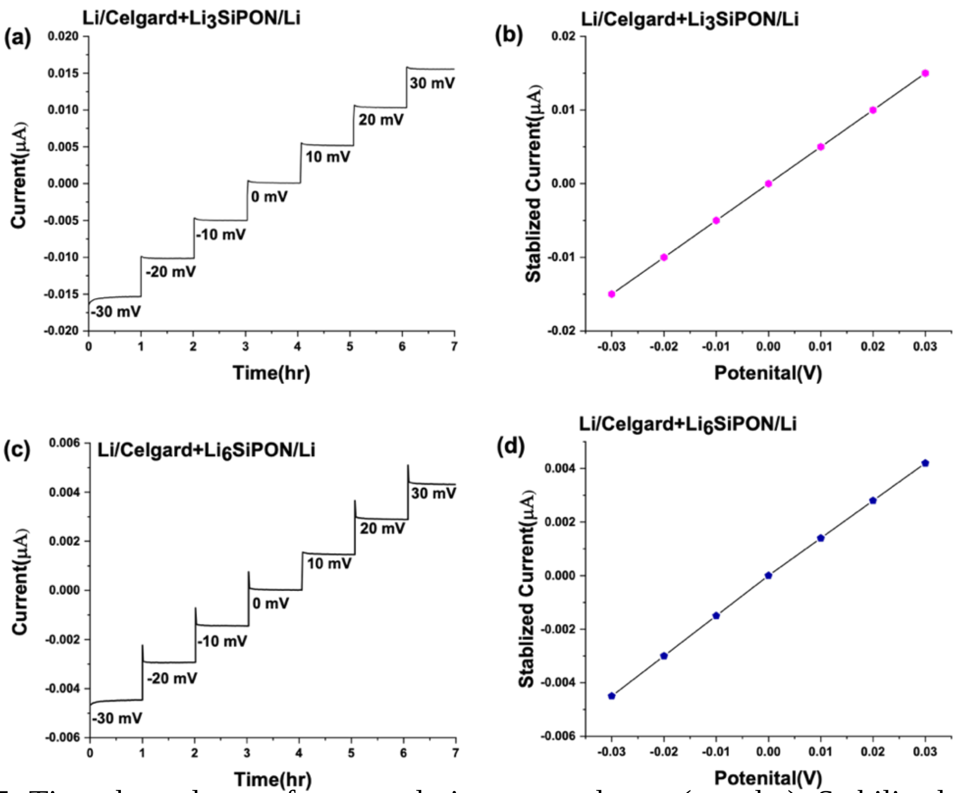

Figure 3.15. Time dependence of current during step voltages (a and c). Stabilized current-voltage relations of Li/Li_xSiPON/Li cells (b and d).

Figure **3.16** shows the results of SPAN/Celgard+Li_6SiPON/Li cells cycled at 0.5 C rates. The Li-SPAN battery cycled for 220 h. without any polarization or voltage fluctuation. The half-cell was cycled from 1 to 3 V for 122 cycles. The half-cell showed initial a capacity ~1500 mAh g_{sulfur}^{-1}; 90 % of theory for Li-S batteries. The capacity decreases to 1000 mAh g_{sulfur}^{-1} after the 40th cycle and gradually to 750 mAh g_{sulfur}^{-1} thereafter. The reported capacity is much improved when compared to Li-S batteries assembled with polymer electrolytes as listed in Table **3.10**.

Table 3.10. Comparison of reported polymer electrolytes for Li-S batteries.

Electrolyte	Retained capacity	C-rate	Columbic efficiency	Ref
1 M LITFSI/DOL/DME/PYR_{14}TFSI	846	0.2	94.2	63
Li[TFSA]/G4/HFE	600	0.5	98	64
$[Li(G4)_1][TFSA]$	450	0.5	98	
1 M LiTFSI/DOL/DME	815	0.5	91.3	65
PEO at 104 °C	200	0.1	N/A	66
PEGDME at 23 °C	100	0.05		
PEMO at 60 °C	50	0.025		
Li_6SiPON at 23 °C	750	0.5	92	This work

The Li_6SiPON polymer electrolyte shows high electrochemical stability at 0.5 C for 122 cycles. The half-cell shows a slight decrease from 95 to 92 % efficiency after the first 40 cycles. It remains ~92 % thereafter. The stability and high performance of the nearly all solid-state battery can be ascribed to the unique performance of SPAN and the polymer electrolyte. The most important feature of SPAN is that the sulfur is covalently bound to a polyaromatic backbone and forms different structural motifs that reduce detrimental polysulfide dissolution.[30,62]

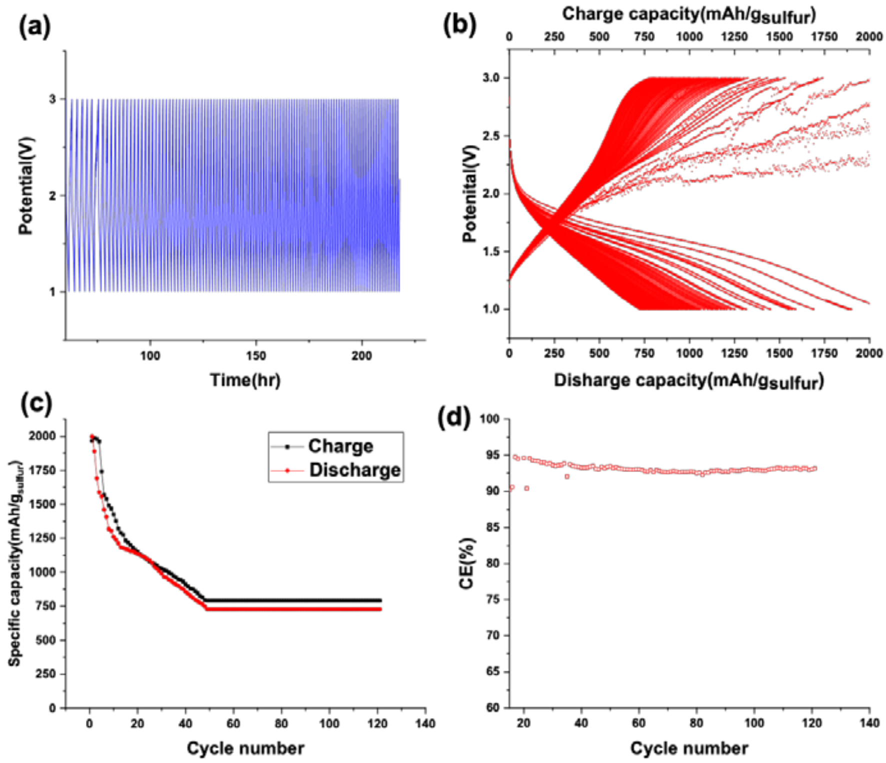

Figure 3.16. Potential vs. time, charge-discharge capacity, and columbic efficiency plots of SPAN/Li_6SiPON+Celgard/Li at 0.5 C.

A high rate of capacity fade is observed for the Li-S battery with polymer electrolytes. Three plausible explanations may be given. One is the irreversibility of some of the polysulfide reactions. Another is the diffusion of polysulfides into the electrolyte. A third is the loss of electrical contact during cycling. The last factor might be due to several phenomena, including the formation of large particles of highly resistive sulfur or lithium sulfide, the migration of polysulfides away from the carbon phase, and the agglomeration of sulfur or carbon particles as a result of the pressure exerted on the cell. Since the SPAN cathode can eliminate the formation of polysulfides that results in a fast capacity loss, future work will rely on the optimization of the electrical contact between the SPAN cathode and the polymer precursor electrolytes. The poor electrical contact is ascribed to result in a decrease in columbic efficiency. Efforts to optimize the critical current densities of the other polymer electrolytes and for assembly of ASBs remains future work. The interfacial behavior directly dictates the lifespan, energy density, and safety of all solid-state batteries. We believe that these polymer electrolytes might lower the interfacial resistance and stabilize the interfacial performance of all solid-state batteries.

3.4 Conclusions

In summary, we have presented the synthesis of a set of polymers that emulate LiPON chemistries and that allow simple and extensive control of composition, degree of lithiation and incorporation of silicon as well as exclusion of oxygen and understand their effects on the ionic conductivity. We will demonstrate in the future their use in generating Li_xPON, Li_xSiPON, and Li_xSiPHN glasses. The intent was to find a simple alternative to the equipment and energy intensive gas phase deposition methods. Our approach involves the synthesis of $O=P(NH_2)_3$ from $OPCl_3$ followed by lithiation with $LiNH_2$.

The ionic conductivity of the polymer electrolytes increases with increasing amounts of Li and optimizing the N/P ratio. Maximum ambient ionic conductivities of ~1×10^{-5} S cm^{-1} are achieved for the Li_6SiPON with 2.4 N/P ratio. The polymer electrolytes also show high ohmic stability against Li metal at current densities of 0.375-3.75 $mAhcm^{-2}$. In addition, the Li_2SiPHN precursor showed an ideal transference number of ~0.9 comparable to solid-state electrolytes. Furthermore, the Li_6SiPON polymer electrolyte was used to assemble a nearly all solid-state Li/SPAN battery. The stability and high performance of the half-cell was attributed to the unique performance of the SPAN and the polymer electrolyte.

References

(1) Put, B.; Vereecken, P. M.; Meersschaut, J.; Sepúlveda, A.; Stesmans, A. Electrical Characterization of Ultrathin RF-Sputtered LiPON Layers for Nanoscale Batteries. *ACS Appl. Mater. Interfaces* **2016**, *8*, 7060–7069. https://doi.org/10.1021/acsami.5b12500.

(2) Oudenhoven, J. F. M.; Baggetto, L.; Notten, P. H. L. All-Solid-State Lithium-Ion Microbatteries: A Review of Various Three-Dimensional Concepts. *Adv. Energy Mater.* **2011**, *1*, 10–33. https://doi.org/10.1002/aenm.201000002.

(3) Zhang, H.; Yu, X.; Braun, P. V. Three-Dimensional Bicontinuous Ultrafast-Charge and-Discharge Bulk Battery Electrodes. *Nat. Nanotechnol.* **2011**, *6*, 277–281. https://doi.org/10.1038/nnano.2011.38.

(4) Vereecken, P. M.; Huyghebaert, C. Conformal Deposition for 3D Thin-Film Batteries. *ECS Trans.* **2013**, *58*, 111–118. https://doi.org/10.1149/05810.0111ecst.

(5) Rubloff, G. W.; Kozen, A. C.; Bok Lee, S. From Nanoscience to Solutions in Electrochemical Energy Storage. *J. Vac. Sci. Technol. A Vacuum, Surfaces, Film.* **2013**, *31*, 058503. https://doi.org/10.1116/1.4816262.

(6) Bates, J. B.; Dudney, N. J.; Gruzalski, G. R.; Zuhr, R. A.; Choudhury, A.; Luck, C. F.; Robertson, J. D. Electrical Properties of Amorphous Lithium Electrolyte Thin Films. *Solid State Ionics* **1992**, *53*, 647–654. https://doi.org/10.1016/0167-2738(92)90442-R.

(7) Wang, B.; Kwak, B. S.; Sales, B. C.; Bates, J. B. Ionic Conductivities and Structure of Lithium Phosphorus Oxynitride Glasses. *J. Non. Cryst. Solids* **1995**, *183*, 297–306. https://doi.org/10.1016/0022-3093(94)00665-2.

(8) Yu, X.; Bates, J. B.; Jellison, G. E.; Hart, F. X. A Stable Thin-Film Lithium Electrolyte: Lithium Phosphorus Oxynitride. *J. Electrochem. Soc.* **1997**, *144*, 524–532. https://doi.org/10.1149/1.1837443.

(9) Bates, J. B.; Dudney, N. J.; Gruzalski, G. R.; Zuhr, R. A.; Choudhury, A.; Luck, C. F.; Robertson, J. D. Fabrication and Characterization of Amorphous Lithium Electrolyte Thin Films and Rechargeable Thin-Film Batteries. *J. Power Sources* **1993**, *43–44*, 103–110. https://doi.org/10.1016/0378-7753(93)80106-Y.

(10) Reyes Jiménez, A.; Nölle, R.; Wagner, R.; Hüsker, J.; Kolek, M.; Schmuch, R.; Winter, M.; Placke, T. A Step towards Understanding the Beneficial Influence of a LIPON-Based Artificial SEI on Silicon Thin Film Anodes in Lithium-Ion Batteries. *Nanoscale* **2018**, *10*, 2128–2137. https://doi.org/10.1039/c7nr06568j.

(11) Nimisha, C. S.; Rao, K. Y.; Venkatesh, G.; Rao, G. M.; Munichandraiah, N. Sputter Deposited LiPON Thin Films from Powder Target as Electrolyte for Thin Film Battery Applications. *Thin Solid Films* **2011**, *519*, 3401–3406. https://doi.org/10.1016/j.tsf.2011.01.087.

(12) Hamon, Y.; Douard, A.; Sabary, F.; Marcel, C.; Vinatier, P.; Pecquenard, B.; Levasseur, A. Influence of Sputtering Conditions on Ionic Conductivity of LiPON Thin Films. *Solid State Ionics* **2006**, *177*, 257–261. https://doi.org/10.1016/j.ssi.2005.10.021.

(13) Zhao, S.; Fu, Z.; Qin, Q. A Solid-State Electrolyte Lithium Phosphorus Oxynitride Film Prepared by Pulsed Laser Deposition. *Thin Solid Films* **2002**, *415*, 108–113. https://doi.org/10.1016/S0040-6090(02)00543-6.

(14) Liu, W. Y.; Fu, Z. W.; Li, C. L.; Qin, Q. Z. Lithium Phosphorus Oxynitride Thin Film Fabricated by a Nitrogen Plasma-Assisted Deposition of E-Beam Reaction Evaporation. *Electrochem. Solid-State Lett.* **2004**, *7*, J36–J40.

https://doi.org/10.1149/1.1778934.
(15) Vereda, F.; Goldner, R. B.; Haas, T. E.; Zerigian, P. Rapidly Grown IBAD LiPON Films with High Li-Ion Conductivity and Electrochemical Stability. *Electrochem. Solid-State Lett.* **2002**. https://doi.org/10.1149/1.1508550.
(16) Kim, Y. G.; Wadley, H. N. G. Lithium Phosphorous Oxynitride Films Synthesized by a Plasma-Assisted Directed Vapor Deposition Approach. *J. Vac. Sci. Technol. A Vacuum, Surfaces, Film.* **2008**. https://doi.org/10.1116/1.2823491.
(17) Nowak, S.; Berkemeier, F.; Schmitz, G. Ultra-Thin LiPON Films - Fundamental Properties and Application in Solid State Thin Film Model Batteries. *J. Power Sources* **2015**, *275*, 144–150. https://doi.org/10.1016/j.jpowsour.2014.10.202.
(18) Kim, H. T.; Mun, T.; Park, C.; Jin, S. W.; Park, H. Y. Characteristics of Lithium Phosphorous Oxynitride Thin Films Deposited by Metal-Organic Chemical Vapor Deposition Technique. *J. Power Sources* **2013**, *244*, 641–645. https://doi.org/10.1016/j.jpowsour.2012.12.109.
(19) Ruzmetov, D.; Oleshko, V. P.; Haney, P. M.; Lezec, H. J.; Karki, K.; Baloch, K. H.; Agrawal, A. K.; Davydov, A. V.; Krylyuk, S.; Liu, Y.; Huang, J.; Tanase, M.; Cumings, J.; Talin, A. A. Electrolyte Stability Determines Scaling Limits for Solid-State 3D Li Ion Batteries. *Nano Lett.* **2012**. https://doi.org/10.1021/nl204047z.
(20) Xu, F.; Dudney, N. J.; Veith, G. M.; Kim, Y.; Erdonmez, C.; Lai, W.; Chiang, Y. M. Properties of Lithium Phosphorus Oxynitride (Lipon) for 3D Solid-State Lithium Batteries. *J. Mater. Res.* **2010**, *25* (8), 1507–1515. https://doi.org/10.1557/jmr.2010.0193.
(21) Kozen, A. C.; Pearse, A. J.; Lin, C. F.; Noked, M.; Rubloff, G. W. Atomic Layer Deposition of the Solid Electrolyte LiPON. *Chem. Mater.* **2015**. https://doi.org/10.1021/acs.chemmater.5b01654.
(22) Laine, R. M.; Babonneau, F. Preceramic Polymer Routes to Silicon Carbide. *Chem. Mater.* **1993**, *5*, 260–279. https://doi.org/10.1021/cm00027a007.
(23) Yi, E.; Temeche, E.; Laine, R. M. Superionically Conducting B″-Al2O3 Thin Films Processed Using Flame Synthesized Nanopowders. *J. Mater. Chem. A* **2018**, *6*, 12411–12419. https://doi.org/10.1039/c8ta02907e.
(24) Okamura, K. Ceramic Fibres from Polymer Precursors. *Composites* **1987**. https://doi.org/10.1016/0010-4361(87)90489-7.
(25) Bill, J.; Aldinger, F. Precursor-Derived Covalent Ceramics. In *Precursor-Derived Ceramics: Synthesis, Structures and High Temperature Mechanical Properties*; 2008. https://doi.org/10.1002/9783527613823.ch4.
(26) Greil, P. Polymer Derived Engineering Ceramics. *Advanced Engineering Materials*. 2000. https://doi.org/10.1002/1527-2648(200006)2:6<339::AID-ADEM339>3.0.CO;2-K.
(27) Lee, S. J.; Bae, J. H.; Lee, H. W.; Baik, H. K.; Lee, S. M. Electrical Conductivity in Li-Si-P-O-N Oxynitride Thin-Films. *J. Power Sources* **2003**. https://doi.org/10.1016/S0378-7753(03)00457-9.
(28) Lee, S. J.; Baik, H. K.; Lee, S. M. An All-Solid-State Thin Film Battery Using LISIPON Electrolyte and Si-V Negative Electrode Films. *Electrochem. commun.* **2003**, *5*, 32–35. https://doi.org/10.1016/S1388-2481(02)00528-3.
(29) Su, Y.; Falgenhauer, J.; Leichtweiß, T.; Geiß, M.; Lupó, C.; Polity, A.; Zhou, S.; Obel, J.; Schlettwein, D.; Janek, J.; Meyer, B. K. Electrochemical Properties and Optical Transmission of High Li+ Conducting LiSiPON Electrolyte Films. *Phys. Status Solidi Basic Res.* **2017**, *254* (2), 1600088. https://doi.org/10.1002/pssb.201600088.
(30) Warneke, S.; Zenn, R. K.; Lebherz, T.; Müller, K.; Hintennach, A.; Starke, U.; Dinnebier, R. E.; Buchmeiser, M. R. Hybrid Li/S Battery Based on Dimethyl Trisulfide and Sulfurized Poly(Acrylonitrile). *Adv. Sustain. Syst.* **2018**, *2* (2), 1700144. https://doi.org/10.1002/adsu.201700144.
(31) Zu, C. X.; Li, H. Thermodynamic Analysis on Energy Densities of Batteries. *Energy Environ. Sci.* **2011**. https://doi.org/10.1039/c0ee00777c.
(32) Wang, S.; Ding, Y.; Zhou, G.; Yu, G.; Manthiram, A. Durability of the Li1+xTi2-XAlx(PO4)3 Solid Electrolyte in Lithium-Sulfur Batteries. *ACS Energy Lett.* **2016**, *1* (6), 1080–1085. https://doi.org/10.1021/acsenergylett.6b00481.
(33) Goodenough, J. B.; Kim, Y. Challenges for Rechargeable Batteries. *J. Power Sources*

2011. https://doi.org/10.1016/j.jpowsour.2010.11.074.
(34) Manthiram, A.; Fu, Y.; Chung, S. H.; Zu, C.; Su, Y. S. Rechargeable Lithium-Sulfur Batteries. *Chemical Reviews*. 2014. https://doi.org/10.1021/cr500062v.
(35) Wang, L.; Wang, Y.; Xia, Y. A High Performance Lithium-Ion Sulfur Battery Based on a Li<inf>2</Inf>S Cathode Using a Dual-Phase Electrolyte. *Energy Environ. Sci.* **2015**. https://doi.org/10.1039/c5ee00058k.
(36) Manthiram, A.; Yu, X.; Wang, S. Lithium Battery Chemistries Enabled by Solid-State Electrolytes. *Nat. Rev. Mater.* **2017**, *2* (4), 16103. https://doi.org/10.1038/natrevmats.2016.103.
(37) Tarascon, J. M.; Armand, M. Issues and Challenges Facing Rechargeable Lithium Batteries. In *Materials for Sustainable Energy: A Collection of Peer-Reviewed Research and Review Articles from Nature Publishing Group*; 2010. https://doi.org/10.1142/9789814317665_0024.
(38) Zhang, X.; Temeche, E.; Laine, R. M. Design, Synthesis, and Characterization of Polymer Precursors to LixPON and LixSiPON Glasses: Materials That Enable All-Solid-State Batteries (ASBs). **2020**. https://doi.org/10.1021/acs.macromol.0c00254.
(39) Laine, R. M.; Sellinger, A. Si-Containing Ceramic Precursors. In *The Chemistry of Organic Silicon Compounds*; 2003. https://doi.org/10.1002/0470857250.ch39.
(40) Yi, J.; Liu, X.; Guo, S.; Zhu, K.; Xue, H.; Zhou, H. Novel Stable Gel Polymer Electrolyte: Toward a High Safety and Long Life Li-Air Battery. *ACS Appl. Mater. Interfaces* **2015**. https://doi.org/10.1021/acsami.5b08462.
(41) Levchik, S. V.; Levchik, G. F.; Balabanovich, A. I.; Weil, E. D.; Klatt, M. Phosphorus Oxynitride: A Thermally Stable Fire Retardant Additive for Polyamide 6 and Poly(Butylene Terephthalate). *Angew. Makromol. Chemie* **1999**, *264* (1), 48–55.
(42) Larson, R. W.; Day, D. E. Preparation and Characterization of Lithium Phosphorus Oxynitride Glass. *J. Non. Cryst. Solids* **1986**, *88* (1), 97–113. https://doi.org/10.1016/S0022-3093(86)80091-6.
(43) Mascaraque, N.; Fierro, J. L. G.; Durán, A.; Muñoz, F. An Interpretation for the Increase of Ionic Conductivity by Nitrogen Incorporation in LiPON Oxynitride Glasses. *Solid State Ionics* **2013**. https://doi.org/10.1016/j.ssi.2012.12.017.
(44) Fleutot, B.; Pecquenard, B.; Martinez, H.; Letellier, M.; Levasseur, A. Investigation of the Local Structure of LiPON Thin Films to Better Understand the Role of Nitrogen on Their Performance. *Solid State Ionics* **2011**, *186* (1), 29–36. https://doi.org/10.1016/j.ssi.2011.01.006.
(45) Pichonat, T.; Lethien, C.; Tiercelin, N.; Godey, S.; Pichonat, E.; Roussel, P.; Colmont, M.; Rolland, P. A. Further Studies on the Lithium Phosphorus Oxynitride Solid Electrolyte. *Mater. Chem. Phys.* **2010**. https://doi.org/10.1016/j.matchemphys.2010.04.001.
(46) Stallworth, P. E.; Vereda, F.; Greenbaum, S. G.; Haas, T. E.; Zerigian, P.; Goldner, R. B. Solid-State NMR Studies of Lithium Phosphorus Oxynitride Films Prepared by Nitrogen Ion Beam-Assisted Deposition. *J. Electrochem. Soc.* **2005**, *152* (3), A516–A522. https://doi.org/10.1149/1.1856922.
(47) Wang, B.; Chakoumakos, B. C.; Sales, B. C.; Kwak, B. S.; Bates, J. B. Synthesis, Crystal Structure, and Ionic Conductivity of a Polycrystalline Lithium Phosphorus Oxynitride with the γ-Li3PO4 Structure. *J. Solid State Chem.* **1995**. https://doi.org/10.1006/jssc.1995.1140.
(48) Roh, N. S.; Lee, S. D.; Kwon, H. S. Effects of Deposition Condition on the Ionic Conductivity and Structure of Amorphous Lithium Phosphorus Oxynitrate Thin Film. *Scr. Mater.* **1999**. https://doi.org/10.1016/S1359-6462(99)00307-3.
(49) Meda, L.; Maxie, E. E. Lipon Thin Films Grown by Plasma-Enhanced Metalorganic Chemical Vapor Deposition in a N 2-H 2-Ar Gas Mixture. *Thin Solid Films* **2012**. https://doi.org/10.1016/j.tsf.2011.08.091.
(50) Hu, Z.; Li, D.; Xie, K. Influence of Radio Frequency Power on Structure and Ionic Conductivity of LiPON Thin Films. *Bull. Mater. Sci.* **2008**. https://doi.org/10.1007/s12034-008-0108-z.
(51) Bachman, J. C.; Muy, S.; Grimaud, A.; Chang, H. H.; Pour, N.; Lux, S. F.; Paschos, O.; Maglia, F.; Lupart, S.; Lamp, P.; Giordano, L.; Shao-Horn, Y. Inorganic Solid-State Electrolytes for Lithium Batteries: Mechanisms and Properties Governing Ion

Conduction. *Chemical Reviews*. 2016. https://doi.org/10.1021/acs.chemrev.5b00563.
(52) West, W. C.; Whitacre, J. F.; Lim, J. R. Chemical Stability Enhancement of Lithium Conducting Solid Electrolyte Plates Using Sputtered LiPON Thin Films. *J. Power Sources* **2004**. https://doi.org/10.1016/j.jpowsour.2003.08.030.
(53) Hu, M.; Pang, X.; Zhou, Z. Review Recent Progress in High-Voltage Lithium Ion Batteries. *J. Power Sources* **2013**, *237*, 2013. https://doi.org/10.1016/j.jpowsour.2013.03.024.
(54) Masquelier, C.; Croguennec, L. Polyanionic (Phosphates, Silicates, Sulfates) Frameworks as Electrode Materials for Rechargeable Li (or Na) Batteries. *Chemical Reviews*. 2013. https://doi.org/10.1021/cr3001862.
(55) Bieker, G.; Winter, M.; Bieker, P. Electrochemical in Situ Investigations of SEI and Dendrite Formation on the Lithium Metal Anode. *Phys. Chem. Chem. Phys.* **2015**. https://doi.org/10.1039/c4cp05865h.
(56) Albertus, P.; Babinec, S.; Litzelman, S.; Newman, A. Status and Challenges in Enabling the Lithium Metal Electrode for High-Energy and Low-Cost Rechargeable Batteries. *Nat. Energy* **2018**, *3* (1), 16. https://doi.org/10.1038/s41560-017-0047-2.
(57) Zhang, S. S.; Xu, K.; Jow, T. R. The Low Temperature Performance of Li-Ion Batteries. *J. Power Sources* **2003**. https://doi.org/10.1016/S0378-7753(02)00618-3.
(58) Su, Y.; Falgenhauer, J.; Polity, A.; Leichtweiß, T.; Kronenberger, A.; Obel, J.; Zhou, S.; Schlettwein, D.; Janek, J.; Meyer, B. K. LiPON Thin Films with High Nitrogen Content for Application in Lithium Batteries and Electrochromic Devices Prepared by RF Magnetron Sputtering. *Solid State Ionics* **2015**. https://doi.org/10.1016/j.ssi.2015.09.022.
(59) Li, J.; Dudney, N. J.; Nanda, J.; Liang, C. Artificial Solid Electrolyte Interphase to Address the Electrochemical Degradation of Silicon Electrodes. *ACS Appl. Mater. Interfaces* **2014**. https://doi.org/10.1021/am5009419.
(60) Chen, Y. T.; Jena, A.; Pang, W. K.; Peterson, V. K.; Sheu, H. S.; Chang, H.; Liu, R. S. Voltammetric Enhancement of Li-Ion Conduction in Al-Doped Li7-XLa3Zr2O12 Solid Electrolyte. *J. Phys. Chem. C* **2017**. https://doi.org/10.1021/acs.jpcc.7b04004.
(61) Shin, B. R.; Nam, Y. J.; Oh, D. Y.; Kim, D. H.; Kim, J. W.; Jung, Y. S. Comparative Study of TiS2/Li-In All-Solid-State Lithium Batteries Using Glass-Ceramic Li3PS4and Li10GeP2S12 Solid Electrolytes. *Electrochim. Acta* **2014**. https://doi.org/10.1016/j.electacta.2014.08.139.
(62) Frey, M.; Zenn, R. K.; Warneke, S.; Müller, K.; Hintennach, A.; Dinnebier, R. E.; Buchmeiser, M. R. Easily Accessible, Textile Fiber-Based Sulfurized Poly(Acrylonitrile) as Li/S Cathode Material: Correlating Electrochemical Performance with Morphology and Structure. *ACS Energy Lett.* **2017**. https://doi.org/10.1021/acsenergylett.7b00009.
(63) Ma, G.; Wen, Z.; Jin, J.; Wu, M.; Wu, X.; Zhang, J. Enhanced Cycle Performance of Li-S Battery with a Polypyrrole Functional Interlayer. *J. Power Sources* **2014**, *267*, 542–546. https://doi.org/10.1016/j.jpowsour.2014.05.057.
(64) Dokko, K.; Tachikawa, N.; Yamauchi, K.; Tsuchiya, M.; Yamazaki, A.; Takashima, E.; Park, J. W.; Ueno, K.; Watanabe, M.; Seki, S.; Serizawa, N. Solvate Ionic Liquid Electrolyte for Li-S Batteries. *J. Electrochem. Soc.* **2013**, *160* (8), A1304–A1310. https://doi.org/10.1149/2.111308jes.
(65) Ma, G.; Wen, Z.; Wang, Q.; Shen, C.; Jin, J.; Wu, X. Enhanced Cycle Performance of a Li-S Battery Based on a Protected Lithium Anode. *J. Mater. Chem. A* **2014**, *2* (45), 19355–19359. https://doi.org/10.1039/c4ta04172k.
(66) Marmorstein, D.; Yu, T. H.; Striebel, K. A.; McLarnon, F. R.; Hou, J.; Cairns, E. J. Electrochemical Performance of Lithium/Sulfur Cells with Three Different Polymer Electrolytes. *J. Power Sources* **2000**, *89* (2), 219–226. https://doi.org/10.1016/S0378-7753(00)00432-8.

Chapter 4

Solid Solutions of Polyethylene Oxide with Li_xPON and Li_xSiPON Based Polymers

4.1 Introduction

The potential benefits from all solid-state batteries (ASSBs) have generated intense academic and commercial efforts to replace lithium battery liquid electrolytes with electrolyte materials that avoid the flammability of current liquids, protect against dendrite growth leading to short circuiting, and offer higher energy densities by allowing the use of metallic lithium as anode with a theoretical capacity of 3860 mAh g^{-1}.[1–3]

The search for solid electrolytes can be divided into polymeric and glass/ceramic with the former having the potential to be easily introduced commercially because it represents "drop-in" technology in that polymeric materials as separators are already widely extant in state-of-the-art liquid electrolyte batteries.[4] Glass/ceramic electrolytes offer potential advantages being stable at temperature extremes and wide electrochemical stability windows not accessible to polymers. However, glass/ceramic electrolytes normally require much higher processing temperatures and their introduction to assembly of ASBs would entail introducing large scale changes to battery assembly processes.[5,6] Polymer electrolytes offer several advantages compared to glass/ceramic electrolytes, such as enhanced resistance to volume variations during cycling, excellent flexible geometries, and as noted just above, processability.[7,8]

Although polymer electrolytes have demonstrated multiped advantages since their discovery in 1973,[9] little progress has been made in commercializing them. Dry solid polymer electrolytes such as poly(ethylene) oxide (PEO)-LiX [X:Tf^-, SO_4^{2-}, ClO_4^-, BF_4^-, SbF_6^- and PF_6^-] systems offer poor Li^+ conductivities of 10^{-5} - 10^{-6} S cm^{-1} at room temperature, representing a significant barrier to practical applications.[10,11] PEO-Li^+ systems have been the subject of multiple studies because the ethyleneoxy monomer units easily coordinate Li^+ ions via a crown-ether like mechanism.[11] These coordination complexes can rigidly bind Li^+ to the point where diffusion is limited primarily because of the ease of crystallization of PEO systems, even when highly crosslinked.[12] In general, Li^+ transport (diffusion) occurs preferentially through the amorphous regions of solid PEO.[13,14]

This process likely occurs via segmental reorientation of neighboring chains coincident with Li^+ diffusion.[15–17] However, an alternate explanation to the segmental motion mechanism and the requirement for amorphous phase in PEO to achieve high ionic conductivities was recently presented in a study that shows that in crystalline PEO-LiX (X: PF_6, AsF_6, SbF_6) Li^+-ions diffuse through the cylindrical tunnels without the efficacy of segmental motion,.[18,19] Perhaps both mechanisms are operative but it is clear that more work must be done.[19]

In particular, significant attempts to enhance the room temperature-ionic conductivities of PEO based electrolytes are reported in many literatures through the use of plasticizers, addition of second phase solids that interfere with crystallization and the choice or concentration of Li^+ salt.[20,21] A primary problem with adding organic second phases (plasticizer) is the deterioration of mechanical properties at the expense of conductivity and some additives are relatively reactive with lithium metal,[22,23] narrowing the electrochemical stability window.

The second approach, introducing an inorganic second phase or filler has also been explored in some detail with inert and active Li^+ conducting fillers.[24–26] Inactive fillers improve Li^+ conductivity by reducing PEO crystallization. Active fillers contribute to Li^+ conductivity by both reducing PEO crystallinity and by promoting surface Li^+ transport at PEO/nanofiller interfaces.[27] In previous work, we explored the use of NASICON type Li^+ ion conducting nanopowders [$Li_{1.3}Al_{0.3}Ti_{1.7}(PO_4)_3$] (LATP) in PEO-$LiClO_4$ systems to realize superior composite electrolytes that exhibit room temperature ionic conductivities of 10^{-4} S cm^{-1}.[28] However, the LATP electrolyte suffers from poor chemical stability due to the irreversible reduction of Ti^{4+} when in direct contact with metallic Li.[29]

Lithium phosphorous oxynitride (LiPON) has been widely studied since its discovery in the early 90's owing to its negligible electrical conductivity (10^{-7} μS cm^{-1}),[30] high critical current density (>10 mA/cm^2),[31] wide electrochemical stability window (0-5 V vs Li^+/Li),[31] and high Li^+ transference number.[32] However, LiPON exhibits poor ionic conductivity (10^{-6} S/cm) at ambient,[33] restricting its application to micro-batteries with limited energy densities and capacities (0.1- 5 mAh).[34]

LiPON and PEO-based electrolytes are recommended interlayer materials because of their compatibility when in direct contact with Li anode.[35–37] Some studies demonstrate the performance of the bilayer structures comprised of LiPON/[$Li_{1.5}Al_{0.5}Ge_{1.5}(PO_4)$].[32,37] The composite structure benefits from these two layers of electrolytes. Specifically, LiPON is desirable interlayer material owing to its high shear modulus (31 GPa) approximately nine times that of Li metal, suggesting that it can suppress Li dendrite penetration of electrolytes.[32]

LiPON thin films are typically deposited onto the ceramic electrolyte by radio frequency magnetron sputtering technique.[32,37] However, gas-phase deposition methods require expensive steps to regulate the coating uniformity, deposition atmospheres, rates, and film thickness.[38–40] Hence, these methods are challenging to assemble ASSBs for large scale applications.[39]

Recently, we have demonstrated the design and synthesis of inorganic polymers/oligomer of Li_xPON, Li_xSiPON, and Li_xSiPHN-like electrolytes by low-temperature, low-cost, and solution- processable route.[38,39] The development of these polymer electrolytes offers desirable properties superior to LiPON glasses.[38] These polymer electrolytes also offer high Li^+ transference number (t_{Li+} 0.7 – 0.9).[38] Dry solid polymer electrolytes are well known bi-ionic conductors with $t_{Li+} < 0.5$.[11] The decrease in the t_{Li+} is ascribed to the fast migration of anions within the polymer matrix, which results in concentration polarization. The electro-polarization results in the decrease of the overall electrochemical performance of the electrolyte attributed to the increase in internal resistance, voltage drops, and dendritic growth.[41]

To minimize the polarization and increase t_{Li+}, the mobility of anions have to be reduced either by anchoring the anions to the polymer backbone or by adding a chelator that selectively traps the anions.[11,42] To the best of our knowledge, no one has sought to apply LiPON derived polymer electrolytes as active filler in PEO systems to achieve single-ion conduction. This provide the motivation to synthesize Li_xPON/PEO composite solid electrolyte that profits from these polymer mixtures.

In our efforts to develop Li_xPON-, Li_xSiPON-, and Li_xSiPHN-like polymer precursors,[39] we realized that it might also be possible to use our precursors as active filler in PEO systems either as a miscible or immiscible but active second phases. We report here efforts to explore the utility of these precursor systems as "active fillers" for PEO to formulate novel solid-solution composite electrolytes. Note that because our polymers on heating turn in to ceramics, these systems are anticipated to offer flame retardance or resistance unlike most liquid or polymer electrolytes. Below we present a systematic study on the role of Li^+-ion concentration in PEO/precursor composites on cation transport properties. Thus, PEO solid solution films exhibit enhanced ionic conductivities of ~ 0.1- 2 mS cm^{-1} at ambient and low activation energies (0.2- 0.5 eV) for cation transport. In addition, galvanostatic cycling of SPAN/PEs/Li battery (SPAN = sulfurized, carbonized polyacrylonitrile) shows discharge capacities of 1000 mAh/g_{sulfur} at 0.25 C, and 800 mAh/g_{sulfur}at 1 C with high (~100%) columbic efficiency over extensive cycles.

4.2 Experimental section

4.2.1 Polymer synthesis

Poly(ethylene oxide)[PEO 4 M and 900k] and Li metal foil(99.9%) was purchased from Sigma-Aldrich (Milwaukee, WI). Acetonitrile (ACN) and Tetrahydrofuran (THF) were purchased from Fischer Scientific (Pittsburgh, PA). All raw materials are regent grade.

Using precursor design principles reported in chapter **2**, we synthesized three Li_xPON-like precursors. The first synthesis method employs oligomeric $OP(NH_2)_3$ which, following lithiation, produce Li_xPON precursor as shown in Scheme **4.1**. A second precursor incorporates Si components based on literature reports that introduction of Si can give rise to fast Li^+ ion conduction in LiPON as shown in Scheme **4.2**,[47–49] providing motivation for this selection. A third precursor was synthesized from chlorophosphazene $[Cl_2P{=}N]_3$ and eliminates all oxygen but also incorporates Si and C. Detailed structural compositions and analysis of the polymer precursors can be found elsewhere.[38,39]

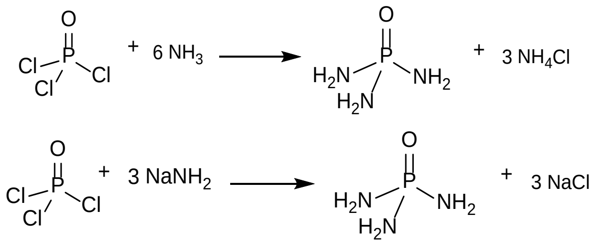

(1)

(2)

Scheme 4.1. The design of LiPON-like oligomer/polymer precursor syntheses.

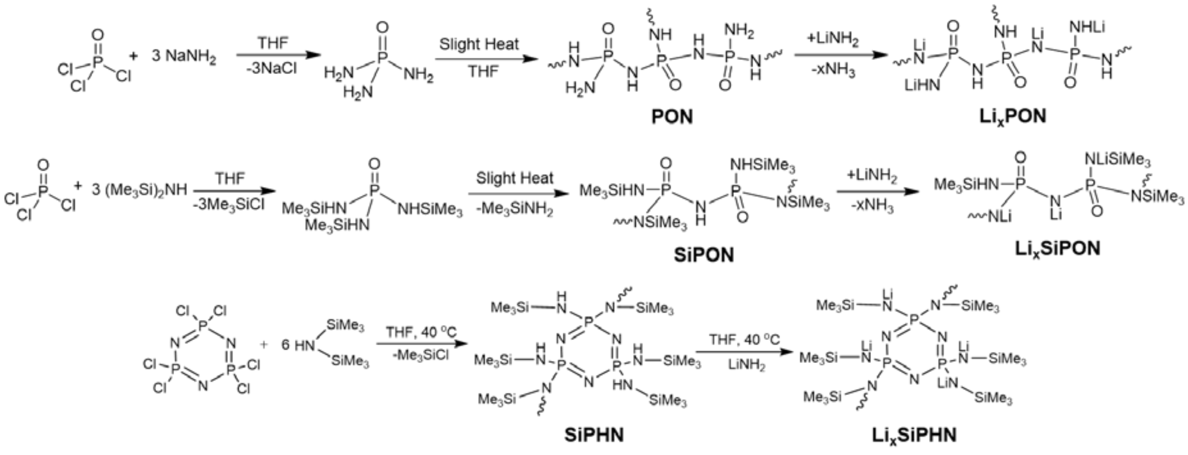

(3)

(4)

(5)

Scheme 4.2. Syntheses of Li_xPON, Li_xSiPON, and Li_xSiPHN precursors.

After some trial and error, it was determined that solid-solutions of all the precursors form readily at 60 wt. % PEO. Such compositions also gave good-to-excellent conductivities. Table **4.1** lists the formulation of such 60 wt.% PEO/40wt. % polymer precursor solid-solutions. PEO (M_w = 900k) powder was first dissolved with 18 ml of ACN. The polymer precursor as a THF solution (6 mL) was mixed with the PEO solution and stirred magnetically for 12 h. The obtained clear solution was then cast onto a Teflon plate.

After slow solvent evaporation at ambient over 24 h, the resulting transparent films were then dried at 3 x 10^{-3} Torr for 24 h at 65 °C. The dried films are referred as polymer electrolytes (PEs). Higher PEO concentrations result in poorer ionic conductivity while lower PEO concentrations result in poorer mechanical properties.

Table 4.1 List of PEO and polymer electrolytes dissolved in 18 ml ACN.

Polymer Electrolyte	Mass of PEO (g)	Mass of polymer electrolyte(g)
Li_3PON	0.6	0.21
Li_6PON	0.6	0.14
Li_2SiPHN	0.9	0.6
Li_3SiPON	0.9	0.6
Li_6SiPON	0.9	0.6

4.2.2 Symmetric cell assembly

Symmetric Li/PEs/Li cells were assembled in a glovebox under Ar. Before cell assembly, metallic Li foil (16 mm diameter) was scraped to expose a clean surface. The symmetric coin cells were cycled at ambient using a potentiostat/galvanostat (BioLogic SP300). The critical current densities of the cells were tested using a DC steady state method in which a constant current ($\pm$0.15- 7.5 mA) was used.[39]

Symmetrical cells using (Li/60 wt.% PEO + polymer electrolytes/Li) were monitored via chronoamperometry at (Direct voltage) DV = 10 mV until a steady-state current was reached. The transference numbers (t_{Li^+}) of the polymer electrolytes were calculated based on the procedure discussed elsewhere.[39] The cyclic voltammetry (CV) data for the polymer electrolytes was acquired in the potential range of -1 – 6 V vs. Li/Li^+ at a sweep rate of 5 mV/s. The CV measurement was performed in a coin 2032 cell using stainless steel (SS) as working electrode and Li as counter and reference electrode.

4.2.3 Half - cell assembly

Half-cells were assembled using SPAN as the cathode, PEs as an electrolyte, and Li metal as the anode. Before cell assembly, the metallic Li (16 mm W X 750 µm T) was scraped to expose a clean surface. The coin 2032 cells were compressed using a ~0.1 kpsi uniaxial pressure. The electrochemical characterization of the coin cells was performed using a potentiostat/galvanostat (BioLogic SP300). A 10 μL solution of polymer precursors {(Li_3PON (0.05 g ml^{-1}), Li_6PON (0.05 g ml^{-1}), Li_2SiPHN (0.08 g ml^{-1}), Li_3SiPON (0.1 g ml^{-1}), and Li_6SiPON (0.1 g ml^{-1})} dissolved in THF was used in assembling the half-cell to minimize the interfacial impedance between the electrodes and the PEs.

Besides, the cathode and the polymer electrolyte were warm pressed at 5 kpsi /40 °C/ 2 min to minimize the IR drop caused by poor interface.

The half-cells were then briefly warmed to 60 °C in the glove box to further improve Li/PEs contact and to prevent hot spots. The cathode slurry was prepared by mixing SPAN (70 wt.%), C65 (15 wt.%), and PVDF (15 wt.%) in 1- methyl pyrrolidin-2-one. The slurry was then coated on the carbon coated Al foil. The electrode was heated to 60 °C/ 12 h/Vacuum before assembly.

4.3 Results and discussion

4.3.1 Characterization of PEO/polymer precursor solid-solution films

Following optimization of the solid-solution systems, we then explored formulation of PEO/precursor solid-solution composite systems and characterized them by FTIR, XRD, XPS, SEM, DSC, and EIS. Detailed analyses of the PEs in symmetric and half-cell are also presented using Li metal and SPAN electrodes.

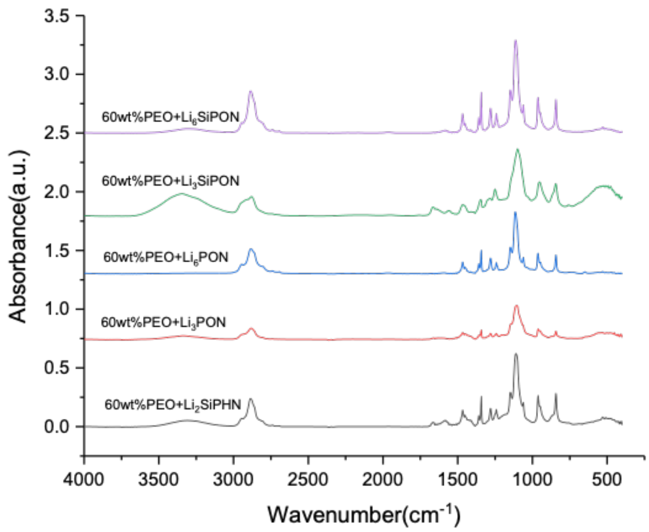

Figure 4.1. FTIRs of polymer electrolyte films heated to 65 °C/24 h/Vac.

The Figure **4.1** FTIRs of films heated to 65 °C/24 h/Vac show a peak near 3300-3500, ascribed to νN-H/O-H. There is a small νC-H peak ≈ 2900 cm^{-1}. The minor peak around 1400 cm^{-1} is typical for N-H bending. Besides, peaks at 1090, 1142, and 839 cm^{-1} correlate to PEO.[28]

4.3.2 In situ XRDs and XPS studies of PEs

Rigaku (Rigaku Denki., Ltd., Tokyo, Japan) was used to analyze the crystal structures of the PEs films, as well as pure PEO. Films were heated from 25° to 65° and 100 °C min^{-1} at 3 °C min^{-1}. The films were then cooled to room temperature. Temperature dependent *in situ* XRD were examined with Cu Kα radiation of wavelength λ=1.541 Å operating at 40 kV and 44 mA with high D/teX Ultra 250 detectors in the 10° to 40° 2θ range using a step width of 0.02°. The slow scan rate was used to minimize the signal-noise ratio. Graphite was used as a substrate for thermal conductivity and as an internal standard for quantifying peak shifts.

The Figure **4.2a** XRD patterns of pure PEO show a large intensity peak at 23.5° 2θ, followed by a second maximum peak at 19.3° and doublet peak at 26.45° 2θ corresponds to (112), (120), and (222) planes (PDF: 00-049-2201) respectively.

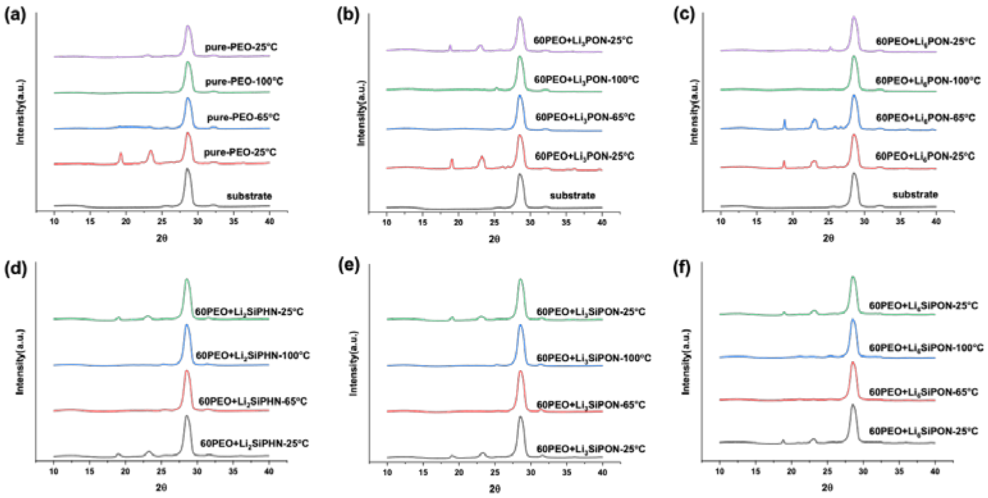

Figure 4.2. *In situ* XRDs of a. pure PEO, b. 60PEO:Li_3PON, c. 60PEO:Li_6PON, d. 60PEO:Li_2SiPHN, e. 60PEO:Li_6SiPON, and f. 60PEO:Li_6SiPON at selected temperatures.

Table **4.2** lists the d-spacing and peaks for the various PE films at selected temperatures. The peak near 2θ ~29 ° is ascribed to the graphite substrate. All peak positions shift with respect of the graphite substrate as standard.

Table 4.2. Peak list, and d spacing of PEO based polymer electrolytes at selected temperatures.

Sample	25 °C		65 °C		Cooled to 25 °C	
	2θ(°)	d-spacing (°)	*2θ*(°)	d-spacing (°)	*2θ*(°)	d-spacing (°)
PEO	19.3	4.55	20.6	4.3	18.8	4.7
	23.5	3.75	25.6	3.4	23	3.86
60PEO/ Li_3PON	19.1	4.64	20.9	4.25	18.8	4.72
	23.1	3.83	25.3	3.52	23	3.85
60PEO/Li_6PON	18.8	4.72	20.9	4.24	18.8	4.72
	23.2	3.82	25.1	3.54	23.2	3.83
60PEO/ Li2SiPHN	18.9	4.67	21	4.21	18.7	4.72
	23.1	3.83	25.4	3.5	23	3.85
60PEO/Li_6SiPON	18.8	4.72	20.9	4.23	18.9	4.67
	22.9	3.87	25.3	3.5	23.1	3.84

Figure **4.2(b-f)** shows *in situ* XRD patterns for PEs films. The composite films show the largest intensity peak at 23.3° 2θ, following a second less intense peak at 19° 2θ and a small peak ~ 26.2° 2θ. The X-ray spectra of PE films at room temperature exhibit peak shifts towards lower diffraction angles compared to pure PEO as listed in Table **4.2**. For example, the (112) peak shifts from 19.3° to 18.8° 2θ when Li_6SiPON precursor is introduced. The d-spacings between (112) planes increase from 4.55 to 4.72 Å suggesting strong interactions with the precursor. Shifts in XRD peaks can be caused by strain or stress.[50] The differences in crystallization kinetics is attributed to the variation in miscibility between PEO and the precursor systems. Addition of the PEs especially with Me_3Si moieties reduces crystallinity considerably as demonstrated by broadening and reduction of PEO peak intensities vs. graphite.

The Figure **4.3** XPS survey of the PE films provides the elemental compositions of the polymer electrolytes showing the expected elements for Li_xPON and Li_xSiPON with an additional peak for C from PEO. Table **4.3** summarizes the obtained XPS results.

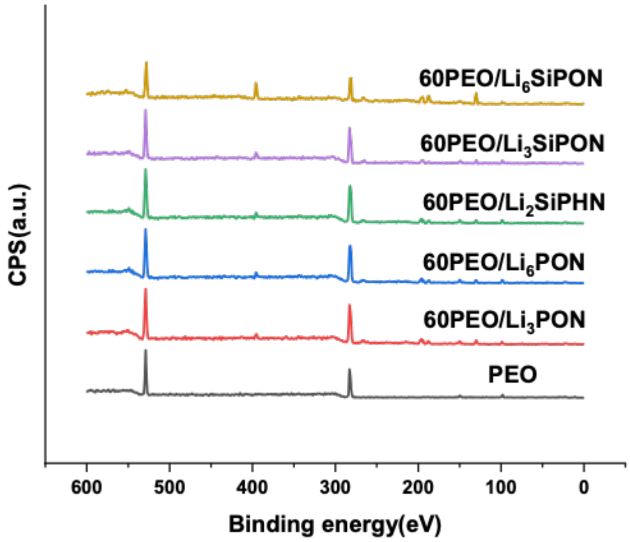

Figure 4.3. XPS spectrum (600 to 0 eV) of PEs and PEO film.

The resulting atomic percentage (at. %) demonstrate that the Li/N ratio increases from ~ 0.9 to 1.3 with the increase $LiNH_2$ amount for 60PEO/Li_6SiPON film. However, this ratio is smaller when compared to Li_3PON (1.9) and Li_6PON (2.5) polymer composite films. This might be attributed to the introduction of silicon in the polymer precursor. The N/P ratio deduced from the XPS analysis (Table **4.3**) is smaller than what is experimentally calculated (3), this decrease is likely associated with loss of nitrogen by polymerization. However, compared to gas phase deposited Li_xPON materials, the obtained N/P ratios (1-1.5) for the PE films are higher.[51]

Table 4.3. The calculated atomic compositions for PE composite films.

Ratio	Li_3PON	Li_6PON	Li_2SiPHN	Li_3SiPON	Li_6SiPON
N/P	1.06	1.1	1.5	1.2	1.01
Li/N	1.9	2.5	1.1	0.9	1.3

The element bonding environments can be obtained from the XPS analysis. The binding energy of the carbon in all the polymer composite films coincides with the most intense PEO carbon peak of the $-CH_2-CH_2-O-$repeat unit.

4.3.3 Microstructure and DSC studies of PEs

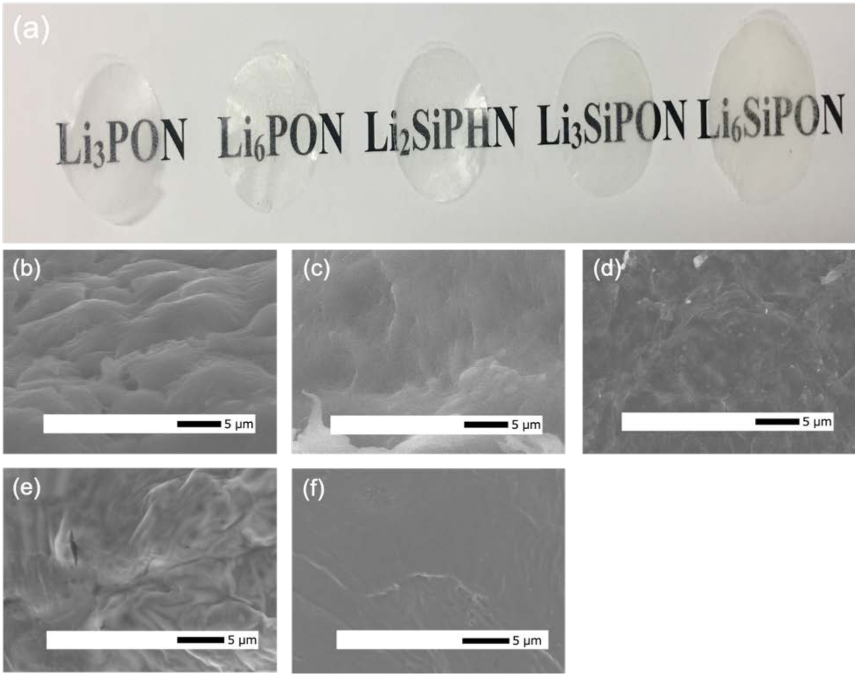

Figure 4.4. a. Optical images of PEs and SEM images of b. 60PEO:Li_3PON, c. 60PEO:Li_6PON, d. 60PEO:Li_2SiPHN, e. 60PEO:Li_3SiPON, f. 60PEO:Li_6SiPON heated to 65 °C/24 h/Vac.

The literature reports that for PEO/Li salt mixtures, the intoduction of adequate excess salt reduces the crystallinity and crystallization temperature of the PEO system as a result of cation and ether oxygen interaction.[44] Our PE films do not contain any salt, thus the cations and ether oxygens interaction is proposed to occur as a result of cations dissociation from the polymer precursor backbone. The PEO crystallization is directly infulenced by the cation dissociation and its interaction with ether oxygens or, indirectly gorvened by the microstrcure of the film during crystallization.

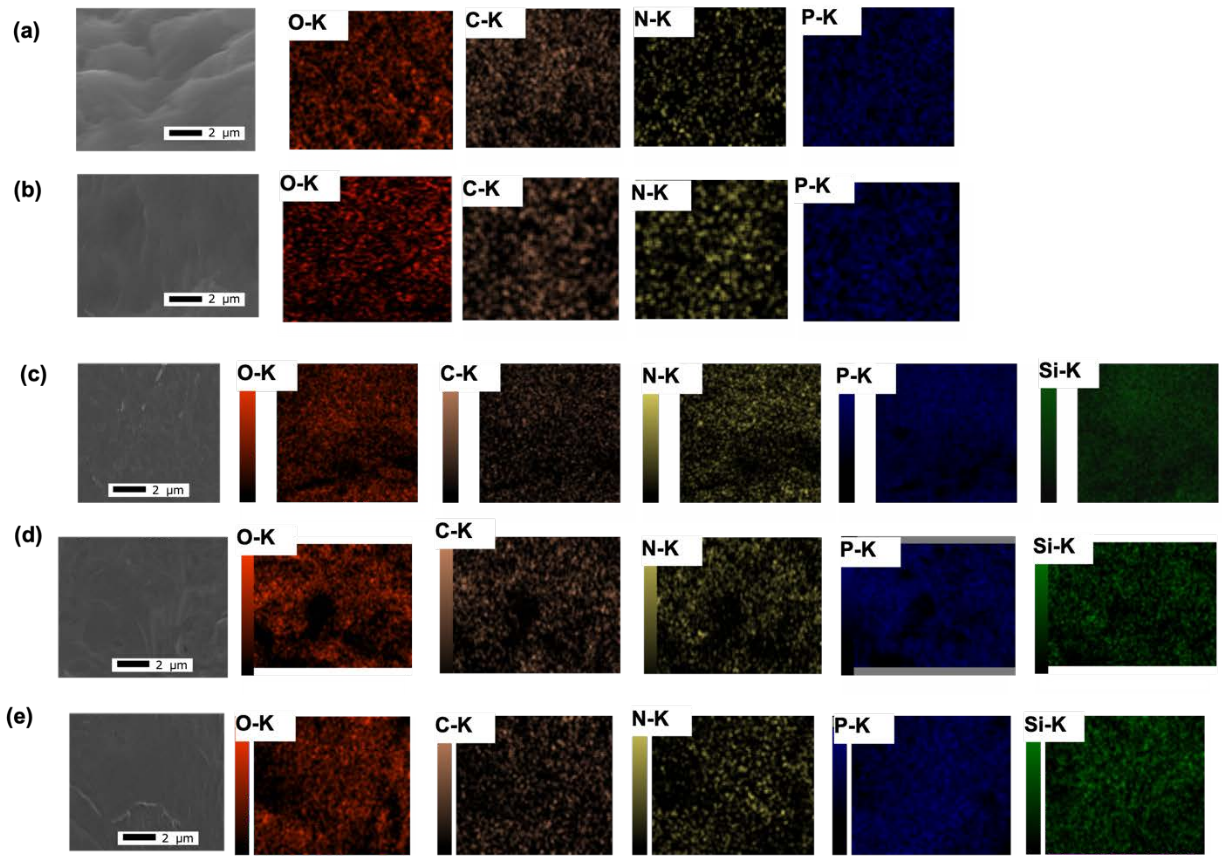

Figure 4.5. EDX images of (a) 60PEO:Li_3PON, (b) 60PEO:Li_6PON, (c) 60PEO:Li_2SiPHN, (d) 60PEO:Li_3SiPON, (e) 60PEO:Li_6SiPON heated to 65 °C/24 h/Vac.

Figures **4.4 b-f** show SEMs of PE films heated to 65°C/24 h/Vac. The film microstructures look very dense. The observed microstructure depends on the preparation procedure which is a critical in optimizing the dispersion of the polymer precursors in the PEO matrix. The 60PEO:Li_xSiPON films' surface morphology appears to be uniform, dense and smooth. The morphology of 60PEO:Li_2SiPHN film showed irregular surface with crystalline domains. The introduction of Li_3PON precursor into the polymer matrix resulted spherulitic structure. The diameter of spherulites seems to increase with the increase Li content (i.e. Li_3PON to Li_6PON), might be ascribed to the increase in nucleating center during film formation.[52] Figure **4.5** presents the elemental distribution of the polymer electrolytes. EDX map of LixPON and Li_xSiPON films show well-dispersed signature elements (P, O, N, and C) and (Si, P, O, N, and C), respectively.

To analyze the influence of polymer precursors on the crystallinity of PEO, we first determined the PEO crystallinity for each PE films using DSC (χ_c). The percent crystallinity was calculated using as $\chi_c = \Delta H_m/(wt._{PEO})\Delta H^0_m$, where ΔH_m is the melting enthalpy acquired from the DSC measurement and ΔH^0_m is the melting enthalpy of pure crystalline PEO.

Literature values for ΔH^0_m range from 188 to 216 J g^{-1}. [50,53,54] As such we assumed that the ΔH^0_m = 206 J g^{-1}.[53]

Figure **4.6** shows the DSC thermogram of a pure PEO film and all the PEs films. For the prisine PEO sample an endotherm is seen at ~ 71 °C for the 1st cycle which shifts to 69 °C after the 2nd and 3rd cycles. This is ascribed to melting of crystalline PEO. Pure PEO also exhibits a crystallization exotherm peak near ~ 38 °C. The peak crystallization temperatures (T_c) can also be determined from the cooling response. The addition of the PEs to PEO decrease T_c slightly.

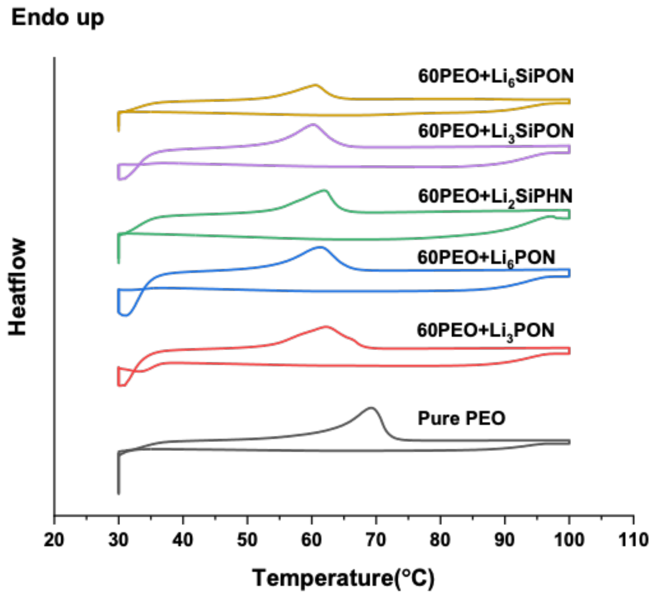

Figure 4.6. DSC thermograms of pristine PEO and PEs films 3rd cycle.

In Figure **4.6** endotherms are observed for all PE films. Table **4.4** lists the calculated percent crystallinity and found melting temperature of these solid-solution electrolyte films. The degree of crystallinity is of the order Li_2SiPHN>Li_6PON>Li_3PON> Li_6SiPON>Li_3SiPON. T_m decreases with the introduction of the PEs, suggesting that PEO crystallization is hindered. The crystallization temperature is also reduced from 40° to 38°-30 °C, comparing pristine PEO vs. the PEs. These results are in good agreement with the XRD peak broadining and smooth surface microstrcuture observed by SEM microgrpahs.

Table 4.4. Thermal properties of PEO derived polymer electrolyte films.

Sample	T_m (°C)	Heat of melting (J/g)	Degree of crystallinity (χ_c)
PEO	69	191	93
60PEO:Li_3PON	62	93	45
60PEO:Li_6PON	62	96	47
60PEO:Li_2SiPHN	61	116	56
60PEO:Li_3SiPON	58	30	15
60PEO:Li_6SiPON	61	60	30

4.3.4 Conductivity studies of PEs

The ionic conductivity is highly corelated with the charge density and mobility of active spices.[55] The key design paraments to enhance the ionic conductivity of the polymer precursor electrolyte are listed in three folds. (1) Decrease the crystallinity of PEO matrix,[56] (2) Increase the charge carrier densities by increasing the Li^+ concentration (i.e. Li_3PON to Li_6PON). This is challenging to attain using gas phase deposited Li_xPON as Li concentration is almost constant regardless of the deposition methode (i.e. rf power).[57] In addition, dispersing ceramic Li_xPON in PEO matrix is very difficult. However, our polymer precursor synthesis method governs the Li^+ concentration by varying $LiNH_2$ contents, and the fact that the as-synthesized polymer precursor is already in THF solution easiness the way to disperse with PEO host. (3) The other is to optimize the intrinsic composition of the polymer to increase Li^+ diffusion (i.e. increasing the N/P ratio) and decrease anion transport. Figure **4.7a** shows Nyquist plots of 60PEO:Li_3PON, Li_6PON, Li_3SiPON, Li_2SiPHN, and Li_6SiPON composite films at ambient.

The in-plane ionic conductivity and activation energies were calculated following the equations (2) and (3), respectively:

$$\sigma = t/(A_e * R) \quad (2)$$

$$\sigma_T = \sigma_o \exp\left(-\frac{E_a}{k_B T}\right) \quad (3)$$

Where t is the thickness of the film, A_e is area of the electrode, R is the resistivity acquired from the Nyquist plot, σ_o is the pre-exponential factor, E_a is the activation energy, k_B is the Boltzmann constant and T is the absolute temperature.

Table **4.5** lists the total room temperature conductivities of PE films heated to 65°C/12 h/Vac. The PEO/Li_3SiPON composite film offers the highest conductivity of 2.8 x 10^{-3}S cm^{-1}. The as-cast and warmed PEO/polymer films offered thicknesses in the range of 25-50 µm.

Table 4.5. Total room temperature conductivity of PEs.

Precursor	Conductivity (S cm^{-1})
Li_3PON	$4.4 \pm 0.6 \times 10^{-4}$
Li_6PON	$3.7 \pm 0.4 \times 10^{-4}$
Li_2SiPHN	$1.1 \pm 0.3 \times 10^{-3}$
Li_3SiPON	$2.8 \pm 0.2 \times 10^{-3}$
Li_6SiPON	$2.7 \pm 0.1 \times 10^{-4}$

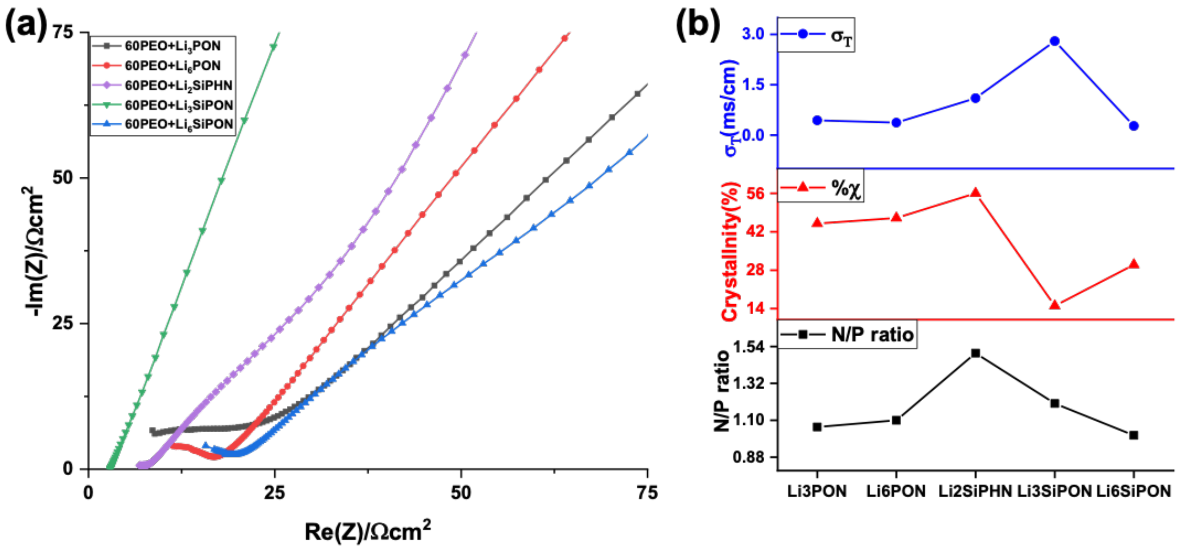

Figure 4.7. a. Nyquist plots of PEs at ambient b. correlation between N/P ratio(black), crystallinity percentage (red) and ionic conductivity of PEs(blue).

Figure **4.7b** demonstrate the relation between N/P ratio, crystallinity percentage, and ionic conductivity of the polymer electrolytes. Here, we have demonstrated that the ionic conduction mechanism of the PEs depends on both the N/P ratio and the nature of amorphous phase obtained from XPS and DSC data respectively. The reported N/P ratios in this study, are relatively high compared to gas phase deposited Li_xPON electrolytes, which result in significant improvement in ionic conductivity.[51] The decrease in electrostatic energy as a result of more P-N$<^{P}_{P}$ cross link structure in the PEs is one of the main factor contributing to the increase in Li^+ mobility.[47,57] The structures of the polymer precursors are shown in Schemes **4.1** and **4.2**. The 60PEO:Li_2SiPHN showed the highest N/P ratio (1.5), resulting in decrease in electrostatic energy; however, this alone did not result in fast ion mobility compared to 60PEO:Li_3SiPON thin film. This is ascribed to the fact that the 60PEO:Li_2SiPHN film showed the highest crystalline percentage (~ 56%). Similar phenomena is observed for the 60 PEO:Li_xPON polymer electrolyte. This indicate that the main limiting factor for fast Li^+ diffusion is the mobility of the PEO matrix. Although some reports show that crystalline PEO can offer fast ionic transport, prevailingly, the crystalline region of the PEO is detrimental factor owning to the slower chain dynamics upon crystallization resulting in decrease ionic conductivity.[58]

The decrease in crystallinity of 60PEO:Li_3SiPON (~ 15%), along with the high N/P ratio resulted in superior ionic conductivity ~ 2.8 mS cm^{-1} at ambient in good agreement with DSC (Figure **4.6**), *In Situ* XRD (Figure **4.2**), and XPS data (Figure 4.**3**). This value is much higher than gas phase deposited Li_xPON typically 10^{-3} mS cm^{-1} [59] at ambient, and higher than simple PEO/Li^+ salt polymers as shown in Table **4.6**.[52]

This is ascribed to solvation ability of polymer backbone and homogenous miscibility of the polymer precursor in the PEO as shown by the optical image of Figure **4.4a**. For comparison, the ionic conductivity of polymer electrolytes with different Li salts and plasticizers at room temperature are listed on Table **4.6**.

Table 4.6. Examples of PEO-based polymer electrolytes with Li salt and plasticizer.

Polymer matrix	Li salt	Plasticizer	σ (S cm^{-1})	Ref.
PEO	LiTF	EC	1.5×10^{-4}	[2]
PEO	LiTFSI	SN	1.5×10^{-3}	[3]
PEO	$LiClO_4$	DMP	$\sim 10^{-5}$	[4]
PEO	LiBOB	SN	$\sim 10^{-4}$	[5]
PEO	$LiBF_4$	$MMPIPF_4$	2×10^{-3}	[6]
PEO	$LiPF_6$	$MMPIPF_6$	1.13×10^{-3}	[6]

[1]EC (ethylene carbonate), SN (succinonitrile), DMP (dimethyl phthalate), MMPIPF4 (1-n-propyl-2,3-dimethylimidazolium tetrafluoroborate). [2]

The solvation state of Li^+ ions highly depend on the polymer backbone, bearing the ionic group. The Li_xSiPON polymer precursor with high nitrogen atoms appears to favor Li solvation compared to Li_xPON polymer precursors. Charge transport requires both efficient ionic solvation and low migration barrier. Hence, the solvated Li^+-ions mobility must be optimized through the polymer matrix to produce superionic polymer electrolyte thin films, which requires the amorphous nature of PEO matrix.[27]

A key design factor for PEO-based electrolytes is generally to suppress the crystallinity and increase amorphous wt.% fraction for ion transport.[12] Generally, lithium salt with bulkier anions are preferred, due the well-delocalized negative charge promoting fast Li^+ diffusion and improving the ionic conductivity.[60] As the predominate ionic diffusion occurs in the amorphous region of PEO, segmental motion and local relaxation of the PEO matrix are needed for Li^+ transport. The proposed Li^+ ion conduction mechanism for the PEO/Li salt is through a segmental motion, where the Li^+ ions are coordinated by the ether oxygen atom.[12] In the PEO/Li salt systems, both the cations and anions are mobile species resulting in a decrease in the transference numbers, which is generally < 0.5 due to the electro-polarization from anion buildup.[61] The electro-polarization can lead to a decrease in the electrochemical performance due to high internal impedance, IR drops, and dendritic growth.[62]

Single-ion conductor can overcome these challenges faced by salt-doped counterparts. Previous studies indicate that high ionic dissociation and enhancement in the concentration of charge carriers can be achieved by introducing nitrogen atoms into the backbone of the polymer, which is known to decrease the anion-cation binding energies.[61,63] The anions of the polymer precursors (Li_XPON and Li_XSiPON) are proposed to be chemically bound with the PEO polymer back bone resulting in only cation transport. The anionic units in these polymer precursors/PEO mixtures are predicted to be immobile in regarding of conductivity. This theory is supported by the achieved high ionic conductivity at ambient, a very low activation energy, high t_{Li}^+, and stability of the PEs in symmetric and half-cell configurations. The difference in solvation might be related to the property of the interface between the PEO functionalized segments and the polymer precursors.

Lithium transference number (t_{Li}^+) was determined following the procedure described elsewhere.[38] The stability of PEs against metallic Li anode was analyzed by observing the Nyquist plots of Li/60 wt.% PEO: PEs/Li symmetrical cells before and after Chronoamperometry measurements at ambient. The Ohmic region of the cell impedance is usually associated with the high-frequency range semicircle, which is associated with the resistance of the PEs, the semicircle at low frequencies is attributed to the capacitive properties, Solid electrolyte interface (SEI).

Table **4.7** lists the t_{Li}^+ of the various polymer precursor electrolytes. The increase in the t_{Li}^+ for the PE films suggests that the chemical interaction between Li and PON, SiPON, and SiPHN, results in fast Li^+ mobility.

Table 4.7. Li^+ transfer numbers of PEs.

Samples	*tLi^+ avg*
Li_3PON	0.6±0.05
Li_6PON	0.5±0.07
Li_2SiPHN	0.8±0.01
Li_6SiPON	0.65±0.05

The t_{Li}^+ of the PEO based polymer precursor electrolytes assembled on symmetric cell configuration. The Li_2SiPHN precursor showed a high t_{Li}^+ of ~0.8 comparable to single-ion conducting polymer electrolytes. [11]The transference number decreased for the PEO based polymer electrolytes compared to the pristine LixPON polymer electrolytes.[38] This might be ascribed to the increasing mobility of both cation and anion in the PE film due to high flexibility of the PEO segments. The increase in the transference number of Li_2SiPHN might be due to the cyclometric structure of SiPHN, the molecule is bulkier than SiPON and PON hence lower anion mobility. One method to obtain single-ion conducting polymer electrolyte is by anchoring the anions to the polymer backbone.[11]

Figure **4.8** shows typical Arrhenius plots for the PEs films, where AC impedance measurements was performed in a frequency range of 7 MHz to 1 Hz at -15 °C to 70 °C. The activation energy is the sum of the energy required to from defects and the ion migration energy, which was obtained by linear fitting the log conductivity with 1/T plots.[52] The linear fit of the Arrhenius plots was used to calculate the activation energies of the PEs as listed in Table **4.8**. The superior ionic conductivity in the PEs is ascribed to the increase in mobile Li^+-ion concentration and the decrease in PEO crystallinity.

Table 4.8. Activation energies of PEs composite films.

Polymer electrolyte	Activation energy (eV)
Li_3PON	0.23
Li_6PON	0.45
Li_2SiPHN	0.5
Li_3SiPON	0.34
Li_6SiPON	0.32

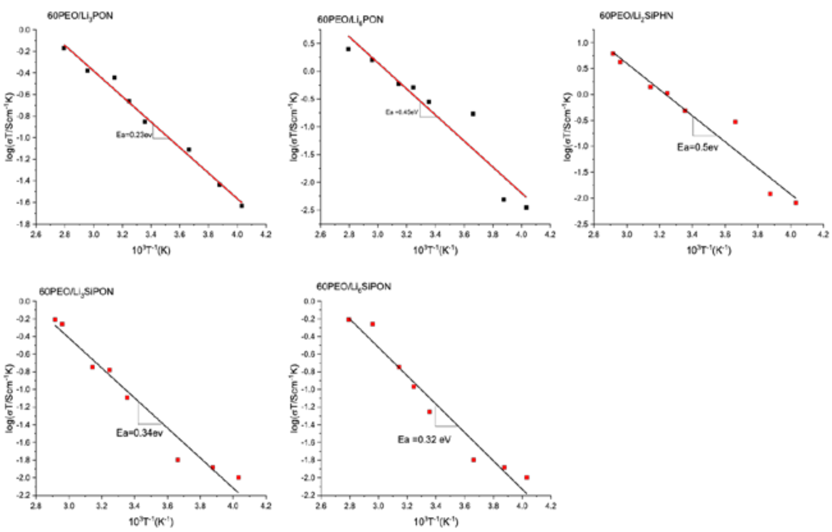

Figure 4.8. Arrhenius plots PEs films (25-50 µm) heated to selected temperatures.

Table **4.9** records the total ionic conductivities of the PE films heated to selected temperatures. Optimization of ionic conductivity was achieved by introducing the ionically conducting PEs which are key to improving the room temperature and reducing the activation energy for cation transport.

Table 4.9. Total conductivities (σ_t) of PEs heated to selected temperatures.

T (°C)	σ(S cm^{-1}) Li_3PON	σ(S cm^{-1}) Li_6PON	σ(S cm^{-1}) Li_2SiPHN	σ(S cm^{-1}) Li_3SiPON	σ(S cm^{-1}) Li_6SiPON
-15	1.4×10^{-4}	1.9×10^{-5}	4.6×10^{-5}	4.2×10^{-5}	4×10^{-5}
0	2.8×10^{-4}	6.3×10^{-4}	1×10^{-4}	5.2×10^{-5}	5×10^{-5}
25	4.7×10^{-4}	9.4×10^{-4}	1.6×10^{-3}	2.8×10^{-4}	2.7×10^{-4}
35	7×10^{-4}	1.7×10^{-3}	3.5×10^{-3}	3.5×10^{-4}	5.4×10^{-4}
45	1.1×10^{-3}	1.9×10^{-3}	4.4×10^{-3}	4.7×10^{-4}	5.6×10^{-4}
65	1.2×10^{-3}	4.7×10^{-3}	1.3×10^{-2}	1×10^{-3}	1.6×10^{-3}
70	1.9×10^{-3}	$7. \times 10^{-3}$	1.8×10^{-2}	1.2×10^{-3}	1.7×10^{-3}

The temperature dependent conductivity of the PEs increases with increases in temperature for all PEO/precursor systems. The activation energies decrease from 0.5 to 0.23 eV for Li_2SiPHN vs. Li_3PON precursor. This latter value is ascribed to the amorphous nature of the PE hindering the crystallinity of the PEO and facilitating fast Li^+ motion as supported by DSC data.

4.3.5 Symmetric studies of Li/PEs/Li

Figure **4.9** shows galvanostatic cycling of Li/60PEO:Li_3PON, Li_2SiPHN, Li_6SiPON /Li at ambient. The symmetric cells show nearly constant voltage response of 3, 2 and 30 mV for Li_3PON, Li_2SiPHN, and Li_6SiPON based PEs respectively. These results suggests that the PEs are stable vs. Li metal at higher current densities (0.325 mA cm^{-2}) compared to conventional PEO/Li salt electrolytes (0.1 mA cm^{-2}).[64,65]

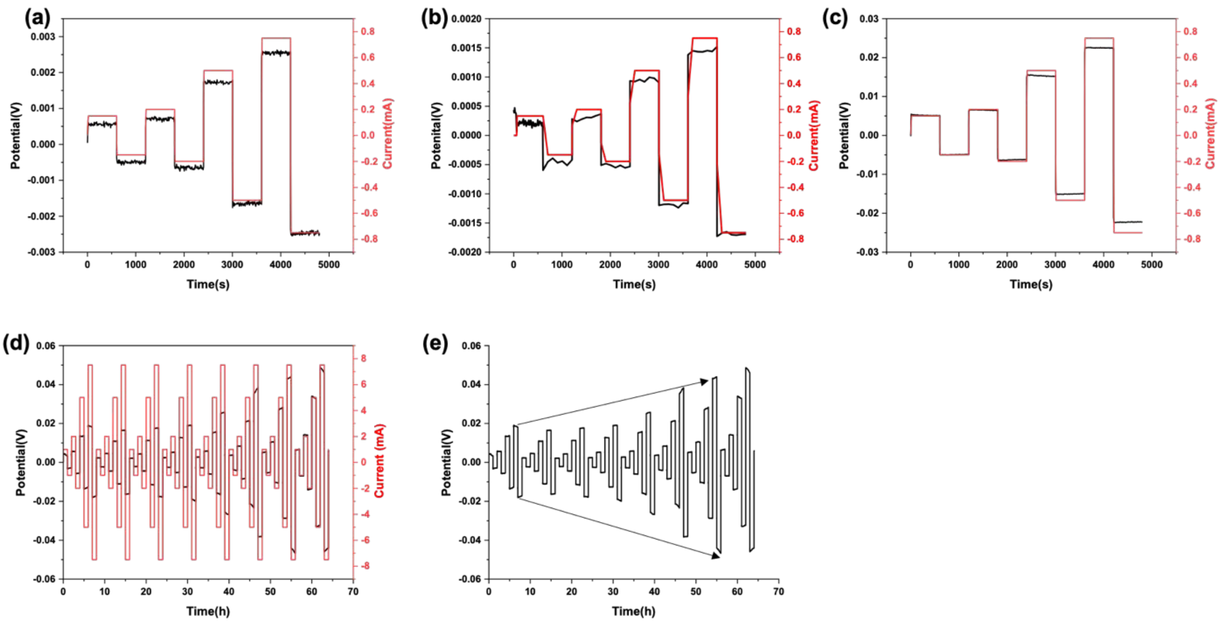

Figure 4.9. Galvanostatic cycling of Li/60PEO: a. Li_3PON, b. Li_2SiPHN, c. Li_6SiPON/Li symmetric cells at the current density of ±0.15-0.75 mA, and d. Li/60PEO:Li_6PON /Li symmetric cells at the current density of ±1.5-7.5 mA at room temperature. e. potential vs. time profile of Li/60PEO:Li_6PON /Li cell.

Figure **4.9d**. shows galvanostatic cycling of Li/60PEO:Li_6PON/Li at room temperature. The main goal of the symmetric cell experiment was to increase the current densities and study the interfacial behavior of the electrode-electrolyte such that an optimal c-rate is used when half-cell is assembled.

The symmetric cell shows a stable voltage response of 0.02 V for the first 40 h, the interfacial resistance seems to increase as demonstrated by the increase in voltage to 0.05V after the 20th cycle. The 60PEO:Li_6PON film is stable vs. Li metal at higher current densities (3.25 mAh cm^{-2}) compared to traditional PEO/Li salt electrolytes (0.1 mA cm^{-2}).[64] It is also worth mentioning that these symmetric cell studies are performed at room temperature while most PEO/Li salt studies are performed at elevated temperatures (>65 °C).[65] Most polymer/solid electrolytes are limited by the solid-solid diffusion at the interface, resulting in a reduction of the critical current densities.[66] Here, we are able to enhance the interface between Li metal electrode and the polymer films by melt-bonding the PEs on top of the Li surface.

The development of high energy density ASSBs depends on the stability of the solid electrolyte at wide potentials. CV was carried out at a scanning rate of 5 mV/s at ambient to examine the electrochemical stability of the PE films. Figure **4.10** shows CVs acquired for the Li/PEs/SS cell in the ranges of -1 V to 6 V. The cathodic and anodic peak ~ 0 V suggests the lithium plating and stripping demonstrating that the Li^+-ions can migrate through PEs and deposit on the stainless-steel side and vice versa. At higher voltage, the current response is quite small, demonstrating the wide electrochemical stability of the PE films.

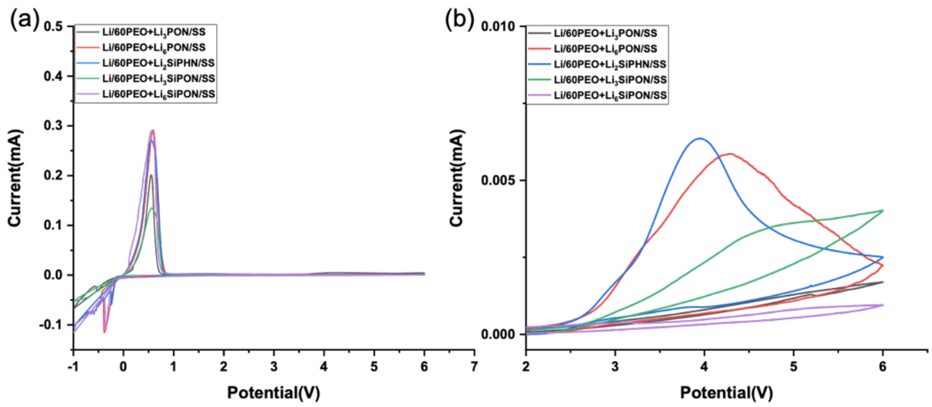

Figure 4.10. Cyclic voltammetry of Li/PEs/SS at a sweep rate of (a) 5 mV/sec and (b) 0.1 mV/sec.

4.3.6 Half-cell studies of SPAN/PEs/Li

The composite cathode shows a 3-D network of structures forming micro globules. The EDX map in Figure **4.11** shows the signature element (S, C, and Al) distribution for SPAN. Figures **4.12** and **4.13** show SEM and EDX images of SPAN-based active material warm pressed with 60PEO:Li_3PON and 60PEO:Li_6PON respectively. There is a noticeable interface between the polymer electrolyte, cathode, and current collector. Elemental mapping of the catholyte shows well-defined phosphorus, aluminum, and sulfur interface distributions. The compiled EDX image also shows a clear elemental layered structure where C, N, and P are in the top region ascribed to the polymer electrolyte and the middle region is mostly occupied by sulfur and the bottom is dominated by Al.

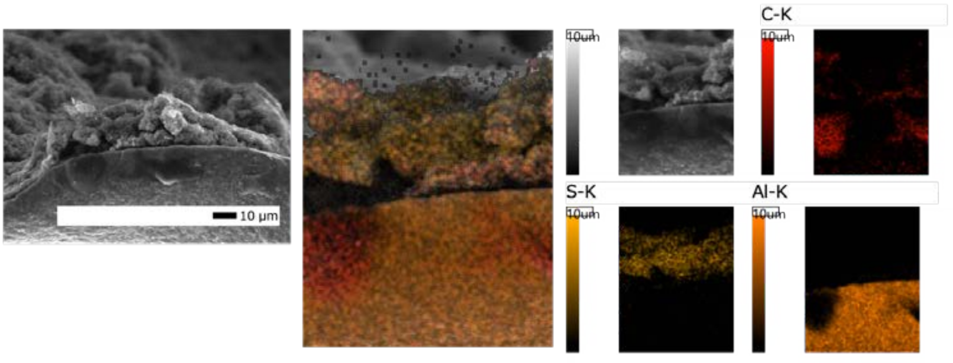

Figure 4.11. SEM fracture surface image of SPAN.

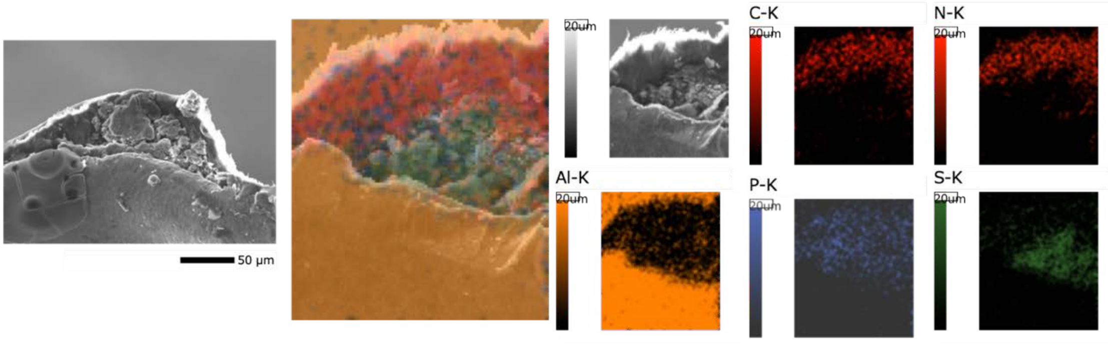

Figure 4.12. SEM and EDX images of SPAN + 60%PEO/Li_3PON pressed at 5 kpsi /40 °C/ 2 min.

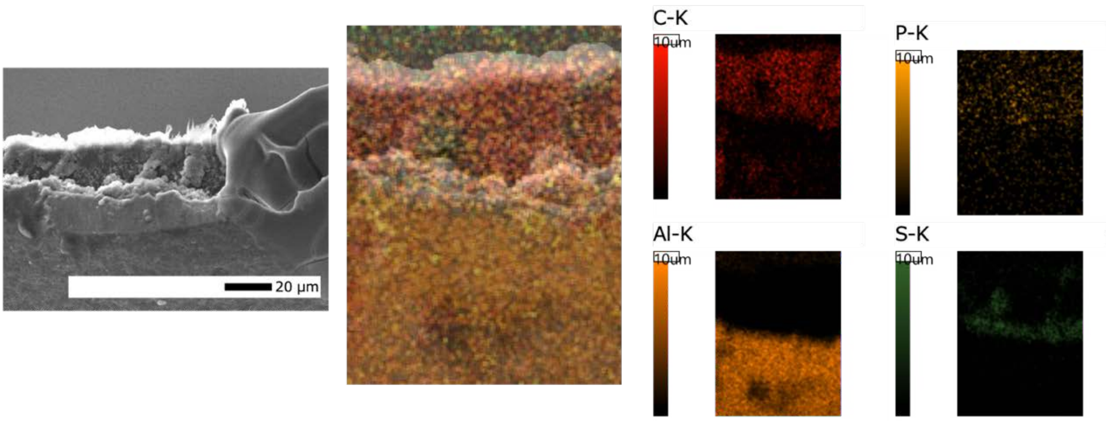

Figure 4.13. SEM and EDX images of SPAN + 60%PEO/Li_6PON pressed at 5 kpsi /40 °C/ 2 min.

Figures **4.14** show SEM and EDX images of SPAN/60PEO:Li_2SiPHN warm pressed at 5 kpsi/40°C/2 min. The SPAN cathode warm pressed with 60PEO:Li_2SiPHN present very smooth and uniform interfaces, ideal catholytes. The EDX map shows a well distributed elements (Si, P, and O) at the top of the image ascribed to the polymer precursors, C is also dominant in the middle region along with S, attributed to the cathode. The bottom interface is mainly composed of Al from the current collector.

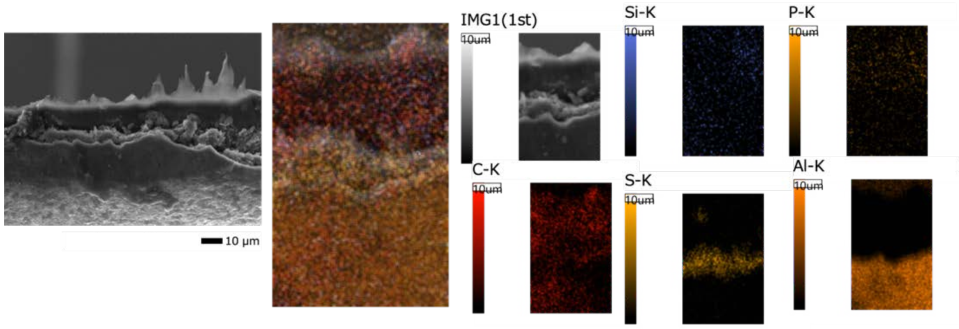

Figure 4.14. SEM and EDX images of SPAN+ 60%PEO/Li_2SiPHN pressed at 5 kpsi /40 °C/ 2 min.

Figure **4.15a** illustrates the result of SPAN/60PEO:Li_6SiPON/Li cells cycled at various C rates. The Li-SPAN battery cycled for 500 h with minimal voltage fluctuation. The half-cell was cycled from 1 to 3 V for 100 cycles. The galvanostatic cycling profile shows that the Li-S cell was cycled for 30 cycles at 0.25 C, 20 cycles at 0.5 and 1C and the last 20 cycles at 0.25 C. During the initial discharge cycle, the obtained voltage plateau (~1.5 V) is lower than the potentials observed in succeeding cycles as shown in Figure **4.15a**. This suggests that the discharge process involves a different reaction. In the subsequent cycles, the voltage profile shows an increase (1.7 and 2.2 V) during the 100 cycles. These voltage plateaus are obviously different from what is commenly reported for Li-S cells, where a two-step discharge plateau is reported ascribed to the reaction of Li^+ and elemental sulfur to form lithium polysulfides ~ 2.4 V. The second plateau ~ 2.1 V is associated with the formation of short-order polysulfide.[53,67,68] The presence of only one voltage plateau ~ 2.2 V is vital as it suggests that lithium polysulfides does not form in Li-SPAN cell, which suppresses polysulfide shuttle effect and maximizes cycle life, this is typical for SPAN cathodes.[69] The plausibility of this hypothesis is also supported by the high columbic efficiency.

The half-cell showed initial discharge capacities of ~ 1800 mAh/g_{sulfur}, higher than the theoretical capacity for sulfur (1672 mAh/g) as seen in Figure **4.15b**. This suggests that the carbon framework of SPAN (π- conjugated pyridinic) contributes to the initial capacity. It is probably a mixture of Faradic capacity as a result of SEI formation on carbon during the initial cycle and a non-Faradic pseudo-capacitance.[68,69]

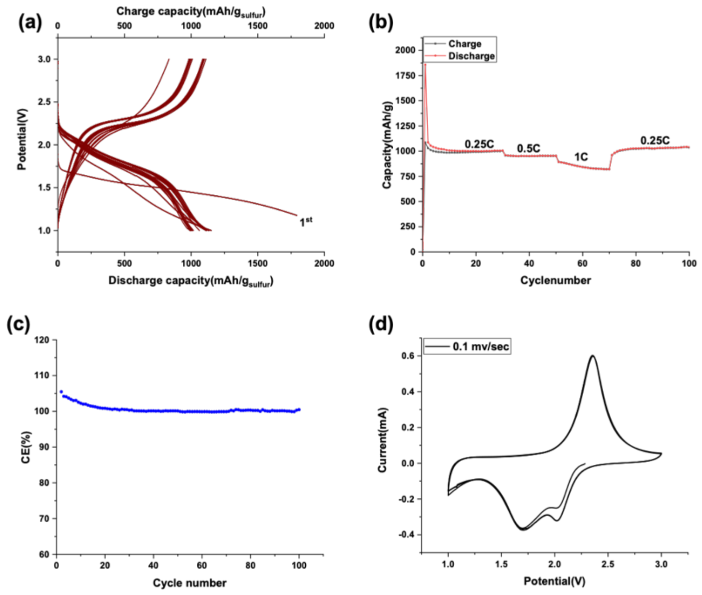

Figure 4.15. Galvanostatic cycling plots of SPAN/60PEO:Li_6SiPON/Li at selected c-rates (a-c) and d. cyclic voltammogram at 0.1 mV sec^{-1}.

The half-cell charges and discharges to the targeted potentials with minimal polarization for 100 cycles at the desired C-rates. The capacity starts to decrease to 1000 mAh g_{sulfur}^{-1}after the 1st cycle. The capacity showed a slight decrease to 950 and 800 mAh g_{sulfur}^{-1} at 0.5 and 1 C, however, the capacity was recovered when cycled back to 0.25 C. The Li/S cathode shows high capacity, high cycle stability, and high discharge/charge capacity. The 60PEO:Li_6SiPON polymer electrolyte also showed high electrochemical stability at a high rate of 0.25, 0.5, and 0.1 C for 100 cycles. A columbic efficiency of ~ 100 % was maintained throughout the cycle (Figure **4.15c)**.

Figure **4.15d** shows cyclic voltammogram of SPAN/60 PEO:Li_6SiPON /Li. CV provides additional information about the electrochemical property of the SPAN cathode and the PE films. It is possible to confirm that sulfur as S_2 and S_3 are the major species in the SPAN electrode.[69,70] The CV curves show multiple redox peaks; note that the lower voltage plateau for the initial discharge process is in a good agrees with the voltage profile obtained from the galvanostatic cycling studies shown in Figure **4.15a**.

If these PEO/polymer precursors can be melt cast onto cathodes and Li metal at the melting point of PEO (65°-75 °C) it may be possible to replace liquid electrolytes in traditional Li-ion batteries with melt cast mixtures of these materials eliminating fire hazards, reducing the extent of containment seals needed and perhaps greatly simplifying ASB assembly.

4.4 Conclusions

A maximum ionic conductivity of 2.8x 10^{-3} S cm^{-1} is achieved for 60PEO:Li_3SiPON films at ambient. The enhancement in conductivity of this PE is ascribed to the suppression of PEO crystallinity and the increase in the N/P ratio. The Li_xSiPON polymer precursor with high nitrogen atoms seems to favor lithium solvation better than Li_xPON polymer precursors. [47,57] Besides, the high Li^+ transference number of Li_2SiPHN indicates that the mobility of anions has been limited ascribed to the polymer precursor backbone. In addition to the enhanced ionic conductivities vs traditional PEO electrolytes, these active polymer precursor fillers offer improved stability against lithium metal at higher current densities. Galvanostatic cycling of SPAN/PEs/Li cell shows discharge capacities of 1000 mAh/g_{sulfur} at 0.25 C and 800 mAh/g_{sulfur} at 1C. The cell also shows high capacity retention over 100 cycles with 100% columbic efficiencies.

References

(1) Xu, W.; Wang, J.; Ding, F.; Chen, X.; Nasybulin, E.; Zhang, Y.; Zhang, J. G. Lithium Metal Anodes for Rechargeable Batteries. *Energy and Environmental Science*. 2014. https://doi.org/10.1039/c3ee40795k.

(2) Manthiram, A.; Yu, X.; Wang, S. Lithium Battery Chemistries Enabled by Solid-State Electrolytes. *Nature Reviews Materials*. 2017. https://doi.org/10.1038/natrevmats.2016.103.

(3) Kalhoff, J.; Eshetu, G. G.; Bresser, D.; Passerini, S. Safer Electrolytes for Lithium-Ion Batteries: State of the Art and Perspectives. *ChemSusChem* **2015**. https://doi.org/10.1002/cssc.201500284.

(4) Fergus, J. W. Ceramic and Polymeric Solid Electrolytes for Lithium-Ion Batteries. *Journal of Power Sources*. 2010. https://doi.org/10.1016/j.jpowsour.2010.01.076.

(5) Yi, E.; Wang, W.; Mohanty, S.; Kieffer, J.; Tamaki, R.; Laine, R. M. Materials That Can Replace Liquid Electrolytes in Li Batteries: Superionic Conductivities in Li1.7Al0.3Ti1.7Si 0.4P2.6O12. Processing Combustion Synthesized Nanopowders to Free Standing Thin Films. *J. Power Sources* **2014**, *269*, 577–588. https://doi.org/10.1016/j.jpowsour.2014.07.029.

(6) Yi, E.; Wang, W.; Kieffer, J.; Laine, R. M. Flame Made Nanoparticles Permit Processing of Dense, Flexible, Li^{+} Conducting Ceramic Electrolyte Thin Films of Cubic-$Li_{7}La_{3}Zr_{2}O_{12}$ (c-LLZO). *J. Mater. Chem. A* **2016**, *4* (33), 12947–12954. https://doi.org/10.1039/C6TA04492A.

(7) Masoud, E. M.; El-Bellihi, A. A.; Bayoumy, W. A.; Mousa, M. A. Effect of LiAlO2 Nanoparticle Filler Concentration on the Electrical Properties of PEO-LiClO4 Composite. *Mater. Res. Bull.* **2013**. https://doi.org/10.1016/j.materresbull.2012.12.012.

(8) Manuel Stephan, A.; Nahm, K. S. Review on Composite Polymer Electrolytes for Lithium Batteries. *Polymer*. 2006. https://doi.org/10.1016/j.polymer.2006.05.069.

(9) Fenton, D. E.; Parker, J. M.; Wright, P. V. Complexes of Alkali Metal Ions with Poly(Ethylene Oxide). *Polymer (Guildf).* **1973**. https://doi.org/10.1016/0032-3861(73)90146-8.

(10) Angulakshmi, N.; Nahm, K. S.; Swaminathan, V.; Thomas, S.; Nimma Elizabeth, R. Nanocomposite Polymer Electrolytes for Lithium Batteries. In *Polymer Processing and Characterization*; 2012. https://doi.org/10.1201/b13105.

(11) Long, L.; Wang, S.; Xiao, M.; Meng, Y. Polymer Electrolytes for Lithium Polymer Batteries. *Journal of Materials Chemistry A*. 2016. https://doi.org/10.1039/c6ta02621d.

(12) Borodin, O.; Smith, G. D. Mechanism of Ion Transport in Amorphous Poly(Ethylene Oxide)/ LiTFSI from Molecular Dynamics Simulations. *Macromolecules* **2006**. https://doi.org/10.1021/ma052277v.

(13) Scrosati, B.; Croce, F.; Persi, L. Impedance Spectroscopy Study of PEO-Based Nanocomposite Polymer Electrolytes. *J. Electrochem. Soc.* **2002**. https://doi.org/10.1149/1.1393423.

(14) Berthier, C.; Gorecki, W.; Minier, M.; Armand, M. B.; Chabagno, J. M.; Rigaud, P. Microscopic Investigation of Ionic Conductivity in Alkali Metal Salts-Poly(Ethylene Oxide) Adducts. *Solid State Ionics* **1983**. https://doi.org/10.1016/0167-2738(83)90068-1.

(15) Cameron, G. G. Solid Polymer Electrolytes: Fundamentals and Technological Applications. Fiona M. Gray. VCH Publishers Inc., New York 1991. Pp. x + 245, Price £44.00. ISBN 0–89573–772–8. *Polym. Int.* **2007**. https://doi.org/10.1002/pi.4990320421.

(16) Stoeva, Z.; Martin-Litas, I.; Staunton, E.; Andreev, Y. G.; Bruce, P. G. Ionic Conductivity in the Crystalline Polymer Electrolytes PEO6:LiXF6, X = P, As, Sb. *J. Am. Chem. Soc.* **2003**. https://doi.org/10.1021/ja029326t.
(17) Sun, J.; Liao, X.; Minor, A. M.; Balsara, N. P.; Zuckermann, R. N. Morphology-Conductivity Relationship in Crystalline and Amorphous Sequence-Defined Peptoid Block Copolymer Electrolytes. *J. Am. Chem. Soc.* **2014**. https://doi.org/10.1021/ja5080689.
(18) MacGlashan, G. S.; Andreev, Y. G. Structure of the Polymer Electrolyte Poly (Ethylene Oxide) 6: LiAsF6. *Nature* **1999**. https://doi.org/10.1039/cc9960002169.
(19) Gadjourova, Z.; Andreev, Y. G.; Tunstall, D. P.; Bruce, P. G. Ionic Conductivity in Crystalline Polymer Electrolytes. *Nature* **2001**. https://doi.org/10.1038/35087538.
(20) Christie, A. M.; Lilley, S. J.; Staunton, E.; Andreev, Y. G.; Bruce, P. G. Increasing the Conductivity of Crystalline Polymer Electrolytes. *Nature* **2005**. https://doi.org/10.1038/nature03186.
(21) Liu, W.; Liu, N.; Sun, J.; Hsu, P. C.; Li, Y.; Lee, H. W.; Cui, Y. Ionic Conductivity Enhancement of Polymer Electrolytes with Ceramic Nanowire Fillers. *Nano Lett.* **2015**. https://doi.org/10.1021/acs.nanolett.5b00600.
(22) Michael, M. .; Jacob, M. M. .; Prabaharan, S. R. .; Radhakrishna, S. Enhanced Lithium Ion Transport in PEO-Based Solid Polymer Electrolytes Employing a Novel Class of Plasticizers. *Solid State Ionics* **2002**. https://doi.org/10.1016/s0167-2738(97)00117-3.
(23) Kumar, Y.; Hashmi, S. A.; Pandey, G. P. Lithium Ion Transport and Ion-Polymer Interaction in PEO Based Polymer Electrolyte Plasticized with Ionic Liquid. *Solid State Ionics* **2011**. https://doi.org/10.1016/j.ssi.2011.08.010.
(24) El Bellihi, A. A.; Bayoumy, W. A.; Masoud, E. M.; Mousa, M. A. Preparation, Characterizations and Conductivity of Composite Polymer Electrolytes Based on PEO-LiClO 4 and Nano ZnO Filler. *Bull. Korean Chem. Soc.* **2012**. https://doi.org/10.5012/bkcs.2012.33.9.2949.
(25) Gao, S.; Yan, X. L.; Zhong, J.; Xue, G. B.; Wang, B. Temperature Dependence of Conductivity Enhancement Induced by Nanoceramic Fillers in Polymer Electrolytes. *Appl. Phys. Lett.* **2013**. https://doi.org/10.1063/1.4803185.
(26) Wang, G. X.; Yang, L.; Wang, J. Z.; Liu, H. K.; Dou, S. X. Enhancement of Ionic Conductivity of PEO Based Polymer Electrolyte by the Addition of Nanosize Ceramic Powders. *J. Nanosci. Nanotechnol.* **2005**. https://doi.org/10.1166/jnn.2005.165.
(27) Wang, Y.-J.; Pan, Y.; Chen, L. Ion-Conducting Polymer Electrolyte Based on Poly(Ethylene Oxide) Complexed with Li1.3Al0.3Ti1.7(PO4)3 Salt. *Mater. Chem. Phys.* **2005**. https://doi.org/10.1016/j.matchemphys.2004.12.004.
(28) Wang, W.; Yi, E.; Fici, A. J.; Laine, R. M.; Kieffer, J. Lithium Ion Conducting Poly(Ethylene Oxide)-Based Solid Electrolytes Containing Active or Passive Ceramic Nanoparticles. *J. Phys. Chem. C* **2017**. https://doi.org/10.1021/acs.jpcc.6b11136.
(29) Zhao, E.; Ma, F.; Guo, Y.; Jin, Y. Stable LATP/LAGP Double-Layer Solid Electrolyte Prepared: Via a Simple Dry-Pressing Method for Solid State Lithium Ion Batteries. *RSC Adv.* **2016**. https://doi.org/10.1039/c6ra19415j.
(30) Bates, J. B.; Dudney, N. J.; Gruzalski, G. R.; Zuhr, R. A.; Choudhury, A.; Luck, C. F.; Robertson, J. D. Fabrication and Characterization of Amorphous Lithium Electrolyte Thin Films and Rechargeable Thin-Film Batteries. *J. Power Sources* **1993**. https://doi.org/10.1016/0378-7753(93)80106-Y.
(31) Yu, X. A Stable Thin-Film Lithium Electrolyte: Lithium Phosphorus Oxynitride. *J. Electrochem. Soc.* **1997**. https://doi.org/10.1149/1.1837443.
(32) Wang, C.; Bai, G.; Yang, Y.; Liu, X.; Shao, H. Dendrite-Free All-Solid-State Lithium Batteries with Lithium Phosphorous Oxynitride-Modified Lithium Metal Anode and Composite Solid Electrolytes. *Nano Res.* **2019**. https://doi.org/10.1007/s12274-018-2205-7.

(33) Liu, W.-Y.; Fu, Z.-W.; Li, C.-L.; Qin, Q.-Z. Lithium Phosphorus Oxynitride Thin Film Fabricated by a Nitrogen Plasma-Assisted Deposition of E-Beam Reaction Evaporation. *Electrochem. Solid-State Lett.* **2004**. https://doi.org/10.1149/1.1778934.
(34) Dudney, N. J. Thin Film Micro-Batteries. *Electrochem. Soc. Interface* **2008**.
(35) Zhang, T.; Imanishi, N.; Hasegawa, S.; Hirano, A.; Xie, J.; Takeda, Y.; Yamamoto, O.; Sammes, N. Li∕Polymer Electrolyte∕Water Stable Lithium-Conducting Glass Ceramics Composite for Lithium–Air Secondary Batteries with an Aqueous Electrolyte. *J. Electrochem. Soc.* **2008**. https://doi.org/10.1149/1.2990717.
(36) Kumar, B.; Kumar, J.; Leese, R.; Fellner, J. P.; Rodrigues, S. J.; Abraham, K. M. A Solid-State, Rechargeable, Long Cycle Life Lithium–Air Battery. *J. Electrochem. Soc.* **2010**. https://doi.org/10.1149/1.3256129.
(37) Jadhav, H. S.; Kalubarme, R. S.; Jadhav, A. H.; Seo, J. G. Highly Stable Bilayer of LiPON and B2O3 Added Li1.5Al0.5Ge1.5(PO4) Solid Electrolytes for Non-Aqueous Rechargeable Li-O2 Batteries. *Electrochim. Acta* **2016**. https://doi.org/10.1016/j.electacta.2016.03.143.
(38) Temeche, E.; Zhang, X.; Laine, R. M. Polymer Precursor Derived Li x PON Electrolytes : Toward Li − S Batteries. *ACS Appl. Mater. Interfaces* **2020**, *12*, 20548–20562. https://doi.org/10.1021/acsami.0c03341.
(39) Zhang, X.; Temeche, E.; Laine, R. M. Design, Synthesis, and Characterization of Polymer Precursors to LixPON and LixSiPON Glasses: Materials That Enable All-Solid-State Batteries (ASBs). **2020**. https://doi.org/10.1021/acs.macromol.0c00254.
(40) Temeche, E.; Yi, E.; Keshishian, V.; Kieffer, J.; Laine, R. M. Liquid-Feed Flame Spray Pyrolysis Derived Nanopowders (NPs) as a Route to Electrically Conducting Calcium Aluminate (12CaO.7Al2O3) Films. *J. Eur. Ceram. Soc.* **2019**. https://doi.org/10.1016/j.jeurceramsoc.2018.11.051.
(41) Zhao, Y.; Zhang, Y.; Gosselink, D.; Doan, T. N. L.; Sadhu, M.; Cheang, H. J.; Chen, P. Polymer Electrolytes for Lithium/Sulfur Batteries. *Membranes*. 2012. https://doi.org/10.3390/membranes2030553.
(42) Bannister, D. J.; Davies, G. R.; Ward, I. M.; McIntyre, J. E. Ionic Conductivities for Poly(Ethylene Oxide) Complexes with Lithium Salts of Monobasic and Dibasic Acids and Blends of Poly(Ethylene Oxide) with Lithium Salts of Anionic Polymers. *Polymer (Guildf).* **1984**. https://doi.org/10.1016/0032-3861(84)90378-1.
(43) *Transformation of Organometallics into Common and Exotic Materials: Design and Activation*; 1988. https://doi.org/10.1007/978-94-009-1393-6.
(44) Laine, R. M.; Sellinger, A. Si-Containing Ceramic Precursors. In *The Chemistry of Organic Silicon Compounds*; 2003. https://doi.org/10.1002/0470857250.ch39.
(45) Okamura, K. Ceramic Fibres from Polymer Precursors. *Composites* **1987**. https://doi.org/10.1016/0010-4361(87)90489-7.
(46) Greil, P. Polymer Derived Engineering Ceramics. *Advanced Engineering Materials*. 2000. https://doi.org/10.1002/1527-2648(200006)2:6<339::AID-ADEM339>3.0.CO;2-K.
(47) Lee, S. J.; Bae, J. H.; Lee, H. W.; Baik, H. K.; Lee, S. M. Electrical Conductivity in Li-Si-P-O-N Oxynitride Thin-Films. *J. Power Sources* **2003**. https://doi.org/10.1016/S0378-7753(03)00457-9.
(48) Lee, S. J.; Baik, H. K.; Lee, S. M. An All-Solid-State Thin Film Battery Using LISIPON Electrolyte and Si-V Negative Electrode Films. *Electrochem. commun.* **2003**, *5*, 32–35. https://doi.org/10.1016/S1388-2481(02)00528-3.
(49) Su, Y.; Falgenhauer, J.; Leichtweiß, T.; Geiß, M.; Lupó, C.; Polity, A.; Zhou, S.; Obel, J.; Schlettwein, D.; Janek, J.; Meyer, B. K. Electrochemical Properties and Optical Transmission of High Li+ Conducting LiSiPON Electrolyte Films. *Phys. Status Solidi Basic Res.* **2017**, *254* (2), 1600088. https://doi.org/10.1002/pssb.201600088.

(50) Laine, R. M.; Kim, S. G.; Rush, J.; Tamaki, R.; Wong, E.; Mollan, M.; Sun, H. J.; Lodaya, M. Ring-Opening Polymerization of Epoxy End-Terminated Polyethylene Oxide (PEO) as a Route to Cross-Linked Materials with Exceptional Swelling Behavior. *Macromolecules* **2004**. https://doi.org/10.1021/ma030295b.
(51) Kim, Y. G.; Wadley, H. N. G. Lithium Phosphorous Oxynitride Films Synthesized by a Plasma-Assisted Directed Vapor Deposition Approach. *J. Vac. Sci. Technol. A Vacuum, Surfaces, Film.* **2008**. https://doi.org/10.1116/1.2823491.
(52) Gurusiddappa, J.; Madhuri, W.; Padma Suvarna, R.; Priya Dasan, K. Studies on the Morphology and Conductivity of PEO/LiClO4. In *Materials Today: Proceedings*; 2016. https://doi.org/10.1016/j.matpr.2016.04.028.
(53) Geschke, D. Physical Properties of Polymers Handbook. *Zeitschrift für Phys. Chemie* **1997**. https://doi.org/10.1524/zpch.1997.199.part_1.128.
(54) Afifi-Effat, A. M.; Hay, J. N. Enthalpy and Entropy of Fusion and the Equilibrium Melting Point of Polyethylene Oxide. *J. Chem. Soc. Faraday Trans. 2 Mol. Chem. Phys.* **1972**. https://doi.org/10.1039/F29726800656.
(55) Roh, N. S.; Lee, S. D.; Kwon, H. S. Effects of Deposition Condition on the Ionic Conductivity and Structure of Amorphous Lithium Phosphorus Oxynitrate Thin Film. *Scr. Mater.* **1999**. https://doi.org/10.1016/S1359-6462(99)00307-3.
(56) Morita, M.; Fujisaki, T.; Yoshimoto, N.; Ishikawa, M. Ionic Conductance Behavior of Polymeric Composite Solid Electrolytes Containing Lithium Aluminate. *Electrochim. Acta* **2001**. https://doi.org/10.1016/S0013-4686(00)00754-4.
(57) Hu, Z.; Li, D.; Xie, K. Influence of Radio Frequency Power on Structure and Ionic Conductivity of LiPON Thin Films. *Bull. Mater. Sci.* **2008**. https://doi.org/10.1007/s12034-008-0108-z.
(58) Meabe, L.; Huynh, T. V.; Lago, N.; Sardon, H.; Li, C.; O'Dell, L. A.; Armand, M.; Forsyth, M.; Mecerreyes, D. Poly(Ethylene Oxide Carbonates) Solid Polymer Electrolytes for Lithium Batteries. *Electrochim. Acta* **2018**. https://doi.org/10.1016/j.electacta.2018.01.101.
(59) Pichonat, T.; Lethien, C.; Tiercelin, N.; Godey, S.; Pichonat, E.; Roussel, P.; Colmont, M.; Rolland, P. A. Further Studies on the Lithium Phosphorus Oxynitride Solid Electrolyte. *Mater. Chem. Phys.* **2010**. https://doi.org/10.1016/j.matchemphys.2010.04.001.
(60) Long, L.; Wang, S.; Xiao, M.; Meng, Y. Polymer Electrolytes for Lithium Polymer Batteries. *Journal of Materials Chemistry A*. 2016. https://doi.org/10.1039/c6ta02621d.
(61) Doyle, R. P.; Chen, X.; Macrae, M.; Srungavarapu, A.; Smith, L. J.; Gopinadhan, M.; Osuji, C. O.; Granados-Focil, S. Poly(Ethylenimine)-Based Polymer Blends as Single-Ion Lithium Conductors. *Macromolecules* **2014**. https://doi.org/10.1021/ma402325a.
(62) Feng, S.; Shi, D.; Liu, F.; Zheng, L.; Nie, J.; Feng, W.; Huang, X.; Armand, M.; Zhou, Z. Single Lithium-Ion Conducting Polymer Electrolytes Based on Poly[(4-Styrenesulfonyl)(Trifluoromethanesulfonyl)Imide] Anions. *Electrochim. Acta* **2013**. https://doi.org/10.1016/j.electacta.2013.01.119.
(63) Pehlivan, I. B.; Marsal, R.; Georén, P.; Granqvist, C. G.; Niklasson, G. A. Ionic Relaxation in Polyethyleneimine-Lithium Bis(Trifluoromethylsulfonyl) Imide Polymer Electrolytes. *J. Appl. Phys.* **2010**. https://doi.org/10.1063/1.3490133.
(64) Appetecchi, G. B.; Passerini, S. PEO-Carbon Composite Lithium Polymer Electrolyte. *Electrochim. Acta* **2000**. https://doi.org/10.1016/S0013-4686(99)00437-5.
(65) Bouchet, R.; Lascaud, S.; Rosso, M. An EIS Study of the Anode Li/PEO-LiTFSI of a Li Polymer Battery. *J. Electrochem. Soc.* **2003**. https://doi.org/10.1149/1.1609997.
(66) Han, X.; Gong, Y.; Fu, K.; He, X.; Hitz, G. T.; Dai, J.; Pearse, A.; Liu, B.; Wang, H.; Rubloff, G.; Mo, Y.; Thangadurai, V.; Wachsman, E. D.; Hu, L. Negating Interfacial Impedance in Garnet-Based Solid-State Li Metal Batteries. *Nat. Mater.* **2017**. https://doi.org/10.1038/nmat4821.

(67) Mikhaylik, Y. V.; Akridge, J. R. Polysulfide Shuttle Study in the Li/S Battery System. *J. Electrochem. Soc.* **2004**. https://doi.org/10.1149/1.1806394.
(68) Cuisinier, M.; Hart, C.; Balasubramanian, M.; Garsuch, A.; Nazar, L. F. Radical or Not Radical: Revisiting Lithium-Sulfur Electrochemistry in Nonaqueous Electrolytes. *Adv. Energy Mater*. **2015**. https://doi.org/10.1002/aenm.201401801.
(69) Wei, S.; Ma, L.; Hendrickson, K. E.; Tu, Z.; Archer, L. A. Metal-Sulfur Battery Cathodes Based on PAN-Sulfur Composites. *J. Am. Chem. Soc.* **2015**. https://doi.org/10.1021/jacs.5b08113.
(70) Frey, M.; Zenn, R. K.; Warneke, S.; Müller, K.; Hintennach, A.; Dinnebier, R. E.; Buchmeiser, M. R. Easily Accessible, Textile Fiber-Based Sulfurized Poly(Acrylonitrile) as Li/S Cathode Material: Correlating Electrochemical Performance with Morphology and Structure. *ACS Energy Lett.* **2017**. https://doi.org/10.1021/acsenergylett.7b00009.

Chapter 5

Polymer Precursors as a Coating and Binder Materials

5.1 Introduction

A well-established problem with cycling lithium-ion batteries with any type of electrolyte is that during recharging, Li deposition can be non-uniform causing metal dendrites to grow more rapidly at the expense of uniform coverage such that they can penetrate the electrolyte layer bridging to the cathode.[1-3] Bridging causes a short circuit that can lead to catastrophic failure.[4,5] Consequently, tremendous efforts have been directed to solve this problem.

In part, these efforts led to the development of ceramic electrolytes originally thought to offer a mechanical solution by blocking dendrite growth, including for example LATP [$Li_{1.3}Al_{0.3}Ti_{1.7}(PO_4)_3$] and c-LLZO ($Li_7La_3Zr_2O_{12}$).[6-11] However, these materials were found to suffer from other problems that render them less than completely practical for battery applications. Thus, LATP undergoes irreversible reduction during cycling.[11] C-LLZO is susceptible to dendrite penetration along grain boundaries again leading to short-circuiting.[12]

Thus, other solutions were sought to resolve all of these problems. To this end, a set of materials has been identified that appears to be resistant to dendrite penetration, also wets with Li metal, and offers sufficient ionic conductivity ($>10^{-3}$ $mScm^{-1}$) to permit use as interfaces with LATP and LLZO. These materials include the family of LiPON glasses, Li_xAlO_y, and Li_xZnO_y among others.[1,13]

However, a key problem with these materials is that their Li^+ conductivities are much lower ($2\text{-}10\times10^{-3}$ mS cm^{-1}) than those of LATP (2-6 $mScm^{-1}$[1,7-9]) or c-LLZO (0.2-2 $mScm^{-1}$ Al vs Ga doping[10-14]) such that they must be introduced as interface materials at thicknesses of 50-200 nm to offer practical Li^+ cycling. This requirement, to-date, has mandated their application via gas phase deposition methods that include a variety of sputtering methods (e.g. magnetron), chemical vapor as well as atomic layer deposition (CVD/ALD).[1,15] Unfortunately, these methods all require specialized apparatus to control deposition atmospheres, rates, film properties and control of coating uniformity.

As such, they represent an expensive and not easily scaled step in the fabrication of all solid-state batteries (ASBs) for large scale commercial applications.

In contrast, polymeric ceramic precursor systems that melt or are soluble offer a facile, low cost alternative for the application of thin ceramic films. Polymer precursor methods of processing ceramics have been the subject of multiple reviews.[15,16] However, to our knowledge, no one has sought to apply this approach to the synthesis of thin LiPON coatings/interfaces for battery applications. This then represents the motivation for the work reported here; the use of polymer precursors that can be applied as overcoats to process thin film coatings of the respective interface systems.

Before presenting a detailed discussion of our efforts in this area, it is helpful to first provide a brief overview of recent efforts in LiPON processing. Table **5.1** summarizes the properties of several LiPON materials produced by vacuum deposition. The examples are not intended to summarize all known data especially that found in the patent literature. These examples are meant to be informative such that the results of precursor processing explored below can be compared to what is commonly known in the literature.

Table 5.1. Examples of LiPON thin film conductivities.

Composition	Thickness	Sintering method (°C/h)	Conductivity RT (S cm^{-1})	Ref.
$Li_{3.3}PO_{3.8}N_{0.24}$ - $Li_{3.6}PO_{3.3}N_{0.69}$	1 μm	N/A	2 (±1) × 10^{-6}	1
$Li_{3.3}PO_{2.1}N_{1.4}$	1 μm	N/A	1.8 × 10^{-6}	23
$Li_{1.35}PO_{2.73}N_{0.30}$	N/A	600-750/3	5.3 × 10^{-8}	24
LiPON	1.05 μm	N/A	1.3 × 10^{-6}	25
$Li_{2.9}PO_{4.5}N_{0.42}$ -$Li_{3.1}PO_{4.1}N_{0.42}$	N/A	550 to 575	2.9 × 10^{-7}	26
Ultra-thin LiPON	12-300 nm	N/A	1~2 × 10^{-7}	27

5.2 Experimental section

To test the utility of synthesized precursors, it is also important to have a set of substrates qualified to be used to test the efficacy of the coatings and processing conditions explored. Given that we want to optimize ion conductivity in the resulting ceramized precursors, we also need well-defined substrates that offer: (1) no lithium ion conductivity; (2) minimal lithium ion conductivity or (3) good lithium ion conductivity.

To this end, we chose a series of substrates produced in our laboratories, 10-50 μm thick and fully or partially dense that meet the above criteria (Figure **5.1**) Thus, we coated thin films of α-Al_2O_3,[17] $LiAlO_2$ and LATSP ($Li_{1.7}Al_{0.3}Ti_{1.7}Si_{0.4}P_{2.6}O_{12}$).[7] These substrates exhibit Li^+ conductivities per Table **5.2**.

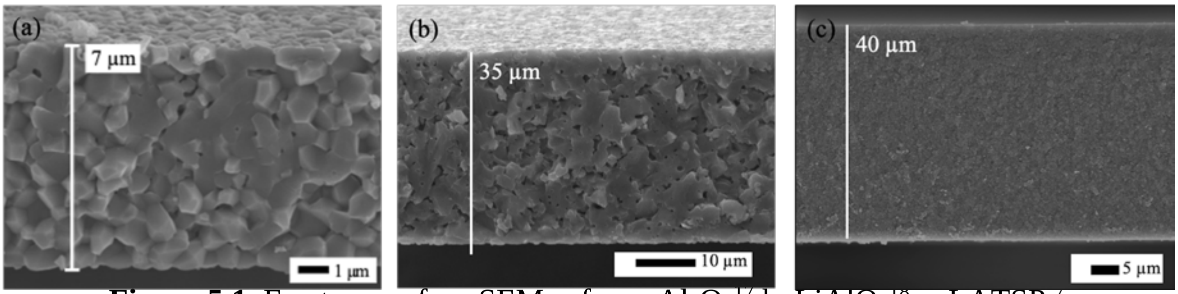

Figure 5.1. Fracture surface SEMs of a. α-Al_2O_3[17] b. $LiAlO_2$[18] c. LATSP.[7]

Table 5.2. Li^+ conductivities of substrates used in coating studies.

Substrate	Thickness	σ_t (S cm^{-1})
α-Al_2O_3[17]	≥25 μm	N/A
$LiAlO_2$[18]	20-60 μm	1.63×10^{-8}
LATSP[7]	20-60 μm	$4.3 \pm 1.4 \times 10^{-4}$

5.2.1 Coating studies

Sintered substrates were dip-coated 1x in the desired precursor (Li_3PON 0.05-0.1 g ml^{-1}, and Li_xSiPON ~0.2 g ml^{-1}) solutions using copper wire to suspend the sample. The coated substrates were left to dry for 12 h under vacuum at 100 °C. Dried samples were then heated to selected temperature and atmosphere.

In the following sections, we characterize the polymer coated substrate films on α-Al_2O_3, $LiAlO_2$, and LATSP by SEM and EIS. The basic objective here is to develop easy and scalable methods of coating thin ceramic electrolyte substrates with the polymer precursors.

5.3 Result and discussion

To establish the best coating interface, it is necessary to fully characterize the effects of coating temperatures and final microstructures when using different polymer precursors and processing conditions. Finally, efforts to optimize the ionic conductivity of coated thin films are assessed using electrochemical impedance measurements.

Figure **5.2** shows the Nyquist plot of $LiAlO_2$+300% (excess Li added to compensate for loss during sintering) films sintered to 1100 °C/2 h/air. The resulting single-phase lithium aluminate film shows a poor ionic conductivity of 1.6×10^{-8} S cm^{-1}. This value is similar to that reported for bulk and thin films of $LiAlO_2$, see for example Table **5.3**; which compares thickness, processing steps, and room temperature ionic conductivity of $LiAlO_2$ samples with values reported previously.

Note that some of the techniques used to generate ionic conducting thin films require very expensive, and energy intensive processes. Despite the simplicity of solid-state reaction methods, high sintering temperatures and longer dwell times are required to achieve dense, single phase $LiAlO_2$; motivating efforts to develop effective mass production methods with fast ion conductivity for ASSB applications.

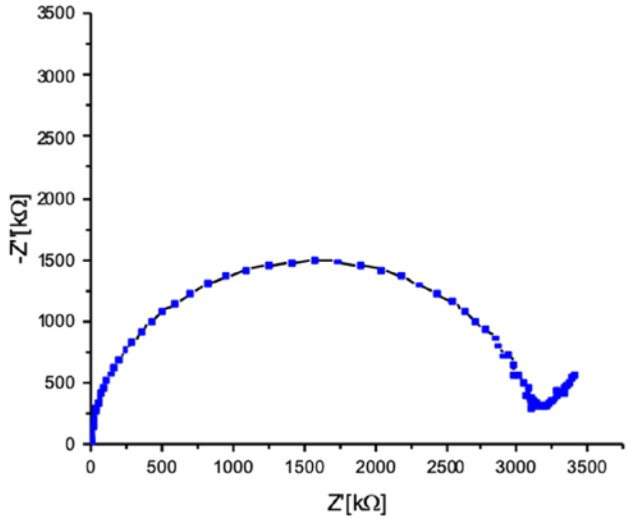

Figure 5.2. Nyquist plot of $LiAlO_2$ film + 300 % excess Li, sintered to 1100 °C/2 h/air.

Table 5.3. Reported room temperature conductivities for $LiAlO_2$.

Processing	Phase composition	Experimental conditions	σ_{RT} (S cm^{-1})	Thickness	Ref.
ALD	Amorphous Li:Al = 1:1.16	Impedance: in-plane	5.1×10^{-9}	90 nm	30
ALD	Amorphous $LiAlO_2$	Impedance: in-plane	5.6×10^{-8}	50 nm	31
CT	Single-crystalline γ-$LiAlO_2$	AC conductivity: 423-623 K	$\sim 1 \times 10^{-17}$	80 mm	32
SSR	Polycrystalline γ-$LiAlO_2$	AC conductivity: 450-1000 °C	2×10^{-14}	2.9 mm	33
TRQ	$0.7Li_2O$-$0.3Al_2O_3$	AC conductivity: 150-400 °C	5×10^{-8}	20 µm	34

TRQ = twin roller quenching, SSR = solid state reaction, TC = tape casting, CT = Czochralski technique, ALD = atomic layer deposition, LF-FSP= liquid flame spray pyrolysis

5.3.1 Characterization of polymer coated $LiAlO_2$ films

$LiAlO_2$+300 substrates were dip-coated for 1 min in Li_3PON (3 ml, 0.05-0.1 g ml^{-1}), Li_3SiPON, and, Li_6SiPON solutions (3 ml, ~0.2 g ml^{-1}). The coated films were left to dry for 12 h/vacuum/100 °C. Dried samples were then heated to 400°, 500°, or 600 °C/2 h/ N_2 at 1 °C min^{-1}. Figure **5.3** presents an SEM of the fracture surface microstructure of $LiAlO_2$ coated with Li_3SiPON and heated to 100 °C/12 h/ vacuum**.**

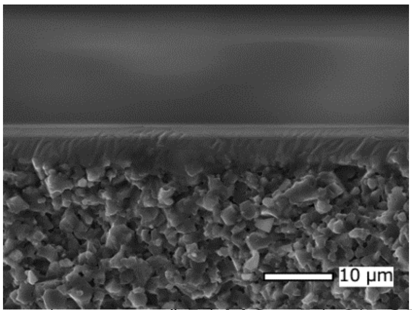

Figure 5.3. SEM facture surface images of $LiAlO_2$+Li_3SiPON films heated to 100 °C/12 h /vac.

Figure **5.4.** shows SEM microstructures of $LiAlO_2$+300% coated with Li_3PON, Li_3SiPON and Li_6SiPON films heated to 400°, 500°, and 600 °C/2 h/N_2. $LiAlO_2$+300%+Li_3PON films heated to 400 °C show a well-defined interface between the coating and the substrate. However, at 500 ° and 600 °C, the coating thickness seems to decrease, suggesting that the coating might be reacting with the substrate. This may also reflect melting but the coating by itself melts close to 600 °C rather than at 500 °C.

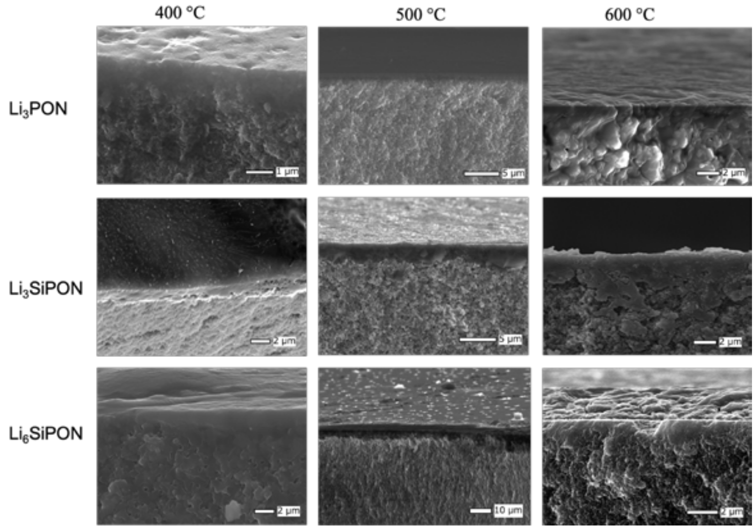

Figure 5.4. SEM fracture surface images of $LiAlO_2$ + Li_3PON, Li_3SiPON or Li_6SiPON films heated to 400 °, 500 °, and 600 °C/2 h/N_2.

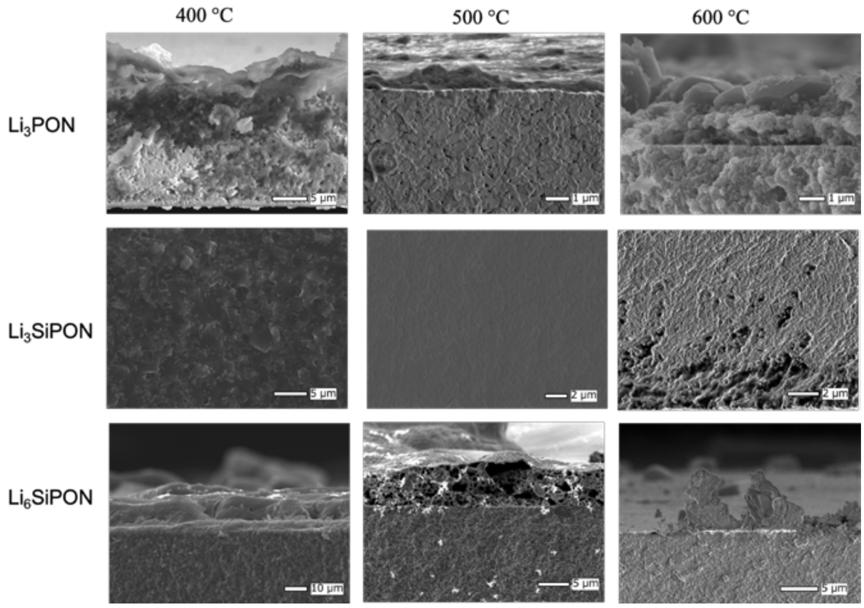

Figure 5.5. SEM facture surface images of Al_2O_3+Li_3PON, Li_3SiPON and Li_6SiPON films heated to 400 °, 500 °, and 600 °C/2 h/N_2.

$LiAlO_2$+300% substrates coated with Li_3SiPON show ideal behavior in that the coating is dense, uniform and stable after heating to 400-600 °C with an average thickness of ~4 µm. Li_6SiPON films heated to 400-600 °C also form uniform and dense coatings on $LiAlO_2$. The bottom part of the substrate did not coat well because of a physical interaction with the Teflon substrate used to hold the films after dip coating leading to a loss of the coating. Similar microstructures are observed for α-Al_2O_3 substrates as seen in Figure **5.5**.

Figure **5.6** shows Nyquist plots of $LiAlO_2$+300% substrates coated with Li_3PON, Li_3SiPON, and Li_6SiPON precursor solutions and heated to 400 °, 500 °, and 600 °C/2 h/N_2. The resulting impedance measurements are summarized in **Table 5**.

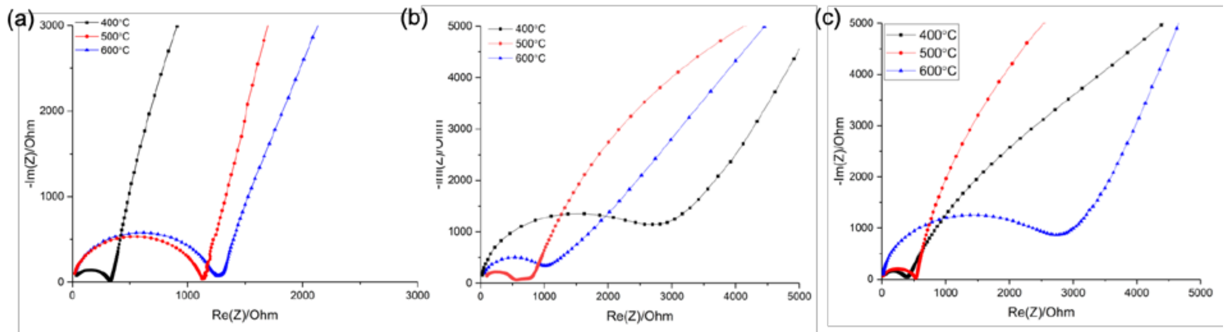

Figure 5.6. Nyquist plots (25 °C) of $LiAlO_2$ + a. Li_3PON, b. Li_3SiPON and c. Li_6SiPON films heated to 400 °, 500 °, and 600 °C/2 h/N_2.

For $LiAlO_2$ substrates coated with Li_3PON precursor, the room temperature impedance increased slightly when the coated substrates were heated from 400 ° to 600 °C suggesting some degradation as seen in the fracture surface SEMs, Figure **5.4**. However, the films show more or less consistent room temperature conductivity (10^{-5} S cm^{-1}) on heating from 400 ° to 600 °C. This may suggest that the coating reacts with the substrate and we are now measuring a composite value.

Table 5.4. Total conductivities (σ_{RT}) of $LiAlO_2$+300% films coated with polymers at selected temperatures.

Film substrate	Polymer coating	Temperature (°C/2 h/N_2)	σ_{RT} (Scm^{-1})
$LiAlO_2$+300%	Li_3PON	400	$6.6 \pm 0.1 \times 10^{-5}$
		500	$4.5 \pm 0.4 \times 10^{-5}$
		600	$3.8 \pm 1.6 \times 10^{-5}$
$LiAlO_2$+300%	Li_3SiPON	400	$1.4 \pm 0.2 \times 10^{-5}$
		500	$5.8 \pm 1.4 \times 10^{-5}$
		600	$4.1 \pm 0.3 \times 10^{-5}$
$LiAlO_2$+300%	Li_6SiPON	400	$1.4 \pm 2.5 \times 10^{-4}$
		500	$0.5 \pm 0.6 \times 10^{-4}$
		600	$1.5 \pm 0.3 \times 10^{-5}$

$LiAlO_2$ +Li_3SiPON films show the highest room temperature conductivity at 500 °C which likely arises from the dense and uniform coating that seems to penetrate into the substrate. The Li_6SiPON coating gives the highest conductivity of ~0.1 mS cm^{-1} for $LiAlO_2$+300% substrates. However, the conductivity drops an order of magnitude at 600 °C. The increase in conductivities of 2-3 orders of magnitude especially for $LiAlO_2$ is surprising and again is likely a result of penetration into the substrate enhancing the overall densification of the film.

In principle, the conductivities measured, except for LATSP, might arise from coatings that “encircle” the sample; via film edges. More likely correct is that the coatings penetrate pores introducing ion-conducting pathways not available before coating. Coatings heated >700 °C lose N_2 forming Li_xPO_y and offer conductivities expected of crystalline lithium phosphates.

Figure **5.7** shows typical Nyquist plots of Li_6SiPON coated $LiAlO_2$+300% films where electrochemical impedance was collected in a frequency range of 7 MHz to 1 Hz at -25 °C to 85 °C. Room temperature conductivities of 0.1 mS cm^{-1} and activation energies of 0.15 eV (15 kJ mol^{-1}) were obtained as shown in Figure **5.7**.

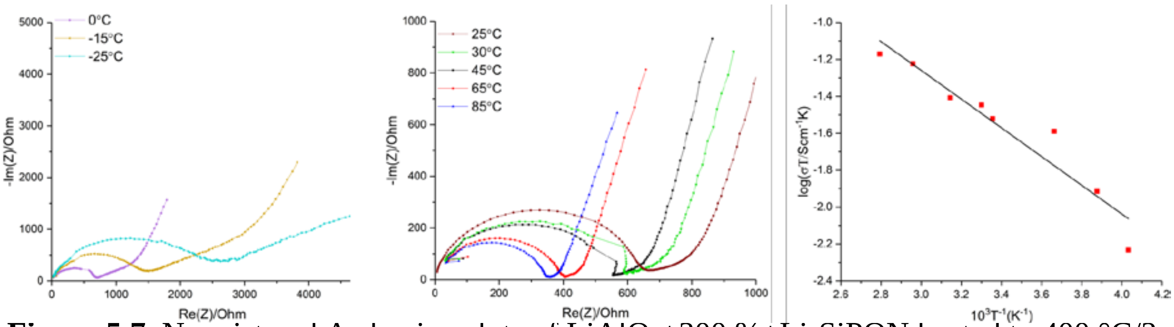

Figure 5.7. Nyquist and Arrhenius plots of $LiAlO_2$+300 %+Li_6SiPON heated to 400 °C/2 h/N_2.

Table **5.4** lists the total conductivity of $LiAlO_2$+Li_6SiPON coated substrates heated to 400 °C/2 h/N_2. Samples treated at higher temperatures show the highest conductivities as expected. The total conductivities are three to four orders of magnitude higher than $LiAlO_2$ substrates without the coating.

5.3.2 Characterization of polymer coated LATSP films

Coatings were made under N_2 using solutions of oligo-phosphoramide precursors with Li_3PON and Li_xSiPON compositions. In general, coatings wet surfaces well, remain adherent on heating to 400 °C and even penetrate the surface to some extent. The initially coated thin films are placed on a Teflon surface and first warmed to 100 °C.

Figure **5.8** shows the microstructures of LATSP substrate dip coated with Li_3SiPON and heated to 100 °C/12 h/vacuum. The fracture surface images of the sintered films look very dense. The substrate thickness is 25 ± 1.5 µm, and the coating average thickness is 3.1 ± 0.1 µm. There is a clear interfacial layer between the Li_3SiPON coating and both LATSP and $LiAlO_2$ substrates as seen in Figures **5.7** and **5.3** respectively. The mud cracking on top of the film corresponds to contact of the coating with the Teflon substrate.

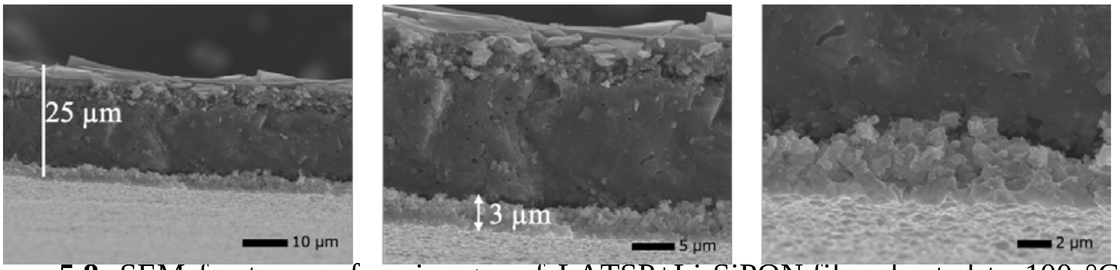

Figure 5.8. SEM fracture surface images of LATSP+Li_3SiPON films heated to 100 °C/12 h/vac.

Figure **5.9** shows SEM microstructures of LATSP+Li_3PON, Li_3SiPON, and Li_6SiPON films heated to 400 °, 500 °, and 600 °C/2 h/N_2. LATSP+Li_3PON films present well defined interfaces between the coating and the substrate for samples heated between 400-600 °C with an average coating thickness of 5 μm. Coating treatments with Li_3SiPON showed thin and dense coatings at 400° and 500 °C. The Li_3SiPON coating seems to percolate into the LATSP substrate at 600 °C, resulting in a denser structure. A similar microstructure is observed for LATSP coated with Li_6SiPON and heated to 400 °C. From the fracture surface image of LATSP+Li_6SiPON films heated to 400 °C, percolation is clearly visible as composite-like features are seen. The surfaced coating has an average thickness of 5 μm.

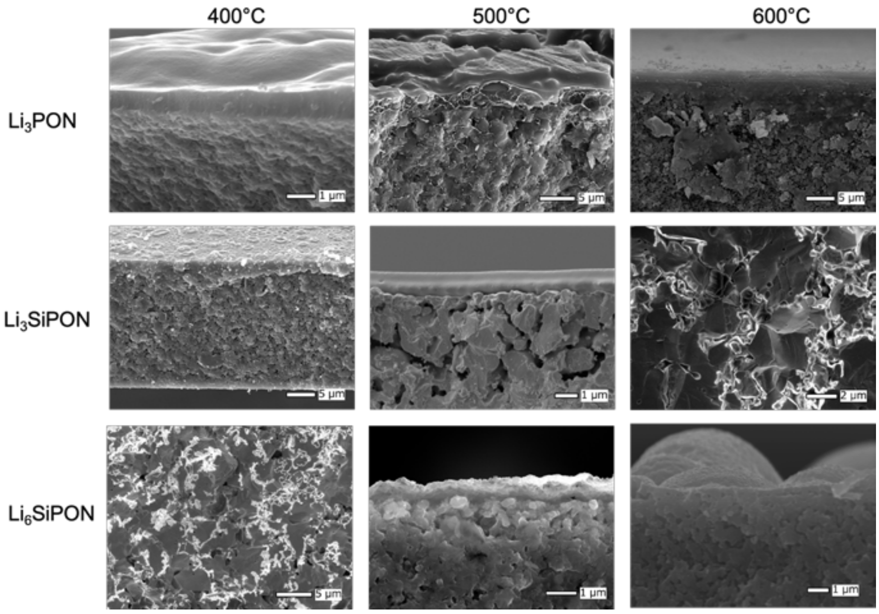

Figure 5.9. SEM fracture surface images of LATSP+Li_3PON, Li_3SiPON and Li_6SiPON films heated to 400 °, 500 °, and 600 °C/2 h/N_2.

Figure **5.10** shows Nyquist plots of LATSP substrates coated with Li_3PON, Li_3SiPON, and Li_6SiPON precursor solutions and heated to 400 °, 500 °, and 600 °C/2 h/N_2. The resulting impedance measurements are summarized in Table **5.5**.

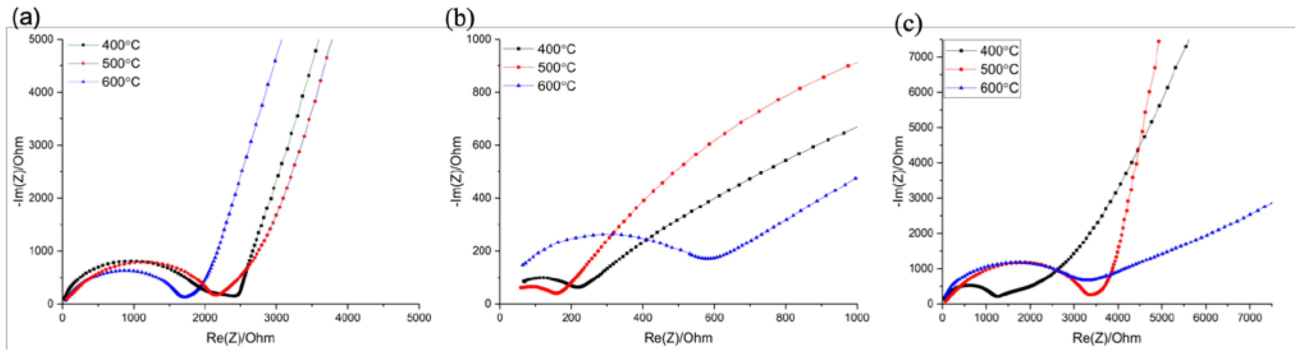

Figure 5.10. Room temperature Nyquist plots of LATSP + (a)Li_3PON, (b)Li_3SiPON and (c) Li_6SiPON films heated to 400 °, 500 °, and 600 °C/2 h/N_2.

Table **5.5** illustrates the total conductivity of LATSP substrates coated with different precursor solutions and heated to 400 °, 500 °, and 600 °C/2 h/N_2. The LATSP substrate coated with Li_3PON precursor exhibits consistent room temperature conductivities (0.03 mS cm^{-1}) at 400-600 °C. There is an order of magnitude decrease in conductivity when compared to pristine LATSP.

Table 5.5. Total conductivities (σ_t) of LATSP films coated with polymers at selected temperatures.

Film substrate	Polymer coating	Temp.(°C/2 h/N_2)	σ RT (S cm^{-1})
LATSP	Li_3PON	400	$2.6 \pm 0.8\times10^{-5}$
		500	$2.4 \pm 1.5\times10^{-5}$
		600	$3.3 \pm 1.6\times10^{-5}$
LATSP	Li_3SiPON	400	$1.8 \pm 0.8\times10^{-4}$
		500	$2.8 \pm 0.3\times10^{-4}$
		600	$8 \pm 0.8\times10^{-5}$
LATSP	Li_6SiPON	400	$3.7 \pm 0.5\times10^{-5}$
		500	$1.6 \pm 1.8\times10^{-5}$
		600	$1.7 \pm 1.4\times10^{-5}$

The Li_3SiPON solutions give the best conductivities when heated to 400 ° and 500 °C. The coating is not stable as an interface when heated to 600 °C as shown by the SEM images in Figure **5.9**. Hence, the conductivity drops by order of magnitude for LATSP substrates coated with Li_6SiPON. The Li_3SiPON coating showed the highest conductivity of all when heated to 500 °C 0.3 mS/cm. This can be attributed to formation of a uniform, thin, and dense coating.

5.3.3 Characterization of polymer precursor as adhesive and binder

The interfacial behavior directly dictates the lifespan, energy density, and safety of all solid-state batteries. We believe that these coatings might lower the interfacial resistance and stabilize the interfacial performance of all solid-state batteries. In the future, we plan to explore the use of $LiAlO_2$ substrates as less costly substitutes for LATP and LLZO and to assemble symmetrical and half-cells to test the performance of the polymer coated ceramic electrolytes. The next step in the use of these precursors will be to demonstrate bonding between single thin film ceramics as suggested in Figure **5.11**.

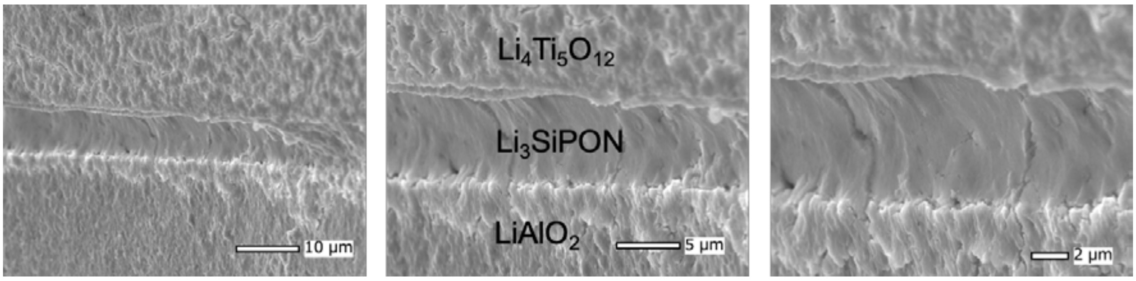

Figure 5.11. Example of Li_3SiPON precursor used to bond thin films of $Li_4Ti_5O_{12}$ and $LiAlO_2$.

Figure **5.11** shows SEM microstructures of $Li_4Ti_5O_{12}$/ Li_3SiPON /$LiAlO_2$ heated to 400 °C/2 h/ N_2. There is clear bonding between ceramic electrolyte $LiAlO_2$ substrates and the anode LTO through Li_3SiPON precursor coating. The resulting coating interface is dense, and uniform as can be seen from the SEM images. The Li_3SiPON coating seems to bind the anode and the ceramic electrolyte, this interposed buffer layer might reduce the cathode/SSE impedance in the space charge regions.

5.4 Conclusions

We describe here a low-temperature route to coatings originally intended to provide properties similar to gas phase deposited LiPON but using solution coating of ceramic precursors containing the same elements with similar thicknesses. The intent was to find a simple alternative to the equipment and energy intensive gas phase deposition methods. Our approach involves the synthesis of $O{=}P(NH_2)_3$ from $OPCl_3$ followed by lithiation with $LiNH_2$. As an alternate method, we also explored the reaction of $OPCl_3$ with $(Me_3Si)_2NH$ to generate Me_3SiCl and $O{=}P(NHSiMe_3)_3$ which can be lithiated again by $LiNH_2$.

To this end, we have made a number of systems that permit dip coating. On heating to various temperatures less than 700 °C, we are able to make Li_3PON, Li_3SiPON, and Li_6SiPON materials with various Li contents. We have characterized the intermediates during heating in air or nitrogen by FTIR, TGA, and XRD. Surprisingly, coatings made on a variety of substrates show Li^+ conductivities several orders of magnitude higher (10^{-1} vs 10^{-3} mS cm^{-1}) than those expected from gas phase deposited materials at coating thicknesses of 1-5 µm.

We were able to systematically characterize Li_3PON and Li_xSiPON materials with various compositions. Thereafter, efforts were made to introduce (<5 µm) thick solutions of the precursors by dip-coating substrates of α-Al_2O_3, $LiAlO_2$, and LATSP. These coatings were heated to temperatures equivalent to those used in the vapor deposition processes.

Surprisingly, $LiAlO_2$ coated with Li_6SiPON and heated to 400 °C resulted in a tremendous improvement in conductivity when compared to pristine $LiAlO_2$ films. Furthermore, these coatings are stable in air and serve as novel protective coatings for substrates such as $LiAlO_2$ and LATSP greatly limiting susceptibility to CO_2 and/or moisture pick up.

The interfacial behavior directly dictates the lifespan, energy density, and safety of ASBs. We believe that these coatings might lower the interfacial resistance and stabilize the interfacial performance of all solid-state batteries. In the future, we plan to explore the use of $LiAlO_2$ substrates as less costly substitutes for LATP and LLZO and to assemble symmetrical and half-cells to test the performance of the polymer coated ceramic electrolytes.

References

(1) Yu, X. A Stable Thin-Film Lithium Electrolyte: Lithium Phosphorus Oxynitride. *J. Electrochem. Soc.* **1997**. https://doi.org/10.1149/1.1837443.

(2) Liu, Y.; Zhou, G.; Liu, K.; Cui, Y. Design of Complex Nanomaterials for Energy Storage: Past Success and Future Opportunity. *Acc. Chem. Res.* **2017**. https://doi.org/10.1021/acs.accounts.7b00450.

(3) Lin, C. F.; Qi, Y.; Gregorczyk, K.; Lee, S. B.; Rubloff, G. W. Nanoscale Protection Layers to Mitigate Degradation in High-Energy Electrochemical Energy Storage Systems. *Acc. Chem. Res.* **2018**. https://doi.org/10.1021/acs.accounts.7b00524.

(4) Cheng, X. B.; Zhang, R.; Zhao, C. Z.; Zhang, Q. Toward Safe Lithium Metal Anode in Rechargeable Batteries: A Review. *Chemical Reviews*. 2017. https://doi.org/10.1021/acs.chemrev.7b00115.

(5) Wen, J.; Yu, Y.; Chen, C. A Review on Lithium-Ion Batteries Safety Issues: Existing Problems and Possible Solutions. *Materials Express*. 2012. https://doi.org/10.1166/mex.2012.1075.

(6) Choi, N. S.; Han, J. G.; Ha, S. Y.; Park, I.; Back, C. K. Recent Advances in the Electrolytes for Interfacial Stability of High-Voltage Cathodes in Lithium-Ion Batteries. *RSC Advances*. 2015. https://doi.org/10.1039/c4ra11575a.

(7) Yi, E.; Wang, W.; Mohanty, S.; Kieffer, J.; Tamaki, R.; Laine, R. M. Materials That Can Replace Liquid Electrolytes in Li Batteries: Superionic Conductivities in Li1.7Al0.3Ti1.7Si 0.4P2.6O12. Processing Combustion Synthesized Nanopowders to Free Standing Thin Films. *J. Power Sources* **2014**, *269*, 577–588. https://doi.org/10.1016/j.jpowsour.2014.07.029.

(8) Zhao, E.; Ma, F.; Guo, Y.; Jin, Y. Stable LATP/LAGP Double-Layer Solid Electrolyte Prepared: Via a Simple Dry-Pressing Method for Solid State Lithium Ion Batteries. *RSC Adv.* **2016**. https://doi.org/10.1039/c6ra19415j.

(9) Wang, S.; Ding, Y.; Zhou, G.; Yu, G.; Manthiram, A. Durability of the Li1+xTi2-XAlx(PO4)3 Solid Electrolyte in Lithium-Sulfur Batteries. *ACS Energy Lett.* **2016**, *1* (6), 1080–1085. https://doi.org/10.1021/acsenergylett.6b00481.

(10) Murugan, R.; Thangadurai, V.; Weppner, W. Fast Lithium Ion Conduction in Garnet-Type Li7La 3Zr2O12. *Angew. Chemie - Int. Ed.* **2007**. https://doi.org/10.1002/anie.200701144.

(11) Ohta, S.; Kobayashi, T.; Asaoka, T. High Lithium Ionic Conductivity in the Garnet-Type Oxide Li7-X La3(Zr2-X, NbX)O12 (X = 0-2). *J. Power Sources* **2011**. https://doi.org/10.1016/j.jpowsour.2010.11.089.

(12) Bucci, G.; Swamy, T.; Chiang, Y. M.; Carter, W. C. Modeling of Internal Mechanical Failure of All-Solid-State Batteries during Electrochemical Cycling, and Implications for Battery Design. *J. Mater. Chem. A* **2017**. https://doi.org/10.1039/c7ta03199h.

(13) Yi, E.; Wang, W.; Kieffer, J.; Laine, R. M. Flame Made Nanoparticles Permit Processing of Dense, Flexible, Li^+ Conducting Ceramic Electrolyte Thin Films of Cubic-$Li_7La_3Zr_2O_{12}$ (c-LLZO). *J. Mater. Chem. A* **2016**, *4* (33), 12947–12954. https://doi.org/10.1039/C6TA04492A.

(14) Yi, E.; Wang, W.; Kieffer, J.; Laine, R. M. Key Parameters Governing the Densification of Cubic-Li7La3Zr2O12 Li+ Conductors. *J. Power Sources* **2017**. https://doi.org/10.1016/j.jpowsour.2017.03.126.

(15) Jung, Y. S.; Cavanagh, A. S.; Riley, L. A.; Kang, S. H.; Dillon, A. C.; Groner, M. D.; George, S. M.; Lee, S. H. Ultrathin Direct Atomic Layer Deposition on Composite Electrodes for Highly Durable and Safe Li-Ion Batteries. *Adv. Mater.* **2010**. https://doi.org/10.1002/adma.200903951.
(16) Laine, R. M.; Babonneau, F. Preceramic Polymer Routes to Silicon Carbide. *Chem. Mater.* **1993**, *5* (3), 260–279. https://doi.org/10.1021/cm00027a007.
(17) Takeuchi, M.; Niedermaier, M.; Jansohn, M.; Umehara, N.; Laine, R. M. Processing Thin (<10¯m), Dense, Flexible ¡-Al 2 O 3 Films from Nanopowders. *J. Ceram. Soc. Japan* **2019**, *127* (2), 81–89. https://doi.org/10.2109/jcersj2.18099.
(18) Temeche, E.; Indris, S.; Laine, R. M. LiAlO 2 /LiAl 5 O 8 Membranes Derived from Flame-Synthesized Nanopowders as a Potential Electrolyte and Coating Material for All-Solid-State Batteries . *ACS Appl. Mater. Interfaces* **2020**. https://doi.org/10.1021/acsami.0c13021.
(19) Laine, R. M.; Sellinger, A. Si-Containing Ceramic Precursors. In *The Chemistry of Organic Silicon Compounds*; 2003. https://doi.org/10.1002/0470857250.ch39.
(20) Chen, H.; Tao, H.; Zhao, X.; Wu, Q. Fabrication and Ionic Conductivity of Amorphous Li-Al-Ti-P-O Thin Film. *J. Non. Cryst. Solids* **2011**. https://doi.org/10.1016/j.jnoncrysol.2011.05.023.
(21) Lee, S. J.; Baik, H. K.; Lee, S. M. An All-Solid-State Thin Film Battery Using LISIPON Electrolyte and Si-V Negative Electrode Films. *Electrochem. commun.* **2003**, *5*, 32–35. https://doi.org/10.1016/S1388-2481(02)00528-3.
(22) Su, Y.; Falgenhauer, J.; Leichtweiß, T.; Geiß, M.; Lupó, C.; Polity, A.; Zhou, S.; Obel, J.; Schlettwein, D.; Janek, J.; Meyer, B. K. Electrochemical Properties and Optical Transmission of High Li+ Conducting LiSiPON Electrolyte Films. *Phys. Status Solidi Basic Res.* **2017**, *254* (2), 1600088. https://doi.org/10.1002/pssb.201600088.
(23) Hamon, Y.; Douard, A.; Sabary, F.; Marcel, C.; Vinatier, P.; Pecquenard, B.; Levasseur, A. Influence of Sputtering Conditions on Ionic Conductivity of LiPON Thin Films. *Solid State Ionics* **2006**, *177*, 257–261. https://doi.org/10.1016/j.ssi.2005.10.021.
(24) Mascaraque, N.; Tricot, G.; Revel, B.; Durán, A.; Muñoz, F. Nitrogen and Fluorine Anionic Substitution in Lithium Phosphate Glasses. *Solid State Ionics* **2014**. https://doi.org/10.1016/j.ssi.2013.10.061.
(25) Vereda, F.; Goldner, R. B.; Haas, T. E.; Zerigian, P. Rapidly Grown IBAD LiPON Films with High Li-Ion Conductivity and Electrochemical Stability. *Electrochem. Solid-State Lett.* **2002**. https://doi.org/10.1149/1.1508550.
(26) Kim, H. T.; Mun, T.; Park, C.; Jin, S. W.; Park, H. Y. Characteristics of Lithium Phosphorous Oxynitride Thin Films Deposited by Metal-Organic Chemical Vapor Deposition Technique. *J. Power Sources* **2013**, *244*, 641–645. https://doi.org/10.1016/j.jpowsour.2012.12.109.
(27) Nowak, S.; Berkemeier, F.; Schmitz, G. Ultra-Thin LiPON Films - Fundamental Properties and Application in Solid State Thin Film Model Batteries. *J. Power Sources* **2015**, *275*, 144–150. https://doi.org/10.1016/j.jpowsour.2014.10.202.
(28) Levchik, S. V.; Levchik, G. F.; Balabanovich, A. I.; Weil, E. D.; Klatt, M. Phosphorus Oxynitride: A Thermally Stable Fire Retardant Additive for Polyamide 6 and Poly(Butylene Terephthalate). *Angew. Makromol. Chemie* **1999**, *264* (1), 48–55.
(29) Larson, R. W.; Day, D. E. Preparation and Characterization of Lithium Phosphorus Oxynitride Glass. *J. Non. Cryst. Solids* **1986**. https://doi.org/10.1016/S0022-3093(86)80091-6.
(30) Hu, Y.; Ruud, A.; Miikkulainen, V.; Norby, T.; Nilsen, O.; Fjellvåg, H. Electrical Characterization of Amorphous $LiAlO_2$ Thin Films Deposited by Atomic Layer

Deposition. *RSC Adv.* **2016**, *6* (65), 60479–60486. https://doi.org/10.1039/C6RA03137D.
(31) Park, J. S.; Meng, X.; Elam, J. W.; Hao, S.; Wolverton, C.; Kim, C.; Cabana, J. Ultrathin Lithium-Ion Conducting Coatings for Increased Interfacial Stability in High Voltage Lithium-Ion Batteries. *Chem. Mater.* **2014**, *26* (10), 3128–3134. https://doi.org/10.1021/cm500512n.
(32) Indris, S.; Heitjans, P.; Uecker, R.; Roling, B. Li Ion Dynamics in a LiAlO 2 Single Crystal Studied by 7Li NMR Spectroscopy and Conductivity Measurements. *J. Phys. Chem. C* **2012**, *116* (27), 14243–14247. https://doi.org/10.1021/jp3042928.
(33) KONISHI, S.; OHNO, H. Electrical Conductivity of Polycrystalline Li2SiO3 and Γ-LiAlO2. *J. Am. Ceram. Soc.* **1984**, *67* (6), 418–419. https://doi.org/10.1111/j.1151-2916.1984.tb19727.x.
(34) Glass, A. M.; Nassau, K. Lithium Ion Conduction in Rapidly Quenched Li2O-Al 2O3, Li2O-Ga2O3, and Li2O-Bi2O3 Glasses. *J. Appl. Phys.* **1980**. https://doi.org/10.1063/1.328164.

Chapter 6

$LiAlO_2/LiAl_5O_8$ Thin Film Electrolytes Derived From Flame Synthesized Nanopowders (NPs)

6.1 Introduction

Lithium-ion batteries (LIBs) used for portable devices are now being commercialized at large scales (e.g. electric and hybrid electrical vehicles) due to their high energy and power densities, cyclability, and high operating voltages.[1] Unfortunately, current LIBs using liquid electrolytes suffer from still limited electrochemical performance, poor thermal stabilities, and flammability.[2] The replacement of liquid electrolytes with solid electrolytes will resolve the fundamental safety issues due to their non-flammability and high thermal stability, thereby offering access to new battery chemistries and designs.[3]

Ceramic Li^+ superionic conductors (0.1 – 1 mS cm^{-1})[4] with rigid skeletal structures, low activation energies (< 0.4 eV),[5] low electronic conductivities (< 1×10^{-8} S cm^{-1}),[6] and thermal stability are proposed to improve battery chemistries, increase energy densities by eliminating peripheral mass and reducing battery pack size.[7] Solid electrolytes with garnet type c-LLZO ($Li_7La_3Zr_2O_{12}$),[8] NASICON [$Li_{1+x}Al_xTi_{2-x}(PO_4)_3$,],[9] and perovskite ($La_{3x}La_{2/3-x}TiO_3$)[10] crystal structures have been engineered to increase Li^+ conductivity by modifying conduction pathways through aliovalent substitution, optimizing Li^+ vacancy sites and concentrations of mobile species.[11–14] However, little attention has been given to lithium aluminate polymorphs as ceramic Li^+ conductors due to their poor ambient ionic conductivities (<10^{-10} S cm^{-1}), which can be compensated for, as with LiPON ($Li_xPO_yN_z$),[15] through the use of thin, defect-free, and dense films.[16,17]

$LiAlO_2$ has been reported to be a good candidate for carbonate fuel cells as an electrolyte matrix,[18] as a substrate for growing GaN epitaxial film,[19] and as a catalyst for biodiesel production.[20] $LiAlO_2$ has also been used as a ceramic filler for polymer electrolytes.[21] Recently, $LiAlO_2$ has been explored as a potential ceramic electrolyte for assembling solid-state microbatteries because of its chemical and thermal stability.[6] In addition to its potential use as a solid-state electrolyte, polymorphs of lithium aluminates have been studied as coatings for LIB electrodes.[17]

The reactivity of LIB electrodes with $LiPF_6$ based electrolytes results in corrosive dissolution of redox-active species from the active materials, which can be suppressed by introducing a coating as a physical protective barrier.[17] The most promising coating materials (Al_2O_3,[12] ZnO,[22] $LiAlO_2$,[17] and Li_2ZrO_3[23]) are expected to offer new opportunities for next-generation ASSBs as intermediate buffers and wetting agents. Recently, $LiAl_5O_8$ was found to form in an alumina coated garnet-LLCZN ($Li_7La_{2.75}Ca_{0.25}Zr_{1.75}Nb_{0.25}O_{12}$) interface with a Li metal anode. The effect was to reduce interfacial impedance.[12] This implies formation of lithiated alumina ($LiAl_5O_8$) improves Li^+ migration through the ceramic electrolyte/Li interface.[12]

Different synthesis approaches have targeted processing single-phase $LiAlO_2$ membranes with desirable morphological, and conductive features.[24] Some of the pathways assessed include solid-state,[20] hydrothermal,[25] sol-gel,[26] combustion,[27] and atomic layer deposition (ALD) synthesis methods.[28] Recently, *Hu et al*. described ALD processing $LiAlO_2$ films 90, 160, and 235 nm thick on different substrates with ambient conductivities of 10^{-10} S cm^{-1} and average activation energies of 0.8 eV.[16]

The fabrication of these extremely thin films requires gas-phase deposition techniques. However, the exploration of Li^+ conductive thin film electrolytes by gas-phase deposition techniques such as ALD,[6] ion beam assisted deposition,[29] and pulse laser deposition,[30] is still at an early stage as such methods are energy and equipment intensive, require high-cost process steps, and offer low deposition rates.[31] Thus, there remains a considerable need to develop alternate methods of processing membranes with optimal conductivity as potential candidates for next-generation all-solid-state-batteries (ASSBs).

Recent developments in microelectronic industries have reduced the energy and power density requirements of electronic devices.[32] Hence, thin-film-microbatteries delivering capacities in the range of 0.1- 5 mAh can be used as power sources for these devices.[33] These microbatteries provide various advantages such as low internal resistance, excellent rechargeability, and enable simple designs in ultra-thin watches, computer memory chips, and micro sensors.[32,34] Typically, microbatteries are assembled using thin solid electrolytes (~1 µm) with the full stack in the range of 10-15 µm thick.[33] However, the presence of a substrate is reported to at least double the overall battery thickness.[33]

The main challenges for thin film batteries are finding thin lightweight substrates to support the battery and protecting the lithium metal and lithium-containing electrodes from air exposure.[33,35] The development of a thin film battery on flexible substrates has been suggested to improve the energy storage capacity per unit weight and allow the use of special designs.[35]

In our previous work, we demonstrated that LF-FSP NPs enable the formation of flexible and dense Al_2O_3 membranes with an average thickness of < 10 µm.[7,36] For conventional microbatteries, thin film electrolytes with room temperature conductivities > 10^{-6} S cm^{-1} are highly desirable.[37] Thus, this provides the motivation to develop Li^+ conducting membranes that can potentially serve as both electrolyte and substrate for such batteries.

The present study aims to demonstrate an effective alternate method of processing $LiAlO_2$ membranes (< 50 µm) using high surface area, flame made NPs produced via LF-FSP, which eliminates traditional solid-state reaction steps (i.e. ball-milling and crushing).[38] $LiAlO_2$ membranes are produced by tape casting the NP/polymer binder slurries followed by thermo-compression of green-films (100 °C/10 kpsi/10 min) and sintering at the desired temperature to obtain fully dense (> 95%) films.

Here we also demonstrate optimization of Li^+ conductivity in $LiAlO_2$ membranes through careful engineering of grain boundary properties by introducing a second phase ($LiAl_5O_8$) and modifying sintering conditions to minimize grain boundary resistance. Mixed phases of $LiAlO_2$ and $LiAl_5O_8$ offer superior ionic conductivities (~ 10^{-6} S cm^{-1}) at ambient greatly increasing their potential utility as ceramic electrolytes that may greatly simplify ASSB designs and significantly reduce costs. These $LiAlO_2$/$LiAl_5O_8$ membranes offer potential utility as ceramic electrolytes in thin-film-microbatteries and coating materials for LIB electrodes. Sintered $LiAlO_2$/$LiAl_5O_8$ and $LiAlO_2$ membranes were characterized by XRD, SEM, ^7Li/^{27}Al NMR, and EIS. Coincidently, we explored the stability of the $LiAlO_2$/$LiAl_5O_8$ membrane when assembled in a symmetric cell with metallic Li.

6.2 Experimental section

6.2.1 $LiAlO_2$ powder synthesis

Lithium propionate [$LiO_2CCH_2CH_3$] and alumatrane [$Al(OCH_2CH_2)_3N$] were synthesized as described previously.[9] $LiAlO_2$ NPs were produced using the LF-FSP apparatus shown in Figure **6.1**. Lithium propionate and alumatrane were quantitatively mixed at selected molar ratios to result in $LiAlO_2$ composition with 60, 80, 150, and 300 wt. % excess lithium, hereafter referred to as $Li_{1.72}AlO_2$, $Li_{1.99}AlO_2$, $Li_{3.1}AlO_2$, and $Li_{6.2}AlO_2$, respectively. Previous studies show that resulting NPs are Li deficient arising from Li_2O volatility as flame temperatures >1000 °C.[7,9]

Hence, excess lithium propionate was introduced to promote formation of phase pure material. The resulting precursor mixture was dissolved in ethanol to give a 3 wt. % ceramic yield solution. The LF-FSP was ignited using CH_4/O_2 pilot torches.

The flame spray pyrolysis was then initiated by injecting the precursor solution aerosol into the combustion chamber (1.5 m long). After combustion and rapid quenching, as-produced NPs were collected downstream in parallel set of electrostatic precipitators (ESP) operated between 5 and 10 kV. Table **6.1**lists the amount of lithium and aluminum precursors used to produce the NPs with varying compositions.

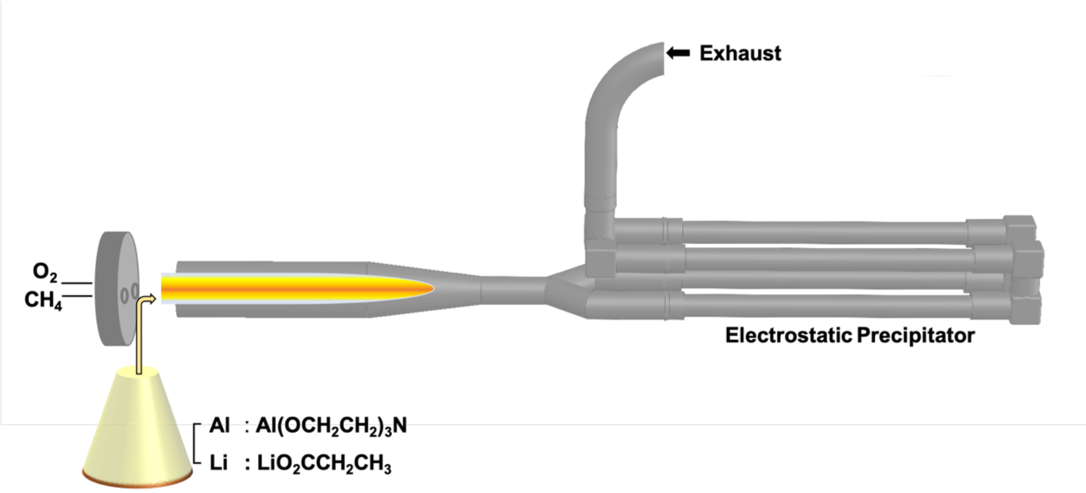

Figure 6.1. Schematic of LF-FSP apparatus.

Table 6.1. Amounts of lithium and alumina precursors dissolved in ethanol (2100 ml).

	$LiO_2CCH_2CH_3$ (g)	$Al[OCH(CH_3)CH_2CH_3]_3$ (g)
$Li_{1.75}AlO_2$	46.5	455.35
$Li_{1.99}AlO_2$	52.3	455.35
$Li_{3.1}AlO_2$	72.7	455.35
$Li_{6.2}AlO_2$	116.3	455.35

Ultrasonic horn ((Vibra-cell VC 505 Sonics & Mater. Inc.) operating at 100 W for 10 -15 min was used to disperse the as-produced $LiAlO_2$ NPs (10 g, 0.15 mol) dissolved in anhydrous ethanol (350 ml). Polyacrylic acid (200 mg, 1.2 mmol) was used as a dispersant. Thereafter, the dispersed solution was left to settle for 4 h. The supernatant was decanted, and the recovered NPs were dried at 60 °C/ 12 h.

6.2.2 $LiAlO_2$ thin film synthesis

Table 6.2. List of components used for formulating $LiAlO_2$ films.

Components	Mass(g)	Role
$LiAlO_2$	0.7	Electrolyte
Benzyl butyl phthalate	0.13	Plasticizer
Polyacrylic acid	0.01	Dispersant
Polyvinyl butryal	0.13	Binder
Ethanol/Acetone	1/1	Solvent

Table **6.2** lists the components used for formulating $LiAlO_2$ films. Briefly, the $LiAlO_2$ NPs were mixed with binder, plasticizer, and dispersant dissolved in ethanol and acetone. Thereafter, the mixtures were ball-milled to homogenize the suspensions.

The wire-wound rod coater (Automatic Film Applicator 1137, Sheen Instrument, Ltd) was used to cast the $LiAlO_2$ green films. Detail procedures to synthesize green films using LF-FSP derived NPs can be found elsewhere.[39,40] To improve packing density, the $LiAlO_2$ films were uniaxially pressed using a heated bench top press (Carve, Inc) at 100 °C/ 10 kpsi/5-10 min.

Sintering studies were conducted by using High-Temperature Vacuum/Gas tube furnace (Richmond, CA). The $Li_{1.72}AlO_2$, $Li_{1.99}AlO_2$, $Li_{3.1}AlO_2$, and $Li_{6.2}AlO_2$ green films were placed between Al_2O_3 disks and sintered to 1100 °C/2 h/air (100 mL min^{-1}).

6.2.3 Symmetric cell assembly

The Li/$Li_{3.1}AlO_2$/Li symmetric coin cell was assembled in an Ar-filled glove box. Prior to symmetric cell assembly, the lithium metal foil (99.9 %, Sigma-Aldrich) was scraped to expose a clean surface. Solid-state symmetric cells were assembled by placing the $Li_{3.1}AlO_2$ (25 µm thick and 18 mm diameter) between the two Li foil disks. The symmetric cell was heated to 200 °C to reduce interfacial impedance. The Li/$Li_{3.1}AlO_2$/Li cell was then transferred to coin 2032 cell and uniaxially pressed at 0.1 kPa. The cell was cycled at ambient using a potentiostat/galvanostat (Bio-logic SP300).

6.3 Results and discussion

In the present work, we first discuss the characterization of LF-FSP produced $LiAlO_2$ NPs with various Li contents by SEM, TGA, FTIR, and XRD. In the second part, we assess the overall conductivity, phase purity, and microstructure of $Li_{1.72}AlO_2$, $Li_{1.99}AlO_2$, $Li_{3.1}AlO_2$, and $Li_{6.2}AlO_2$ membranes. In addition, the electrochemical performance of the $LiAlO_2$ membrane in a symmetric cell-configuration is also presented.

6.3.1 Characterization of as-produced NPs

NPs of $LiAlO_2$ with 60, 80, 150 and 300 wt.% excess lithium propionates were produced using LF-FSP as shown in Figure **6.1**. Excess Li is used to compensate for loss during combustion and sintering. Most studies indicate that excess Li (10-15 wt.%) is required to sinter 1-2 mm thick pellets of Li based ceramics.[7,41]

Figure **6.2a** shows FTIRs of $LiAlO_2$ as produced NPs. The spectra show sharp peaks at 595 and 656 cm^{-1} assigned to υAl–O for octahedral Al. Bands centered near 715 cm^{-1} and 972 cm^{-1} are ascribed to υAl–O for tetrahedral Al and symmetric bending of Al–O–H, respectively.[24,42,43] A broad peak at ~1500 cm^{-1} corresponds to carbonate υC=O.[7] The υC=O intensity increases with lithium content corresponding to increases in Li_2CO_3. The presence of Li_2CO_3 is in good agreement with TGA mass losses (~ 700 °C) and XRD plots, see Figures **6.4d** and **6.5** respectively.

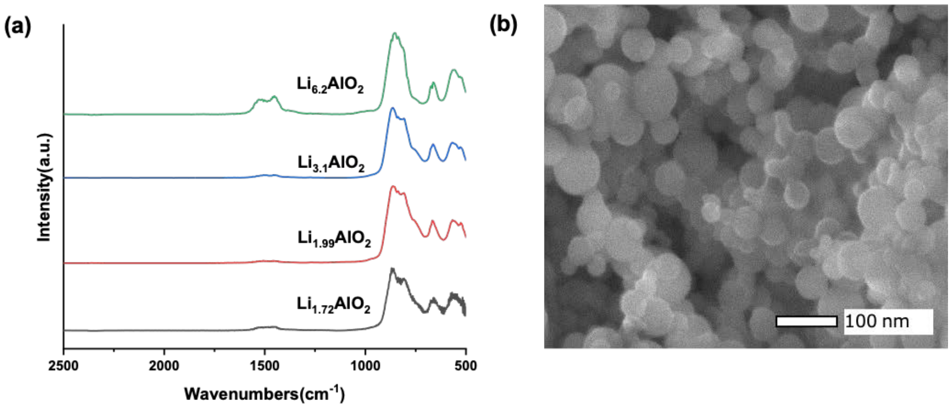

Figure 6.2. a. FTIRs and b. SEM of a typical $LiAlO_2$ as-produced NP.

Figure **6.2b** shows SEMs of as-produced $Li_{6.2}AlO_2$ NPs showing spherical morphologies typical of flame made NPs with average particle sizes (APSs) < 100 nm.[39,40] No noticeable differences in morphologies were observed for $LiAlO_2$ NPs with varying Li contents as shown in Figure **6.3**. The particles are agglomerated (electrostatically bonded) but not aggregated (necked), which is highly desirable for facile dispersion, tape casting and sintering dense thin films with average grain sizes (AGSs) < 10 μm. The BET N_2 adsorption derived SSAs and APSs for the $LiAlO_2$ NPs are listed in Table **6.3**. The spherical NPs offer a narrow size distribution with APSs of ~33- 64 nm.

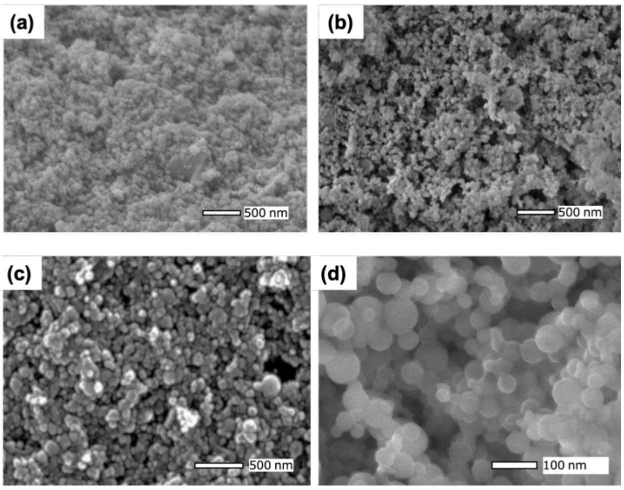

Figure 6.3. SEM images of as-produced NPs a. a. $Li_{1.72}AlO_2$, b. $Li_{1.99}AlO_2$ c. $Li_{3.1}AlO_2$, d. $Li_{6.2}AlO_2$

Table 6.3. SSAs and APSs of $LiAlO_2$ NPs.

	SSAs(m^2g^{-1})	APSs(nm)
$Li_{1.75}AlO_2$	53	33
$Li_{1.99}AlO_2$	46	40
$Li_{3.1}AlO_2$	43	47
$Li_{6.2}AlO_2$	38	64

The Figure **6.4** TGA-DTA curves for $LiAlO_2$ NPs, after heating to 1000 °C/10 °C min^{-1}/air, reveal mass losses below 250 °C, ascribed to physi/chemi-absorbed water on the as-produced NP surfaces. As the Li content increases to 300 wt.%, the TGA plot displays an endotherm associated with a mass loss starting at ~ 700 °C, as Li_2CO_3 melts/decomposes with loss of CO_2 ending at ~ 900 °C.[7] The slightly higher mass losses for $Li_{6.2}AlO_2$ suggest a hygroscopic nature coincident with a higher propensity to pick up CO_2 as might be expected with the higher Li content. This mass loss behavior is further confirmed by XRD data indicating the presence of Li_2CO_3 as seen in Figure **6.5**.

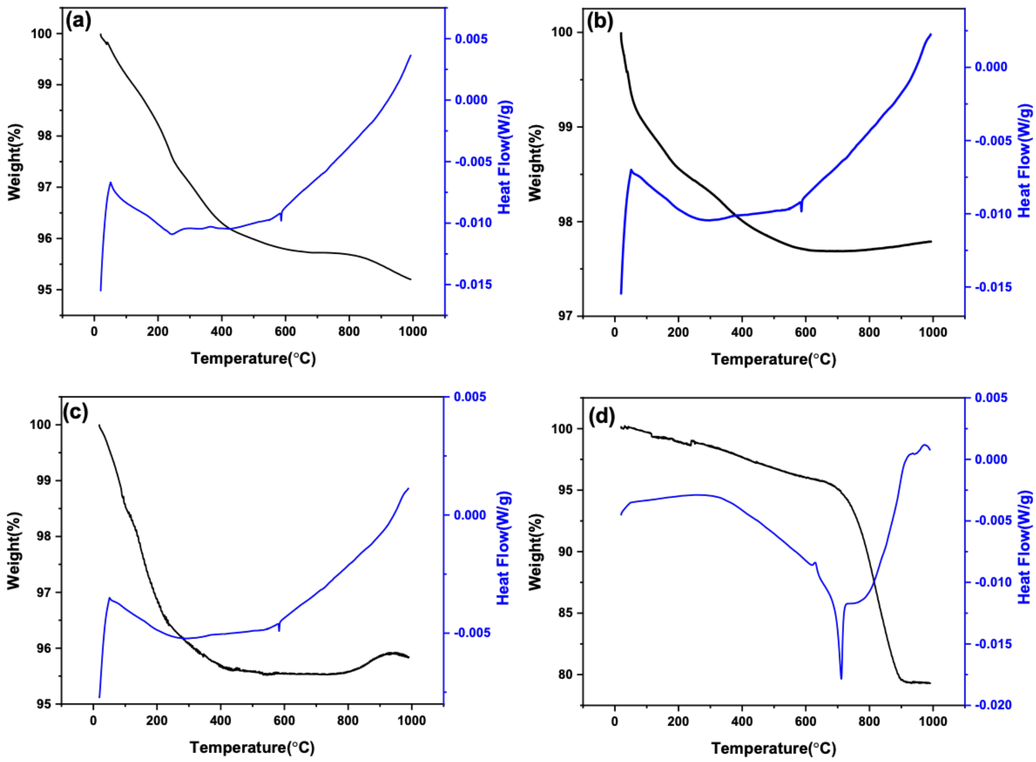

Figure 6.4. TGA-DTA (1000 °C/air) of $LiAlO_2$ as produced NPs a. $Li_{1.75}AlO_2$, b. $Li_{1.99}AlO_2$, c. $Li_{3.1}AlO_2$, and d. $Li_{6.2}AlO_2$.

The crystal structures of lithium aluminate polymorphs have been studied since the '60s[44] based on the $A^{+1}B^{+3}O_2$ formula using powder neutron and single-crystal X-ray techniques.[45] Polymorphs of lithium aluminum oxides with six different crystal systems have been identified to date.[46] As might be expected, phase formation depends on the processing conditions used. Here, we only focus on cubic $LiAl_5O_8$ and γ-$LiAlO_2$.

Figure **6.5** shows XRDs of as-produced $LiAlO_2$ NPs with varying Li amounts. The primary phase is $LiAlO_2$ with a secondary Al rich $LiAl_5O_8$ phase also present. Table **6.4** shows the wt. % fraction of each phase.

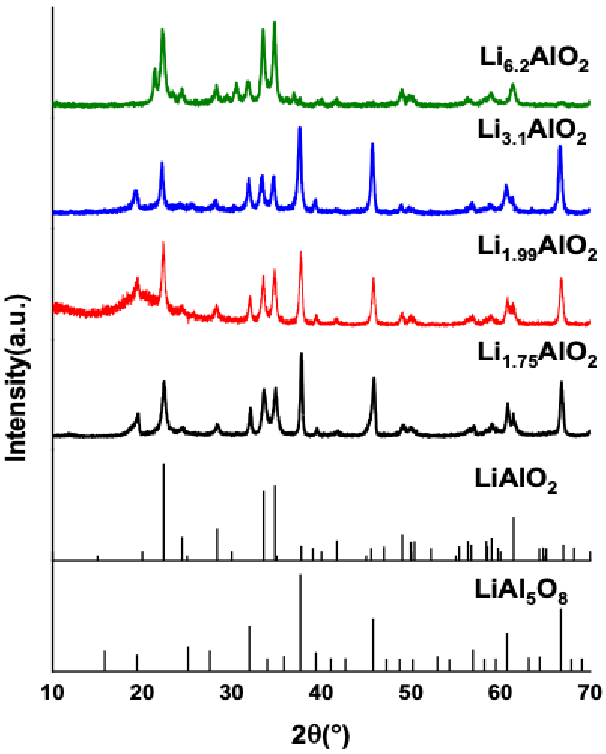

Figure 6.5. XRD plots of $LiAlO_2$ as produced NPs.

Table 6.4. Relative contents of phases in as-produced $LiAlO_2$ NPs.

	$LiAlO_2$(wt.%)	$LiAl_5O_8$(wt.%)	Li_2CO_3(wt.%)
$Li_{1.75}AlO_2$	25±0.2	74±0.8	-
$Li_{1.99}AlO_2$	42±0.5	57±0.5	-
$Li_{3.1}AlO_2$	67±0.2	32±0.8	-
$Li_{6.2}AlO_2$	85±0.4	5±0.2	9.6±0.6

The combustion by-products H_2O and CO_2 at high flame temperatures (>1000 °C) accelerate decomposition, hence, the formation of single-phase $LiAlO_2$ was inhibited even with 300 wt.% excess Li. In general, LF-FSP made NPs are pure oxides.[39,47] However, here we obtain a mixture of $LiAl_5O_8$, Li_2CO_3, and $LiAlO_2$. Owing to combustion followed by rapid quenching, LF-FSP produced NPs often exhibit kinetic rather than thermodynamically favored phases; consequently, as-produced NPs are often mixed phases.[7,40,48] The XRD plots show broad peaks ~ 19° 2θ suggesting the amorphous nature of the as-produced powders. LF-FSP derived electrolyte NPs are frequently at least partially amorphous as a result of the fast combustion and quenching process.[9,39]

The observed broad diffraction peaks for the as-produced NPs are due to the combined effect of microstrain induced by dislocation (strain broadening) and shrinkage of the coherent scattering volume (size broadening).[49] Williamson-Hall (W-H)[50] analysis was used to calculate the crystallite size (βs) and microstrain (β_e) by considering the broadening of the peak width as a function of 2θ. The total broadening can be expressed as:

$$\beta_t = \beta_s + \beta_e \qquad (1)$$

Where β_t represents the total broadening, β_s is the broadening due to crystalline size and β_e is due to the micro-strain. It is well known that the Scherrer formula provides the APSs of crystallites in a direction perpendicular to particular (hkl) planes.[51] Thus, the $LiAlO_2$ NP crystallite sizes are estimated using the Scherrer formula (2):

$$D = k\lambda/\beta_s cos\theta \qquad (2)$$

Where D is crystallite size, k = 0.94 is the shape factor, λ is the x-ray wavelength (0.154 nm) β_s is the width at half max (FWHM) in radians, and θ is the diffraction angle of Bragg. The XRD peak broadening due to microstrain is given by equation (3),

$$\beta_e = 4\varepsilon tan\theta \qquad (3)$$

The W-H method assumes that the strain is uniform throughout the crystallographic direction; given by introducing equations (2) and (3) into equation (1),

$$\beta_t cos\theta = k\lambda/D + 4\,\varepsilon \sin\theta \qquad (4)$$

In equation (4), D and ε correspond to crystallite size and microstrain, respectively. Figure **6.6** shows the W-H plots for the as-produced $LiAlO_2$ NPs. The non-linearity in the W-H plot (**Figure 6.6b**) indicates the presence of anisotropic strain.[52] The gradient of $\beta_t cos\theta$ vs sinθ plot gives the NP microstrain and the Y-axis intercept gives the $k\lambda/D$ value.

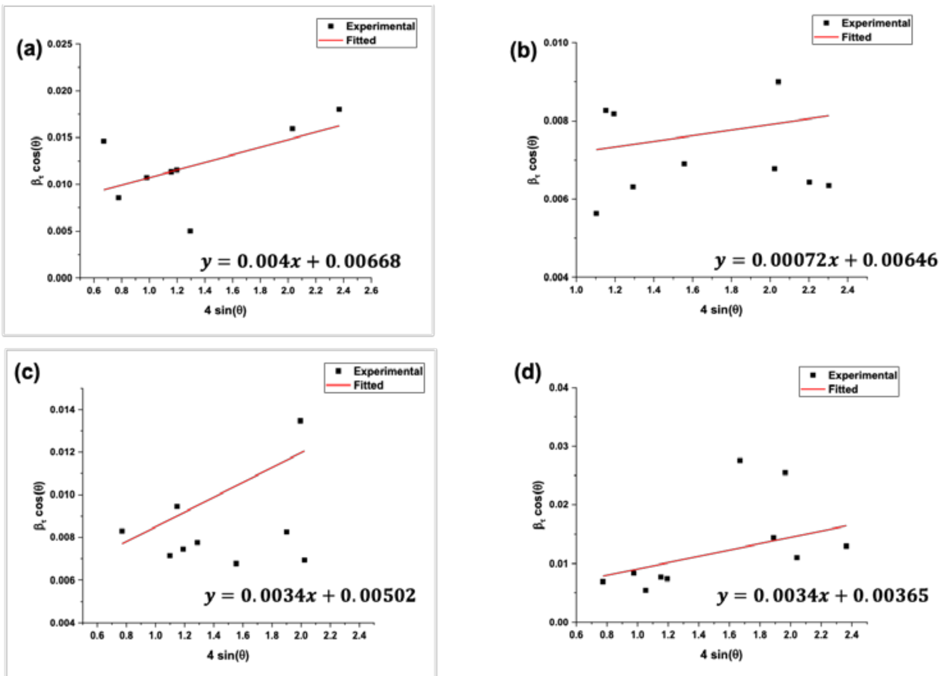

Figure 6.6. W-H plots of as-produced NPs. a. $Li_{1.72}AlO_2$, b. $Li_{1.99}AlO_2$ c. $Li_{3.1}AlO_2$, d. $Li_{6.2}AlO_2$.

Table **6.5** lists the estimated average values for crystallite size and microstrain based on W-H plots. The reported BET APSs (Table **6.3**) are relatively larger than the XRD crystallite size.

The variation between these measurements indicates that the NPs are agglomerated,[53] in good agreement with the NP microstructures shown by the Figure **6.2b** SEMs. Although the Scherrer formula provides only a lower limit of crystallite size; both BET APSs and XRD crystallite sizes increase linearly with excess Li for the as-produced $LiAlO_2$ NPs as shown in Figure **6.7**.

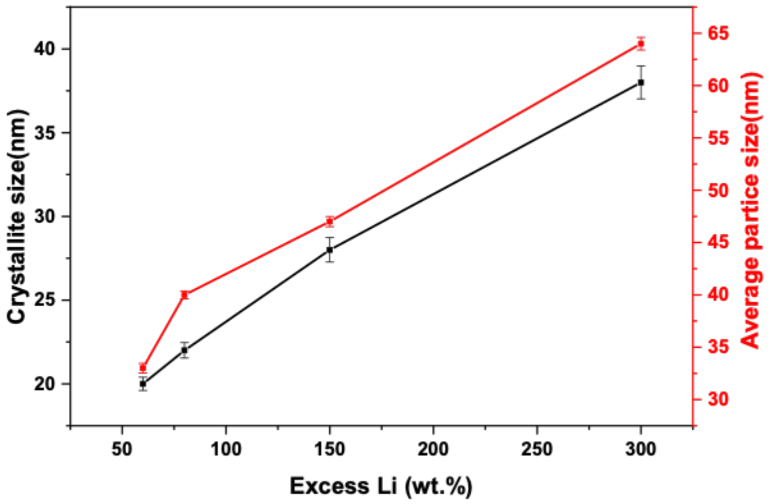

Figure 6.7. Comparison of BET APSs and XRD crystallite size.

Figures **6.8 a** and **b** show ^{7}Li and ^{27}Al MAS NMR spectra for $Li_{6.2}AlO_2$ NPs, respectively. The ^{7}Li MAS NMR spectrum shows a single peak at 0.3 ppm consistent with the crystal structure of $LiAlO_2$ that contains only a single Li site with tetrahedral oxygen coordination. The ^{27}Al MAS NMR spectrum shows two peaks. The first, at 76.2 ppm, is characteristic of [AlO_4] units,[54,55] as expected from the crystal structure of $LiAlO_2$. The second peak at 14.0 ppm clearly shows the presence of [AlO_6] units.[54,55] This might hint at the presence of some residual $LiAl_5O_8$, where Al is present both on tetrahedral and octahedral sites of the spinel structure, supporting the XRD results present in Figure **6.5**. Furthermore, since both peaks are quite broad, some amorphous fractions might be present in the sample.

The crystal structure of $LiAl_5O_8$ (Figure **6.9**) shows corner-linked Al-O forming tetrahedra and edge-shared Li/Al-O octahedra. The four Li ions in the unit cells labeled Li1, Li2, Li3, and Li4 are distributed on octahedral sites.[56] Whereas, Al^{3+} is equally distributed between tetrahedral and octahedral sites. $LiAl_5O_8$, owing to its high symmetry, has four equivalent Li^+ sites with the same diffusion path(s).[56] Hence, it has been suggested that $LiAl_5O_8$ might show high ionic conductivities.[56] Table **6.5** lists the lattice parameters for $LiAl_5O_8$ obtained from experimental data and theoretical modeling.

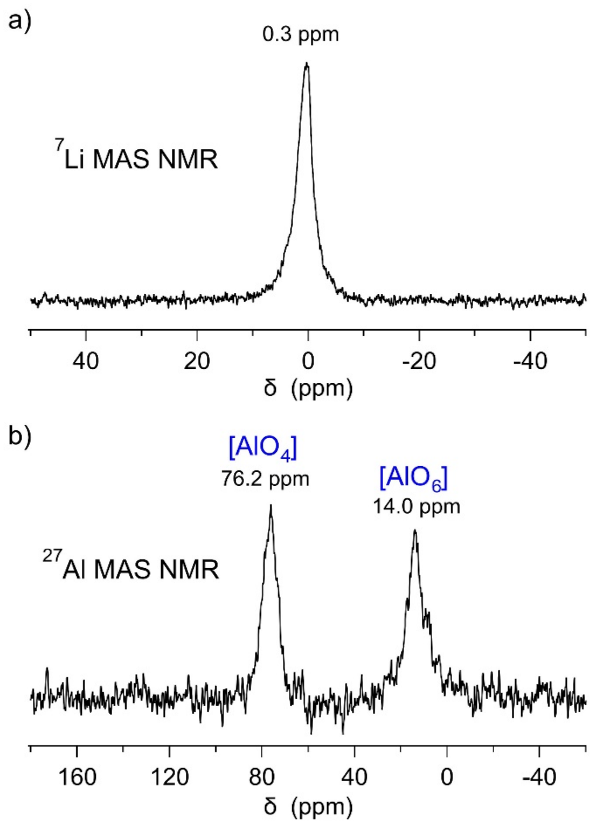

Figure 6.8. a.^{7}Li and b.^{27}Al MAS NMR spectra of $LiAlO_2$ NPs.

As mentioned above, the large interfacial resistivity between the metallic Li anode and garnet type $Li_7La_{2.75}Ca_{0.25}Zr_{1.75}Nb_{0.25}O_{12}$ (LLCZN) was effectively decreased by introduction of an ultra-thin alumina coating.[12] The rationale for these observations suggests formation of a lithiated alumina that permits rapid diffusion of Li^+ through the interface.[12] One implication is that the $LiAl_5O_8$ framework may permit high Li^+ mobility via 3-D diffusion.[56]

Table 6.5. Lattice parameters for $LiAl_5O_8$ obtained from the experimental data and theoretical modeling.

		Experimental (this work)	Calculated (ref.[1])
Crystal system		Cubic	Cubic
Space group		P4332	P4332
Volume (Å^3)		510	507
Density (g/cm^3)		3.6	3.6
a (Å)		7.98	7.97
Atom	Site	*(x,y,z)*	*(x,y,z)*
Li	4b	*(0.12,0.87,0.37)*	*(0.125,0.875,0.375)*
Al	8d	*(0.37,0.89,0.13)*	*(0.368,0.882,0.125)*
Al	4a	*(0.003,0.45,0.5)*	*(0.003,0.497,0.503)*
O	8d	*(0.36,0.38,0.87)*	*(0.365,0.382,0.866)*

Pan et al[56] studied Li^+ diffusion mechanisms in $LiAl_5O_8$ and alumina using first-principles density functional theory (DFT) calculations. They find that the Li^+ diffusion coefficient for $LiAl_5O_8$ ($D_{Li+} = 3.6x10^{-8}$ cm^2s^{-1}) is significantly higher than that of alumina ($D_{Li+} = 9.3x10^{-48}$

cm^2s^{-1}) at room temperature, suggesting that Li^+ mobility in $LiAl_5O_8$ is substantially improved. Therefore, reduced interfacial impedance may be accessed by replacing alumina coatings with $LiAl_5O_8$, implying better battery performance. In addition, $LiAl_5O_8$ offers a wide electrochemical stability window of 0.8-4.08V vs. Li/Li^+ making it an attractive coating for next-generation LIB electrodes [56] and potential solid electrolyte for assembling microbatteries.

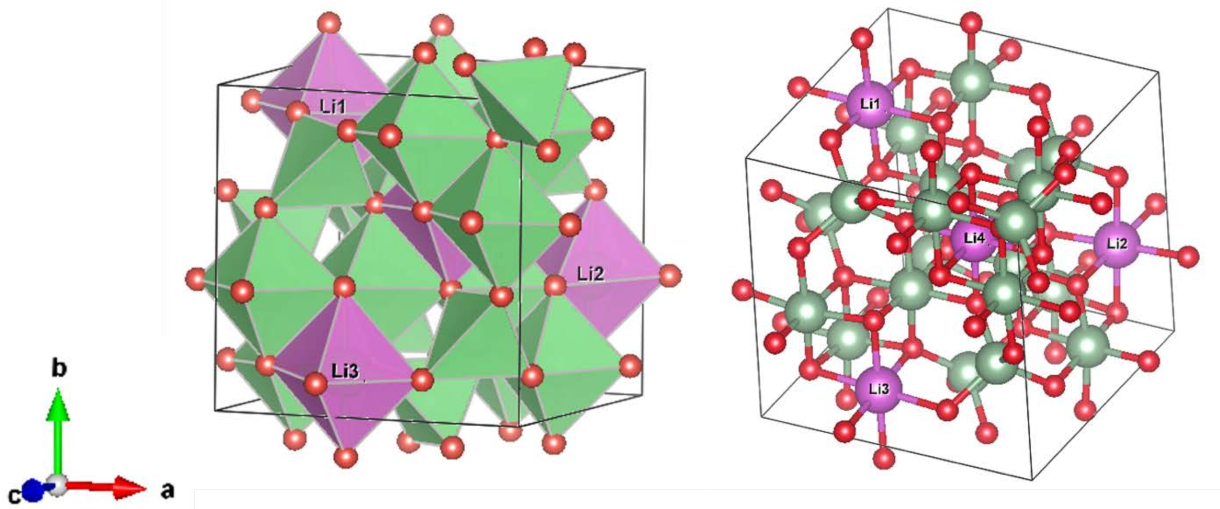

Figure 6.9. Crystal structures of $LiAl_5O_8$. The Li, Al, O are shown in pink, green, and red, respectively, unit cell in black.

6.3.2 Microstructure and crystallinity of $LiAlO_2$ membranes

Multiple studies have used conventional solid-state synthesis methods to produce $LiAlO_2$ powders.[42] However, this technique often produces aggregated materials with broad particle-size distributions, low SSAs, and requiring multiple process steps to fabricate dense, single phase, thick films.[39] In contrast, we have reported using flame made NPs with narrow APSs to directly process green films by ball-milling the NPs with polymer additives followed by conventional tape casting. Thermo-pressing the green films at 100 °C/10 kpsi/10 min results in uniform green body densities that can drive densification at lower sintering temperatures with control of final grain sizes and mechanical properties in thin (< 50 µm) films.

Prior to sintering, solids loadings were confirmed by TGA (Figure **6.10**) presenting an expected ceramic yield of 70 wt.% matching theory. The mass loss between 200-400 °C is ascribed to decomposition of the polymeric additives. This step is necessary to establish gentle binder burn out temperatures (300 °C/2 h) to avoid cracking the polymer free films. Green films of $LiAlO_2$ with varying Li amounts were subsequently sintered at various densification temperatures. Figure **6.11** shows SEMs of the green films. Microstructures demonstrate that the NPs are well mixed with the polyacrylic acid, dispersant. Green films of $LiAlO_2$ were inserted between α-Al_2O_3 disks and debindered at 300 °C/2 h and 665 °C/2 h/5 °C min^{-1} followed by sintering at 1100 °C/2 h /1 °C min^{-1} under 120 ml min^{-1} air flow.

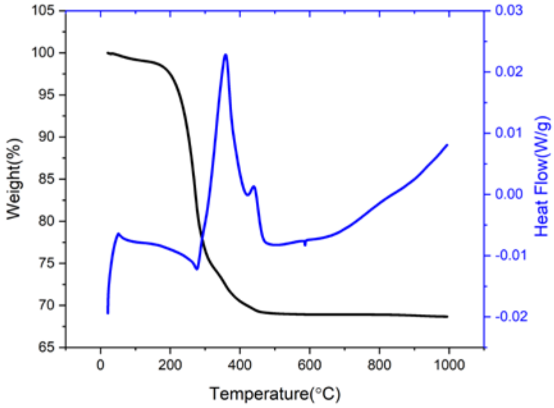

Figure 6.10. TGA/DTA (1000 °C/air) of $LiAlO_2$ green films.

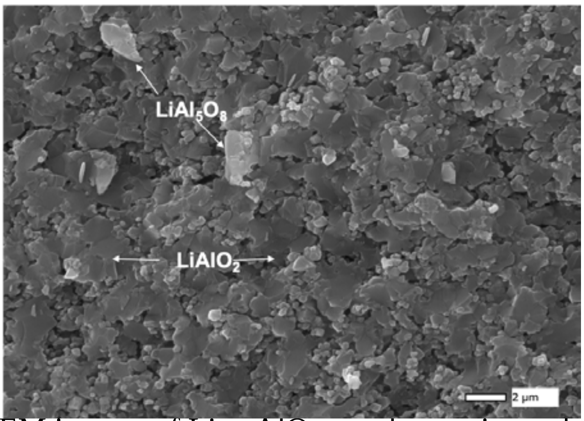

Figure 6.11. SEM images of $Li_{1.72}AlO_2$ membrane sintered to 1100 °C/2 h.

Figure **6.12a** shows XRD patterns of $LiAlO_2$ membranes sintered at 1100 °C/2 h /air. The dwell time was minimized to 2 h, to reduce Li volatility, preferably resulting in a single phase, dense $LiAlO_2$. $LiAlO_2$ membranes with 60, 80, and 150 wt.% excess Li showed the targeted γ-$LiAlO_2$ and $LiAl_5O_8$. Table **6.6** shows the relative wt.% fraction of the phases present. For Rietveld refinement, a model was imported from the Inorganic Crystal Structure Database (ICSD), $LiAlO_2$ (PDF-01-095-3721) and $LiAl_5O_8$ (PDF-04-022-2622). $Li_{6.2}AlO_2$ membranes show single-phase-$LiAlO_2$ (space group $P4_12_12$) indicating that loss of Li is compensated by using excess lithium propionate. Hence, the LF-FSP synthesis method allows exceptional control of phase purity and stoichiometry.

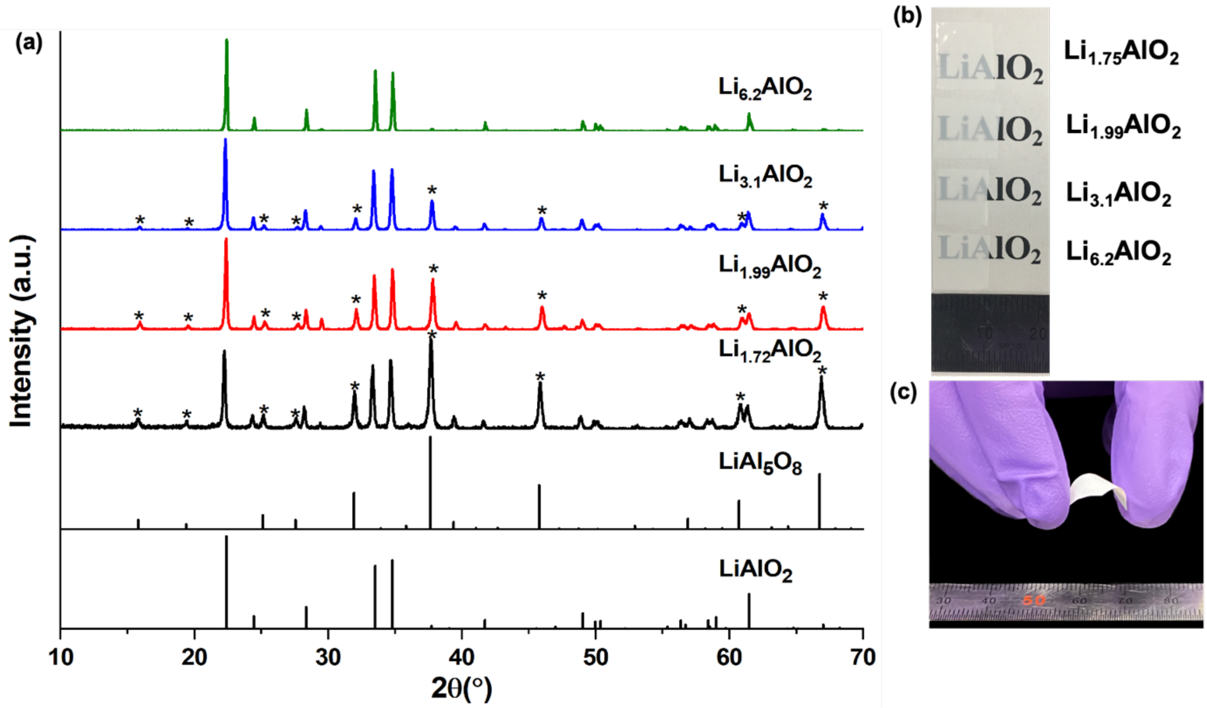

Figure 6.12. a. XRDs of sintered $LiAlO_2$ membranes (1100 °C/2 h /air). b. Optical images of translucent $LiAlO_2$ membranes, and c. flexible $Li_{3.1}AlO_2$ film. (*corresponds to $LiAl_5O_8$).

It is common to account for the loss of Li in sputtering techniques to synthesize phase pure γ-$LiAlO_2$.[46] However, such processing requires subsequent ball milling of raw materials, followed by compacting pellets and sintering at high temperatures (~1100 °C) and long dwell times (20 h) to produce dense targets.[46]

Table 6.6. Weight fraction of phases in $LiAlO_2$ thin films sintered to 1100 °C/2 h/air.

	$LiAlO_2$(wt.%)	$LiAl_5O_8$(wt.%)
$Li_{1.75}AlO_2$	35±0.6	64±0.4
$Li_{1.99}AlO_2$	53±0.8	46±0.2
$Li_{3.1}AlO_2$	72±0.8	27±0.2
$Li_{6.2}AlO_2$	100	-

Marezio et al.[44] reported that the XZ plane of γ-$LiAlO_2$ consists of distorted MO_4 tetrahedra (M = Li, Al) forming a 3-D network. The unit cell contains four formula units. One edge of the tetrahedron is shared by other tetrahedra containing a metal ion of a different kind.

As seen in Figure **6.13**, the edge-sharing topology generates distorted hexagonal channels. In this study, the experimental *c/a* ratio (1.212) for $Li_{6.2}AlO_2$ membrane is consistent with that reported in the literature (within 1% error).[46,57] The calculated average Li-O distance in the tetrahedral structure is ~ 2 Å, also in good agreement with the theoretical modeling work.[57] To locate the equilibrium structure, the unit cell parameters and atomic coordinates were fully relaxed. The lattice parameters for $LiAlO_2$ obtained from experimental and theoretical calculations are listed in Table **6.7**.

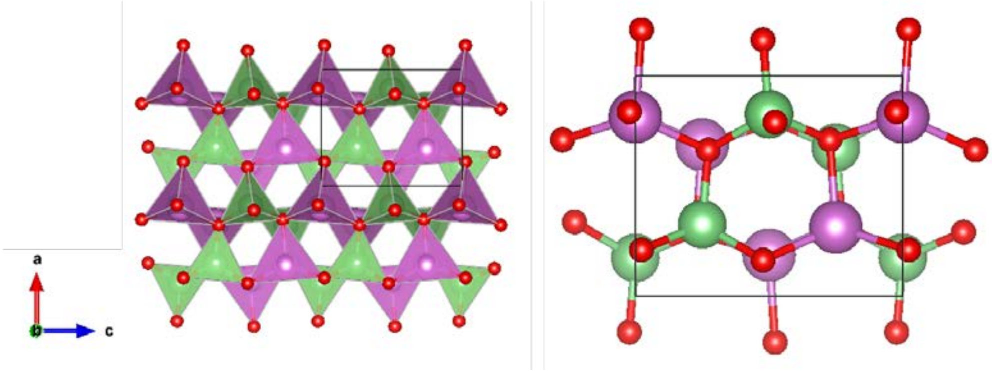

Figure 6.13. Crystal structures of $LiAlO_2$. The Li, Al, O are shown in pink, green, and red, respectively; unit cell in black.

Table 6.7. Lattice parameters for $LiAlO_2$ obtained from the experimental data and theoretical modeling.

		Experimental (this work)	Calculated (ref.[2])
Crystal system		Tetragonal	Tetragonal
Space group		$P4_12_12$	$P4_12_12$
Volume ($Å^3$)		166.87	166.87
Density (g/cm^3)		2.6	2.62
a (Å)		5.16	5.152
C (Å)		6.27	6.24
Atom	Site	*(x,y,z)*	*(x,y,z)*
Li	4a	*(0.82,0.82,0.0)*	*(0.8132,0.8132,0.0)*
Al	4b	*(0.18,0.18,0.0)*	*(0.1752,0.7152,0.0)*
O	8b	*(0.36,0.3,0.77)*	*(0.3332,0.2929,0.7695)*

Figures **6.12b** and **6.14** show optical images and SEM fracture surfaces of $LiAlO_2$ membranes with various Li contents sintered to 1100 °C/2 h/air, respectively. The optical images with dimensions of ~1x1 cm^2 reveal semi-transparent, sintered membranes. Translucency arises because of high densities.[40] The $Li_{1.72}AlO_2$ membrane, with the highest $LiAl_5O_8$ phase fraction (64.4 wt.%), exhibits a glossy surface, Figure **6.12b**. The dense, membranes offer thicknesses of 20-50 µm. SEM fracture surface images show uniform sized submicron pores, ascribed to the small and uniform NP APSs. This is significant because macroscopic pores (> 10 µm) in ceramic electrolytes, aside from engendering poor mechanical properties, result in poor ionic conductivity from local in-homogeneous ion mobility, decreasing battery cycle life.[58]

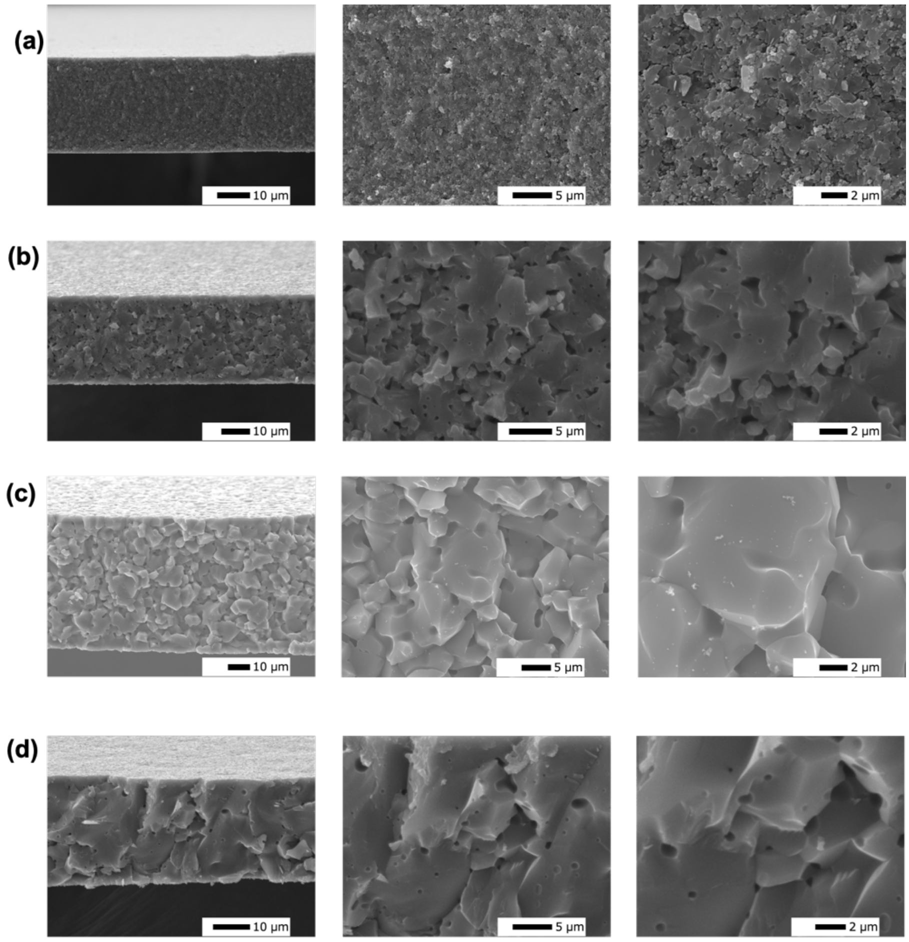

Figure 6.14. SEM fracture surface images of $LiAlO_2$ membranes sintered at 1100 °C/2 h. a. $Li_{1.75}AlO_2$, b. $Li_{1.99}AlO_2$, c. $Li_{3.1}AlO_2$, and d. $Li_{6.2}AlO_2$.

Figure **6.12c** shows that the $Li_{3.1}AlO_2$ thin membrane offers mechanical properties that allow it to flex, which can be expected to permit roll-to-roll processing and facilitate assembly of microbatteries. This flexible electrolyte membrane also enables development of new ASSB designs. In general, fine grained membranes ensure flexibility in ceramics attributed to the tortuous crack propagation pathways, resulting in superior mechanical stability. The flexibility of the membrane also indicates the absence of surface flaws that may initiate cracking.

Table 6.8. Relative densities of $LiAlO_2$ thin films sintered to 1100 °C/2 h/air**.**

	Density (%)	AGSs (µm)
$Li_{1.75}AlO_2$	83±0.2	2.2±0.3
$Li_{1.99}AlO_2$	87±0.5	4.5±0.7
$Li_{3.1}AlO_2$	90±0.6	6.6±0.2
$Li_{6.2}AlO_2$	95±0.2	7.2±0.5

In, general, high-density microstructures were achieved at low sintering temperatures for all $LiAlO_2$ films. Transgranular fracture surfaces reveal very high densities. The density of the membranes seems to increase as excess Li increases as the $Li_{6.2}AlO_2$ membrane shows the highest relative densities ~ 95 ± 0.2% as determined by the Archimedes method (Table **6.8**). This may also be attributed to the fact that as-produced $Li_{6.2}AlO_2$ NPs contains excess Li_2CO_3 which aids in liquid phase/reaction driven sintering as seen previously.[48] The average grain sizes (AGSs) for the $LiAlO_2$ films were calculated using the linear intercept method.[59] Table **6.8** shows AGSs increased from 2.2 ± 0.3 µm (for $Li_{1.72}AlO_2$) to 7.2 ± 0.5 µm (for $Li_{6.2}AlO_2$) with increasing γ-$LiAlO_2$ phase. The small AGSs for $Li_{1.72}AlO_2$ (Figure **6.14a)** and $Li_{1.99}AlO_2$ translate to increases in grain boundary volume fractions, which reduce the relative densities for these membranes. Thus, the found densities reported may actually be somewhat higher because the exact volume fraction and densities of the grain boundaries are not known.

6.3.3 Ionic conduction mechanisms in $LiAlO_2/LiAl_5O_8$ membranes

$LiAlO_2$ is a known electrical insulator and a very poor Li^+ conductor (~10^{-10} S cm^{-1}) at room temperature.[46] Efforts have been made to improve its ionic conductivity by introducing an amorphous phase,[6] silicate-based Li^+ conducting components with higher ionic conductivity,[60] structural disordering via point defects, and higher dimensional defects.[38] However, significant improvements in ionic conductivity have not been reported, to the best of our knowledge. In this work, we examined the effect of a secondary phase, $LiAl_5O_8$, on $LiAlO_2$ membrane conductivity.

Figure **6.15** shows typical Nyquist plots for the $LiAlO_2$ membranes, where electrochemical impedance data was collected from 7 MHz to 1 Hz at 25 °C. The Nyquist plots in the temperature range of -10 ° to 100° C are presented in Figures **6.16** and **6.17**. The $LiAlO_2$ + 150% membranes offer the highest ionic conductivity of ~ 5.2 ± 0.7x10^{-6} S cm^{-1} at room temperature. Table **6.9** records total ionic conductivities of the membranes heated to selected temperatures.

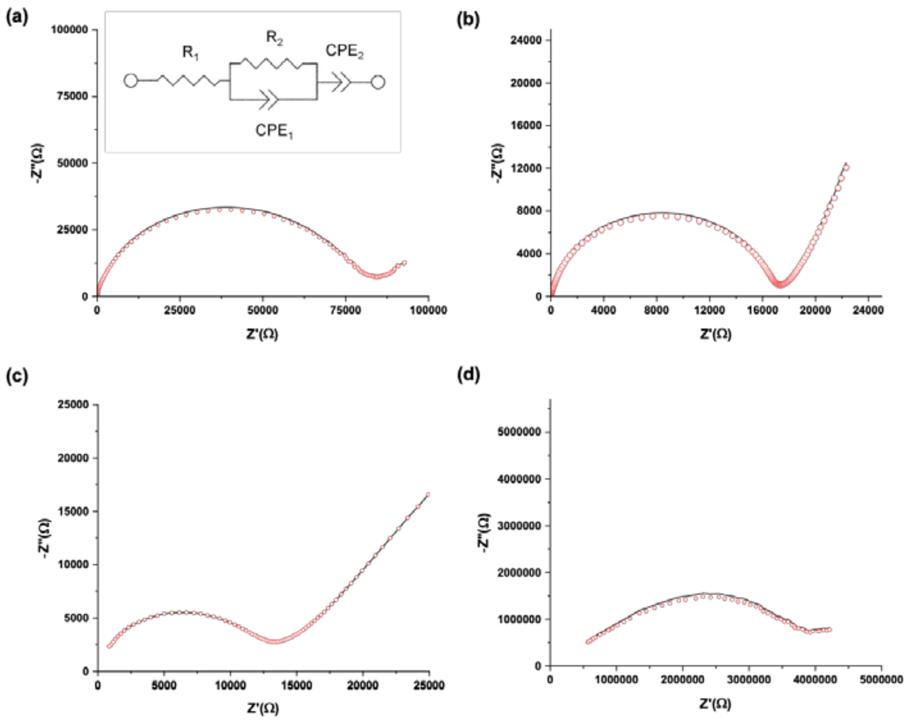

Figure 6.15. Nyquist plots of a. $Li_{1.72}AlO_2$, b. $Li_{1.99}AlO_2$, c. $Li_{3.1}AlO_2$, and d. $Li_{6.2}AlO_2$ membranes at 25 °C. Marked lines indicate experimental data and the circles represent the equivalent circuit modelling data.

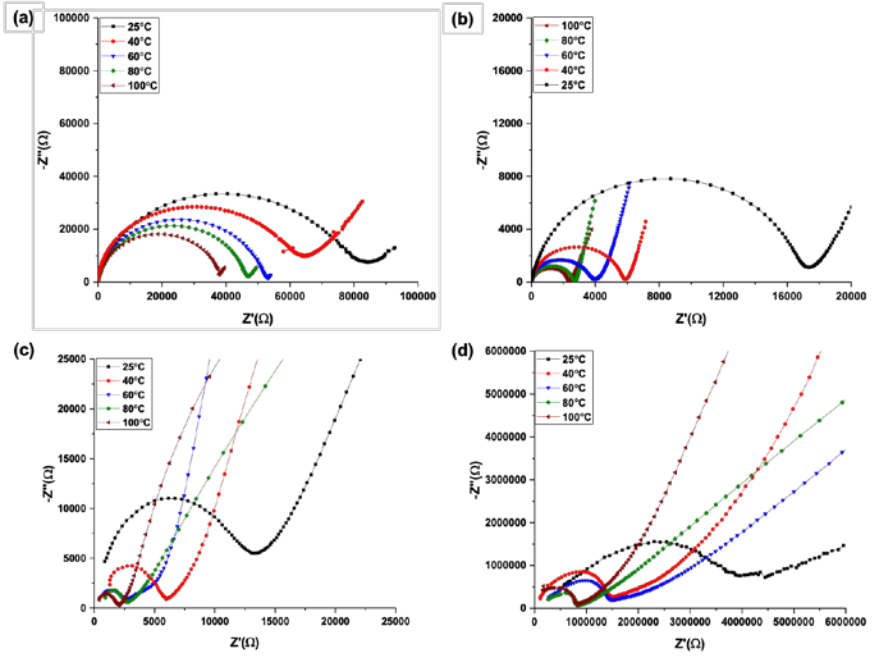

Figure 6.16. Nyquist plots a. $Li_{1.72}AlO_2$, b. $Li_{1.99}AlO_2$ c. $Li_{3.1}AlO_2$, d. $Li_{6.2}AlO_2$ membranes at 25° to 100 °C.

Optimization of the ionic conductivity of γ-$LiAlO_2$ was achieved by introducing $LiAl_5O_8$. Pristine γ-$LiAlO_2$ membranes show room-temperature conductivities of $2.4\pm1.2\times10^{-8}$ S cm^{-1}, still two orders of magnitude higher than typically reported for γ-$LiAlO_2$.[16] For conventional all-solid-state microbatteries, thin film electrolytes with ambient conductivities >10^{-6} S cm^{-1}

are highly desirable.[61,62] Hence, these new $LiAlO_2/LiAl_5O_8$ membranes are solid electrolyte alternatives to LiPON for assembly of microbatteries.

The Li^+ migration pathways in $LiAlO_2/LiAl_5O_8$ mixed phases are proposed to be shorter than the distance between nearest Li^+ sites in pristine γ-$LiAlO_2$, which implies occupation of interstitial sites with lower activation energies. $LiAl_5O_8$ ionic conductivity originates from diffusion of point defects (V^-_{Li} and Li_i^+).[56] The Li^+ interstitial diffusion pathway has been reported to show a substantial decrease in the interstitial migration barrier (0.33 eV) compared to Li^+ vacancy diffusion.[56]

Table 6.9. Total conductivities (σ_t) of $LiAlO_2$ thin films heated to selected temperatures.

T (°C)	σ(S cm^{-1}) $Li_{1.75}AlO_2$	σ(S cm^{-1}) $Li_{1.99}AlO_2$	σ(S cm^{-1}) $Li_{3.1}AlO_2$	σ(S cm^{-1}) $Li_{6.1}AlO_2$
-10	1.0×10^{-8}	1.1×10^{-7}	3.5×10^{-7}	1.1×10^{-9}
0	1.1×10^{-8}	1.2×10^{-7}	5.9×10^{-7}	1.4×10^{-8}
25	8.3×10^{-7}	4.0×10^{-6}	5.2×10^{-6}	2.4×10^{-8}
40	1.6×10^{-6}	1.2×10^{-5}	1.7×10^{-5}	5.3×10^{-8}
60	2.0×10^{-6}	1.8×10^{-5}	2.1×10^{-5}	7.0×10^{-8}
80	2.3×10^{-6}	2.0×10^{-5}	3.9×10^{-5}	1.3×10^{-7}
100	2.8×10^{-6}	$2.4. \times 10^{-5}$	5.3×10^{-5}	1.5×10^{-7}

This is ascribed to a direct-hopping mechanism, where interstitial Li^+ diffuses through the shared edge between two LiO_4 tetrahedra, resulting in comparatively shorter Li-O bonds (~1.4 Å).[56] Whereas, the vacancy migration activation energy is reported to be as high as 2.86 eV due to electrostatic repulsion from adjacent Al^{3+} at the midpoint between two Li vacant sites.[56]

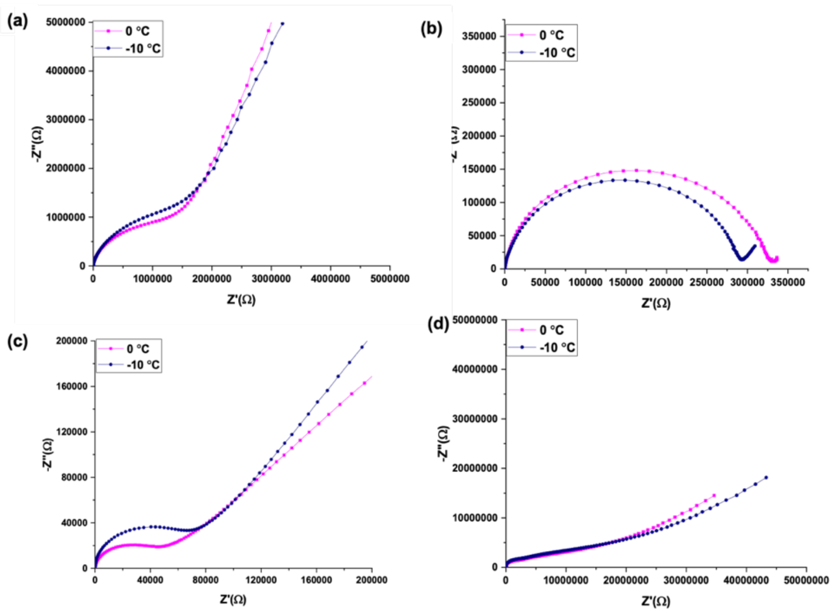

Figure 6.17. Nyquist plots a. $Li_{1.72}AlO_2$, b. $Li_{1.99}AlO_2$ c. $Li_{3.1}AlO_2$, d. $Li_{6.2}AlO_2$ membranes in the temperature range of -10 ° to 0°C.

Wiedemann et al.[46] showed that Li^+ diffusion in $LiAlO_2$ occurs along a strongly curved pathway in 2-D via hopping of Li^+ between Li positions and adjacent vacancies. The reported migration barrier for this diffusion mechanism is ~ 0.72 eV, which was determined using temperature-dependent neutron diffraction studies. The other diffusion mechanism reported is through long-range diffusion along the [001] direction which results in a higher activation energy of 0.87 eV.[46] Indris et al.[63] investigated Li^+ diffusion in a $LiAlO_2$ single crystals using ^7Li NMR spectroscopy and conductivity measurements. They reported an activation barrier energy of 0.72 eV ascribed to Li^+ diffusion via a vacancy mechanism.[63]

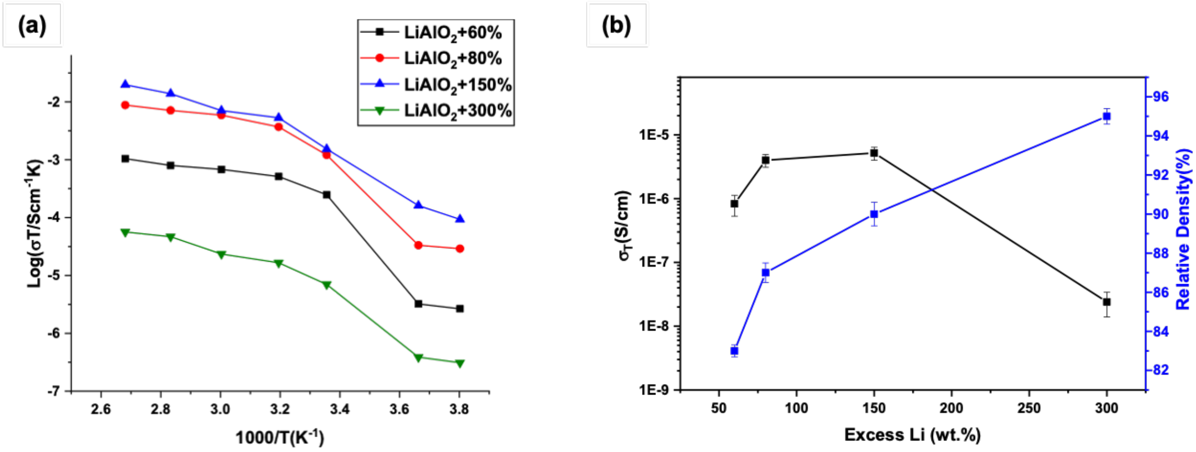

Figure 6.18. a. Arrhenius plots for the ionic conductivity. b. Relation between room temperature ionic conductivities and relative densities of $LiAlO_2$ membranes sintered at 1100 °C/2 h.

The introduction of structural disorder caused by point defects and higher-dimensional defects in γ-$LiAlO_2$ has been reported to increase the room-temperature ionic conductivity, experimentally studied by temperature-dependent impedance spectroscopy.[38] A recent study elucidates the local diffusion mechanism for γ-$LiAlO_2$ using a climbing image nudged-elastic-band approach with periodic quantum-mechanical density function theory.[57]

It was concluded that Li^+ can diffuse between two LiO_4 tetrahedral sites via Li point defects (V^-_{Li}) and via a Li^+ Frenkel defect (V^-_{Li} and Li_i^+).[57] The low activation barriers reported here are ascribed to the presence of extrinsic defects generated by the introduction of $LiAl_5O_8$. The Arrhenius plots for the ionic conductivity of $LiAlO_2$ membranes are shown in Figure **6.18a**. The conductivity of the $LiAlO_2$ membranes increases with increasing temperature, indicating a thermally activated mechanism. Table **6.10** presents activation energies ranging from 0.43 to 0.5 eV for $LiAlO_2$ membranes with various Li compositions.

Table 6.10. Activation energies of $LiAlO_2$ membranes.

Electrolytes	Activation energy (eV)
$Li_{1.75}AlO_2$	0.48±0.07
$Li_{1.99}AlO_2$	0.48±0.02
$Li_{3.1}AlO_2$	0.42±0.08
$Li_{6.1}AlO_2$	0.42±0.06

The ionic conduction mechanism for γ-$LiAlO_2$ is disparate, with activation barriers ranging from 0.5 -1.47 eV.[46,63,64] These findings are based on polycrystalline, microcrystalline, single-crystal and nano-crystalline γ-$LiAlO_2$.[46,57,63,64] The discrepancies in the calculated activation energies might be ascribed to the fact that only isolated vacancies are considered as possible defects, disregarding contributions from grain boundaries and complex morphologies. In addition, Frenkel defect type Li^+ migration involves local Li^+ jumps as a function of V^-_{Li} and the distance between migrating Li—Li_i^+, which explains the relatively large scatter in the experimental activation energy values.[57]

Figure **6.18b** shows the relationship between room temperature ionic conductivities and relative densities of $LiAlO_2$ membranes with various Li amounts sintered at 1100 °C/2 h. The single-phase γ-$LiAlO_2$ film, with a high relative density of ~95%, shows two orders of magnitude lower ionic conductivity (2.4×10^{-8} S/cm) compared to the mixed-phase $LiAlO_2$/$LiAl_5O_8$ films, with slightly lower densities. The presence of the $LiAl_5O_8$ phase results in superior Li^+ diffusivity (3.6×10^{-8}) and lower migration barriers.[56] Moreover, the fine grained membranes (AGSs < 5 µm) ensure that cracks propagate via a tortuous path that absorbs the energy driving propagation, offering superior mechanical stability.

Table **6.11** lists the thicknesses, processing methods, and ambient ionic conductivities of various $LiAlO_2$ films/pellets reported in the literature. The gas phase deposition techniques (i.e. ALD) generally require expensive and energy intensive process. Regardless the simplicity of the SSR method, achieving dense, single-phase γ-$LiAlO_2$ sample requires high sintering temperatures and long dwell times. Utility for cost effective mass production with fast ion conducting properties for ASSBs using this approach seems problematic at best.

Table 6.11. Conductivities of $LiAlO_2$ samples with various processing methods.

Processing	Phase composition	Experimental conditions	σ (S cm^{-1})	Thickness	Ref.
LF-FSP/TC	γ-$LiAlO_2$ (~73 wt. %) $LiAl_5O_8$ (~27 wt. %)	AC Impedance: RT	5.2×10^{-6}	25 µm	This work
ALD	Amorphous Li:Al = 1:1.16	Impedance: in-plane	5.1×10^{-9}	90 nm	16
ALD	Amorphous $LiAlO_2$	Impedance: in-plane	5.6×10^{-8}	50 nm	17
ALD	Amorphous $LiAlO_2$	Impedance: cross-plane	2.8×10^{-10}	160 nm	16
CT	Single crystalline γ-$LiAlO_2$	AC Impedance:150-350 °C	1×10^{-17}	80 mm	63
SSR	Polycrystalline γ-$LiAlO_2$	AC Impedance:450-1000 °C	2×10^{-14}	2.9 mm	60
TRQ	$0.7Li_2O$-$0.3Al_2O_3$	AC Impedance:150-400 °C	5×10^{-8}	20 µm	65

TRQ = twin roller quenching, SSR = solid state reaction, TC = tape casting, CT = Czochralski technique, ALD = atomic layer deposition, LF-FSP= liquid flame spray pyrolysis

6.3.4 Symmetric cell studies of Li/$Li_{3.1}AlO_2$/Li

An Li/$Li_{3.1}AlO_2$/Li symmetric cell was constructed and cycled at ambient using a DC steady state method using various current densities (0.05-0.375 mA/cm^2). **Figure 6.19a** demonstrates the potential response of the Li/$Li_{3.1}AlO_2$/Li symmetric cell. At relatively low current densities (0.05- 0.15 mA/cm^2), the symmetric cell exhibits an ideal voltage response indicating that there is a minimal interfacial impedance at ambient. The $Li_{3.1}AlO_2$ membrane wets well with Li metal (Figure **6.20)**, supporting the first-principle computational studies that demonstrate the strong chemical binding between Li metal and $Li_xAl_2O_{3+x/2}$ (x = 0.4 -1.4).[12]

The voltage plateaus during cycling at higher current density (0.375 mA/cm^2) do show polarization that follows Ohmic behavior. This polarization is consistent across all cycles as shown in Figure **6.20**, which does not suggest degradation of the $LiAlO_2$ membrane. Typically, solid electrolyte degradation is indicated by a reduction in voltage during galvanostatic cycling. Long-term cycling at 0.25 mA/cm^2 current density shows that the potential profile becomes constant (~6.5 mV) for 60 h, confirming that lithiated $Li_{3.1}AlO_2$ membrane is a good Li^+ conductor that provides effective Li^+ migration path.

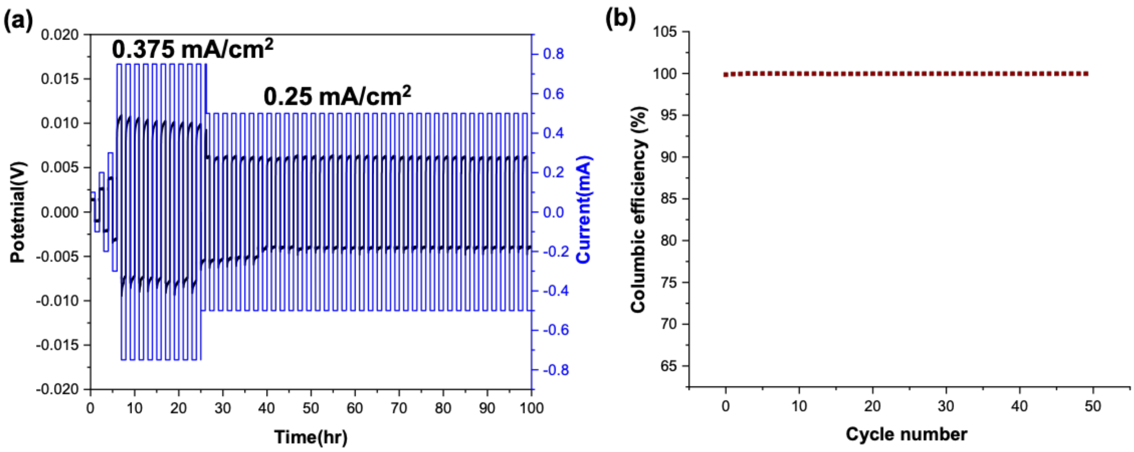

Figure 6.19. Galvanostatic cycling of Li/$Li_{3.1}AlO_2$/Li cell at ambient using various current densities of 0.05 – 0.375 mA/cm^2. a. Voltage vs. time profile, and b. columbic efficiency vs. cycle number plot of the symmetric cell.

The columbic efficiency is ~ 100 % (Figure **6.19b**), suggesting that the primary charge carrier through $Li_{3.1}AlO_2$ is Li^+ with negligible electronic conductivity. This is also supported by the electronic conductivity determined by DC polarization experiments. The electronic conductivities were calculated following the procedure described elsewhere.[66,67] Figure **6.21** shows that the stabilized current increases linearly with the step increase in voltage as expected from Ohms law. The $Li_{3.1}AlO_2$ membrane showed an average electrical conductivity of 6.7 ± 0.4 × 10^{-10} S/cm. The lithium transference number (t_{Li^+}) was calculated using equation (5).

$$t_{Li^+} = (\sigma_{Li^+}) / (\sigma_{Li^+} + \sigma_{e^-}) \qquad (5)$$

where σ_{Li^+} is the ionic conductivity of the $Li_{3.1}AlO_2$ membrane obtained from the Nyquist plot and the σ_{e^-} is the electrical conductivity deduced from the DC polarization experiments. The $Li_{3.1}AlO_2$ membrane exhibits high lithium transference number of ~1, enabling the mitigation of electrode concentration polarization.

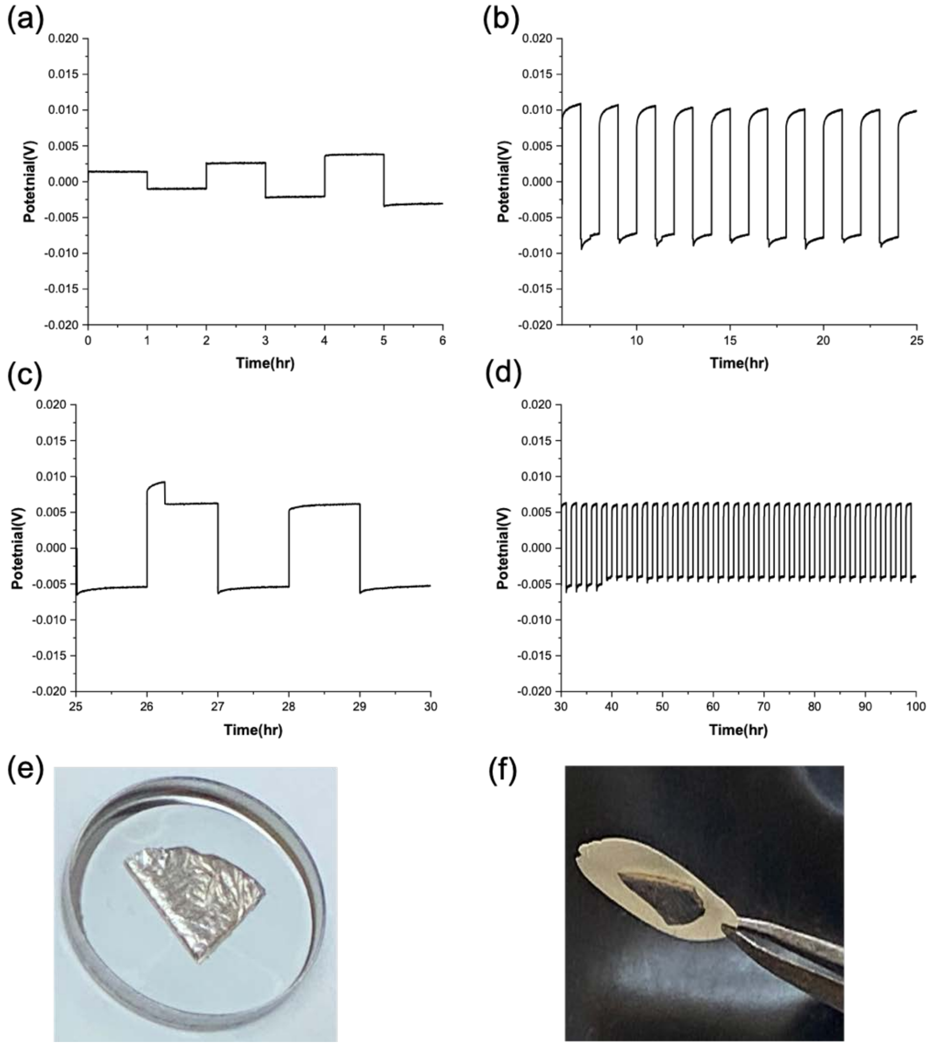

Figure 6.20. Galvanostatic cycling of Li/$Li_{3.1}AlO_2$/Li symmetric cell at a. 0.05- 0.15, b. 0.375 c. 0.375 - 0.25, and d.0.25 mA/cm^2 current densities. Optical images of Li melt bonded with $Li_{3.1}AlO_2$ membrane(e-f).

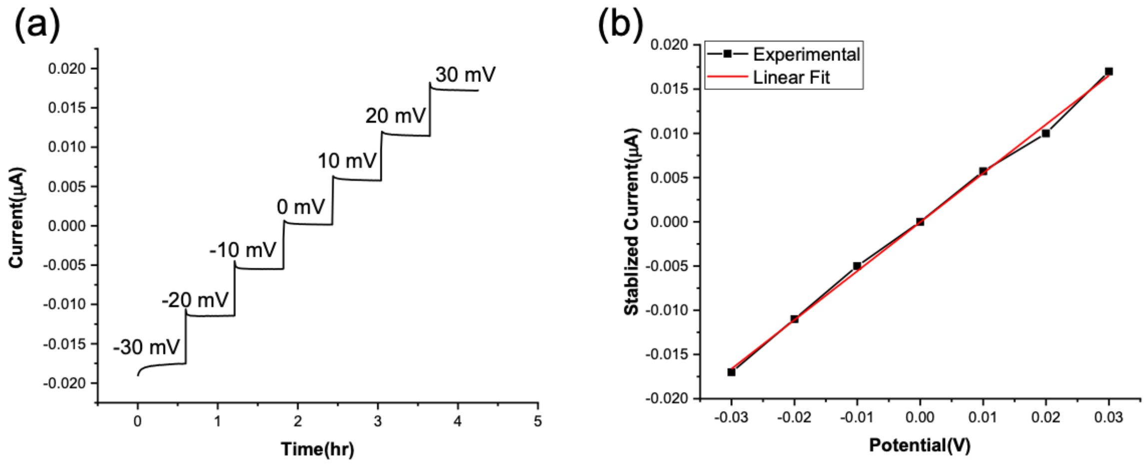

Figure 6.21. a. Time dependence of current during step voltages b. stabilized current-voltage relations of Li/$Li_{3.1}AlO_2$/Li symmetric cell.

6.3.5 $LiAlO_2$ NP coated $Li_4Ti_5O_{12}$(LTO) electrode

An additional benefit of $LiAlO_2$ solid electrolyte is that it can be used as a coating material for LIB electrodes. Even though LTO demonstrates excellent structural stability, it suffers from poor conductivity, which limits its application for high energy density Li^+ batteries. The very low electronic conductivities (< 10^{-13} S/cm) and the sluggish Li^+ diffusion coefficient of LTO result in its poor capacity. It has been demonstrated that the LTO rate capability can be improved by doping with aliovalent ions,[68] reducing particle size, and incorporating conductive additives.[69] Thus, LF-FSP produced LTO NPs were coated with $LiAlO_2$ NPs to enhance the conductivity and rate performance. Detailed electrochemical performance of LTO NPs is discussed in chapter **7**. Prior to electrode synthesis, the LTO powder, carbon black (C-65), and the $LiAlO_2$ NPs were heated to 60 °C/24 h/Vacuum. The electrode slurry was prepared by mixing LTO (80 wt.%), Carbon black (C65, 5 wt.%), $LiAlO_2$ NPs (5 wt.%), and polyvinylidene fluoride (PVDF,10 wt.%) in 1- methyl pyrrolidin-2-one. The slurry was then coated on Cu foil.

Figure **6.22** shows SEM fracture surface and EDX map images of the $LiAlO_2$ coated LTO electrode. The EDX map shows well distributed (Al, C, F, Ti, and O) ascribed to the $LiAlO_2$ electrolyte, carbon additive, PVDF binder, and LTO powder, respectively. The top interface is mainly composed of Cu from the current collector. Here, we demonstrate that it is possible to introduce $LiAlO_2$ coatings onto electrodes by simply ball-milling and tape casting method.

Furthermore, the tape-casting process permits stacking of these $LiAlO_2$/$LiAl_5O_8$ green films onto electrodes which simplifies battery design. Figure **6.23** shows the SEM and EDX fracture surface images of LTO/$LiAlO_2$ membranes. The SEM fracture surface image shows that the interface between the anode and the electrolyte is smooth and uniform. The thickness of LTO and $LiAlO_2$ is ~ 45 and 25 μm respectively.

The EDX map shows an even distribution of Al in the top layer and Ti in the bottom layer ascribed to $LiAlO_2$ and LTO respectively. The distribution of O and C is uniform throughout the anolyte electrode. This preliminary work demonstrates that the $LiAlO_2$ membranes have the potential to be assembled in ASSBs. The electrochemical performance of the $LiAlO_2$ coated LTO electrode is beyond the scope of this chapter.

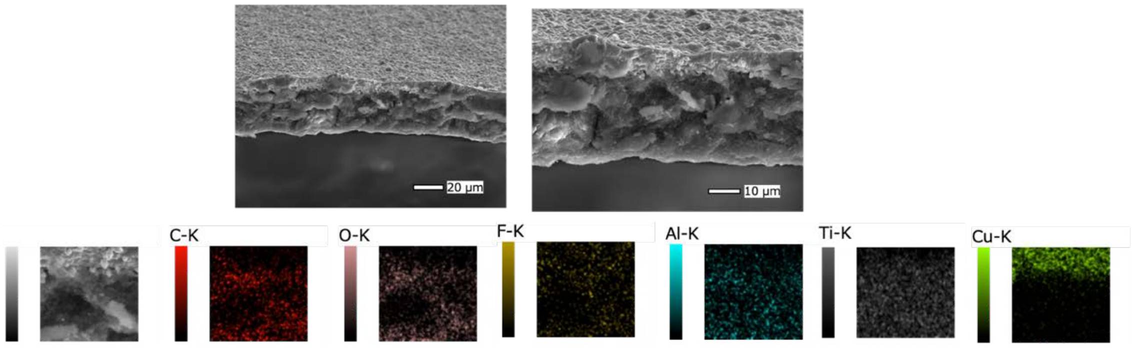

Figure 6.22. SEM fracture surface and EDX map images of $LiAlO_2$ coated LTO electrode**.**

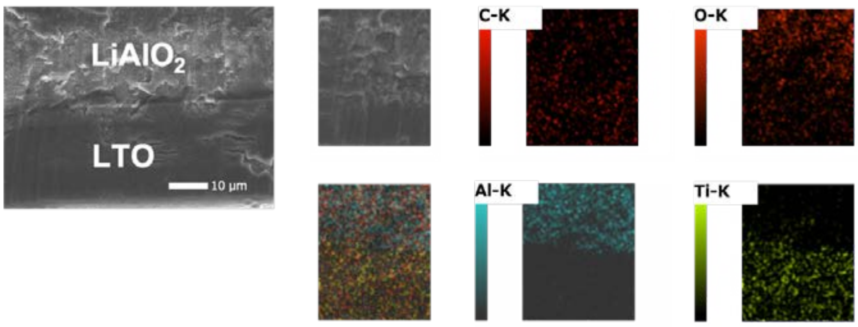

Figure 6.23. SEM and EDX fracture surface images of LTO/$LiAlO_2$ membranes.

6.4 Conclusions

Solid electrolytes are proposed as key components in developing next-generation ASSBs due to their unique merits in terms of wide operating voltage, high thermal and mechanical stability, and safety. The LF-FSP method's facility in synthesizing nanoparticles with spherical morphologies enables low temperature sintering that limits grain growth during densification leading to dense $LiAlO_2$ membranes that are thermally and chemically stable and therefor of use as coatings and electrolyte for next-generation LIBs. The new composite $LiAl_5O_8$/$LiAlO_2$ membranes offer four orders of magnitude improvement in ionic conductivity compared to pristine γ-$LiAlO_2$. This is ascribed to the decreases in the Li^+ migration barrier by incorporating a 3-D percolating network through the introduction of extrinsic defects and $LiAl_5O_8$. Long-term cycling of Li/$Li_{3.1}AlO_2$/Li symmetric cell indicate that the membrane is stable with metallic Li at current densities of 0.375 mA/cm^2.

References

(1) Goodenough, J. B.; Kim, Y. Challenges for Rechargeable Batteries. *J. Power Sources* **2011**. https://doi.org/10.1016/j.jpowsour.2010.11.074.

(2) Tarascon, J. M.; Armand, M. Issues and Challenges Facing Rechargeable Lithium Batteries. In *Materials for Sustainable Energy: A Collection of Peer-Reviewed Research and Review Articles from Nature Publishing Group*; 2010. https://doi.org/10.1142/9789814317665_0024.

(3) Manthiram, A.; Yu, X.; Wang, S. Lithium Battery Chemistries Enabled by Solid-State Electrolytes. *Nat. Rev. Mater.* **2017**, *2* (4), 16103. https://doi.org/10.1038/natrevmats.2016.103.

(4) Fergus, J. W. Ceramic and Polymeric Solid Electrolytes for Lithium-Ion Batteries. *Journal of Power Sources*. 2010. https://doi.org/10.1016/j.jpowsour.2010.01.076.

(5) Murugan, R.; Thangadurai, V.; Weppner, W. Fast Lithium Ion Conduction in Garnet-Type Li7La 3Zr2O12. *Angew. Chemie - Int. Ed.* **2007**. https://doi.org/10.1002/anie.200701144.

(6) Hu, Y.; Ruud, A.; Miikkulainen, V.; Norby, T.; Nilsen, O.; Fjellvåg, H. Electrical Characterization of Amorphous $LiAlO_2$ Thin Films Deposited by Atomic Layer Deposition. *RSC Adv.* **2016**, *6* (65), 60479–60486. https://doi.org/10.1039/C6RA03137D.

(7) Yi, E.; Wang, W.; Kieffer, J.; Laine, R. M. Flame Made Nanoparticles Permit Processing of Dense, Flexible, Li^+ Conducting Ceramic Electrolyte Thin Films of Cubic-$Li_7La_3Zr_2O_{12}$ (c-LLZO). *J. Mater. Chem. A* **2016**, *4* (33), 12947–12954. https://doi.org/10.1039/C6TA04492A.

(8) Fu, K. K.; Gong, Y.; Liu, B.; Zhu, Y.; Xu, S.; Yao, Y.; Luo, W.; Wang, C.; Lacey, S. D.; Dai, J.; Chen, Y.; Mo, Y.; Wachsman, E.; Hu, L. Toward Garnet Electrolyte–Based Li Metal Batteries: An Ultrathin, Highly Effective, Artificial Solid-State Electrolyte/Metallic Li Interface. *Sci. Adv.* **2017**. https://doi.org/10.1126/sciadv.1601659.

(9) Yi, E.; Wang, W.; Mohanty, S.; Kieffer, J.; Tamaki, R.; Laine, R. M. Materials That Can Replace Liquid Electrolytes in Li Batteries: Superionic Conductivities in Li1.7Al0.3Ti1.7Si 0.4P2.6O12. Processing Combustion Synthesized Nanopowders to Free Standing Thin Films. *J. Power Sources* **2014**, *269*, 577–588. https://doi.org/10.1016/j.jpowsour.2014.07.029.

(10) Kwon, W. J.; Kim, H.; Jung, K. N.; Cho, W.; Kim, S. H.; Lee, J. W.; Park, M. S. Enhanced Li+ Conduction in Perovskite Li3XLa2/3-X□1/3-2xTiO3 Solid-Electrolytes via Microstructural Engineering. *J. Mater. Chem. A* **2017**. https://doi.org/10.1039/c7ta00196g.

(11) Monchak, M.; Hupfer, T.; Senyshyn, A.; Boysen, H.; Chernyshov, D.; Hansen, T.; Schell, K. G.; Bucharsky, E. C.; Hoffmann, M. J.; Ehrenberg, H. Lithium Diffusion Pathway in Li1.3Al0.3Ti1.7(PO4)3 (LATP) Superionic Conductor. *Inorg. Chem.* **2016**. https://doi.org/10.1021/acs.inorgchem.5b02821.

(12) Han, X.; Gong, Y.; Fu, K.; He, X.; Hitz, G. T.; Dai, J.; Pearse, A.; Liu, B.; Wang, H.; Rubloff, G.; Mo, Y.; Thangadurai, V.; Wachsman, E. D.; Hu, L. Negating Interfacial Impedance in Garnet-Based Solid-State Li Metal Batteries. *Nat. Mater.* **2017**. https://doi.org/10.1038/nmat4821.

(13) Arbi, K.; Rojo, J. M.; Sanz, J. Lithium Mobility in Titanium Based Nasicon Li1+xTi2-XAlx(PO4)3 and LiTi2-x Zrx(PO4)3 Materials Followed by NMR and Impedance Spectroscopy. *J. Eur. Ceram. Soc.* **2007**. https://doi.org/10.1016/j.jeurceramsoc.2007.02.118.

(14) Rangasamy, E.; Wolfenstine, J.; Sakamoto, J. The Role of Al and Li Concentration on the Formation of Cubic Garnet Solid Electrolyte of Nominal Composition Li 7La 3Zr

2O 12. *Solid State Ionics* **2012**. https://doi.org/10.1016/j.ssi.2011.10.022.
(15) Liu, W.-Y.; Fu, Z.-W.; Li, C.-L.; Qin, Q.-Z. Lithium Phosphorus Oxynitride Thin Film Fabricated by a Nitrogen Plasma-Assisted Deposition of E-Beam Reaction Evaporation. *Electrochem. Solid-State Lett.* **2004**. https://doi.org/10.1149/1.1778934.
(16) Hu, Y.; Ruud, A.; Miikkulainen, V.; Norby, T.; Nilsen, O.; Fjellvåg, H. Electrical Characterization of Amorphous LiAlO2 Thin Films Deposited by Atomic Layer Deposition. *RSC Adv.* **2016**. https://doi.org/10.1039/c6ra03137d.
(17) Park, J. S.; Meng, X.; Elam, J. W.; Hao, S.; Wolverton, C.; Kim, C.; Cabana, J. Ultrathin Lithium-Ion Conducting Coatings for Increased Interfacial Stability in High Voltage Lithium-Ion Batteries. *Chem. Mater.* **2014**, *26* (10), 3128–3134. https://doi.org/10.1021/cm500512n.
(18) Choi, H. J.; Lee, J. J.; Hyun, S. H.; Lim, H. C. Phase and Microstructural Stability of Electrolyte Matrix Materials for Molten Carbonate Fuel Cells. *Fuel Cells* **2010**. https://doi.org/10.1002/fuce.200900199.
(19) Chou, M. M. C.; Chang, L.; Chen, C.; Yang, W. F.; Li, C. A.; Wu, J. J. Growth Behavior of Nonpolar GaN on the Nearly Lattice-Matched (1 0 0) γ-LiAlO2 Substrate by Chemical Vapor Deposition. *J. Cryst. Growth* **2009**. https://doi.org/10.1016/j.jcrysgro.2008.09.053.
(20) Dai, Y. M.; Wu, J. S.; Chen, C. C.; Chen, K. T. Evaluating the Optimum Operating Parameters on Transesterification Reaction for Biodiesel Production over a LiAlO2 Catalyst. *Chem. Eng. J.* **2015**. https://doi.org/10.1016/j.cej.2015.06.045.
(21) Morita, M.; Fujisaki, T.; Yoshimoto, N.; Ishikawa, M. Ionic Conductance Behavior of Polymeric Composite Solid Electrolytes Containing Lithium Aluminate. *Electrochim. Acta* **2001**. https://doi.org/10.1016/S0013-4686(00)00754-4.
(22) Zhu, B.; Liu, N.; McDowell, M.; Jin, Y.; Cui, Y.; Zhu, J. Interfacial Stabilizing Effect of ZnO on Si Anodes for Lithium Ion Battery. *Nano Energy* **2015**. https://doi.org/10.1016/j.nanoen.2015.03.019.
(23) Sun, S.; Du, C.; Qu, D.; Zhang, X.; Tang, Z. Li2ZrO3-Coated LiNi0.6Co0.2Mn0.2O2 for High-Performance Cathode Material in Lithium-Ion Battery. *Ionics (Kiel).* **2015**. https://doi.org/10.1007/s11581-015-1469-0.
(24) Ovalle-Encinia, O.; Pfeiffer, H.; Fabián-Anguiano, J. A.; Ortiz-Landeros, J. Nanosized Lithium Aluminate (γ-LiAlO2) Synthesized by EDTA-Citrate Complexing Method, Using Different Thermal Conditions. *J. Mex. Chem. Soc.* **2019**. https://doi.org/10.29356/jmcs.v63i4.1030.
(25) Cheng, J.; Guo, L.; Xu, S.; Zhang, R.; Li, C. Submicron γ-LiAlO 2 Powder Synthesized from Boehmite. *Chinese J. Chem. Eng.* **2012**. https://doi.org/10.1016/S1004-9541(11)60248-6.
(26) Xu, X.; Wen, Z.; Lin, J.; Li, N.; Wu, X. An Aqueous Gel-Casting Process for γ-LiAlO2 Ceramics. *Ceram. Int.* **2010**. https://doi.org/10.1016/j.ceramint.2009.07.017.
(27) Wen, Z.; Gu, Z.; Xu, X.; Zhu, X. Research on the Preparation, Electrical and Mechanical Properties of γ-LiAlO2 Ceramics. In *Journal of Nuclear Materials*; 2004. https://doi.org/10.1016/j.jnucmat.2004.04.230.
(28) Miikkulainen, V.; Nilsen, O.; Li, H.; King, S. W.; Laitinen, M.; Sajavaara, T.; Fjellvåg, H. Atomic Layer Deposited Lithium Aluminum Oxide: (In)Dependency of Film Properties from Pulsing Sequence. *J. Vac. Sci. Technol. A Vacuum, Surfaces, Film.* **2015**. https://doi.org/10.1116/1.4890006.
(29) Utke, I.; Hoffmann, P.; Melngailis, J. Gas-Assisted Focused Electron Beam and Ion Beam Processing and Fabrication. *J. Vac. Sci. Technol. B Microelectron. Nanom. Struct.* **2008**. https://doi.org/10.1116/1.2955728.
(30) Zhao, S.; Fu, Z.; Qin, Q. A Solid-State Electrolyte Lithium Phosphorus Oxynitride Film Prepared by Pulsed Laser Deposition. *Thin Solid Films* **2002**, *415*, 108–113. https://doi.org/10.1016/S0040-6090(02)00543-6.
(31) Zhang, X.; Temeche, E.; Laine, R. M. Design, Synthesis, and Characterization of Polymer Precursors to Li XPON and Li XSiPON Glasses: Materials That Enable All-Solid-State Batteries (ASBs). *Macromolecules* **2020**, 53(7), 2701-2712 https://doi.org/10.1021/acs.macromol.0c00254.
(32) Park, Y. J.; Kim, J. G.; Kim, M. K.; Chung, H. T.; Um, W. S.; Kim, M. H.; Kim, H. G. Fabrication of LiMn2O4 Thin Films by Sol-Gel Method for Cathode Materials of

Microbattery. *J. Power Sources* **1998**. https://doi.org/10.1016/S0378-7753(98)00133-5.
(33) Dudney, N. J. Thin Film Micro-Batteries. *Electrochem. Soc. Interface* **2008**, 17(3), 44
(34) Patil, V.; Patil, A.; Choi, J. W.; Lee, Y. P.; Yoon, Y. S.; Kim, H. J.; Yoon, S. J. LiCoO2 Thin Film Cathodes Grown by Sol-Gel Method. *J. Electroceramics* **2009**. https://doi.org/10.1007/s10832-007-9401-2.
(35) Lee, S. H.; Liu, P.; Tracy, C. E. Lithium Thin-Film Battery with a Reversed Structural Configuration SS/Li/Lipon/LixV2O5/Cu. *Electrochem. Solid-State Lett.* **2003**. https://doi.org/10.1149/1.1623171.
(36) Takeuchi, M.; Niedermaier, M.; Jansohn, M.; Umehara, N.; Laine, R. M. Processing Thin (<10¯m), Dense, Flexible ¡-Al 2 O 3 Films from Nanopowders. *J. Ceram. Soc. Japan* **2019**, *127* (2), 81–89. https://doi.org/10.2109/jcersj2.18099.
(37) Bates, J. B.; Dudney, N. J.; Gruzalski, G. R.; Zuhr, R. A.; Choudhury, A.; Luck, C. F.; Robertson, J. D. Fabrication and Characterization of Amorphous Lithium Electrolyte Thin Films and Rechargeable Thin-Film Batteries. *J. Power Sources* **1993**, *43–44*, 103–110. https://doi.org/10.1016/0378-7753(93)80106-Y.
(38) Wohlmuth, D.; Epp, V.; Bottke, P.; Hanzu, I.; Bitschnau, B.; Letofsky-Papst, I.; Kriechbaum, M.; Amenitsch, H.; Hofer, F.; Wilkening, M. Order vs. Disorder - A Huge Increase in Ionic Conductivity of Nanocrystalline LiAlO2 Embedded in an Amorphous-like Matrix of Lithium Aluminate. *J. Mater. Chem. A* **2014**. https://doi.org/10.1039/c4ta02923b.
(39) Temeche, E.; Yi, E.; Keshishian, V.; Kieffer, J.; Laine, R. M. Liquid-Feed Flame Spray Pyrolysis Derived Nanopowders (NPs) as a Route to Electrically Conducting Calcium Aluminate (12CaO.7Al2O3) Films. *J. Eur. Ceram. Soc.* **2019**, 39(4), 1263-1270. https://doi.org/10.1016/j.jeurceramsoc.2018.11.051.
(40) Yi, E.; Temeche, E.; Laine, R. M. Superionically Conducting B″-Al2O3thin Films Processed Using Flame Synthesized Nanopowders. *J. Mater. Chem. A* **2018**, 6(26), 12411-12419 https://doi.org/10.1039/c8ta02907e.
(41) Imagawa, H.; Ohta, S.; Kihira, Y.; Asaoka, T. Garnet-Type Li6.75La3Zr1.75Nb 0.25O12 Synthesized by Coprecipitation Method and Its Lithium Ion Conductivity. *Solid State Ionics* **2014**. https://doi.org/10.1016/j.ssi.2013.10.059.
(42) Chen, G.; Fu, Y. F.; Hu, K. A.; Zhang, D. Preparation of LiAlO2 Powders for the Electrolyte Matrix Material. *Shanghai Jiaotong Daxue Xuebao/Journal Shanghai Jiaotong Univ.* **2003**.
(43) Ouahdi, N.; Guillemet, S.; B. Durand; Ouatib, R. El; Rakho, L. E.; Moussa, R.; Samdi, A. Synthesis of CoAl2O4 by Double Decomposition Reaction between LiAlO2 and Molten KCoCl3. *J. Eur. Ceram. Soc.* **2008**. https://doi.org/10.1016/j.jeurceramsoc.2007.12.035.
(44) Marezio, M. The Crystal Structure and Anomalous Dispersion of γ-LiAlO 2 . *Acta Crystallogr.* **1965**. https://doi.org/10.1107/s0365110x65003511.
(45) Chou, M. M. C.; Chun Tsao, P.; Chun Huang, H. Study on Czochralski Growth and Defects of LiAlO2 Single Crystals. *J. Cryst. Growth* **2006**. https://doi.org/10.1016/j.jcrysgro.2006.04.061.
(46) Wiedemann, D.; Nakhal, S.; Rahn, J.; Witt, E.; Islam, M. M.; Zander, S.; Heitjans, P.; Schmidt, H.; Bredow, T.; Wilkening, M.; Lerch, M. Unravelling Ultraslow Lithium-Ion Diffusion in γ-LiAlO2: Experiments with Tracers, Neutrons, and Charge Carriers. *Chem. Mater.* **2016**. https://doi.org/10.1021/acs.chemmater.5b04608.
(47) Laine, R. M.; Marchal, J.; Sun, H.; Pan, X. Q. A New Y3Al5O12 Phase Produced by Liquid-Feed Flame Spray Pyrolysis (LF-FSP). *Adv. Mater.* **2005**, *17* (7), 830–833. https://doi.org/10.1002/adma.200401001.
(48) Yi, E.; Wang, W.; Kieffer, J.; Laine, R. M. Key Parameters Governing the Densification of Cubic-Li7La3Zr2O12 Li+ Conductors. *J. Power Sources* **2017**. https://doi.org/10.1016/j.jpowsour.2017.03.126.
(49) Irfan, H.; Mohamed Racik, K.; Anand, S. Microstructural Evaluation of CoAl2O4 Nanoparticles by Williamson–Hall and Size–Strain Plot Methods. *J. Asian Ceram. Soc.* **2018**. https://doi.org/10.1080/21870764.2018.1439606.
(50) Williamson, G. K.; Hall, W. H. X-Ray Line Broadening from Filed Aluminium and Wolfram. *Acta Metall.* **1953**. https://doi.org/10.1016/0001-6160(53)90006-6.

(51) Scherrer, P. Bestimmung Der Größe Und Der Inneren Struktur von Kolloidteilchen Mittels Röntgenstrahlen. *Nachrichten von der Gesellschaft der Wissenschaften zu Göttingen, Math. Klasse* **1918**.
(52) Kr Kalita, A.; Karmakar, S. Synthesis and Structural Characteristics of Fe Doped ZnO Nanoparticles at Different Molarities and Temperatures. *J. Nanosci. Technol.* **2019**. https://doi.org/10.30799/jnst.213.19050118.
(53) *Advanced Processing and Manufacturing Technologies for Structural and Multifunctional Materials*; 2007. https://doi.org/10.1002/9780470339718.
(54) Issac, I.; Heinzmann, R.; Becker, S. M.; Bräuniger, T.; Zhao-Karger, Z.; Adelhelm, C.; Kiran Chakravadhanula, V. S.; Kübel, C.; Ulrich, A. S.; Indris, S. Synthesis of Nanocrystalline Solid Solutions AlySn 1-YO2-y/2 (y = 0.57, 0.4) Investigated by XRD, 27Al/119Sn MAS NMR, and Mössbauer Spectroscopy. *RSC Adv.* **2012**. https://doi.org/10.1039/c2ra21540c.
(55) Bräuniger, T.; Jansen, M. Solid-State NMR Spectroscopy of Quadrupolar Nuclei in Inorganic Chemistry. *Zeitschrift fur Anorganische und Allgemeine Chemie*. 2013. https://doi.org/10.1002/zaac.201300102.
(56) Mo, S.; Zhang, B.; Zhang, K.; Li, S.; Pan, F. LiAl5O8 as a Potential Coating Material in Lithium-Ion Batteries: A First Principles Study. *Phys. Chem. Chem. Phys.* **2019**. https://doi.org/10.1039/c9cp02650a.
(57) Islam, M. M.; Bredow, T. Interstitial Lithium Diffusion Pathways in γ-LiAlO2: A Computational Study. *J. Phys. Chem. Lett.* **2015**. https://doi.org/10.1021/acs.jpclett.5b01780.
(58) Falco, M.; Ferrari, S.; Appetecchi, G. B.; Gerbaldi, C. Managing Transport Properties in Composite Electrodes/Electrolytes for All-Solid-State Lithium-Based Batteries. *Molecular Systems Design and Engineering*. 2019. https://doi.org/10.1039/c9me00050j.
(59) Han, J. H.; Kim, D. Y. Determination of Three-Dimensional Grain Size Distribution by Linear Intercept Measurement. *Acta Mater.* **1998**. https://doi.org/10.1016/S1359-6454(97)00442-4.
(60) KONISHI, S.; OHNO, H. Electrical Conductivity of Polycrystalline Li2SiO3 and Γ-LiAlO2. *J. Am. Ceram. Soc.* **1984**, *67* (6), 418–419. https://doi.org/10.1111/j.1151-2916.1984.tb19727.x.
(61) Park, M.; Zhang, X.; Chung, M.; Less, G. B.; Sastry, A. M. A Review of Conduction Phenomena in Li-Ion Batteries. *Journal of Power Sources*. 2010. https://doi.org/10.1016/j.jpowsour.2010.06.060.
(62) Bates, J. B.; Dudney, N. J.; Gruzalski, G. R.; Zuhr, R. A.; Choudhury, A.; Luck, C. F.; Robertson, J. D. Fabrication and Characterization of Amorphous Lithium Electrolyte Thin Films and Rechargeable Thin-Film Batteries. *J. Power Sources* **1993**. https://doi.org/10.1016/0378-7753(93)80106-Y.
(63) Indris, S.; Heitjans, P.; Uecker, R.; Roling, B. Li Ion Dynamics in a LiAlO 2 Single Crystal Studied by 7Li NMR Spectroscopy and Conductivity Measurements. *J. Phys. Chem. C* **2012**, *116* (27), 14243–14247. https://doi.org/10.1021/jp3042928.
(64) Hu, Q.; Lei, L.; Jiang, X.; Feng, Z. C.; Tang, M.; He, D. Li Ion Diffusion in LiAlO2 Investigated by Raman Spectroscopy. *Solid State Sci.* **2014**. https://doi.org/10.1016/j.solidstatesciences.2014.08.017.
(65) Glass, A. M.; Nassau, K. Lithium Ion Conduction in Rapidly Quenched Li2O-Al 2O3, Li2O-Ga2O3, and Li2O-Bi2O3 Glasses. *J. Appl. Phys.* **1980**. https://doi.org/10.1063/1.328164.
(66) Temeche, E.; Zhang, X.; Richard, M. L. *Solid Electrolytes for Li-S Batteries. Solid Solutions of Polyethylene Oxide with LixPON and LixSiPON Based Polymers*; **2020**, 12(27), 30353-30364
(67) Temeche, E.; Zhang, X.; Laine, R. M. Polymer Precursor Derived LiXPON Electrolytes: Toward Li-S Batteries. *ACS Appl. Mater. Interfaces* **2020**, 12(18) 20548-20562 https://doi.org/10.1021/acsami.0c03341.
(68) Huang, S.; Wen, Z.; Zhu, X.; Lin, Z. Effects of Dopant on the Electrochemical Performance of Li4Ti5O12 as Electrode Material for Lithium Ion Batteries. *J. Power Sources* **2007**. https://doi.org/10.1016/j.jpowsour.2006.12.010.
(69) Zhang, J.; Zhang, J.; Cai, W.; Zhang, F.; Yu, L.; Wu, Z.; Zhang, Z. Improving

Electrochemical Properties of Spinel Lithium Titanate by Incorporation of Titanium Nitride via High-Energy Ball-Milling. *J. Power Sources* **2012**. https://doi.org/10.1016/j.jpowsour.2012.03.088.

Chapter 7

Improved Electrochemical Properties of $Li_4Ti_5O_{12}$ Nanopowders (NPs)

7.1 Introduction

Lithium-ion batteries (LIBs) are used widely in portable electronics, electric vehicles, stationary power storage and a multitude of related renewable energy applications due to their high energy and power densities.[1,2] However in current designs, LIBs based on commercial carbonaceous anode materials cannot meet the fast charge capabilities required for many large-scale applications due to serious safety problems associated with high charge/discharge rates.[3,4]

Given the low galvanostatic potential (~0 vs Li^+/Li) of current graphitic anodes,[5,6] higher charging rates may cause (especially uneven) lithium plating generating internal short-circuits leading to catastrophic failure of traditional LIBs.[7,8] Thus, to enable fast charging and improve LIB safety; numerous non-carbonaceous anodes have been explored.[9–11] Among the possible alternate anode materials, LTO has been considered very promising due to its excellent thermal stability, high structural stability, good cyclability at high current densities, and negligible irreversible capacity.[12–14]

Spinel LTO anodes can accommodate up to three Li^+ ions per formula unit and deliver theoretical capacities ≈175 mAh g^{-1} without significant volume changes (<1 %) when cycled.[15–17] Graphite anodes in contrast expand up to 10 vol.% during charging.[12] LTO's negligible volume change (zero-strain) property provides high structural stability, potentially enabling high charge/discharge rates thereby improving LIBs' versatility.[12,18,19] In addition, LTO's operating potential is above the reduction potential of common electrolyte solvents (propylene carbonate and ethylene carbonate), a favorable feature for high rate and low-temperature operation.[20,21]

Unfortunately, pristine spinel LTO exhibits low electronic conductivity (10^{-13} S cm^{-1})[22] due to the Ti^{4+} valence state and a poor Li^+ diffusion coefficient (10^{-9}–10^{-14} cm^2 s^{-1}) resulting in capacity loss and poor rate capability, which limits its use in large-scale applications.[22–24] To date, several effective ways have been proposed and explored to ameliorate the electronic conductivity and Li^+ diffusivity.[12,25–27]

The most common method focuses on doping with metallic (Cr^{3+}, Ca^{2+}, Ga^{3+}, Mg^{2+}, Ta^{5+} and Al^{3+})[28–31] and non-metallic (Br^-, Cl^-, and F^-)[32–34] ions to increase lattice electrical conductivity through partial reduction of Ti^{4+} to Ti^{3+}.

Great efforts have also been made to increase the surface electrical conductivity of LTO through surface modifications via conductive coatings.[35–38] Although carbon-coatings offer a very efficient way to improve LTO anode rate capabilities, they also decrease LTO cell volumetric energy densities.[12,39] Furthermore, fabrication of uniform and optimized carbon coated LTO using economically facile techniques remains challenging.[12]

Syntheses of nano LTO particles including nanorods, nanotubes, and nanowires offers an efficient strategy to improve LTO electrochemical performance.[40–42] It is well-known that nanostructured active materials can facilitate both electron and Li^+ transport by shortening diffusion pathways and providing excess surface lithium storage owing to their small sizes and large surface areas.[2,27] In addition, LTO NPs will have larger contact area between electrolyte and electrode, resulting in improved intercalation kinetics. These phenomena contribute to enhance the rate capabilities of nanostructured LTO compared to bulk LTO. Multiple synthesis methods have been explored in efforts to prepare spinel LTO including sol-gel, hydrothermal synthesis, solution-combustion, and spray pyrolysis.[43–46] However, these routes often offer low yields, involve complicated procedures, high costs, and toxic precursors and byproducts detracting from commercialization practicality.

Therefore, the synthesis of nanoscale LTO materials with controlled morphologies, phase purity, and using low-cost methods is highly desirable for assembly of LTO batteries. This provides the motivation to prepare LTO NPs using liquid-feed flame spray pyrolysis (LF-FSP).

Recent publications indicate that modification of LTO particles by introducing appropriate amounts of solid electrolytes [$LiAlO_2$, $Li_{1.3}Al_{0.3}Ti_{1.7}(PO_4)_3$ (LATP), and $Li_{0.33}La_{0.56}TiO_3$] is an effective, low-cost route to enhance the electronic and ionic conductivities of LTO anodes.[24,39,47] Thus, Han et al[24] reported that added LATP can coat and/or bridge LTO particles, thereby facilitating both Li^+ migration from electrolyte to LTO and electron transfer from LTO to a Cu current collector by virtue of its high ionic (6.2×10^{-5} S/cm)[48] and electronic conductivities (5×10^{-11} S/cm).[49] However, these studies use solid-state reaction methods (calcining >700 °C) to synthesize LTO-solid electrolyte composites, which makes it difficult to obtain nanostructured LTO particles as a result of particle necking.

Recently, we demonstrated that LF-FSP derived $LiAlO_2$ ceramic electrolytes offer optimal ionic conductivities (~10^{-6} S/cm) and electronic conductivities of 6.7 x 10^{-10} S/cm at ambient, both three orders of magnitude higher than those reported for LTO (Table **7.1**).[50] With this background, LTO-$LiAlO_2$ composite anodes with high rate performance were synthesized using simple ball-milling.

Table 7.1. Ionic and electronic conductivities of LTO, $LiAlO_2$, Li_6SiON at room temperature.

Compounds	Ionic conductivity (S/cm)	Electronic conductivity (S/cm)	Ref
LTO	10^{-13} - 10^{-9}	< 10^{-13}	22,23
$LiAlO_2$	10^{-6}	10^{-10}	50
Li_6SiON	10^{-6}	10^{-7}	51

We also reported the synthesis and characterization of a novel polymer electrolyte (Li_6SiON) starting from rice hull ash (RHA), an agricultural waste, providing a green route to all-solid-state batteries (Scheme **7.1**).[51] In our efforts to synthesize the Li_6SiON polymer electrolyte, we realized that it might also be possible to use this precursor to coat LTO NPs. The Li_6SiON electrolyte offers a room temperature (Table **7.1**) ionic conductivity of 10^{-6} S/cm and electrical conductivity of 10^{-7} S/cm 6 orders of magnitude greater than that of LTO.

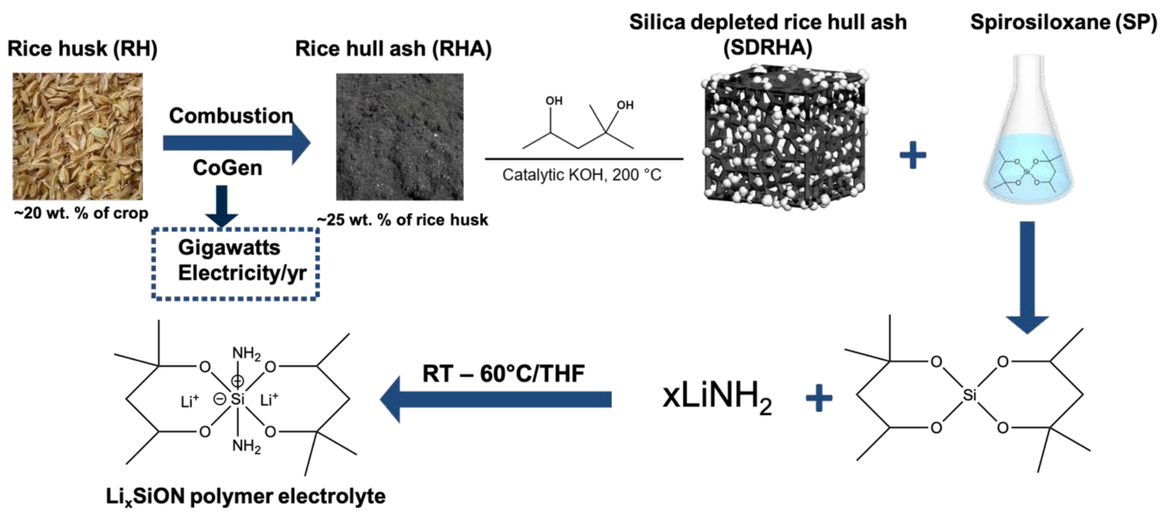

Scheme 7.1. Synthesis of Li_xSiON polymer electrolyte.

On the basis of the above considerations, in this work, we synthesized high surface area (~38 m^2/g) spinel LTO NPs using LF-FSP, which eliminates traditional solid-state reaction steps (i.e. glass forming, grinding, and ball milling). In addition, LF-FSP derived LTO NPs are agglomerated but not aggregated which is highly desirable for facile dispersion and tape-casting. To optimize the ionic and electronic conductivity of LTO anodes, the LTO was mixed with flame made $LiAlO_2$ NPs (APS = 64 nm, 5 and 10 wt.%) and coated with Li_6SiON polymer precursors (5 and 10 wt.%).

To the best of our knowledge, this is the first time three component composite anodes, e.g. LTO-$LiAlO_2$-Li_6SiON have been explored as an approach to improving LTO rate capabilities. The composite anode delivered a reversible capacity of 260 and 140 mAh/g at 0.5 and 10 C, over 90 cycles respectively. The modified LTO NPs were characterized via XRD, XPS, SEM, EIS and performance tests, as described in the following sections.

7.2 Experimental section

Materials

Lithium hydroxide monohydrate ($LiOH \cdot H_2O$) and propionic acid [(CH_3CH_2COOH), 99%] were purchased from Sigma-Aldrich (Milwaukee, WI). Titanium isopropoxide [$Ti(OiPr)_4$] and Hexane were purchased from Fischer Scientific (Pittsburgh, PA). Absolute ethanol was purchased from Decon Labs (King of Prussia, PA).

RHA was provided by Wadham Energy LP (Williams, CA). The solvent and reactants, 2-Methyl-2,4-pentanediol (hexylene glycol, HG) and lithium amide ($LiNH_2$) were purchased from Acros Organics. Lithium metal foil (~750 μm), polyvinylidene fluoride [PVDF, (Mw ~ 534 kg/mol)], sodium hydroxide (NaOH), hydrochloric acid (HCl), and tetrahydrofuran (THF) were purchased from Sigma-Aldrich (St louis, MO). Super C65 conductive powder (~ 62 m^2/g), Celgard 2400 separator (~25 μm), and coin cell parts were purchased from MTI Corporation (Richmond, CA). The mixed solvent of ethylene carbonate (EC), dimethyl carbonate (DMC), and Ethyl methyl carbonate (EMC) (1 : 1 : 1 wt.%) containing 1 M $LiPF_6$ as the Li salt with the addition of 10 wt.% fluoroethylene carbonate (FEC) was purchased from Soulbrain (Northville, MI). THF was distilled over sodium benzophenone ketyl prior to use. All other chemicals were used as received.

7.2.1 Synthesis of LTO NPs

Titanatrane {$Ti(OCH_2CH_2)_3N[OCH_2CH_2N(CH_2CH_2OH)_2]$} and lithium propionate ($LiO_2CCH_2CH_3$) were synthesized as described in previous work.[52]

Lithium propionate (26.5 g) and titanatrane (236. 8 g) were dissolved in anhydrous ethanol (1650 ml) to give a 3 wt.% ceramic yield solution. To avoid the loss of lithium during the combustion process, excess lithium propionate (100 wt.%) was used. The resulting precursor solution was aerosolized with oxygen into a combustion chamber where the LF-FSP was ignited with CH_4/O_2 pilot torches.

The as-produced LTO NPs were then collected downstream in a parallel set of rod-in-tube electrostatic precipitators (ESP) operating between 5-10 kV. Detail description of LF-FSP process can be found elsewhere.[53]

The as-produced LTO NPs (10 g) were dispersed in anhydrous ethanol (350 mL) with 2 wt.% polyacrylic acid as a dispersant using an ultrasonic horn (Vibra-cell VC 505 Sonics & Mater. Inc.) operating at 100 W for 10-15 min. The suspension was left to settle for 5 h to remove impurities and allow larger particles to settle. Thereafter, the supernatant was decanted, and the recovered LTO NPs were dried at 100 °C/24 h. To further remove impurities, the dried LTO NPs were then heated to 700 °C/2 h/O_2, hereafter referred to as pristine LTO.

7.2.2 Preparation of LTO/$LiAlO_2$/Li_6SiON composites

$LiAlO_2$ NPs were also synthesized using LF-FSP as described in our previous work.[50] Recently, we have described the direct extraction of silica from RHA as the spirosiloxane, [SP = $(C_6H_6O_2)_2Si$], which in turn can be reacted with $xLiNH_2$ to provide in short periods Li_xSiON (x = 2, 4, and 6) polymers with varying Li and N contents as shown in Scheme **7.1**. The Li_6SiON product is almost fully soluble and stable in THF which makes it easier to coat LTO NPs, offering a simple and cos-effective green synthesis route to fabricate composite electrodes.

In our effort to improve the ionic and electronic conductivity of LTO, composite anodes were processed by adding selected wt.% $LiAlO_2$ solid electrolyte and Li_6SiON polymer electrolyte during electrode formulation. Table **7.2** lists the target compositions of the electrode systems assessed here.

Table 7.2. Lists of pristine and composite electrodes (wt.%).

Electrodes	$LiAlO_2$ (wt.%)	Li_6SiON (wt.%)
LTO	0	0
LTO-5$LiAlO_2$	5	0
LTO-10$LiAlO_2$	10	0
LTO-5Li_6SiON	0	5
LTO-10Li_6SiON	0	10
LTO-5$LiAlO_2$-5Li_6SiON	5	5
LTO-5$LiAlO_2$-10Li_6SiON	5	10
LTO-10$LiAlO_2$-5Li_6SiON	10	5
LTO-10$LiAlO_2$-10Li_6SiON	10	10

The LTO and $LiAlO_2$ NPs (5 and 10 wt.%) were dry ground for ~30 min/air to ensure uniform mixing. The LTO-$LiAlO_2$ mixtures, dispersed in anhydrous ethanol (5 ml), were ball-milled for 24 h using ZrO_2 beads (6 g) in 20 ml vial under nitrogen. The slurries were then dried at 100 °C/24 h/vacuum.

In a separate step, LTO NPs and Li_6SiON polymer precursor (5 and 10 wt.%) dissolved in THF were mixed using an ultrasonic operating at 100 W for 5 -10 min. The recovered mixtures were then dried at 100 °C/24 h/vacuum. To evaluate the synergistic effects of the $LiAlO_2$ and Li_6SiON electrolytes, composite electrodes are synthesized by mixing the LTO-$LiAlO_2$ powders with LTO-Li_6SiON powders. Scheme **7.2** depicts the preparation of the LTO-composite anode systems.

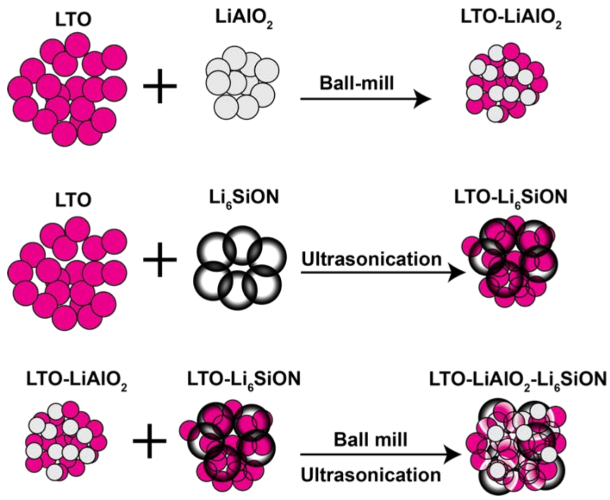

Scheme 7.2. Schematic representation of the preparation of the LTO-composite anodes.

Prior to electrode synthesis, pristine LTO and carbon black (C-65) were heated to 100 °C/24 h/vacuum to remove trace moisture. Electrode slurries were prepared by mixing pristine LTO or LTO composites (80 wt.%), C65, (10 wt.%), and polyvinylidene fluoride [PVDF, (10 wt.%)] in 1-methyl pyrrolidin-2-one. The mixtures were ultrasonicated for 10-15 min/N_2 to form homogenous slurries. The mixtures were then ball milled for 24 h using ZrO_2 beads (6 g) in 20 ml vials. The slurries were then coated on Cu foils. The films were dried at 80 °C/12 h/vacuum and cut into 8 mm discs, and thermo-pressed at 40-50 MPa/50 °C/5 min using a heated bench top press (Carver, Inc.) to improve packing density. The electrodes have areal loading densities ranging from 3-4 mg/cm^2. Half-cells were assembled with LTO composite electrodes and a lithium metal anode separated by porous polypropylene film (Celgard 2300, 9 mm radius). Prior to cell assembly, the metallic Li (16 mm W X 750 μm T) was scraped to expose a clean surface. The electrolyte system was 1.1 M $LiPF_6$ mixed solvent (1:1:1 wt.% ratio) EC:DEC:EMC with 10 wt. % FEC. The 2032 coin cells were compressed using digital pressure controlled electric crimper (MSK-160E, MTI Corporation).

7.3 Results and discussion

In the following sections, we first characterize the pristine LTO NPs and composite anodes by XRD, FTIR, SEM, and TGA. In the second part, we discuss the electrochemical properties of half-cells assembled using the LTO-composite electrodes. The effect of the $LiAlO_2$ solid electrolyte and Li_6SiON polymer electrolyte additives on the rate performance of the LTO were also investigated.

7.3.1 Structure and morphology characterization

Figure **7.1** shows the XRD powder pattern of as-produced LTO NP composed primarily of spinel LTO phase (92 wt.%). Weak diffraction peaks ~ 27.6° and 55.5° 2θ can be assigned to TiO_2 rutile phase and the small peak~ 20.3° 2θ is attributed to Li_2TiO_3.[54] The Figure **7.1** broad peaks at low 2θ angles decrease and the intensity of the peak corresponding to Li_2TiO_3 decrease on heating the LTO NPs to 700 °C, suggesting formation of phase pure spinel LTO without impurities.

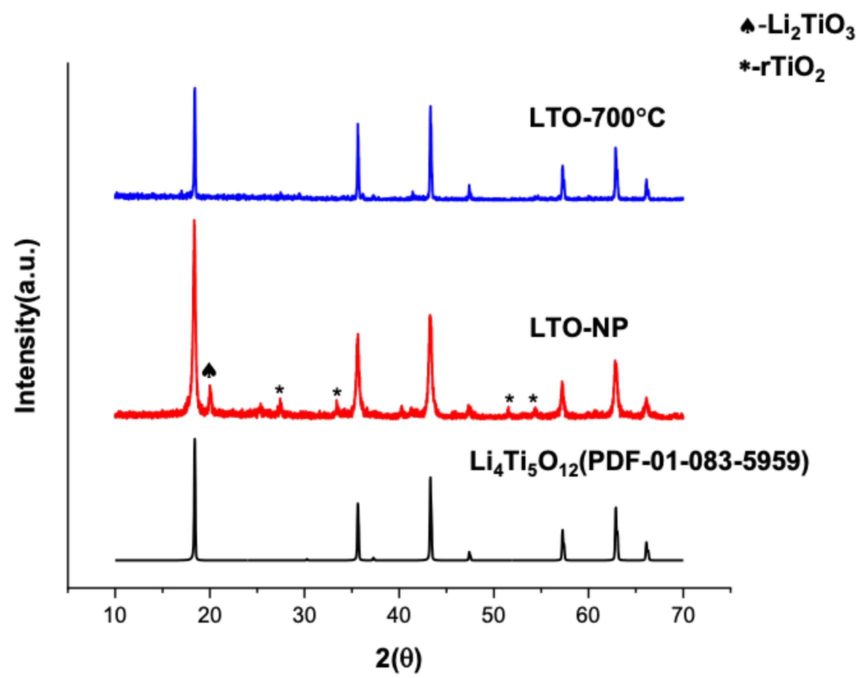

Figure 7.1.XRD plots of LTO NP and LTO heated to 700 °C/2 h/N_2.

The XRD powder patterns of pristine LTO, LTO-$LiAlO_2$, LTO-Li_6SiON composites are shown in Figure **7.2**. The diffraction patterns of pristine LTO and LTO-5$LiAlO_2$ samples are similar with all the peaks indexable to the Fd3-m space group with a cubic lattice.[47] However, additional diffraction peaks related to $LiAlO_2$ are observed for the LTO-10$LiAlO_2$ powder (Figure **7.2a**). The broad and low-intensity peak ~ 21° and the doublet peaks ~ 34° 2θ can be indexed to γ-$LiAlO_2$ (PDF:04-009-6438).

However, no obvious lattice fringes corresponding to $LiAlO_2$ are found due to its low content and the fact that the LTO-$LiAlO_2$ composite powder was produced through a simple ball-milling without any heat treatment.

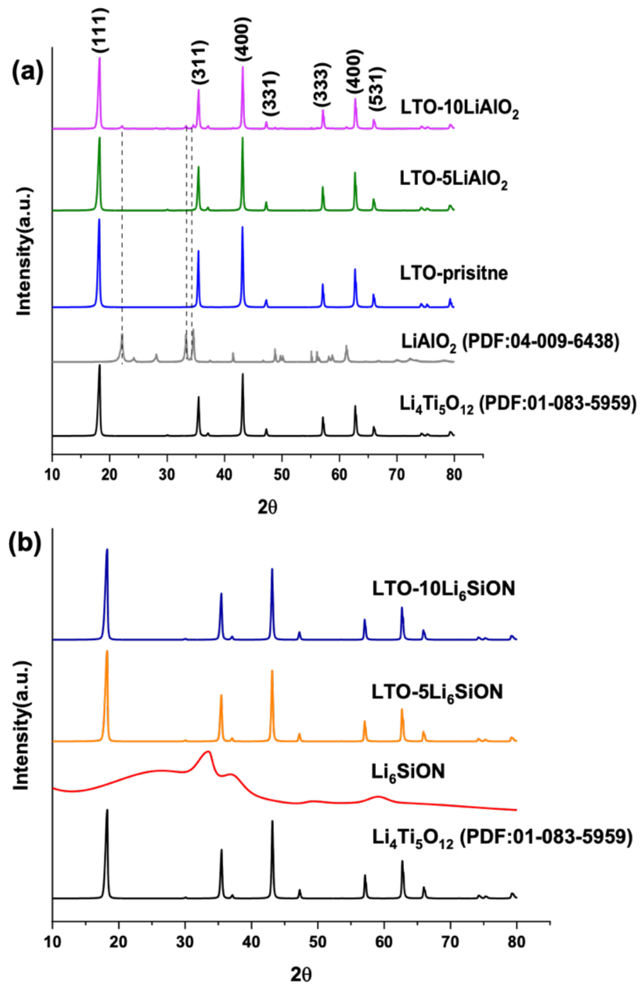

Figure 7.2. XRD plots of (a) pristine LTO, LTO-$LiAlO_2$, and (b) LTO-Li_6SiON powders.

Figure **7.2b** shows the XRD plot of the Li_6SiON powder heated to 100 °C/12 h/vacuum. The broad peak centered ~ 35° 2θ suggests the absence of any ordered crystalline structure.[51] Amorphous Li_6SiON generates no discernible diffraction peaks in the LTO-Li_6SiON composite powder. The XRD patterns of LTO-$LiAlO_2$-Li_6SiON composite powders are presented in Figure **7.3**. The lattice parameters for the LTO-$LiAlO_2$-Li_6SiON (a = 8.362 Å) powder are essentially the same as those of pristine material (8.364 Å).

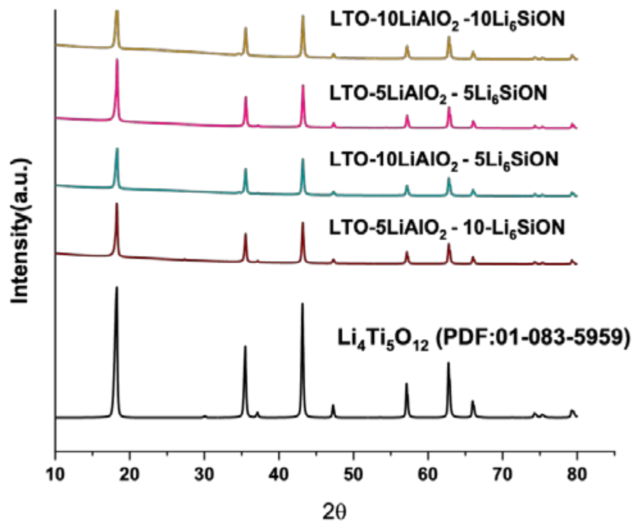

Figure 7.3. XRD plots of LTO-$LiAlO_2$-Li_6SiON powders

The FTIR spectra of pristine LTO, and LTO-composite powders are shown in Figure **7.4**. The spectra of all samples change slightly with addition of $LiAlO_2$ and Li_6SiON polymer electrolytes. The broad peak ~1450-1500 cm^{-1} corresponds to carbonate νC=O, typical for LF-FSP derived powders.[50] The two broad absorption bands centered at 650 and 465 cm^{-1}, respectively, are due to the symmetric and asymmetric stretching vibrations of the octahedral groups [MO_6] lattice, confirming the presence of spinel LTO.[55]

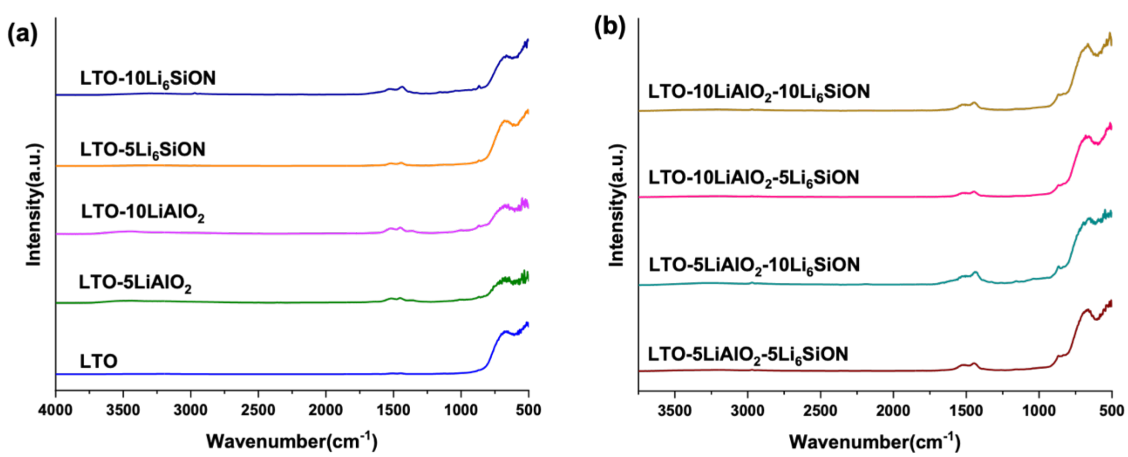

Figure 7.4. FTIR spectra of (a) pristine LTO, LTO-$LiAlO_2$, LTO-Li_6SiON, and (b) LTO-$LiAlO_2$-Li_6SiON powders.

High performance LTO anodes are available using nanostructured materials because such materials offer larger contact areas with electrolyte, shorter diffusion distances for Li^+ and electrons, and excess near-surface lithium storage in comparison with micron-size LTO anodes.[27,41] The solid-state reaction method is simple; however, product quality is not satisfactory due to particle inhomogeneities, large APSs, and irregular morphologies. In contrast, we are able to the design and prepare uniform, nanoscale LTO electrodes for high performance applications.

Figure **7.5** shows SEMs of pristine LTO, LTO-composite powders. Powder morphologies of the pristine LTO (Figure **7.5a**) and LTO-$LiAlO_2$ (Figure **7.5 b-c**) are similar agglomerates with uniform APSs < 60 nm. Table **7.3** lists the SSAs and APSs of the LTO-composite powders.

As noted above, high surface area is an important characteristic of nanostructured materials. The BET SSA of pristine LTO is 37 ± 0.8 m^2/g. The calculated APS using the BET surface area is ~ 46 nm for the pristine LTO. The LTO-10$LiAlO_2$ sample shows a slight decrease to 31 m^2/g and increase in APS (54 nm) attributed to the relatively larger $LiAlO_2$ APS of 64 nm.[50]

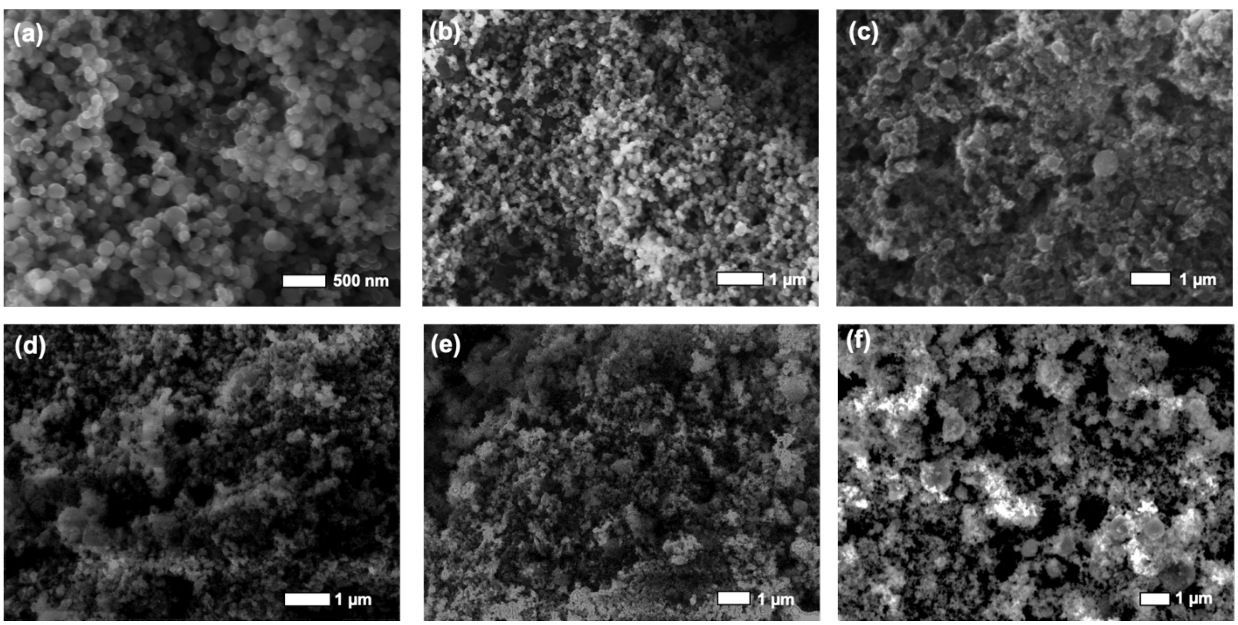

Figure 7.5. SEM images of pristine LTO (a), LTO-5$LiAlO_2$ (b), LTO-10$LiAlO_2$ (c), LTO-5Li_6SiON (d), LTO-10Li_6SiON(e), and LTO-10$LiAlO_2$-10Li_6SiON (f) powders.

Table 7.3. Lists of SSAs and APSs of the LTO-composite powders.

Electrodes	SSA(m^2/g)	APS (nm)
LTO	37 ± 0.8	46
LTO-5$LiAlO_2$	35 ± 0.2	48
LTO-10$LiAlO_2$	31 ± 0.5	54
LTO-5Li_6SiON	36 ± 0.3	47
LTO-10Li_6SiON	37 ± 0.8	47

Figure 7.5 **d-e** shows highly dispersed small particles on the LTO particles, which indicates that the polymer electrolyte is coated on the LTO particles, supporting the EDX studies presented below. The powder surface morphology of the LTO-10$LiAlO_2$-10Li_6SiON composite reveals denser particle accumulation attributed to the electrolyte additives.

The thermal stability of the composite powders was investigated by TGA. Figure **7.6** shows representative TGA plots (700 °C/10°C min^{-1}/N_2) for pristine LTO and LTO-composite powders. The mass losses below 250 °C are attributed to physi/chemisorbed water on the surfaces of the LTO-$LiAlO_2$ composite powders. The LTO-Li_6SiON composite powder exhibits relatively larger mass loss (8 wt.%) from 100 °- 450 °C ascribed to evaporation/or decomposition of organics. Figure **7.6c** TGA confirms the expected ceramic yield of the LTO-composite powders, matching the theoretical ceramic yield calculated using the rule of mixtures.

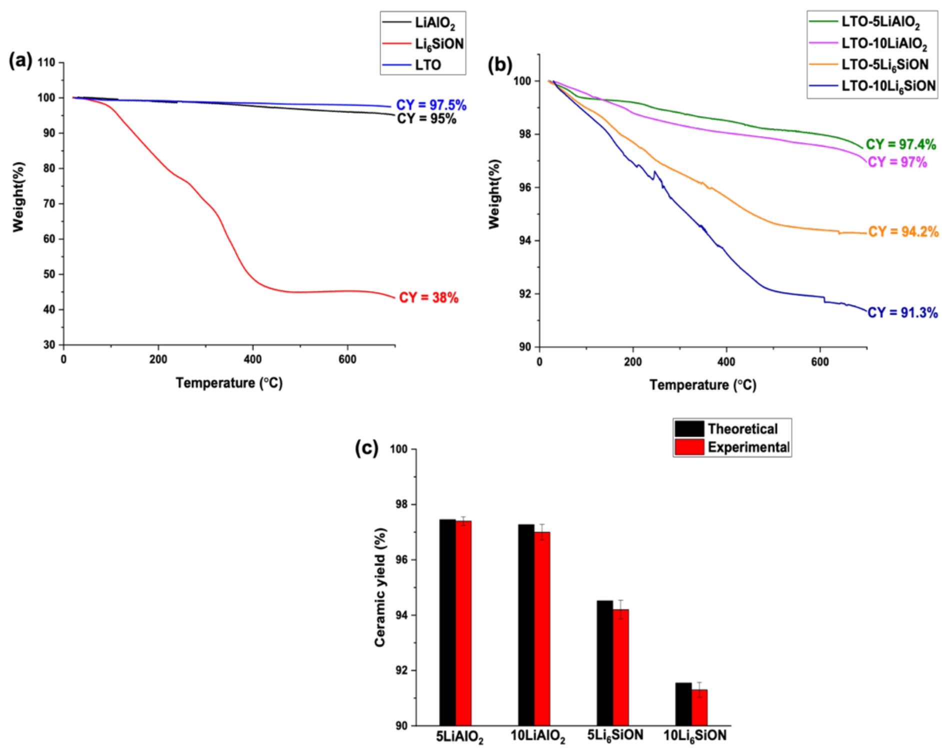

Figure 7.6. TGA (700 °C/10°C min^{-1}/N_2) of (a) pristine LTO, $LiAlO_2$, Li_6SiON, and (b) LTO-$LiAlO_2$ and LTO-Li_6SiON powders.

7.3.2 Surface characterization

The surface chemical composition and binding energies of the pristine LTO and LTO-composite electrodes were analyzed by XPS. The survey spectra (Figure **7.7a**) reveal signature peaks (Li, Ti, C, and O) for the pristine LTO, LTO-composite electrodes. All electrodes show a small F 1s peak (2.3-3.5 At. %) ascribed to the presence of PVDF. The resulting deduced elements from XPS are listed in Table **7.4** and **7.5.**

Table 7.4. XPS analysis of pristine LTO, LTO-$LiAlO_2$ electrodes.

Elements	Binding energy (eV)	At. %		
		LTO-pristine	LTO-5$LiAlO_2$	LTO-10$LiAlO_2$
F 1s	685	2.3	2.6	2.4
O 1s	526	18.2	19.1	16
Ti 2p	455	5.6	6.3	6
C 1s	281	27.1	21	20
Al 2p	70	-	3.3	7.3
Li 1s	58	46.8	47.7	48.3

Table 7.5. XPS analysis of pristine LTO, LTO-Li_6SiON electrodes.

Elements	Binding energy (eV)	At. %	
		LTO -5Li_6SiON	LTO-10Li_6SiON
F 1s	685	3.5	2.85
O 1s	526	16	14.5
Ti 2p	455	5.8	6.6
N 1s	397	-	3.2
C 1s	281	25.6	22.75
Si 2p	99	1.9	2.3
Li 1s	58	47.2	47.8

Figure **7.7b** presents high resolution XPS spectra of electrode Ti 2p. Deconvoluted peaks are centered at ~ 464.4 and 458.5 eV corresponding to the Ti $2P_{1/2}$ and Ti $2P_{3/2}$ core level binding energies of Ti^{4+} of spinel $Li_4Ti_5O_{12}$, respectively.[24,27] No noticeable change is observed in the Ti 2p core peak for the pristine LTO and LTO-$LiAlO_2$ electrodes. The Ti $2p_{3/2}$ peak seems to shift slightly to higher binding energy (459 eV) for the LTO-Li_6SiON electrode compared to the pristine LTO electrode. This suggests that introducing the polymer electrolyte changes bonding at the LTO surface. Figure **7.8** shows the deconvolution of Ti 2p peak for the pristine LTO and LTO-composite electrodes. The Ti^{3+} contents at $2p_{1/2}$ increase to 10.2 and 15.7 % for the LTO-5Li_6SiON and LTO-10Li_6SiON electrodes, respectively, which are much higher than the content in pristine LTO electrode. (4.2 wt.%). This suggests that Ti^{4+} partial reduction to Ti^{3+} during the coating process. As noted above, the presence of Ti^{3+} in LTO can effectively improve electron-hole concentrations enhancing bulk electrical conductivity.[12,29] As a consequence, the LTO-Li_6SiON electrode exhibits superior electrical conductivity as discussed below.

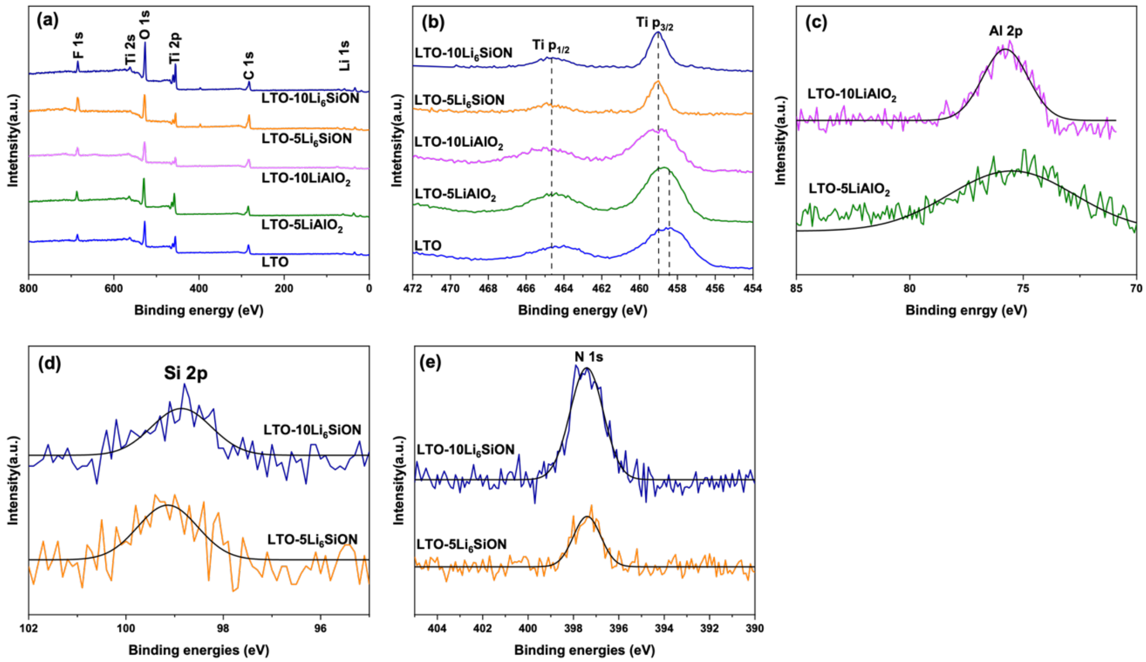

Figure 7.7.XPS survey spectra(a), core level spectra of Ti 2p (b), Al 2p (c), Si 2p (d), and N 1s (e) for LTO, LTO-$LiAlO_2$ and LTO-Li_6SiON electrodes.

The core level spectra of Al 2p (74.8 eV) peak increases with increasing $LiAlO_2$ content (10 wt.%), a consequence of $LiAlO_2$ particles associated with the surface of LTO particles (Figure **7.7c**). The core level spectra of Si 2p (99 eV) is similar in shape and peak position for the LTO electrode coated with 5 and 10 wt.% Li_6SiON polymer electrolytes as shown in Figure **7.7d**. The overall atomic concentration of N (Figure **7.7e)** increases with the introduction of 10 wt.% Li_6SiON, suggesting that the surface of the LTO particles is coated uniformly with the polymer electrolyte.

The survey spectra (Figure **7.9**) reveal signature peaks (Li, Ti, C, and O) for the LTO-$LiAlO_2$-Li_6SiON electrodes, while Al, Si, and N peaks are detected in the LTO composite electrodes ascribed to the presence of $LiAlO_2$ and Li_6SiON powders. The XPS derived compositions are listed in Table **7.6**.

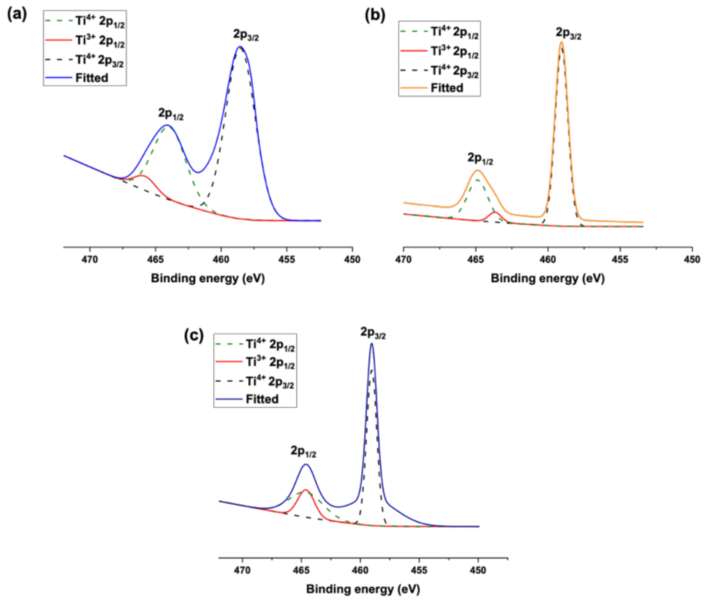

Figure 7.8. Ti 2p core XPS spectra of (a)pristine LTO (b) LTO-5Li_6SiON and (c) LTO-10Li_6SiON electrodes.

Table 7.6. XPS analysis of LTO-5$LiAlO_2$+ Li_6SiON (5 and 10 wt.%) electrodes.

	Binding energy (eV)	At. %	
Elements		LTO-5$LiAlO_2$-5 Li_6SiON	LTO-5$LiAlO_2$-10Li_6SiON
F 1s	684	5.6	4.8
O 1s	527	22.5	16.1
Ti 2p	455	5.1	6.6
N 1s	397	1	1
C 1s	281	32.2	32.7
Si 2p	99	1.3	1.5
Al 2p	73	4.8	6.2
Li 1s	58	27.5	31.1

Figure **7.10a** shows SEMs and EDX mapping of the pristine LTO electrode revealing a relatively porous microstructure. The EDX map shows well-distributed signature elements (C, O, F, and Ti), supporting the XPS studies. The elemental map of F results from the binder PVDF.

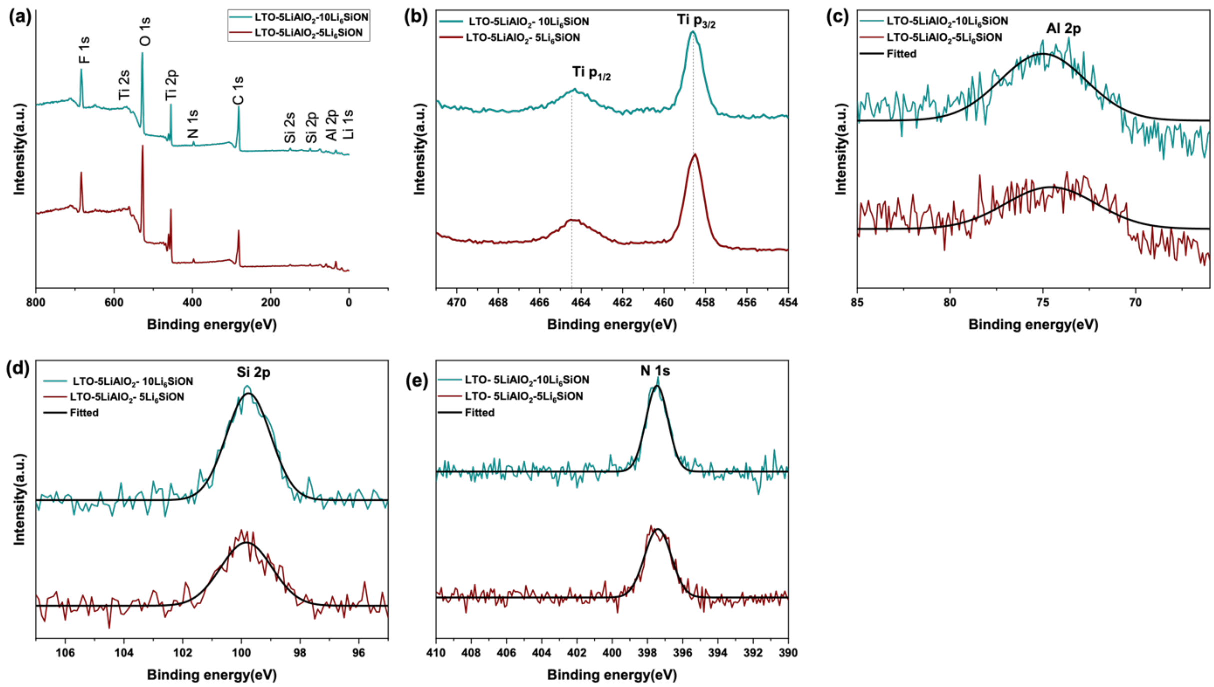

Figure 7.9. XPS survey spectra(a), core level spectra of Ti 2p (b), Al 2p (c), Si 2p (d), and N 1s (e) LTO-LiAlO$_2$-Li$_6$SiON electrodes.

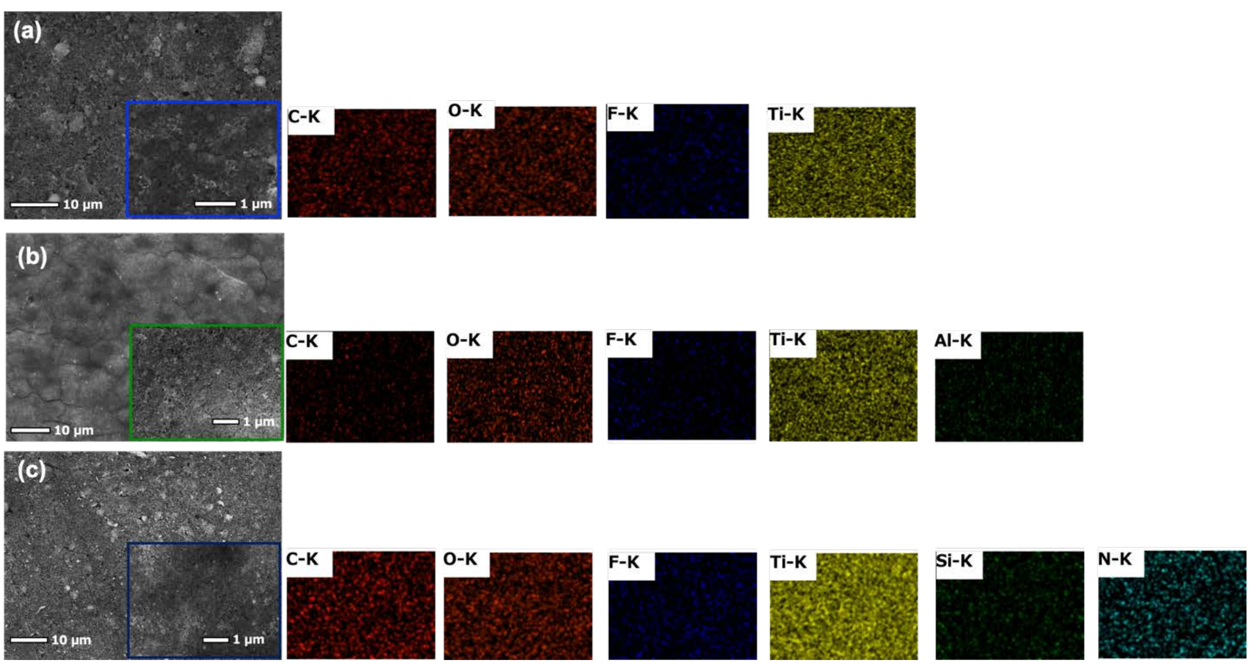

Figure 7.10. SEM and EDX images for the pristine LTO (a), LTO-5LiAlO$_2$ (b), and LTO-10Li$_6$SiON(c) electrodes.

Figure **7.10b** shows SEMs and EDX mapping of an LTO-5$LiAlO_2$ electrode revealing a relatively dense microstructure. The LTO-5$LiAlO_2$ electrode seems to offer a smoother morphology compared to the electrode with higher $LiAlO_2$ content. Careful examination of the 10 wt.% $LiAlO_2$ modified electrode reveals some uneven $LiAlO_2$ coatings (Figure **7.11a**). This might be ascribed to incomplete dispersion of the active particles with higher $LiAlO_2$ content. The EDX map shows well-distributed signature elements (C, O, Ti, F, and Al). The Al elemental map is also uniform for LTO-5$LiAlO_2$ in good agreement with the XPS data. Table **7.7** lists the deduced atomic percentages based on EDX analyses for the LTO electrodes. As expected, the Al At. % increased with increasing $LiAlO_2$ content.

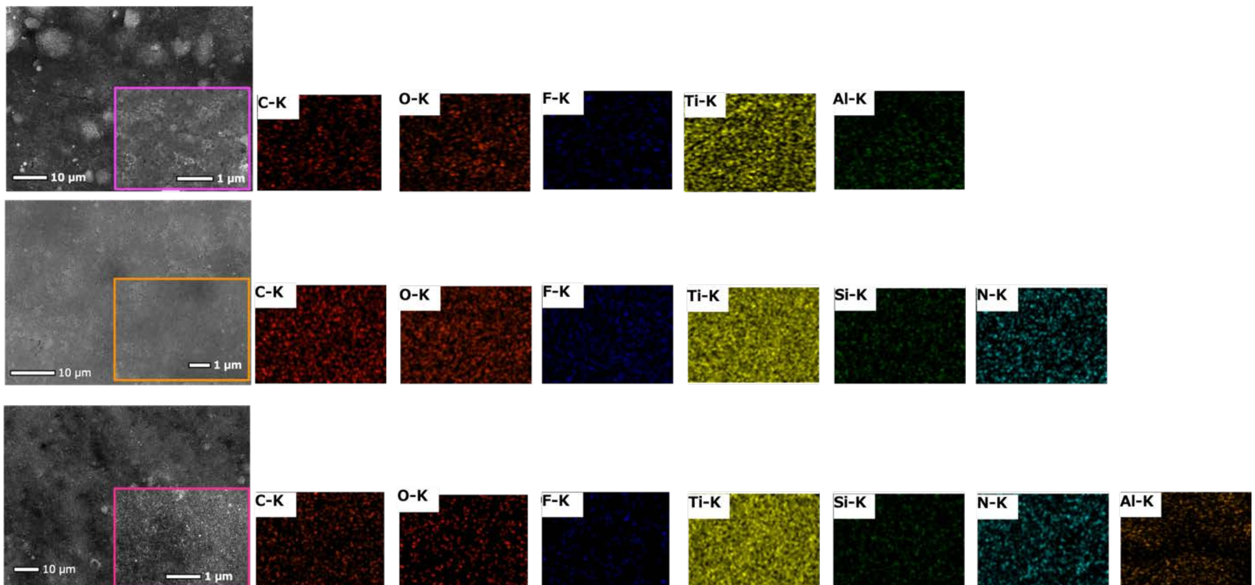

Figure 7.11. SEM and EDX images for the pristine LTO-10$LiAlO_2$ (a), LTO-5Li_6SiON (b), and (c) LTO-10$LiAlO_2$-5Li_6SiON electrodes.

Table 7.7. Average atomic percentage (At. %) based on EDX analysis for LTO-composite electrodes.

Electrodes	At. %						
	C	F	O	Ti	Al	Si	N
LTO-pristine	29.7	6.3	48.4	15.6	-		
LTO-5$LiAlO_2$	29.6	4.9	47.5	16.8	1.2		
LTO-10$LiAlO_2$	28.3	7.0	50.3	12	2.4		
LTO-5Li_6SiON	23.7	8.2	52.5	13	-	1.4	1.2
LTO-10Li_6SiON	23.1	7.5	50	15.4	-	2.2	1.8

Figures **7.10c** and **7.11b** show SEM and EDX images of LTO + 5 and 10 wt.% Li_6SiON electrodes, respectively. The Si and N elemental maps indicate uniform distributions for both electrodes in good agreement with the XPS data. As expected, the Si and N At. % increase with increased Li_6SiON content.

The LTO-Li_6SiON electrodes show a relatively denser microstructure. Several notable experiments have demonstrated that the rate performance depends strongly on the composition of additives, binder types, and degree of electrode compaction.[56] Besides being an additive with superior ionic and electronic conductivities, the Li_6SiON polymer electrolyte can behave like a binder promoting intimate contact between the active material and the current collector. These properties strongly enhance the LTO rate performance as discussed below.

7.3.3 Electrochemical performance

Electrochemical impedance spectroscopy (EIS) was performed on the LTO composite electrode-Li half-cells before cycling. The corresponding Nyquist plots are presented in Figures **7.12a** and **c**. The impedance curves were fitted with the modified Randle-Ershler equivalent circuit model (Figure **7.13**). The intersection of the Nyquist plot with the Z' axis; the ohmic resistance (R_s), is a measure of the internal resistance of electrode and electrolyte. The charge transfer resistance (R_{ct}) is associated with the semicircle in the intermediate frequency region. Warburg impedance (W) is the solid-state diffusion resistance, reflected in the sloped line in the low frequency-region. The constant phase elements (CPE) are ascribed to the double-layer capacitance. The diffusion coefficient (D_{Li}) of lithium-ion can be calculated from the plots in the low-frequency region. The equation for the calculation of D_{Li} values by EIS can be expressed as[39]:

$$Z_{re} = R_{ct} + R_s + \sigma\omega^{-1/2} \qquad (1)$$

$$\omega = 2\pi f \qquad (2)$$

$$D_{Li} = \frac{R^2T^2}{2A^2n^4F^2{C_{Li}}^2\sigma^2} \qquad (3)$$

Where R is the gas constant, T is the absolute temperature, F is the Faraday constant, A is the area of the electrode, n is the number of electrons per molecule during oxidation, C_{Li} is the concentration of Li^+ in solid, ω is the angular frequency, f is the frequency, and σ is the Warburg factor which is related to Zre obtained from the slope of the line in Figures **7.12b** and **d**.

All the Nyquist spectra (Figures **7.12 a** and **c**) consist of a semicircle in the high frequency region and an inclined line in the low frequency region. The high frequency intercept of the semicircle (R_{ct}) reflects the electrochemical activity at the interface and electron/ion conductivity. The inclined line attributed to W, is related to the diffusion of the Li^+ into the bulk of the electrode material. Appropriate $LiAlO_2$ (5 wt. %) and Li_6SiON (10 wt. %) modification improves the conduction of the spinel $Li_4Ti_5O_{12}$ material; evident from Figure **7.12**.

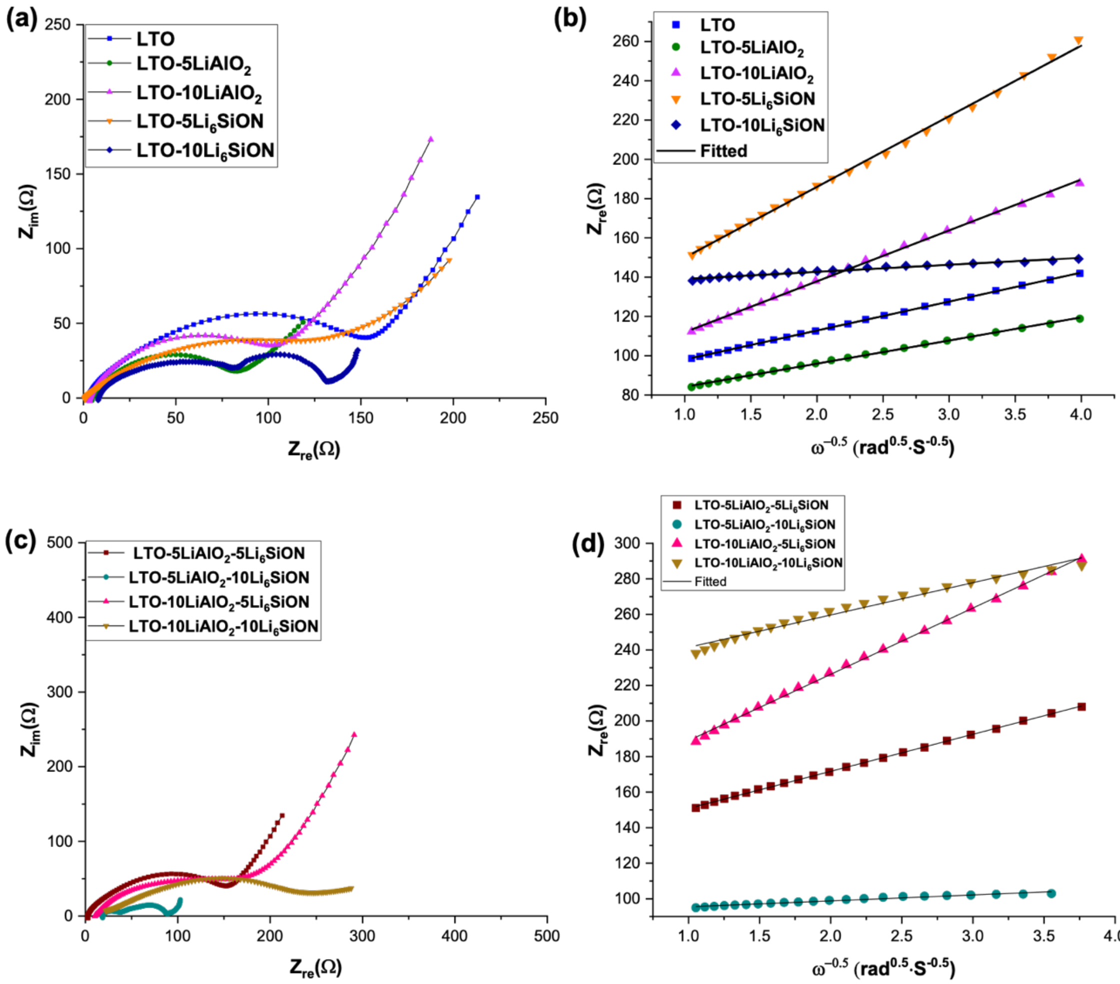

Figure 7.12. Nyquist plot of LTO composite – Li half-cell (a and c), and graph of Z_{re} plotted against $\omega^{-0.5}$ at a low-frequency region (b and d). The dotted line represents the experimental value and the solid line indicates the fitted data.

This indicates that the appropriate $LiAlO_2$ modification enhances LTO conductivity and decreases charge transfer resistance, suggesting that the LTO-$LiAlO_2$ composite (5 wt. %) may have better electrochemical activity and kinetic behavior than pristine LTO during cycling.

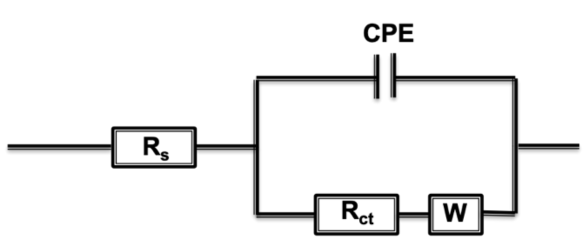

Figure 7.13. Randle-Ershler equivalent circuit model was used to fit the Nyquist plot.

However, a dramatic increase in charge transfer resistance is noted for the LTO-10$LiAlO_2$ composite compared to the pristine LTO and LTO-5$LiAlO_2$ electrode. It is likely the high $LiAlO_2$ content (10 wt. %) provides a thicker barrier to Li^+ ion transport at the LTO surface limiting both electronic and ionic conduction. This is supported by the Figure **7.14** CV data. The Li^+ diffusivity result can be compared (Table **7.8**) to reported LTO-$LiAlO_2$ and LTO−$Li_{0.33}La_{0.56}TiO_3$ composite electrodes.[39,47]

Table 7.8. Comparison of Li^+ diffusivities for various LTO-composite electrodes.

Electrodes	D_{Li}(cm^2/s)	Ref
LTO-$LiAlO_2$ (5 wt.%)	1.19 x10^{-13}	1
LTO-$LiAlO_2$ (10 wt.%)	3.51 x10^{-15}	1
LTO-$Li_{0.33}La_{0.56}TiO_3$ (5 wt.%)	1.92 x10^{-14}	2
LTO-$Li_{0.33}La_{0.56}TiO_3$ (10 wt.%)	1.23 x10^{-14}	2

The calculated Li^+ diffusion coefficients for pristine LTO, LTO-$LiAlO_2$, and LTO-Li_6SiON are listed in Table **7.9**. LTO-5$LiAlO_2$-10Li_6SiON has the highest diffusion coefficient (~2.7 x 10^{-12}) among the LTO electrodes reported here. This study demonstrates that introduction of an appropriate amount of electrolyte has a positive effect on the electrochemical performance of LTO with the increase in electronic conductivity and Li^+ diffusivity.

Table 7.9. List of diffusivities and potential gap for pristine and composite LTO electrodes.

Electrodes	DLi(cm2/s)	$\Delta\varphi$p (mV)
LTO-pristine	4.6 ± 0.5 x 10^{-14}	400
LTO-5$LiAlO_2$	6.1 ± 0.7 x 10^{-13}	340
LTO-10$LiAlO_2$	4.8 ± 0.2 x 10^{-14}	410
LTO-5Li_6SiON	6.7 ± 0.6 x 10^{-14}	380
LTO-10Li6SiON	1.2 ± 0.3 x 10^{-12}	320
LTO-5$LiAlO_2$ - 5Li_6SiON	2.3 ± 0.3 x 10^{-13}	300
LTO-5$LiAlO_2$ -10Li_6SiON	2.7 ± 0.3 x 10^{-12}	290
LTO-10$LiAlO_2$ - 5Li_6SiON	3.0 ± 0.5 x 10^{-14}	350
LTO-10$LiAlO_2$ - 10Li_6SiON	1.3 ± 0.6 x 10^{-14}	370

As shown in Figure **7.14a**, CV curves were measured at a scan rate of 1 mV/s between 0 and 2.5 V (vs. Li/Li^+). A pair of typical cathodic/anodic peaks are observed ~ 1.8/1.5 V for all samples, which is the characteristic of two-phase redox reaction mechanism of LTO ($Li_4Ti_5O_{12} + 3Li^+ + 3e^- \rightleftarrows Li_7Ti_5O_{12}$). This suggests that the introduction of $LiAlO_2$ and Li_6SiON polymer electrolyte does not change LTO electrochemistry (Figure **7.14b**). In addition, another pair of weak redox peaks in the range 0.4–0.6 V is attributed to the multistep restoration of Ti^{4+}.[57]

This is ascribed to the insertion of additional Li^+ ions into rock salt-structured ($Li_7Ti_5O_{12}$) to form quasi-rock-salt ($Li_{8.5}Ti_5O_{12}$) and reduce all of the $Ti^{4+}$to Ti^{3+}.[58]

Table **7.9** also lists the peak parameters of the various electrodes from the CV plots. The degree of polarization of the electrode is reflected in the potential difference between anodic and cathodic peaks. LTO-5$LiAlO_2$-10Li_6SiON exhibits the smallest potential gap ($\Delta\varphi_p$ = 0.29 V) between reduction and oxidation peaks compared to the pristine LTO electrode (($\Delta\varphi_p$ = 0.4 V). This suggests that the composite electrode has lower electrochemical polarization and better diffusion kinetics than pristine LTO. This could be attributed to faster Li^+ and electron transfer processes imparted by the ceramic and polymer electrolyte additives. This is consistent with the excellent rate capability of the LTO-5$LiAlO_2$-10Li_6SiON composite electrode.

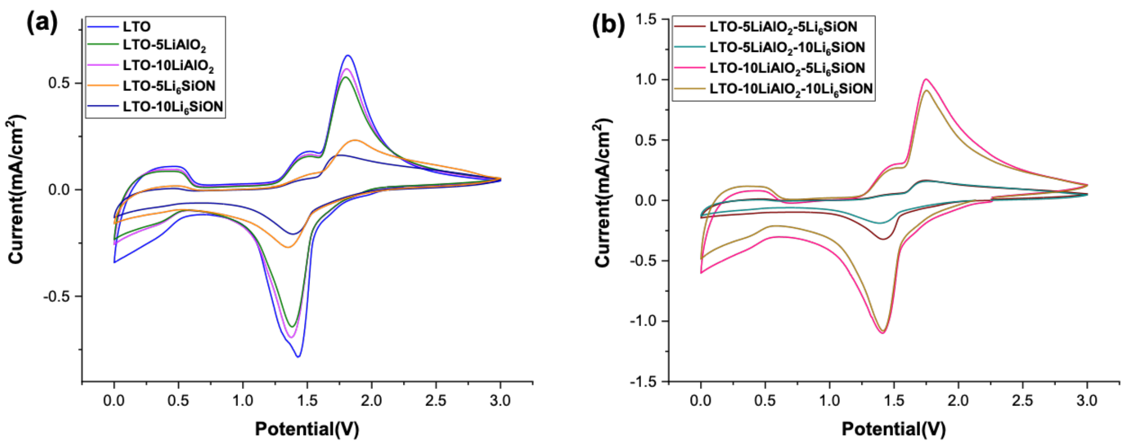

Figure 7.14. Cyclic voltammograms of the pristine LTO, LTO-$LiAlO_2$, and LTO-Li_6SiON (a), and LTO-$LiAlO_2$-Li_6SiON(b) half-cells.

The electrochemical performance of pristine LTO, LTO-$LiAlO_2$, LTO-Li_6SiON, and LTO-$LiAlO_2$-Li_6SiON electrodes was evaluated by galvanostatic discharge/charge testing at different C-rates (0.5, 1 and 5C) between 1 and 2.5 V. Pristine LTO (Figure **7.15a**) shows an initial discharge capacity of ~180 mAh/g at 0.5 C. The reversible capacity at 0.5 C rate is ~ 154 mAh/g after 100 cycles, which is 88 % of the theoretical capacity. This is consistent with previous reports and corresponds to the transformation of $Li_4Ti_5O_{12}$ to $Li_7Ti_5O_{12}$.[12]

Cells were further tested at 5C to explore stability at high rates. The discharge capacity for pristine LTO half-cell decreases to ~125 mAh/g at 5 C. However, capacities for LTO-5$LiAlO_2$ and LTO-10Li_6SiON fade slowly remaining stable at 146 and 160 mAh/g at 5C, respectively. The

LTO-5$LiAlO_2$-10Li_6SiON exhibits a discharge capacity (~140 mAh/g) at 5C. On the whole, the LTO-Li_6SiON and LTO-$LiAlO_2$ electrodes reveal enhanced rate capacity relative to pristine LTO.

After 100 cycles, the specific capacities are 155±0.7, 142±1.4, 156±0.5, and 162±0.2 mAh/g at 0.5C for the half-cells assembled with LTO-5$LiAlO_2$, LTO-10$LiAlO_2$, LTO-5Li_6SiON, LTO-10Li_6SiON electrodes, respectively. The reversible capacities of LTO-Li_6SiON decrease slowly compared to LTO-$LiAlO_2$, and pristine LTO electrodes. However, the LTO-10$LiAlO_2$-5Li_6SiON and LTO-10$LiAlO_2$-10Li_6SiON composite electrodes show relatively low discharge capacities of 127 and 131 mAh/g after 100 cycles.

To understand the reason why the capacities of the LTO−10$LiAlO_2$-5Li_6SiON and LTO−10$LiAlO_2$-10Li_6SiON (Figure **7.15b**) drop abruptly, the discharge/charge curves for the selected cycles are displayed in Figure **7.15**. The polarization degree of the electrode is explored by calculating the potential difference (ΔE) between charge and discharge plateaus. As presented in Figures **7.16** and **7.17,** the ΔE of LTO−10$LiAlO_2$-10Li_6SiON increases gradually with increasing cycle number ($\Delta E \sim 70$ mV), indicating relatively higher degrees of polarization compared to LTO−5$LiAlO_2$-10Li_6SiON electrode ($\Delta E \sim 50$ mV) after 70 cycles. This might be ascribed to the larger amount of $LiAlO_2$, which significantly reduces the content of electrochemical active material LTO, resulting in the observed low capacity retention. This is consistent with what is reported in literature for LTO-$LiAlO_2$ (10 wt.%) composite electrodes.[47] In addition, as discussed above in the diffusivity section, the LTO-10$LiAlO_2$-10Li_6SiON composite did not show as high a Li^+ diffusivity coefficient when compared to the LTO-5$LiAlO_2$-10Li_6SiON electrode.

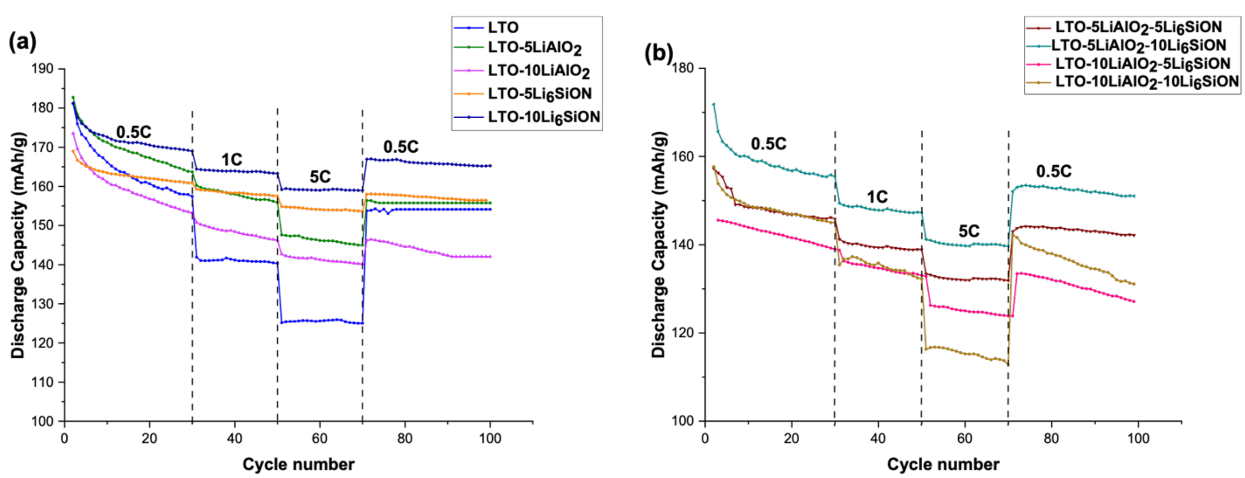

Figure 7.15. Cycling performance of the pristine LTO, LTO-$LiAlO_2$, and LTO-Li_6SiON (a), and LTO-$LiAlO_2$-Li_6SiON(b) half-cells cycled between 1 – 2.5V.

Figure **7.18** shows the rate performance of the pristine LTO and LTO-composite electrodes cycled in the range of 0.01-2.5 V. The initial discharge capacity of all samples exceeds the theoretical capacity (260 mAh/g) of LTO. The extra capacity could be attributed to the formation of a solid electrolyte interface (SEI), composed of organic lithium alkyl carbonates at the surface, and trapped Li^+ in the conductive additive carbon black. The LTO electrodes (Figure **7.18a**) display excellent cycling stability for both cut-off voltages (0.01 and 1V), suggesting the process for the extra lithiation beyond $Li_7Ti_5O_{12}$ is highly reversible.

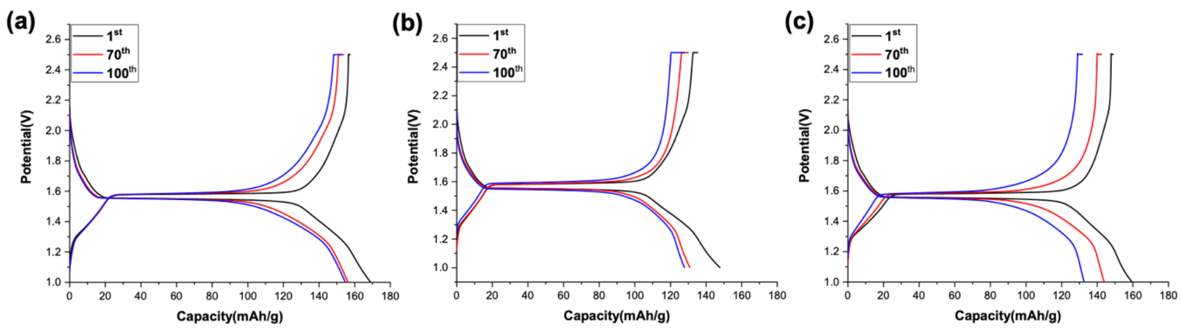

Figure 7.16. Potential vs. capacity plots at selected cycle numbers for half-cells assembled with (a) LTO-5$LiAlO_2$-10Li_6SiON, (b) LTO-10$LiAlO_2$-5Li_6SiON, and (c) LTO-10$LiAlO_2$-10Li_6SiON electrodes.

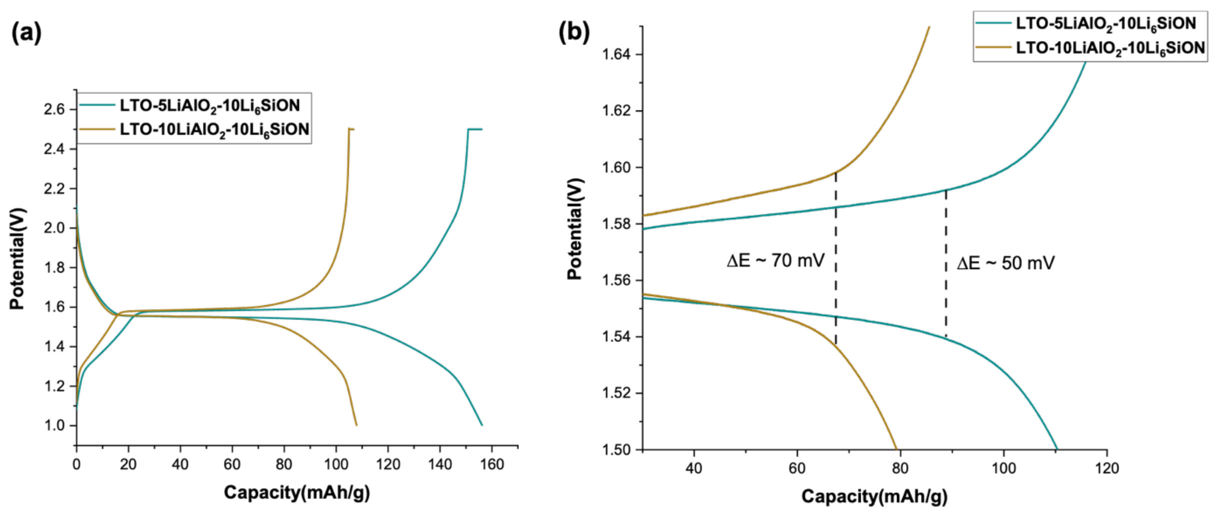

Figure 7.17. (a) Potential vs. capacity plots at 70 cycles and (b) enlarged charge-discharge curves of LTO-$LiAlO_2$-Li_6SiON electrodes.

The reversible capacities of LTO-5$LiAlO_2$-10Li_6SiON (260 mAh/g) and LTO-10Li_6SiON (231 mAh/g) are much higher than those of pristine LTO electrodes (202 mAh/g) at 0.5C as shown in Figure **7.18b**. LTO-5$LiAlO_2$-10Li_6SiON maintains a high discharge capacity of 255 mAh/g at

0.5C, which is much higher than the pristine LTO (185 mAh/g) after 90 cycles. At 10 C charge/discharge rate, the LTO-10Li_6SiON shows the highest discharge capacity of 190 mAh/g. The LTO-5$LiAlO_2$ also delivered high discharge capacity of 174 mAh/g, which is more than double the capacity obtained for the pristine LTO (70 mAh/g). The introduction of appropriate amounts of $LiAlO_2$ NPs shortens diffusion distances for Li^+ and electrons, increases the contact interface with electrolyte and provides abundant surface Li^+ storage sites, or excess near-surface Li^+ storage.

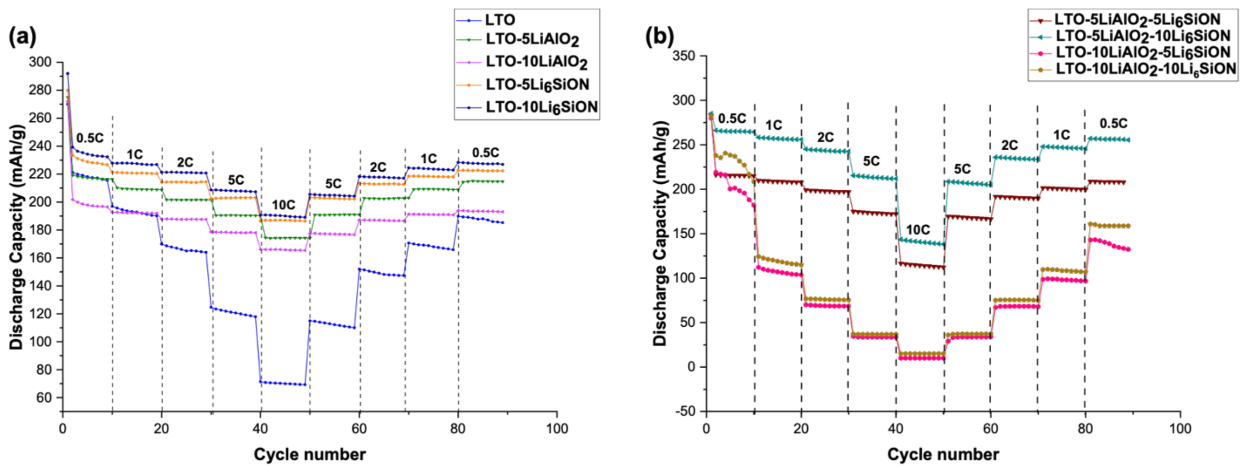

Figure 7.18. Cycling performance of the pristine LTO, LTO-$LiAlO_2$, and LTO-Li_6SiON (a), and LTO-$LiAlO_2$-Li_6SiON (b) half-cells cycled between 0.01 – 2.5V.

Figure **7.19** compares the rate performance of pristine LTO and LTO composite electrodes cycled with different voltage windows at various current densities. The LTO-pristine half-cell cycled between 1.0 – 2.5 V potential range (Figure **7.19a**) exhibited a stable average capacity of 160 mAh/g at 0.5C after 100 cycles. The pristine LTO half-cell was also discharged to 0.01V delivering a reversible capacity of 202 mAh/g and 120 mAh/g at 0.5C and 5C as shown in Figure **7.19b**, respectively. These electrochemical results indicate that LF-FSP derived LTO powders enable high rate performance at different discharge voltage ranges.

Figure **7.19 a-b** shows that the LTO-10$LiAlO_2$-5Li_6SiON and LTO-10$LiAlO_2$-10Li_6SiON composite electrodes show poor discharge capacities compared to the pristine LTO electrode when discharged to different voltages. This suggests that $LiAlO_2$ has a strong impact on the rate capability of LTO-composite electrodes. Hence, it is important that optimal content of $LiAlO_2$ (5 wt.%) is introduced to achieve superior cell performance.

Compared with pristine LTO, $Li_4Ti_5O_{12}$-$LiAlO_2$ (5wt.%),[47] and $Li_4Ti_5O_{12}$-$Li_{0.33}La_{0.56}TiO_3$ (5wt.%)[39] composites prepared by solid-state methods, the rate performance of LF-FSP derived LTO-5$LiAlO_2$-10Li_6SiON composite electrodes is much higher in the range of 0.01-2.5 V at higher C-rates (Table **7.10**). This clearly indicates that moderate modification of LTO particle surfaces is substantially beneficial to rate performance.

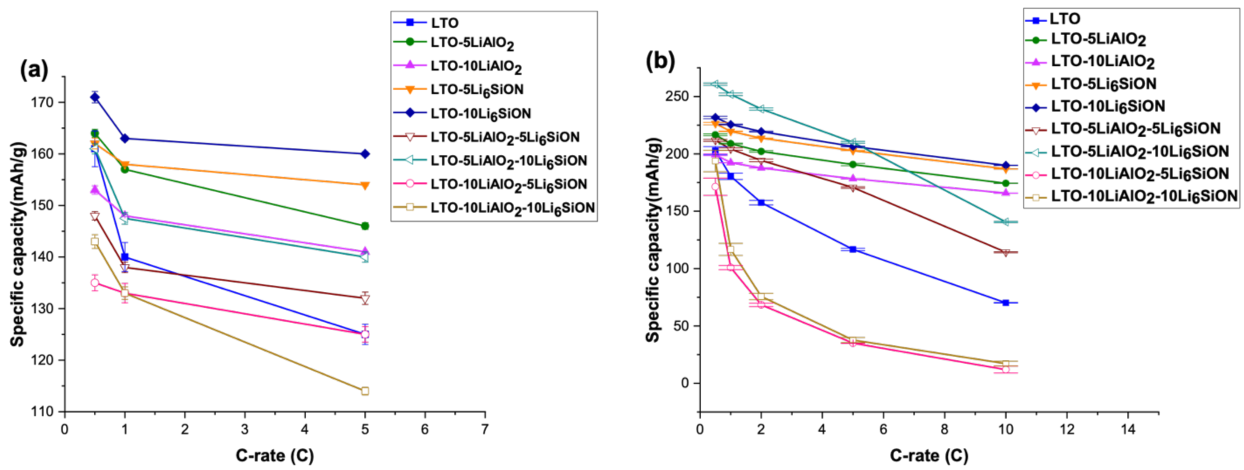

Figure 7.19. Comparison of discharge capacities of the various electrodes cycled between 1.0 -2.5 V (a) and 0.01 – 2.5 V (b) at selected c-rates.

Table 7.10. Comparison of discharge capacities of LTO-composite anode materials at 5C.

Electrodes	Discharge capacities (mAh/g)	Ref
LTO-$LiAlO_2$ (5 wt.%)	127	47
LTO-$LiAlO_2$ (10 wt.%)	~50	47
LTO-$Li_{0.33}La_{0.56}TiO_3$ (5 wt.%)	146	39
LTO-$Li_{0.33}La_{0.56}TiO_3$ (10 wt.%)	137	39
$Li_4Ti_{4.9}La_{0.1}O_{12}$	181	60
LTO-TiO_2	117	61
LTO-TiO_2/C	140	62
LTO-5$LiAlO_2$	190	This work
LTO-10Li_6SiON	206	This work
LTO-5$LiAlO_2$-10Li_6SiON	210	This work

Figure **7.20** show the Nyquist plots of the half-cells in delithation state after 100 cycles. Table **7.11** lists the electrolyte resistance (R_e) and charge transfer impedance (R_{ct}) of these half-cells. The R_{ct} values of LTO-5$LiAlO_2$-10Li_6SiON decreases markedly, suggesting improved charge transfer due to the introduction of polymer electrolyte with higher electronic conductivity than pristine LTO anode. Zhang et al[59] suggest that local charge disequilibrium promote the electron transfer; thus, the modification of LTO surface improves the electronic conductivity.

Table 7.11. List of impedance values for pristine and composite LTO-Li half-cells.

Electrodes	Re(Ω)	Rct(Ω)
LTO-pristine	3.5	60
LTO-5$LiAlO_2$	2.8	6
LTO-10$LiAlO_2$	3.3	75
LTO-5Li_6SiON	3.8	20
LTO-10Li_6SiON	3.6	15
LTO-5$LiAlO_2$ -10Li_6SiON	3.0	8.5

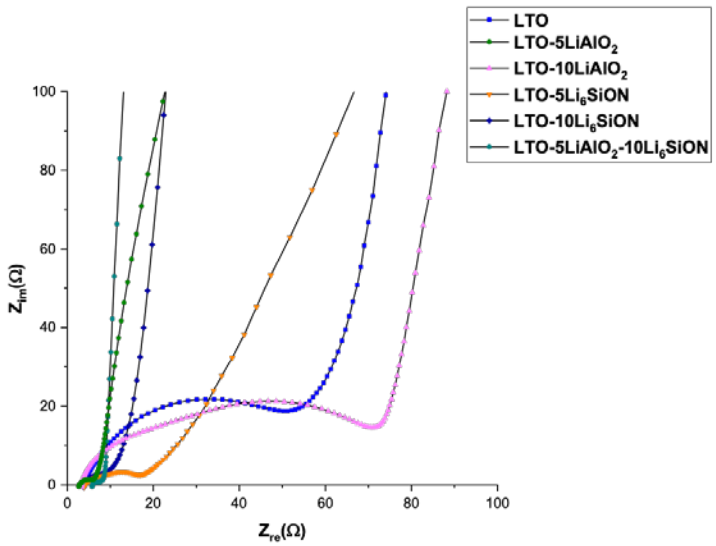

Figure 7.20. Nyquist plots of pristine and composite LTO – Li half-cells after 100 cycles.

The high rate capability of the LTO-5$LiAlO_2$-10Li_6SiON electrodes is attributed to:

(1) Optimal amounts of $LiAlO_2$ (5 wt.%) and Li_6SiON (10 wt.%) between or on the LTO particle surfaces enhancing the ionic conductivity as demonstrated by the increase in lithium-ion diffusivity.

(2) Li_6SiON polymer electrolyte reorganizing LTO surface bonding, resulting in an increase in the electronic conductivity due to the local change imbalance.

(3) Diminishing potential differences between anodic and cathodic plateaus, and polarization, via introduction of appropriate $LiAlO_2$ and Li_6SiON electrolyte contents.

(4) The enhanced electrical conductivities of electrolyte additives coupled with uniform particle morphology and high surface area of LTO NPs resulted in long-term cycling stability over 500 cycles delivering revisable capacity of ~217 mAh/g at 5C (Figure **7.21**).

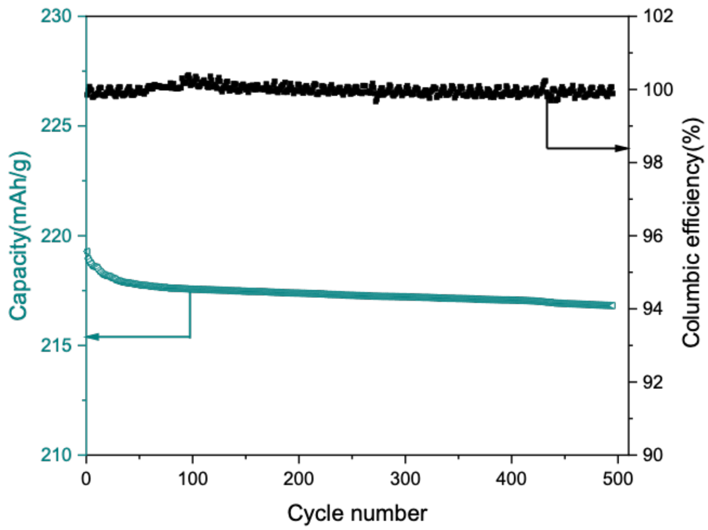

Figure 7.21. Long-term cycling stability of LTO-5$LiAlO_2$-10Li_6SiON -Li half-cell at 5C.

7.4 Conclusions

Herein, a facile LF-FSP method enabled the synthesis of high surface area, phase pure LTO NPs using a low-cost precursor. Pristine LTO was mixed with $LiAlO_2$ and Li_6SiON electrolytes to improve the ionic and electronic conductivity by simple ball-milling and ultrasonication methods. The microstructure studies show that the composite powders are homogeneous with particle sizes < 60 nm. XPS and EDX studies further confirm that the surface of the LTO particles is uniformly coated with the polymer electrolyte. By virtue of the high ionic and electronic conductivity of $LiAlO_2$ and Li_6SiON electrolyte, the LTO composite electrodes with optimal $LiAlO_2$ (5 wt.%) and Li_6SiON (10 wt.%) electrolyte additives exhibit excellent electrochemical performance delivering reversible capacity of 260 and 140 mAh/g at 0.5 and 10 C respectively.

References

(1) Zubi, G.; Dufo-López, R.; Carvalho, M.; Pasaoglu, G. The Lithium-Ion Battery: State of the Art and Future Perspectives. *Renewable and Sustainable Energy Reviews*. 2018. https://doi.org/10.1016/j.rser.2018.03.002.

(2) Nitta, N.; Wu, F.; Lee, J. T.; Yushin, G. Li-Ion Battery Materials: Present and Future. *Materials Today*. 2015. https://doi.org/10.1016/j.mattod.2014.10.040.

(3) Tarascon, J. M.; Armand, M. Issues and Challenges Facing Rechargeable Lithium Batteries. In *Materials for Sustainable Energy: A Collection of Peer-Reviewed Research and Review Articles from Nature Publishing Group*; 2010. https://doi.org/10.1142/9789814317665_0024.

(4) Ma, L.; Hendrickson, K. E.; Wei, S.; Archer, L. A. Nanomaterials: Science and Applications in the Lithium-Sulfur Battery. *Nano Today*. 2015. https://doi.org/10.1016/j.nantod.2015.04.011.

(5) Uhlmann, C.; Illig, J.; Ender, M.; Schuster, R.; Ivers-Tiffée, E. In Situ Detection of Lithium Metal Plating on Graphite in Experimental Cells. *J. Power Sources* **2015**. https://doi.org/10.1016/j.jpowsour.2015.01.046.

(6) Liu, Q.; Du, C.; Shen, B.; Zuo, P.; Cheng, X.; Ma, Y.; Yin, G.; Gao, Y. Understanding Undesirable Anode Lithium Plating Issues in Lithium-Ion Batteries. *RSC Adv*. **2016**. https://doi.org/10.1039/c6ra19482f.

(7) Aurbach, D.; Zinigrad, E.; Cohen, Y.; Teller, H. A Short Review of Failure Mechanisms of Lithium Metal and Lithiated Graphite Anodes in Liquid Electrolyte Solutions. In *Solid State Ionics*; 2002. https://doi.org/10.1016/S0167-2738(02)00080-2.

(8) Doughty, D.; Roth, E. P. A General Discussion of Li Ion Battery Safety. *Electrochem. Soc. Interface* **2012**. https://doi.org/10.1149/2.F03122if.

(9) Aravindan, V.; Lee, Y. S.; Madhavi, S. Research Progress on Negative Electrodes for Practical Li-Ion Batteries: Beyond Carbonaceous Anodes. *Advanced Energy Materials*. 2015. https://doi.org/10.1002/aenm.201402225.

(10) Pfanzelt, M.; Kubiak, P.; Fleischhammer, M.; Wohlfahrt-Mehrens, M. TiO2 Rutile - An Alternative Anode Material for Safe Lithium-Ion Batteries. *J. Power Sources* **2011**. https://doi.org/10.1016/j.jpowsour.2010.09.109.

(11) Zuo, X.; Zhu, J.; Müller-Buschbaum, P.; Cheng, Y. J. Silicon Based Lithium-Ion Battery Anodes: A Chronicle Perspective Review. *Nano Energy*. 2017. https://doi.org/10.1016/j.nanoen.2016.11.013.

(12) Sun, X.; Radovanovic, P. V.; Cui, B. Advances in Spinel Li4Ti5O12 Anode Materials for Lithium-Ion Batteries. *New Journal of Chemistry*. 2015. https://doi.org/10.1039/c4nj01390e.

(13) Yi, T. F.; Jiang, L. J.; Shu, J.; Yue, C. B.; Zhu, R. S.; Qiao, H. Bin. Recent Development and Application of Li4Ti5O 12 as Anode Material of Lithium Ion Battery. *J. Phys. Chem. Solids* **2010**. https://doi.org/10.1016/j.jpcs.2010.05.001.

(14) Zhao, B.; Ran, R.; Liu, M.; Shao, Z. A Comprehensive Review of Li4Ti5O12-Based Electrodes for Lithium-Ion Batteries: The Latest Advancements and Future Perspectives. *Materials Science and Engineering R: Reports*. 2015. https://doi.org/10.1016/j.mser.2015.10.001.

(15) Zhang, Q.; Li, X. Recent Developments in the Doped-Li4Ti5O12 Anode Materials of Lithium-Ion Batteries for Improving the Rate Capability. *International Journal of Electrochemical Science*. 2013.
(16) Zaghib, K.; Simoneau, M.; Armand, M.; Gauthier, M. Electrochemical Study of Li4Ti5O12 as Negative Electrode for Li-Ion Polymer Rechargeable Batteries. *J. Power Sources* **1999**. https://doi.org/10.1016/S0378-7753(99)00209-8.
(17) Mukai, K.; Kato, Y.; Nakano, H. Understanding the Zero-Strain Lithium Insertion Scheme of Li[Li 1/3Ti5/3]O4: Structural Changes at Atomic Scale Clarified by Raman Spectroscopy. *J. Phys. Chem. C* **2014**. https://doi.org/10.1021/jp412196v.
(18) Sandhya, C. P.; John, B.; Gouri, C. Lithium Titanate as Anode Material for Lithium-Ion Cells: A Review. *Ionics*. 2014. https://doi.org/10.1007/s11581-014-1113-4.
(19) Yuan, T.; Tan, Z.; Ma, C.; Yang, J.; Ma, Z. F.; Zheng, S. Challenges of Spinel Li4Ti5O12 for Lithium-Ion Battery Industrial Applications. *Advanced Energy Materials*. 2017. https://doi.org/10.1002/aenm.201601625.
(20) Yao, X. L.; Xie, S.; Chen, C. H.; Wang, Q. S.; Sun, J. H.; Li, Y. L.; Lu, S. X. Comparisons of Graphite and Spinel Li1.33Ti1.67O 4 as Anode Materials for Rechargeable Lithium-Ion Batteries. *Electrochim. Acta* **2005**. https://doi.org/10.1016/j.electacta.2005.01.034.
(21) Xiang, H. F.; Jin, Q. Y.; Wang, R.; Chen, C. H.; Ge, X. W. Nonflammable Electrolyte for 3-V Lithium-Ion Battery with Spinel Materials LiNi0.5Mn1.5O4 and Li4Ti5O12. *J. Power Sources* **2008**. https://doi.org/10.1016/j.jpowsour.2007.12.089.
(22) Chen, C.; Vaughey, J.; Jansen, A.; Dees, D.; Kahaian, A.; Goacher, T.; Thackeray, M. Studies of Mg-Substituted Li42xMgxTi5O12 Spinel Electrodes (0 x 1) for Lithium Batteries. *J. Electrochem. Soc.* **2001**.
(23) Zhao, L.; Hu, Y. S.; Li, H.; Wang, Z.; Chen, L. Porous Li4Ti5O12 Coated with N-Doped Carbon from Ionic Liquids for Li-Ion Batteries. *Adv. Mater.* **2011**. https://doi.org/10.1002/adma.201003294.
(24) Han, J. P.; Zhang, B.; Wang, L. Y.; Zhu, H. L.; Qi, Y. X.; Yin, L. W.; Li, H.; Lun, N.; Bai, Y. J. Li1.3Al0.3Ti1.7(PO4)3 Behaving as a Fast Ionic Conductor and Bridge to Boost the Electrochemical Performance of Li4Ti5O12. *ACS Sustain. Chem. Eng.* **2018**, *6* (6), 7273–7282. https://doi.org/10.1021/acssuschemeng.7b04361.
(25) Gao, J.; Jiang, C.; Ying, J.; Wan, C. Preparation and Characterization of High-Density Spherical Li4Ti5O12 Anode Material for Lithium Secondary Batteries. *J. Power Sources* **2006**. https://doi.org/10.1016/j.jpowsour.2005.04.008.
(26) Bai, X.; Li, W.; Wei, A.; Li, X.; Zhang, L.; Liu, Z. Preparation and Electrochemical Properties of Mg2+ and F− Co-Doped Li4Ti5O12 Anode Material for Use in the Lithium-Ion Batteries. *Electrochim. Acta* **2016**. https://doi.org/10.1016/j.electacta.2016.11.073.
(27) Tian, Q.; Zhang, Z.; Yang, L.; Xiang, Y. Improving the Lithium Storage Properties of Li4Ti5O12anodes by Facile Two-Phase Formation and Nanostructure Engineering Strategy. *J. Alloys Compd.* **2017**, *705*, 638–644. https://doi.org/10.1016/j.jallcom.2017.02.175.
(28) Wolfenstine, J.; Allen, J. L. Electrical Conductivity and Charge Compensation in Ta Doped Li4Ti5O12. *J. Power Sources* **2008**. https://doi.org/10.1016/j.jpowsour.2008.02.019.
(29) Ji, S.; Zhang, J.; Wang, W.; Huang, Y.; Feng, Z.; Zhang, Z.; Tang, Z. Preparation and Effects of Mg-Doping on the Electrochemical Properties of Spinel Li4Ti5O12 as Anode Material for Lithium Ion Battery. *Mater. Chem. Phys.* **2010**. https://doi.org/10.1016/j.matchemphys.2010.05.006.

(30) Zhao, H.; Li, Y.; Zhu, Z.; Lin, J.; Tian, Z.; Wang, R. Structural and Electrochemical Characteristics of Li4-XAlxTi5O12 as Anode Material for Lithium-Ion Batteries. *Electrochim. Acta* **2008**. https://doi.org/10.1016/j.electacta.2008.05.038.
(31) Lee, B.; Yoon, J. R. Preparation and Characteristics of Li4Ti5O 12with Various Dopants as Anode Electrode for Hybrid Supercapacitor. *Curr. Appl. Phys.* **2013**. https://doi.org/10.1016/j.cap.2013.04.002.
(32) Huang, S.; Wen, Z.; Gu, Z.; Zhu, X. Preparation and Cycling Performance of Al3+and F-Co-Substituted Compounds Li4AlxTi5-XF YO12-Y. *Electrochim. Acta* **2005**. https://doi.org/10.1016/j.electacta.2004.12.036.
(33) Salvatore, K. L.; Lutz, D. M.; Guo, H.; Yue, S.; Gan, J.; Tong, X.; Liu, P.; Takeuchi, E. S.; Takeuchi, K. J.; Marschilok, A. C.; Wong, S. S. Solution-Based, Anion-Doping of Li4Ti5O12 Nanoflowers for Lithium-Ion Battery Applications. *Chem. - A Eur. J.* **2020**. https://doi.org/10.1002/chem.202002489.
(34) Qi, Y.; Huang, Y.; Jia, D.; Bao, S. J.; Guo, Z. P. Preparation and Characterization of Novel Spinel Li4Ti5O12-XBrx Anode Materials. *Electrochim. Acta* **2009**. https://doi.org/10.1016/j.electacta.2009.04.010.
(35) Li, X.; Qu, M.; Huai, Y.; Yu, Z. Preparation and Electrochemical Performance of Li4Ti5O12/Carbon/Carbon Nano-Tubes for Lithium Ion Battery. *Electrochim. Acta* **2010**. https://doi.org/10.1016/j.electacta.2010.01.015.
(36) Wang, G. J.; Gao, J.; Fu, L. J.; Zhao, N. H.; Wu, Y. P.; Takamura, T. Preparation and Characteristic of Carbon-Coated Li4Ti5O12 Anode Material. *J. Power Sources* **2007**. https://doi.org/10.1016/j.jpowsour.2007.06.107.
(37) Jung, H. G.; Kim, J.; Scrosati, B.; Sun, Y. K. Micron-Sized, Carbon-Coated Li4Ti5O12 as High Power Anode Material for Advanced Lithium Batteries. *J. Power Sources* **2011**. https://doi.org/10.1016/j.jpowsour.2011.04.019.
(38) Luo, H.; Shen, L.; Rui, K.; Li, H.; Zhang, X. Carbon Coated Li4Ti5O12 Nanorods as Superior Anode Material for High Rate Lithium Ion Batteries. *J. Alloys Compd.* **2013**. https://doi.org/10.1016/j.jallcom.2013.03.247.
(39) Zhu, Y. R.; Yuan, J.; Zhu, M.; Hao, G.; Yi, T. F.; Xie, Y. Improved Electrochemical Properties of Li4Ti5O12-Li0.33La0.56TiO3 Composite Anodes Prepared by a Solid-State Synthesis. *J. Alloys Compd.* **2015**, *646*, 612–619. https://doi.org/10.1016/j.jallcom.2015.05.239.
(40) Poizot, P.; Laruelle, S.; Grugeon, S.; Dupont, L.; Tarascon, J. M. Nano-Sized Transition-Metal Oxides as Negative-Electrode Materials for Lithium-Ion Batteries. *Nature* **2000**. https://doi.org/10.1038/35035045.
(41) Wang, Y.; Liu, H.; Wang, K.; Eiji, H.; Wang, Y.; Zhou, H. Synthesis and Electrochemical Performance of Nano-Sized Li 4Ti5O12 with Double Surface Modification of Ti(III) and Carbon. *J. Mater. Chem.* **2009**. https://doi.org/10.1039/b908025b.
(42) Jaiswal, A.; Horne, C. R.; Chang, O.; Zhang, W.; Kong, W.; Wang, E.; Chern, T.; Doeff, M. M. Nanoscale LiFePO[Sub 4] and Li[Sub 4]Ti[Sub 5]O[Sub 12] for High Rate Li-Ion Batteries. *J. Electrochem. Soc.* **2009**. https://doi.org/10.1149/1.3223987.
(43) Shen, C. M.; Zhang, X. G.; Zhou, Y. K.; Li, H. L. Preparation and Characterization of Nanocrystalline Li4Ti5O12 by Sol-Gel Method. *Mater. Chem. Phys.* **2003**. https://doi.org/10.1016/S0254-0584(02)00225-0.
(44) Zhou, Q.; Liu, L.; Tan, J.; Yan, Z.; Huang, Z.; Wang, X. Synthesis of Lithium Titanate Nanorods as Anode Materials for Lithium and Sodium Ion Batteries with Superior Electrochemical Performance. *J. Power Sources* **2015**. https://doi.org/10.1016/j.jpowsour.2015.02.061.

(45) Ju, S. H.; Kang, Y. C. Characteristics of Spherical-Shaped Li4Ti5O12 Anode Powders Prepared by Spray Pyrolysis. *J. Phys. Chem. Solids* **2009**. https://doi.org/10.1016/j.jpcs.2008.09.003.
(46) Chou, S. L.; Wang, J. Z.; Liu, H. K.; Dou, S. X. Rapid Synthesis of Li4Ti5O12 Microspheres as Anode Materials and Its Binder Effect for Lithium-Ion Battery. *J. Phys. Chem. C* **2011**. https://doi.org/10.1021/jp2039256.
(47) Fang, Z. K.; Zhu, Y. R.; Yi, T. F.; Xie, Y. Li4Ti5O12-LiAlO2 Composite as High Performance Anode Material for Lithium-Ion Battery. *ACS Sustain. Chem. Eng.* **2016**, *4* (4), 1994–2003. https://doi.org/10.1021/acssuschemeng.5b01271.
(48) Monchak, M.; Hupfer, T.; Senyshyn, A.; Boysen, H.; Chernyshov, D.; Hansen, T.; Schell, K. G.; Bucharsky, E. C.; Hoffmann, M. J.; Ehrenberg, H. Lithium Diffusion Pathway in Li1.3Al0.3Ti1.7(PO4)3 (LATP) Superionic Conductor. *Inorg. Chem.* **2016**. https://doi.org/10.1021/acs.inorgchem.5b02821.
(49) Wu, X. M.; Li, X. H.; Wang, S. W.; Wang, Z.; Zhang, Y. H.; Xu, M. F.; He, Z. Q. Preparation and Characterization of Lithium-Ion-Conductive Li1.3Al0.3Ti1.7(PO4)3 Thin Films by the Solution Deposition. *Thin Solid Films* **2003**. https://doi.org/10.1016/S0040-6090(02)01094-5.
(50) Eleni Temeche, Sylvio Indris, and R. M. L. LiAlO2/LiAl5O8 Membranes Derived from Flame Synthesized Nanopowders as a Potential Electrolyte and Coating Materials for All Solid-State Batteries (ASSBs). *Appl. Mater. Interfaces*.
(51) Zhang, X.; Temeche, E.; Laine, R. M. LixSiON (X= 2, 4, 6); A Novel Solid Electrolyte System Derived from Agricultural Waste. **2020**, 48–50. https://doi.org/10.1039/d0gc02580a.
(52) Yi, E.; Wang, W.; Mohanty, S.; Kieffer, J.; Tamaki, R.; Laine, R. M. Materials That Can Replace Liquid Electrolytes in Li Batteries: Superionic Conductivities in Li1.7Al0.3Ti1.7Si 0.4P2.6O12. Processing Combustion Synthesized Nanopowders to Free Standing Thin Films. *J. Power Sources* **2014**, *269*, 577–588. https://doi.org/10.1016/j.jpowsour.2014.07.029.
(53) Temeche, E.; Yi, E.; Keshishian, V.; Kieffer, J.; Laine, R. M. Liquid-Feed Flame Spray Pyrolysis Derived Nanopowders (NPs) as a Route to Electrically Conducting Calcium Aluminate (12CaO.7Al2O3) Films. *J. Eur. Ceram. Soc.* **2019**. https://doi.org/10.1016/j.jeurceramsoc.2018.11.051.
(54) Alias, N. A.; Kufian, M. Z.; Teo, L. P.; Majid, S. R.; Arof, A. K. Synthesis and Characterization of Li4Ti5O12. *J. Alloys Compd.* **2009**. https://doi.org/10.1016/j.jallcom.2009.07.057.
(55) Prosini, P. P.; Mancini, R.; Petrucci, L.; Contini, V.; Villano, P. Li4Ti5O12 as Anode in All-Solid-State, Plastic, Lithium-Ion Batteries for Low-Power Applications. *Solid State Ionics* **2001**. https://doi.org/10.1016/S0167-2738(01)00891-8.
(56) Du, Z.; Wood, D. L.; Daniel, C.; Kalnaus, S.; Li, J. Understanding Limiting Factors in Thick Electrode Performance as Applied to High Energy Density Li-Ion Batteries. *J. Appl. Electrochem.* **2017**. https://doi.org/10.1007/s10800-017-1047-4.
(57) Yi, T. F.; Shu, J.; Zhu, Y. R.; Zhu, X. D.; Zhu, R. S.; Zhou, A. N. Advanced Electrochemical Performance of Li4Ti4.95V0.05O12 as a Reversible Anode Material down to 0 V. *J. Power Sources* **2010**. https://doi.org/10.1016/j.jpowsour.2009.07.040.
(58) Tian, B.; Xiang, H.; Zhang, L.; Wang, H. Effect of Nb-Doping on Electrochemical Stability of Li 4Ti 5O 12 Discharged to 0 V. *J. Solid State Electrochem.* **2012**. https://doi.org/10.1007/s10008-011-1305-z.

(59) Zhang, Q.; Verde, M. G.; Seo, J. K.; Li, X.; Meng, Y. S. Structural and Electrochemical Properties of Gd-Doped Li4Ti5O12 as Anode Material with Improved Rate Capability for Lithium-Ion Batteries. *J. Power Sources* **2015**. https://doi.org/10.1016/j.jpowsour.2015.01.124.
(60) Yi, T. F.; Xie, Y.; Wu, Q.; Liu, H.; Jiang, L.; Ye, M.; Zhu, R. High Rate Cycling Performance of Lanthanum-Modified Li 4Ti 5O 12 Anode Materials for Lithium-Ion Batteries. *J. Power Sources* **2012**. https://doi.org/10.1016/j.jpowsour.2012.04.101.
(61) Rahman, M. M.; Wang, J. Z.; Hassan, M. F.; Chou, S.; Wexler, D.; Liu, H. K. Basic Molten Salt Process-A New Route for Synthesis of Nanocrystalline Li4Ti5O12-TiO2 Anode Material for Li-Ion Batteries Using Eutectic Mixture of LiNO3-LiOH-Li2O2. *J. Power Sources* **2010**. https://doi.org/10.1016/j.jpowsour.2010.01.073.
(62) Wang, J.; Zhao, H.; Yang, Q.; Wang, C.; Lv, P.; Xia, Q. Li4Ti5O12-TiO2 Composite Anode Material for Lithium-Ion Batteries. *J. Power Sources* **2013**. https://doi.org/10.1016/j.jpowsour.2012.08.082.

Chapter 8

Silica Depleted Rice Hull Ash (SDRHA), An Agricultural Waste, As a High-Performance Hybrid Lithium-Ion Capacitor

8.1 Introduction

Global warming provides intense motivation to find ways to supplant commercial-scale CO_2 generating processes to offset envisioned catastrophic effects on the environment.[1–5] To this end, the world is rapidly adopting electric vehicles as one part of societal efforts to mitigate the anticipated rapid changes in our global environment.[6–10]

The development of high rate lithium-ion batteries (LIBs) is essential to ensure the efficacy of portable electronic devices.[11–13] Due to their unique merits in terms of high energy density (100-250 Wh kg^{-1}), wide operating voltage, and absence of memory, LIBs are now rapidly undergoing commercialization for fast charging electronics, electric vehicles, and hybrid electric vehicles.[14–16] However, conventional LIBs using graphite anode cannot meet the increasing demand for power density, operational reliability, system integration, and safety requirements in many of these applications.[11,13,17] LIBs specific power is usually < 0.5kW kg^{-1}, with poor cycle life of < 5000 cycles.[18,19]

In contrast, lithium-ion capacitors (LICs) that combine both battery and electric double-layer capacitors (EDLC) properties provide ~ 5-10 times greater energy densities than traditional EDLCs, higher power densities and longer cycle lives than conventional LIBs.[18,20] LIC devices are desirable because they can meet the demand for high power density requirements. Typically, LICs contain a pre-lithiated anode and an EDLC cathode.[18,21–23] Extensive research has been done to optimize the electrochemical performance of hybrid-LICs. [20,24–28] Recently Zheng et al[29] demonstrated LICs with improved specific energy through use of a hybrid positive electrode of $LiNi_{0.5}Co_{0.2}Mn_{0.3}O_2$ (NMC) as an additive with activated carbon.

Improvements in the energy densities of LICs were achieved by optimizing the electrode components by using polymer-derived porous carbon as a cathode,[30] pre-lithiated graphene nanosheets as the negative electrode,[31] and "soft" carbon, a promising alternative to graphite in high rate applications.[32]

The specific surface area (SSA) of the EDLC component is known to directly affect the electrical energy storage capacity of LICs. Hence, various porous carbon materials with the high SSAs (> 1000 m^2/g) have been successfully synthesized by catalytic activation,[33] carbonization of polymer blends,[34] and chemical vapor deposition methods.[35] However, these methods require complicated synthesis procedures that are high cost and/or use toxic reagents.[36] As a consequence, development of alternative anode materials that offer high capacities, fast charge/discharge, low potentials, reduced cost of manufacturing, as well as being environmentally friendly, and safe have attracted attention from both academia and industry.[37–39]

One less appreciated source of energy is one in which the combustion of agricultural waste is used to generate steam to produce electricity. Combustion of agricultural waste (Ag waste) such as rice hulls, corn, and coconut husks, etc.[36,40,41] takes advantage of the fact that the carbon in these sources derives directly from photosynthetic fixing of CO_2, such that the energy generated can be CO_2 neutral. Often, the combustion of Ag waste generates materials which themselves can be used to make value-added products (valorized).[40,42,43] In previous work done in this group, we demonstrated that rice hull ash (RHA), produced world-wide in millions of tons/year quantities, can be used to produce solar grade silicon (99.999 % pure),[40] distillable forms of alkoxysilanes,[44] and high surface area silica for vacuum insulation panels.[45]

In this work, the residual carbon recovered from distilling "silica" out of the RHA (silica depleted RHA or SDRHA) has been explored as a "green" source of anode material for high power applications. The SDRHA carbon/silica composites produced offer potential access to better, cheaper and safer EDLC electrodes while also generating value-added utility for this Ag waste. Several studies examine the advantages of RH based activated carbon as active material for the electrodes of EDLCs and LICs.[42,43,46–50] Recently, Kumagai et al.[51] demonstrated the use of micro and mesoporous activated carbon prepared from RH and beet sugar as the cathode material, and RH-derived C/SiO_x as the composite anode material. It was revealed that the RH carbon with partially removed SiO_x (41 wt.%) is a promising anode active material with high resistance to facile pre-lithiation.[51] The durability against Li dendrite growth and Li-aged by product is attributed to the transformation of SiO_x into Li_ySiO_x, reducing the number of excess Li ions that could contribute to uneven Li deposition.[51,52] Hence, the optimization of SiO_x amount in SDRHA is necessary to deliver high performance LICs.

In this study, we assess the potential of battery electrodes assembled using Li metal foil or $LiNi_{0.6}Co_{0.2}Mn_{0.2}O_2$ (NMC622) with the SDRHA as hybrid LICs. The most significant advantage to using NMC is its high specific capacity and high voltage to enhance the energy density.[29] The cell design for new generation hybrid LICs devices is discussed in detail. The specific capacity of lithiated SDRHA is calculated to be 250 mAh/g at 0.5 C and remains 200 mAh/g at 2 C indicating excellent rate performance. The reversibility of Li-ion insertion in SDRHA and release of Li_ySiO_x is also discussed. The hybrid LICs assembled with NMC622 exhibit long-term cycle life, high specific capacitance of 325 F/g at 1C, and excellent coloumbic efficiency (~100%). This suggests the development of SDRHA from Ag waste is highly suitable for fabrication of supercapacitor carbon-based electrodes without prior activation.

8.2 Experimental section

RHA was provided by Wadham Energy Inc. (Williams, CA). Typical impurity contents and detail analyses of RHA can be found elsewhere.[40] 2-Methyl-2,4-pentanediol (Hexylene glycol, ARCOS Organic) was used as received. Lithium metal foil (~750 µm), polyvinylidene fluoride (Mw ~534 kg/mol), potassium hydroxide (KOH), hydrochloric acid (HCl), and *N*-methylpyrrolidone (NMP) were purchased from Sigma-Aldrich (St Louis, MO). The super C65 conductive carbon black powder (~62 m^2/g), Celgard 2400 separator (~25 µm), and coin cell parts were purchased from MTI Corporation (Richmond, CA). The lithium nickel cobalt manganese oxide powder (NMC622) was purchased from BASF Catalysts (Cleveland, OH). The mixed solvent of ethylene carbonate (EC), dimethyl carbonate (DMC), and Ethyl methyl carbonate (EMC) (1 : 1 : 1 wt.%) containing 1 M $LiPF_6$ as the Li salt with the addition of 10 wt.% fluoroethylene carbonate was purchased from Soulbrain (Northville, MI).

8.2.1 Synthesis of SDRHA

SDRHA was synthesized as reported elsewhere.[48] In brief, rice hull ash (RHA) was first milled in dilute hydrochloric acid to remove impurities. RHA (200 g) was placed in a 2L bottle with 200 g of milling media and 2 L of HCl solution (3.7 wt.% HCl). Media was yttria-stabilized zirconia, 3 mm diameter spheres. The RHA was milled for 48 h. Thereafter, the acid milled RHA was recovered by suction filtration through a Buchner funnel. The recovered RHA was then washed with 500 mL DI.

The acid milled RHA and 1 L of deionized water were then introduced to a 2 L glass flask equipped with a stir bar and a reflux condenser. The suspension was then boiled for 24 h before separation by filtration through a Buchner funnel. The boiling and filter processes were repeated one more time. After the second filtration, the pH of water filtered off was neutral. Then, the RHA was dried at 60 °C/vacuum overnight.

A mixture of 250 mL hexylene glycol (HG) and 4.2 g KOH (75 mmol) was first heated to 190 °C in a 250 mL three-neck flask equipped with a stir bar to remove water for 3 h. Dried RHA powders (~50 g) were added to the HG + KOH solution. The mixture was heated to 200 °C in a pyrex distillation setup. After 100 mL HG was distilled, another 100 mL HG was added until 500 mL HG was reacted and/or distilled out coincident with the water during silica depolymerization. After 24 h, 40-50 wt.% of the silica is extracted as the spirosiloxane [2,4-dimethylpentanedionato]$_2$Si as shown in Scheme **8.1**.

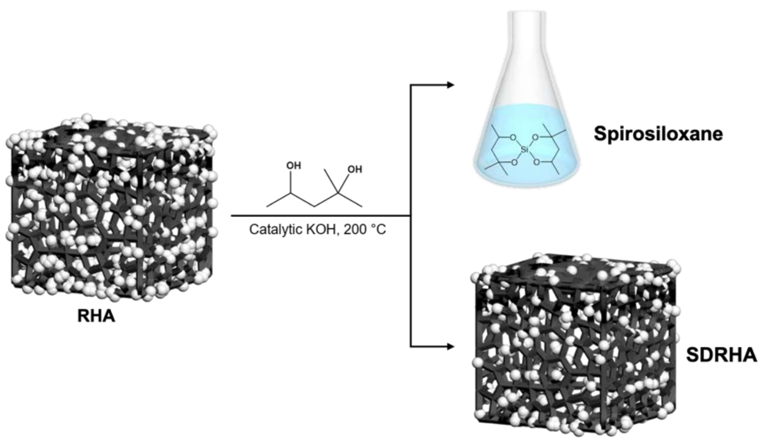

Scheme 8.1. Synthesis of SDRHA from rice hull ash.

8.2.2 Electrode preparation

In brief, SDRHA was mixed with super C65 conductive carbon and polyvinylidene fluoride (PVDF) at a weight ratio of 80:5:15 in an NMP solvent, respectively. The positive electrode was prepared by mixing NMC 622 (94 wt. %), super C65 conductive carbon (3 wt. %), and PVDF (3 wt. %) dissolved in NMP. To form uniform slurries, the two mixtures were ball-milled with Al_2O_3 media (~ 3 mm) for 24 h, then coated onto current collectors. Copper and aluminum foils were used for the SDRHA and NMC622-based electrodes, respectively. The loading density of the active materials was in the range of 1.3 - 4 mg cm^{-2}. The electrodes were arch punched out into 14 mm circle-shaped cathodes and anodes. The electrodes were then subsequently dried in a vacuum oven at 100 °C overnight prior to being transferred to a glove box filled with pure argon gas.

Electrochemical measurements. Electrochemical properties of SDRHA and NMC622 electrodes were evaluated using CR2032 coin cells. The SDRHA working electrodes were incorporated into CR2032 coin cells, in which Li metal foils (16 mm) were used as counter and reference electrodes and Celgard 2400 as separators. Before cell assembly, the metallic Li (16 mm W X 750 µm T) was scraped to expose a clean surface. Half-cells were constructed using a standard procedure. In addition, full cells were assembled using the SDRHA as the anode and NMC622 as the cathode. A solution of 1.1 M $LiPF_6$ in a mixture solvent of EC: DC: DMC (weight ratio of 1:1:1) with 10 wt. % FEC additives was used as the electrolyte. The assembly process was conducted in an argon-filled glove box having O_2 and H_2O contents below 0.5 ppm. The coin cells were compressed using a ~0.1 kpsi uniaxial pressure (MTI).

SP-300 (Bio-Logic Science Instruments, Knoxville, TN) was used to measure the AC impedance, cyclic voltammetry, and galvanostatic charge/discharge. AC impedance data was recorded in a frequency range of 7 MHz to 1 Hz with an AC amplitude of 10 mV. The charge/discharge tests of the SDRHA/Li and SDRHA/NMC622 were performed between 0.01 – 2.5 V and 2.7- 4.2 V, respectively. The electrode specific capacitance was calculated according to:

$$C = (\int I dv)/(V * m * s) \qquad (1)$$

where I is the current density, V is the potential, s is the potential scan rate, and m is the mass of the electroactive materials in the electrode.

8.3 Results and discussion

In the following sections, we discuss detailed analyses of the RHA and SDRHA powders using FTIR, XRD, XPS, TGA, SEM and BET measurements. In addition, the development of a hybrid LIC system using an organic electrolyte, SDRHA as the negative electrode, Li metal, and NMC622 as the cathode are also investigated.

8.3.1 Characterization of RHA and SDRHA powders

Figure **8.1a** shows the FTIR spectra of washed RHA and SDRHA powders. The predominant band at 1090 $cm^{-1}$is assigned to νSi–O–Si bonds in amorphous silica.[42,53] The bands located ~780 and 470 cm^{-1} are associated with Si–O symmetric stretching and bending vibrations, respectively. The 3500 cm^{-1} absorption reflects νO-H from physi- and chemi-sorbed water.

The ~2925 cm^{-1} peak for the SDRHA powder corresponds to νC–H and is not apparent in the starting RHA powder. The absorption intensities of all ν(Si–O–Si) vibrations are broader following silica dissolution.

This is likely associated with the reduction in SiO_2 content (TGA, Figure **8.2**) and may also arise because of the nanoscale mixing of the remaining SiO_2 partially encapsulated in the amorphous carbon. The FTIR spectrum also indicates a small carboxyl (νC=O) peak 1550 cm^{-1}, suggesting the potential for additional pseudocapacitance, as seen previously in carbon materials.[43]

XRD patterns of the washed RHA and SDRHA are shown in Figure **8.2b**. The diffraction patterns show a broad peak from ~15 ° to 40 ° 2θ with a central peak at ~ 22 ° 2θ associated with amorphous phases (both carbon and SiO_2) confirming the absence of any ordered, crystalline structure.[42] The weak (002) diffraction also suggests the disordered (graphene-like) nature of the porous carbon in SDRHA. XPS studies (Figure **8.3)** further confirm the presence of disordered stacking of graphene layers, ascribed to the hard carbon nature of the SDRHA. These along with the hydroxyl groups at the surface suggest that SDRHA should offer superior super capacitive properties as discussed in detail in the electrochemical performance section.

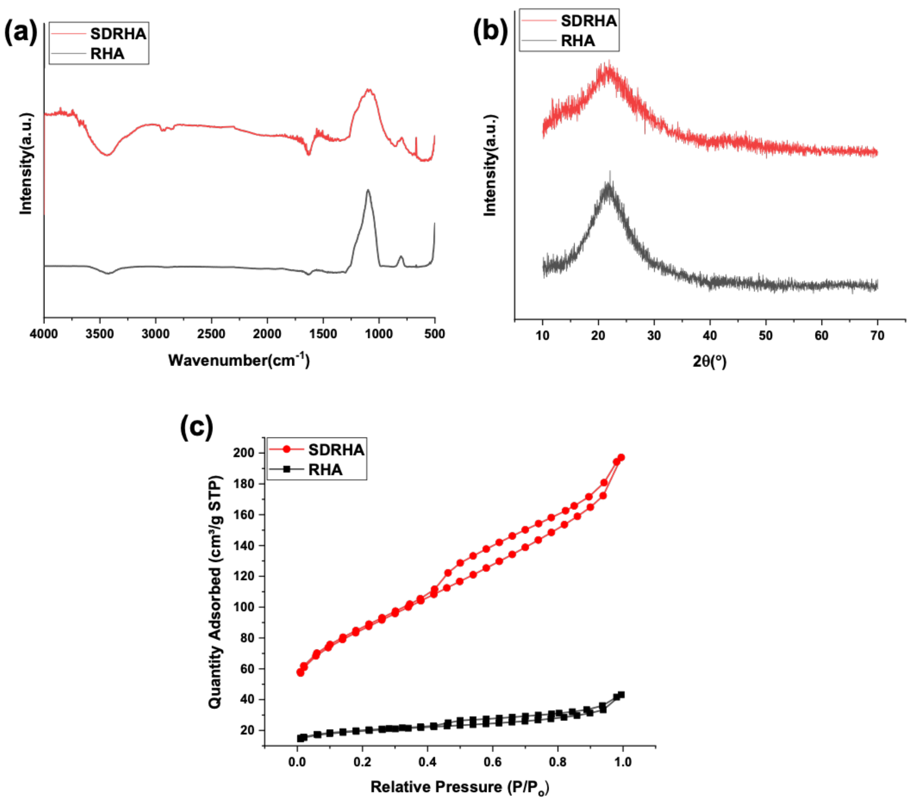

Figure 8.1. a. FTIR spectra, b. XRD patterns, and c. nitrogen adsorption-desorption isotherms measured on RHA and SDRHA powders.

Figure **8.1c** shows the N_2 adsorption-desorption isotherms of RHA and SDRHA. The adsorption isotherms show type IV character with Type H3 hysteresis loops at a relative pressure P/P_0 between 0.4 and 1.[54] Loops of this type may arise from non-rigid aggregates of plate-like particles,[54] in good agreement with the morphology of the SDRHA powders as seen in the Figure **8.4** SEMs. At low values of P/P_0, the isotherms look similar to microporous adsorbents.[42]

The SDRHA hysteresis loop suggests the existence of mesopores, as the adsorption increases markedly above 0.4 relative pressure P/P_0. Adsorption capacity is highly dependent on the micropore and mesopore content present in the SDRHA. The BET reported surface area of RHA is ~ 80 m^2/g, similar to that reported in the literature.[53] The nominal BET surface area increased from 80 to 220 m^2/g after removing SiO_2, suggesting the surface area increases with silica depletion. Hence, the amorphous silica easily dissolved during the chemical depletion process is a key factor determining the surface area of the SDRHA. The development of micropores and mesopores in SDRHA is attributed to both the intrinsic properties of hard carbon and partial removal of SiO_2.

The BET SSA of SDRHA (220 m^2/g) is higher than what is reported for rice hull derived carbon (RHC, 113 m^2/g), which is prepared by carbonizing RH at 600 °C/1 h/N_2 and partially leaching SiO_x in aqueous NaOH.[51]

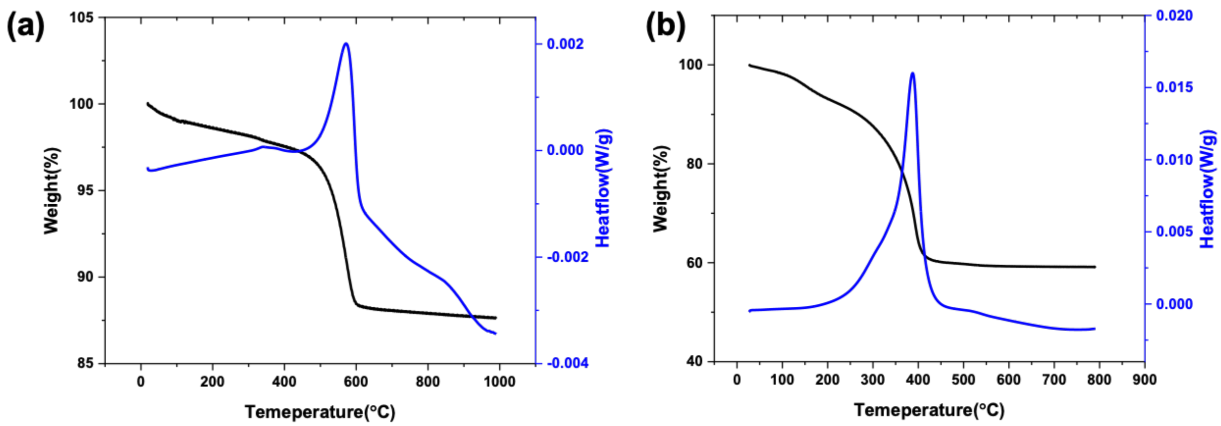

Figure 8.2. TGA-DSC profile of a. RHA and b. SDRHA powders in air.

The thermal stability of the washed RHA and SDRHA were analyzed by TGA at 25 – 800 °C/air as shown in Figure **8.2**. Two major mass loss regions were observed. The first mass loss of 2-3 wt.% below 200 °C is ascribed to loss of physisorbed water and volatile compounds, supported by the Figure **8.1a** FTIR. The mass loss from 200°– 600 °C is ascribed to oxidation of carbonaceous materials. No further obvious mass losses are observed up to 800 °C.

TGA studies were carried out to estimate the net volatile matter on the rice hull ash and the amount of carbon present in SDRHA powder. The surface carbon or the trapped carbon in the RHA is considered as an impurity. Studies show that temperature plays a significant role in the amount of carbon associated with the silica in the rice hull ash.[55] The total amount of carbon in SDRHA (35-40 wt.%) was calculated by subtracting the mass loss between 200°-600 °C **(Figure 2b)**. The final SiO_2 ceramic yield was reduced from 87 to 60-65 wt. % after distillative removal of silica as the spirosiloxane. The partial removal of SiO_2 is necessary to create voids to allow the volume expansion resulting from SiO_x lithiation, which enhances the cycle life of SDRHA anode.

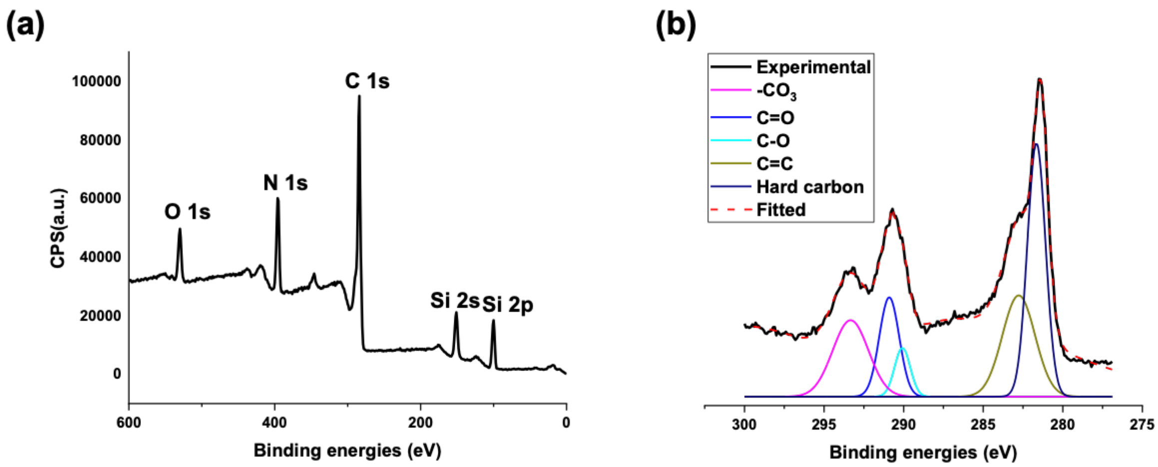

Figure 8.3. a. Wide survey XPS spectrum and b. C 1s core-level spectrum of SDRHA powder.

To further understand the surface chemistries and reaction mechanisms, XPS analysis was conducted on the SDRHA powder. Figure **8.3a** reveals signature, C, Si, O, and N peaks and minor Ca peaks; the latter residue from RHA. The deduced atomic composition shows 69 ± 0.3 at. % carbon. It is known that photoelectrons can probe as deeply as ≈ 5 nm below the surface, hence a carbon 1s spectrum can provide a reasonable map of all the carbon species present.[56] Figure **8.3b** shows the C 1s core-level is similar to that found for hard carbon electrodes.[56] The peak near 283 eV is related to hard carbon although this binding energy is lower than pristine hard carbon (284.5 eV).[56]

The XPS C1s peaks for the SDRHA can be assigned to two components- one is hard carbon and the other originates from various functional groups (i.e. C=O, C-O, and C=C) on the hard carbon surface, in good agreement with the Figure **8.1a** FTIR. The literature suggests that the oxygen-containing functional groups can improve the electrochemical reactivity of hard carbon electrodes.[54]

SDRHA has oxygen-containing functional groups on the carbon surface as confirmed by FTIR, XPS, and EDX in Figures **8.1a**, **8.3**, and 8.**4** respectively. The surface redox reactions can be suggested to occur between C-O functional groups and Li^+ (i.e., -C=O + Li^++ e ↔ -C-O-Li).[54] SDRHA exhibits a much larger SSA compared to washed RHA (Figure **8.1c**), hence one can anticipate a greater number of oxygen-containing functional groups, resulting in high specific capacity and excellent rate performance arising from surface redox reactions.

The removal of SiO_2 from RHA is a simple, low cost, and eco-friendly method of producing porous, functionalized hard carbon as a high-performance electrode material for hybrid LICs. In addition, as we demonstrate elsewhere,[44] spirosiloxane provides access to fumed silica and since it can be distilled to high purity, it also offers potential access to high purity silica in multiple forms potentially replacing other alkoxysilanes that are currently produced from silicon metal.

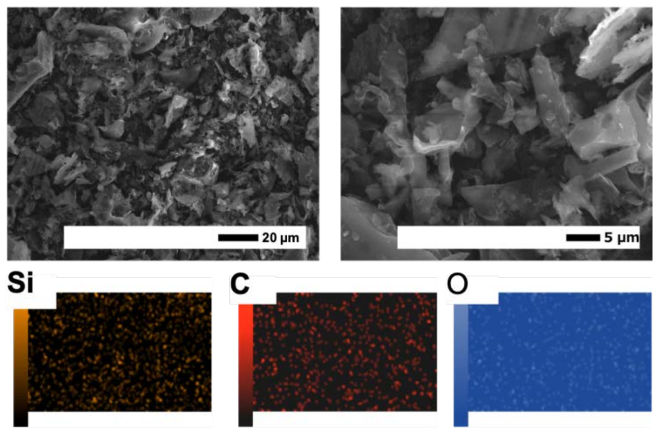

Figure 8.4. SEM and EDX images of SDRHA powder.

Figure **8.4** shows SEM and EDX images of SDRHA powder. SDRHA consists of particles ranging from 2 to 20 μm, with the majority in the 5-10 μm range. There is some degree of topological irregularity, the SEM microstructure shows agglomerated plate-like particles as also suggested by the BET analysis. The particle morphology was improved by ball-milling with 15 wt.% PVDF binder when used to make the slurry for the hybrid LIC electrode. It is known that ball-milling reduces particle irregularity and improves surface topology, allowing increased packing efficiency. It is worth noting that the preparation of conventional electrodes containing carbon black is normally less elaborate.[23] The microstructure shows homogenous particle morphology with optimal packing efficiency. The super C65 (5 wt.%) additives can be seen encompassing the SDRHA particles. This encompassing nature is highly desirable as it will establish a highly conductive route, increasing the power performance by linking more particles to form an electrically conductive network.[18] The energy-dispersive X-ray (EDX) map reveals a uniform elemental distribution of Si, C, and O for the SDRHA powder.

8.3.2 Electrochemical performance of half-cell

Hybrid LICs refer to devices using both electrical double-layer and faradic mechanisms to store charge. These devices are usually assembled using an electrode with an electric double layer or pseudocapacitive material combined with another rechargeable battery-type electrode. Here, the high SSA SDRHA (33 wt.% C) serves as the negative electrode and Li metal or NMC622 are the battery positive electrodes. Electrochemical performance and cycling stability depend on the properties of the electrolyte used.[57] Device capacitance relies on the nature of the contact between the electrode materials and electrolyte as it determines the double layer area. Organic-based electrolytes with high dielectric constant, high ionic conductivity, along with wide potential windows give rise to higher specific capacitance and energy densities compared to aqueous electrolytes.[58] In addition, organic electrolyte fills pore volumes inside the electrode layers to maximize the capacitance of the active material. Hence, 1.1 M $LiPF_6$ in the mixed solvent (1:1:1wt.% ratio) EC: DEC: EMC with 10 wt. % FEC was used as the electrolyte.

The CV curves, at different scan rates, elucidate the reversible surface reaction on the SDRHA porous electrode. Figure **8.5a** shows CV curves of SDRHA/Li cells at scan rates of 10, 5, and 0. 1 mv/sec in the potential range of 3 - 0.01 V. The hump at lower potential < 0.5 V might be ascribed to intercalation of Li in the SDRHA layers, suggesting a faradic mechanism. At a slower scan rate of 0.1 mV/sec (Figure **8.5b**), a small irreversible peak appears at 0.45 V in the first anodic process, which can be ascribed to formation of a solid electrolyte interface (SEI).[54] The CV curve from 1 to 3 V seems to have a rectangular shape, indicating ideal capacitive behavior.

Table **8.1** shows the calculated average specific capacitance of SDRHA/Li devices (three) at various scan rates, considering the active mass of SDRHA. The high specific capacitance of ~ 243 F/g_{SDRHA} is found for SDRHA/Li at 5 mV/sec.

Table 8.1. Performance of the SDRHA/Li device at various scan rates.

Specific capacitance (F/g_{SDRHA})	Scan rate (mv/sec)	Cell voltage
198±3	0.1	2.6
243±2	5	2.6
182±4	10	2.6

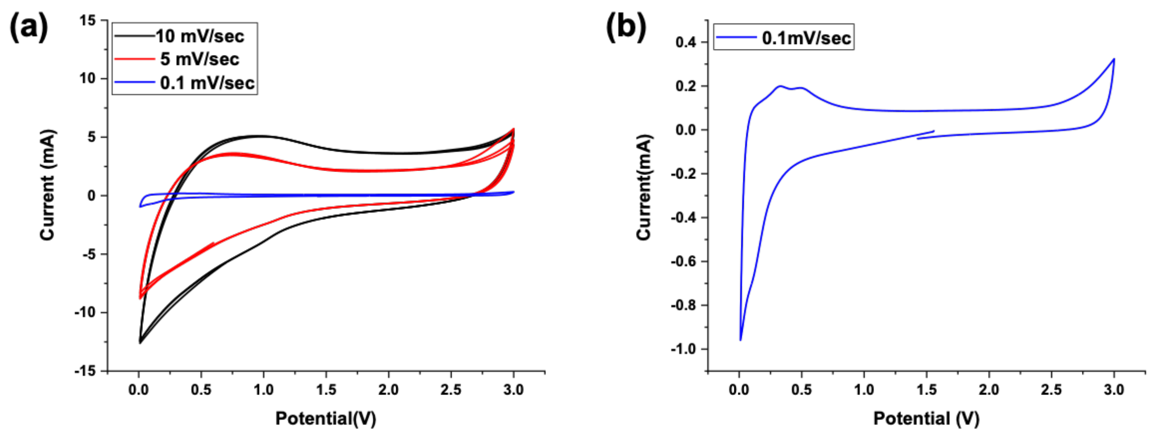

Figure 8.5. a. CV plots of SDRHA/ Li half-cell in a potential range of 3 - 0.01 V at a scan rate of 10 mV/sec (black), 5 mV/sec (red), and b. 0.1 mV/sec (blue).

For comparison, Table **8.2** lists typical supercapacitor systems using rice hull derived, activated carbon electrodes and their associated performance. These reported EDLCs offer high specific capacitance similar to the hybrid LICs assembled with SDRHA electrodes. Even though most of the studies demonstrate high surface area carbons from rice hulls, it was found that the specific capacitance is not linearly proportional to surface area.[46] It is important to note that the specific capacitance of these hybrid LICs is calculated based on the SDRHA mass, hence it is expected to increase if one only considers the active material to be carbon (33 wt.%). In addition, the electrolytes used in these systems play a great role in limiting the operating voltage of the capacitors, which limits the energy density. The cell voltage of EDLCs based on aqueous electrolyte is lower than 1 V compared to organic electrolytes (3 V).[57]

Table 8.2. Carbon based supercapacitors and their performance.

Electrolyte	Electrode	Capacitance (F/g)	Scan rate (mv/sec)	Ref
1 M H_2SO_4	Activated RHA	116±2	5	59
1 M $TEMABF_4$/PC	Activated RHA	80±13	5	59
6 M KOH	Nanoporous-activated RH	250	-	43
6 M KOH	Porous carbon-RH	368	2	36
3 M KCl	Activated porous carbon-RH	210	-	46
1 M Et_4NBF_4/PC	Carbon black	115	20	23
1 M $LiPF_6$ EC/DMC	Graphite/activated carbon	90	5	19
0.5 M Bu_4NBF_4/ACN	PANI/graphite	420	50	60
1 M $LiPF_6$/EC/DEC	Porous carbon flakes	126	-	61
1 M $TEABF_4$/ACN	Porous carbon nanosheets	120-150	1	62
1 M $TEABF_4$/HFIP	AC	110	1	63
1 M $TEABF_4$/PC	Graphene-CNT composite	110	-	64
1.1 M $LiPF_6$/EC/DEC/EMC	SDRHA/Li	243	5	This work

H_2SO_4 - sulfuric acid, $TEMABF_4$ - triethylmethylammonium tetrafluoroborate, PC - propylene carbonate, KOH - potassium hydroxide, KCl - potassium chloride, Et_4NBF_4 - tetraethylammonium tetrafluoroborate, DMC - dimethyl carbonate, Bu_4NBF_4 –

tetrabutylammonium tetrafluroborate, ACN – acetonitrile, HFIP- 1,1,1,3,3,3-hexafluoropropan-2-ol, and AC – activated carbon

The electrochemical performance of the SDRHA was tested using galvanostatic charge-discharge studies at selected c-rates. Figure **8.6** shows galvanostatic cycling of a SDRHA/Li half-cell between 2.5 – 0.01V. The half-cell was cycled at 0. 1C for 5 cycles to form a stable SEI as shown in the potential vs. time plot (Figure **8.6b**). The half-cell was then cycled at 0. 5C for 20 cycles between the range of 100 -150 h (Figure **8.6c**), 1C for 40 cycles (Figure **8.6d**), and 2C for 20 cycles (Figure **8.6e**), and finally back to 0.1C for 10 cycles.

The potential vs. time profile shows that the half-cell cycled to the targeted potentials with minimal polarization and IR drop for 400 h. The linear symmetric potential profile at various c-rates suggests capacitance behavior in the SDRHA/Li half-cell. The initial relatively flat plateau below 0.25 V, when cycled at a very slow scan rate of 0.1 C (Figure **8.6b**), corresponds to reaction between Li^+ and the nano-SiO_2 in the SDRHA. In contrast, the voltage profile of the SDRHA electrode, at higher c-rates (Figures **8.6c-e**), slopes down during discharge without any noticeable plateau, indicating silica depletion results in a more disordered crystal structure similar to hard carbon.[65]

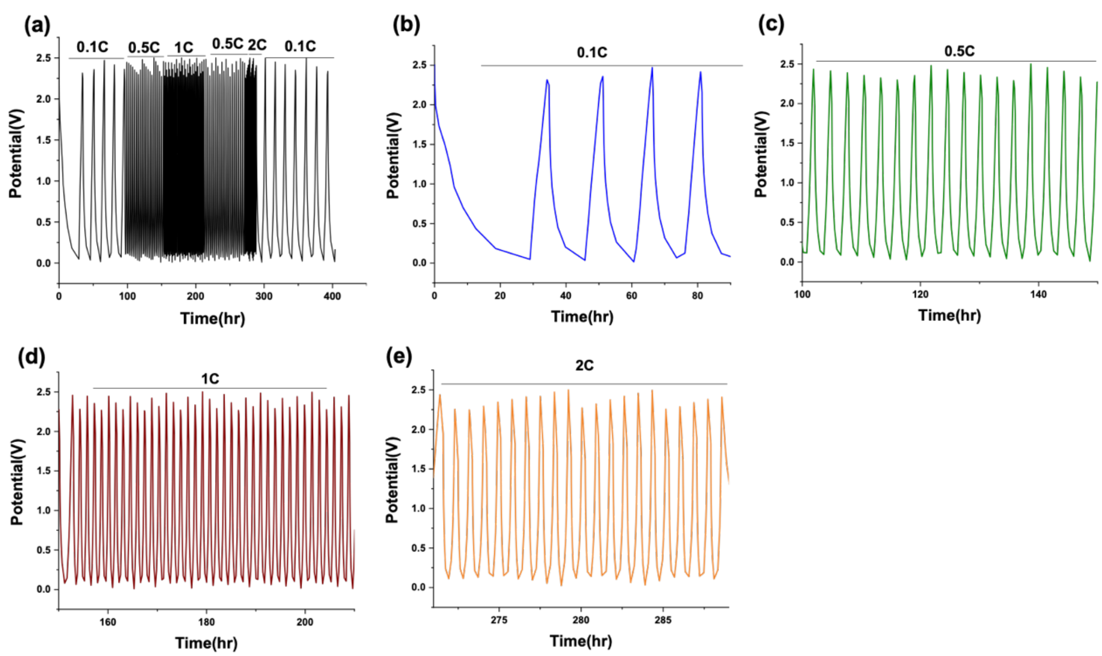

Figure 8.6. a. Potential vs. time plots of SDRHA/Li half-cell cycled between (2.5 - 0.01 V) at 0.1C b., 0.5C c., 1 C d., and 2 C e. rates.

The SDRHA/Li half-cell shows an initial capacity of 1000 mAh/g at 0.1C (Figure **8.6a**), which is much larger than of the reversible capacity of hard carbon (300 mAh/g).[52] Hence, the extra capacity is due to the presence of nano-SiO_2 in the SDRHA powder. Recent STEM studies, done by our group,[40] suggests homogenous nanoscale mixing of the amorphous SiO_2 and C in RHA. The particles sizes are reported to be on the order of 20-50 nm.[40] In general, SiO_2 is believed to be electrochemically inactive for lithium storage. In contrast, Wang et al.[52] demonstrated that composite nano-SiO_2 and hard carbon can react with Li to deliver a reversible capacity of 630 mAh/g. This means that the specific capacity of SDRHA (C_{SDRHA}) in the composite is ~1171 mAh/g_{SDRHA} which is calculated based on the reversible capacity of hard carbon (300 mAh/g) and SiO_2 (1675 mAh/g) as shown in equation *2*.

$$C_{SDRHA} = (300\ mAh/g \times 0.33) + (1675\ mAh/g \times 0.64) \qquad (2)$$

The initial specific capacity of SDRHA/Li is 1000 mAh/g_{SDRHA} which is 85 % of the theoretical capacity. However, this initial capacity is not reversible as shown by the fast capacity decay (400 mAh/g_{SDRHA}) in the second cycle, suggesting the formation of irreversible reduction of SiO_2. It has been reported that amorphous nano-SiO_2 can be reduced to form Si and amorphous Li_2O or crystalline Li_4SiO_4.[52] This irreversible formation of Li_4SiO_4 and Li_2O is supported by the CV peak and discharge plateau ~0.25 V in the initial discharge cycle as demonstrated in Figures **8.5b** and **8.6a**, respectively. The reduced Si is proposed to react with Li^+ to form Li-Si alloys resulting in the extra reversible capacity of the hybrid LICs at lower c-rate (0.1C). The formation of Li_4SiO_4/Li_2O reduced the excess Li^+ content that could contribute to uneven Li deposition or Li-related aging byproducts.[51]

The initial irreversible capacity could also be attributed to the formation of SEI as supported by the current response ~ 0.45 V (CV, Figure **8.5b**). It is known that the Li ions that accumulate in the free spaces of hard carbons can become passivated.[47] Hence, the initial irreversible capacity of hard carbon is higher than graphite.[66,67] However, superior rate and cycle performance can be obtained from hard carbons, making it attractive electrode for hybrid LICs. [68,69]

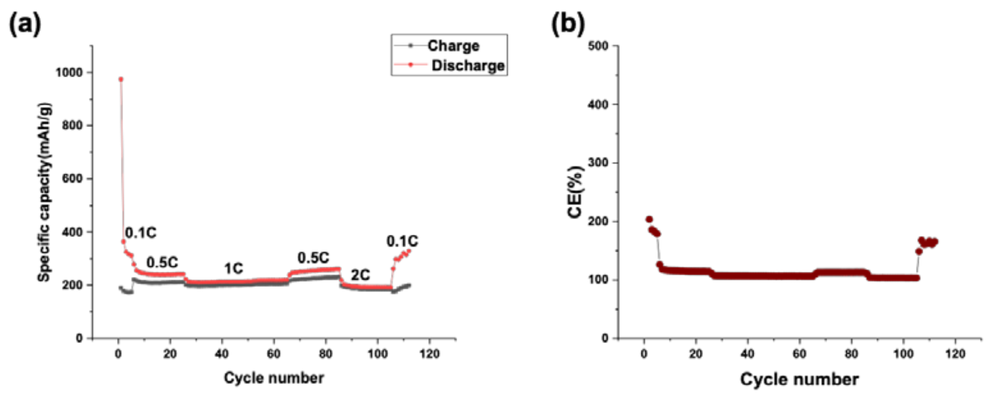

Figure 8.7. a. galvanostatic plots of SDRHA/Li half-cell cycled between (2.5 - 0.01 V). The specific capacity is based on the carbon wt.%. in SDRHA. b. columbic efficiency vs. cycle number plot.

The capacity decreases to 250 mAh/g_{SDRHA} at 0.5 C and further decreases to 225 mAh/g_{SDRHA} at 1C **(**Figure **8.7a)**. The capacity loss is retained (~250 mAh/g_{SDRHA}) when the c-rate was decreased to 0.5C. However, the capacity decreases to 200 mAh/g_{SDRHA} when the c-rate was increased to 2C. Gradually, the SDRHA/Li cell shows an increase in discharge capacity (400 mAh/ g_{SDRHA}) when the c-rate is returned to 0.1C. The half-cell maintained a columbic efficiency ~100 % for 400 h as shown in Figure **8.7b**. The increase in columbic efficiency at 0.1C is ascribed to the increase in irreversible discharge capacity, attributed to formation of Li_4SiO_4 and Li_2O with consumption of Li.

The capacity depends on the interfacial area which relies on electrode preparation such as size, shape, binder, and porosity (SSA). The potential vs. time profile offers highly linear and symmetrical curves with little IR drop (0.01V), indicating a rapid *I-V* response and excellent electrochemical reversibility, supported by high coloumbic efficiency. Hence, this leads to the conclusion that the SDRHA electrode offers superior electrochemical properties as supported by the CV and galvanostatic cycling studies shown in Figures **8.5** and **8.7** respectively. This might be ascribed to the highly irregular and disordered microstructure, composed of closely and randomly connected graphene layers (Figure **8.4**), which is reported to enhance fast Li^+ mobility during the charge/discharge process.[65] The reversibility of Li^+ uptake and formation of Li_4SiO_4 or Li_2O could be further improved by optimizing the surface of SiO_2 in SDRHA, which remains future work.

8.3.3 Electrochemical performance of full cells

The energy density of a hybrid electrochemical supercapacitor is proportional to the square of the operating voltage multiplied by the capacitance.

Improving both the electrochemical stability potential window and the capacitance will greatly contribute to enhancing both energy and power densities. Hence, hybrid LICs were assembled using the high potential NMC622 cathode, and SDRHA as the anode with 1.1 M $LiPF_6$/EC/DEC/EMC as the electrolyte. This hybrid LIC is proposed to bridge the gap between the high energy density offered by LIBs and the high-power densities obtained from the EDLCs.[18] The open circuit voltage increased from 2.5 to 3.2 V by changing the Li electrode with high potential NMC622 cathode. Many hybrid LICs have been studied extensively using composite cathode electrodes with Li-ion battery materials diluted with EDLC materials to enhance the rate performance, tap density, and increase specific capacity.[18,20,39,65] The main limitations to these hybrid LICs are the lack of a composite cathode electrode and the stability of the pre-lithiated anode.

Figure **8.8a** shows CV curves for SDRHA/NMC622 cells at scan rates of 5, 10, 20, 50, 100 and 500 mv/sec with potential range 2.4-4.2 V. The rectangular shape of the CV curves becomes distorted with increasing scan rate. A slightly distorted and symmetric rectangular-like shape is typical for EDLC electrodes.[19,53] All the CV curves do not show any redox behavior demonstrating the clear capacitance behavior resulting from high conductivity and stable porous structure of SDRHA electrode. Figure **8.8b** shows that the relationship between scan rates and peak currents are nearly linear (correlation r = 0.98), which indicates that the redox reaction is confined to the surface and not diffusion-limited.[54]

Table **8.3** shows the calculated specific capacitance of the SDRHA/NMC622 device at various scan rates, considering that the active mass of SDRHA. The highest specific capacitance of ~ 354 F/g_{SDRHA} is reported for SDRHA/NMC622 at 5 mV/sec.

Table 8.3. Performance of the SDRHA/NMC622 device at various scan rates.

Specific capacitance (F/g_{SDRHA})	Scan rate (mv/sec)	Cell voltage
354±5	5	3.2
269±2	10	3.2
184±3	20	3.2
108±4	50	3.2
65±2	100	3.2

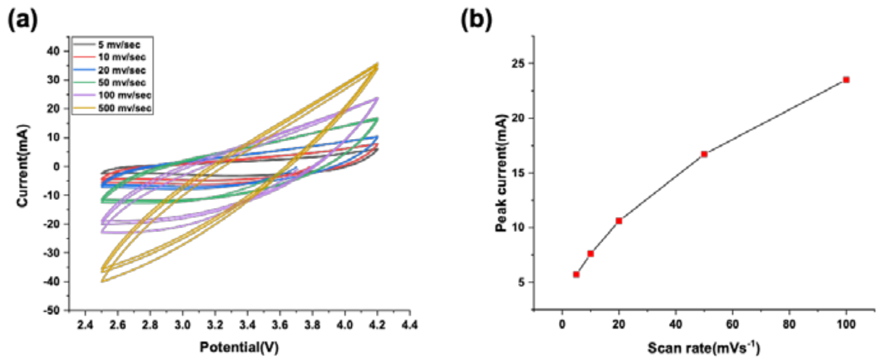

Figure 8.8. a. CV plots of SDRHA/NMC622 half-cell at different scan rates and b. relationship between the redox peak current and scanning rates.

The capacity ratio of the cathode to anode is calculated based on the reversible lithium intercalation and de-intercalation specific capacity of the hard carbon (~300 mAh/g_{carbon}). There is a competing relationship between the ionic adsorption of the EDLC contributed by the SDRHA and the faradic electrochemical redox reaction caused by Li-ion intercalation in the NMC622. In general, the faradic process is suppressed by the fast surface adsorption/desorption process, thus it has been suggested that one should not fully discharge the cathode to minimize the capacity loss and maintain the high energy density.[65]

Hence, it is necessary to optimize the initial cycling stages. A special procedure targeting formation cycles was investigated to overcome the potential drop. The hybrid LICs were charged at 0.5 C to a given voltage and were allowed to relax at open circuit. Figure **8.9a** shows the variation of the cell potential and its effect on formation of a stable SEI as a potential vs. time plot. The hybrid LICs voltage falls to 3.7 V during the relaxation period. It is worth noting that the total self-discharge of the hybrid LICs is the sum of the individual self-discharges taking place at each electrode.[19] Hence, the formation step (Figure **8.9b**) is necessary to overcome voltage drops and minimize the self-discharge rate. The NMC/SDRHA cell showed an almost ideal linear voltage profile for the last four cycles, indicating the formation of a stable SEI. This is also supported by the increase in columbic efficiency in the last four cycles (Figure **8.9c**).

Figure **8.9d** shows the specific capacity vs cycle number. The hybrid LIC cells show an initial charge capacity of 375 mAh/g at 0.5 C. This capacity is maintained through the first 14 cycles. The discharge capacity gradually increases from 50 to 300 mAh/g as the cell matures and a stable SEI forms. The specific capacitance (Figure **8.9e**) also showed similar phenomena where the charge capacitance is consistent (100 F/g) and the discharge capacitance gradually increases from

25 to 100 F/g as a stable SEI forms on the SDRHA surface. This simple formation step results in optimal behavior for the hybrid LICs as demonstrated in **Figure 8.10**.

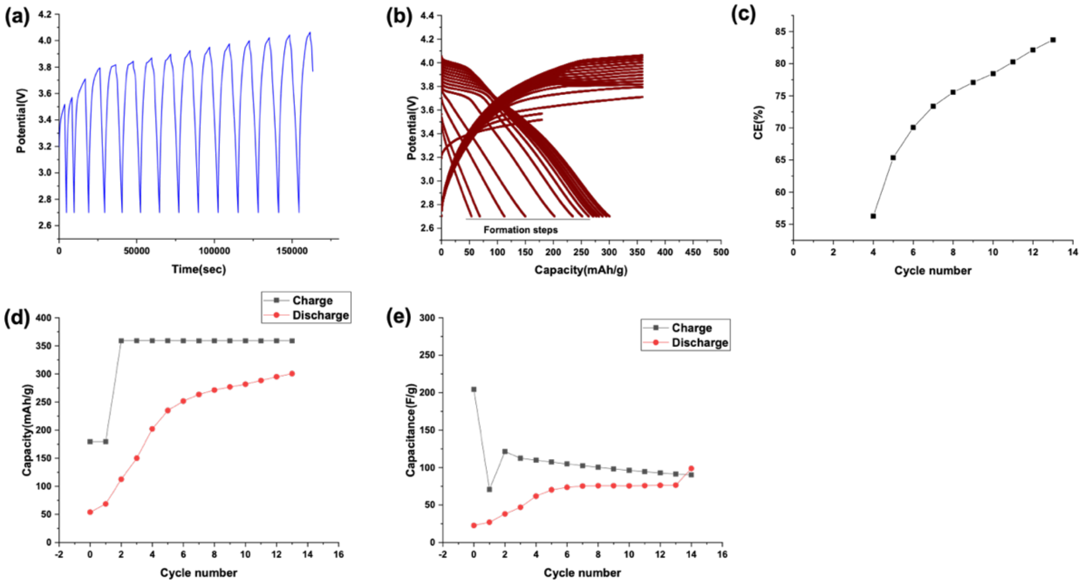

Figure 8.9. Electrochemical performance of and SDRHA/NMC622. a. potential versus time profile and (b) charge-discharge curves, c. columbic efficiency, d. specific capacity, and e. specific capacitance as function of cycle number.

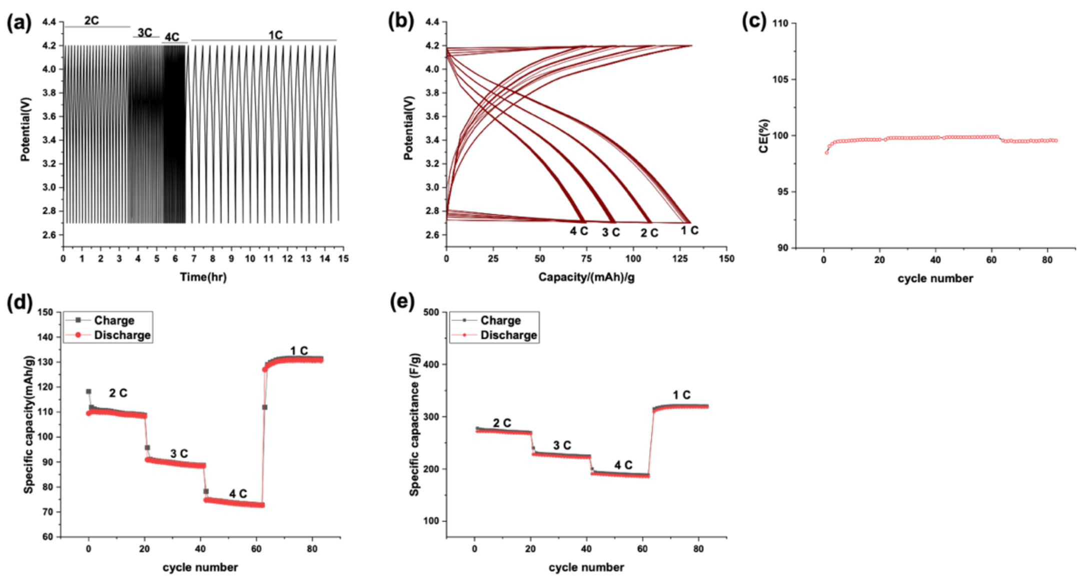

Figure 8.10. Electrochemical performance of and SDRHA/NMC622 after SEI formation. a. potential versus time profile and b. charge-discharge curves, c. columbic efficiency, d. specific capacity, and e. specific capacitance as function of cycle number.

Figure **8.10a** presents the voltage profile curves for SDRHA/NMC full-cells between 2.7– 4.2 V after SEI formation. The full cell shows a linear voltage profile with a downward slope during the lithium intercalation process without showing any noticeable plateau, which is ascribed to the amorphous or disordered crystal structure of SDRHA. The anodic/cathodic curves (Figure **8.10b**) of the full cell also show a linear shape indicating the capacitive nature of the device. The full cell charges and discharges to the targeted potentials without shorting at very high c-rates (1-4 C).

Figure **8.10d** presents the galvanostatic charge-discharge cycling performance of SDRHA/NMC622 cells. The full cell was cycled at 2, 3, 4, and 1 C for 20 cycles. The full cell showed an initial charge capacity of 110 mAh/g at 2 C. This capacity was maintained throughout the first 20 cycles. The capacity gradually decreased to 90 and 70 mAh/g as the C-rate increased to 3 and 4 C, respectively. The capacity increased to ~130 mAh/g when the C-rate was decreased to 1 C. The space gap between the adjacent carbon layers is proposed to be larger than graphite, ascribed to the hard carbon nature of SDRHA, which enhances Li-ion mobility during the charge/discharge processes.

The full cell shows an initial specific capacitance of ~300 F/g at 2 C as seen in Figure **8.10e**. This capacity was maintained throughout the first 20 cycles. The specific capacitance gradually decreased to 250 and 200 F/g as the C-rate increased to 3 and 4 C, respectively. The capacity increased to ~325 F/g when the C-rate was decreased to 1 C. This superior rate performance is ascribed to the high surface area and microstructure of SDRHA. High efficiency of ~ 100% was maintained for the 80 cycles, Figure **8.10c**, indicating the reversibility and high-power rate performance of SDRHA/NMC hybrid LICs.

Table 8.4. High potential-based hybrid LICs and their performance.

Electrolyte	Electrode	Capacity (mAh/g)	Ref
1 M $LiPF_6$/EC/DMC	AC/$LiFePO_4$	18	[70]
1 M $LiPF_6$/EC/DMC	AC/$LiNi_{0.5}Mn_{1.5}O_4$	25	[21]
1 M $LiPF_6$/EC/DMC/EMC	AC+$LiFePO_4$/$Li_4Ti_5O_{12}$	30	[71]
1 M $LiPF_6$/EC	AC+$LiNi_{0.5}Co_{0.2}Mn_{0.3}O_2$/graphite	80	[72]
$LiClO_4$/AN	AC/$LiMn_2O_4$	106	[73]
1 M $LiPF_6$/EC/DMC/DEC	AC/$LiNi_{0.5}Co_{0.2}Mn_{0.3}O_2$	107	[65]
1 M $LiPF_6$/EC/DMC	AC/$LiNi_{0.5}Co_{0.2}Mn_{0.3}O_2$	114	[74]
1 M $LiPF_6$/EC/DMC	AC/$LiNi_{0.5}Co_{0.2}Mn_{0.3}O_2$	120	[29]
1 M $LiPF_6$/EC/DMC	AC/$LiNi_{0.5}Co_{0.2}Mn_{0.3}O_2$	225	[18]
1.1 M $LiPF_6$/EC/DEC/EMC	SDRHA/NMC622	130	This work

For comparison, Table **8.4** lists typical hybrid LICs previously reported using high potential cathode electrodes and their associated performance.

The SDRHA/NMC622 cell showed relatively higher specific capacity compared to cells assembled with activated carbons. A further improvement in energy/power density could be achieved by using composite cathodes. In the future, SDRHA/NMC composite cathodes will be investigated to enhance the double layer area and charge storage on the positive electrode. It is important to identify and charge storage mechanisms in the composite electrodes.

Electrochemical impedance spectra (EIS) in the form of Nyquist plots of SDRHA/Li and SDRHA/NMC are shown in Figure **8.11**. In general, EIS is used to understand the electrochemical behavior at the interface between the electrode and the electrolyte. The solid electrolyte interface resistance (R_{SEI}) is related to the high-frequency region. The lower frequency semi-circle is related to the charge transfer resistance (R_{ct}), and the 45° capacitive slope is related to the Warburg impedance. The R_{ct} of the SDRHA with Li metal and NMC622 electrodes using organic electrolyte is presented in Table **8.5**. The total resistance of the half-cell is much higher than the full cell, which is ascribed to the increase in resistance between the Li metal and solid electrolyte interface, and the intrinsic resistance of Li metal. Due to the presence of SDRHA, capacitive materials, both hybrid LICs deliver larger Faradic responses than conventional batteries. The SDRHA/NMC622 cell showed ideal capacitive behavior with a nearly vertical line parallel to the imaginary axis.

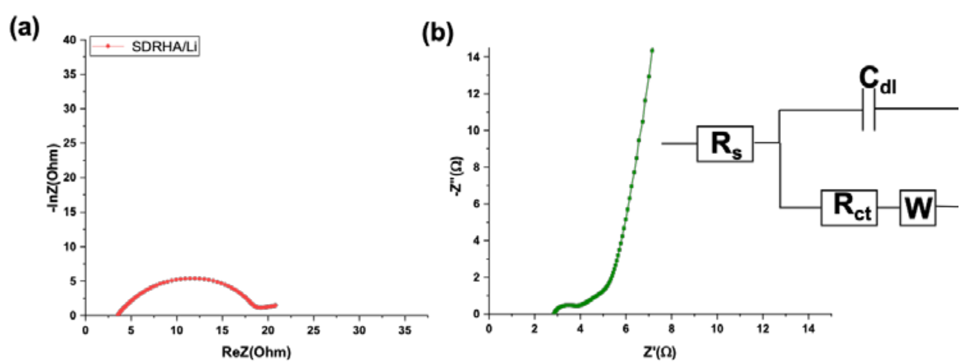

Figure 8.11. Nyquist impedance spectra of (a) SDRHA/Li, and (b) SDRHA/NMC. The inset shows the equivalent electrical circuit.

Table 8.5. Charge-transfer resistance of the half and full hybrid LICs.

Electrode	R_e (Ω)	C_{dl} (μF)	Rct (Ω)
SDRHA/Li	3.5	1 .2	4.5
SDRHA/NMC622	3	2.5	18.4

8.4 Conclusions

In summary, we have demonstrated the use of SRHA, derived from a renewable bio-source, RHA, as a potential electrode material for hybrid LICs without any chemical activation. The high surface area and the microstructure of the SDRHA results in high Li-ion mobility and increase surface charge absorption/desorption when assembled in both half and full-cell configurations. The cyclic voltammetry at a scanning rate of 5 mV/sec demonstrates a high specific capacitance of 243 and 354 F/g_{SDRHA} for the half and full hybrid LICs, respectively. Traditional organic electrolyte based EDLCs demonstrate specific capacities in the ranges of 100-150 F/g. The galvanostatic charge-discharge profiles also indicate high specific capacity and excellent columbic efficiencies. We have demonstrated the synthesis of a clean and eco-friendly electrode that is an alternative to activated carbon. Finally, SDRHA is a carbon neutral material.

Reference

(1) Jacobson, M. Z. Review of Solutions to Global Warming, Air Pollution, and Energy Security. *Energy and Environmental Science*. 2009. https://doi.org/10.1039/b809990c.

(2) Botkin, D. B.; Saxe, H.; Araújo, M. B.; Betts, R.; Bradshaw, R. H. W.; Cedhagen, T.; Chesson, P.; Dawson, T. P.; Etterson, J. R.; Faith, D. P.; Ferrier, S.; Guisan, A.; Hansen, A. S.; Hilbert, D. W.; Loehle, C.; Margules, C.; New, M.; Sobel, M. J.; Stockwell, D. R. B. Forecasting the Effects of Global Warming on Biodiversity. *Bioscience* **2007**. https://doi.org/10.1641/b570306.

(3) Walther, G. R.; Post, E.; Convey, P.; Menzel, A.; Parmesan, C.; Beebee, T. J. C.; Fromentin, J. M.; Hoegh-Guldberg, O.; Bairlein, F. Ecological Responses to Recent Climate Change. *Nature*. 2002. https://doi.org/10.1038/416389a.

(4) Hansen, J.; Sato, M.; Ruedy, R.; Lacis, A.; Oinas, V. Global Warming in the Twenty-First Century: An Alternative Scenario. *Proc. Natl. Acad. Sci. U. S. A.* **2000**. https://doi.org/10.1073/pnas.170278997.

(5) Frölicher, T. L.; Winton, M.; Sarmiento, J. L. Continued Global Warming after CO2 Emissions Stoppage. *Nat. Clim. Chang.* **2014**. https://doi.org/10.1038/nclimate2060.

(6) Tie, S. F.; Tan, C. W. A Review of Energy Sources and Energy Management System in Electric Vehicles. *Renewable and Sustainable Energy Reviews*. 2013. https://doi.org/10.1016/j.rser.2012.11.077.

(7) Hu, M.; Pang, X.; Zhou, Z. Review Recent Progress in High-Voltage Lithium Ion Batteries. *J. Power Sources* **2013**, *237*, 2013. https://doi.org/10.1016/j.jpowsour.2013.03.024.

(8) European Association for Battery Electric Vehicles. Energy Consumption , CO2 Emissions and Other Considerations Related to Battery Electric Vehicles. *Energy* **2009**.

(9) Kamaya, N.; Homma, K.; Yamakawa, Y.; Hirayama, M.; Kanno, R.; Yonemura, M.; Kamiyama, T.; Kato, Y.; Hama, S.; Kawamoto, K.; Mitsui, A. A Lithium Superionic Conductor. *Nat. Mater.* **2011**, *10* (9), 682–686. https://doi.org/10.1038/nmat3066.

(10) Hidrue, M. K.; Parsons, G. R.; Kempton, W.; Gardner, M. P. Willingness to Pay for Electric Vehicles and Their Attributes. *Resour. Energy Econ.* **2011**. https://doi.org/10.1016/j.reseneeco.2011.02.002.

(11) Nitta, N.; Wu, F.; Lee, J. T.; Yushin, G. Li-Ion Battery Materials: Present and Future. *Materials Today*. 2015. https://doi.org/10.1016/j.mattod.2014.10.040.

(12) Lu, L.; Han, X.; Li, J.; Hua, J.; Ouyang, M. A Review on the Key Issues for Lithium-Ion Battery Management in Electric Vehicles. *Journal of Power Sources*. 2013. https://doi.org/10.1016/j.jpowsour.2012.10.060.

(13) Zubi, G.; Dufo-López, R.; Carvalho, M.; Pasaoglu, G. The Lithium-Ion Battery: State of the Art and Future Perspectives. *Renewable and Sustainable Energy Reviews*. 2018. https://doi.org/10.1016/j.rser.2018.03.002.

(14) Chen, Y. T.; Jena, A.; Pang, W. K.; Peterson, V. K.; Sheu, H. S.; Chang, H.; Liu, R. S. Voltammetric Enhancement of Li-Ion Conduction in Al-Doped Li7-XLa3Zr2O12 Solid Electrolyte. *J. Phys. Chem. C* **2017**. https://doi.org/10.1021/acs.jpcc.7b04004.

(15) Notter, D. A.; Gauch, M.; Widmer, R.; Wäger, P.; Stamp, A.; Zah, R.; Althaus, H. J. Contribution of Li-Ion Batteries to the Environmental Impact of Electric Vehicles. *Environ. Sci. Technol.* **2010**. https://doi.org/10.1021/es903729a.
(16) Väyrynen, A.; Salminen, J. Lithium Ion Battery Production. *J. Chem. Thermodyn.* **2012**. https://doi.org/10.1016/j.jct.2011.09.005.
(17) Buqa, H.; Goers, D.; Holzapfel, M.; Spahr, M. E.; Novák, P. High Rate Capability of Graphite Negative Electrodes for Lithium-Ion Batteries. *J. Electrochem. Soc.* **2005**. https://doi.org/10.1149/1.1851055.
(18) Hagen, M.; Yan, J.; Cao, W. J.; Chen, X. J.; Shellikeri, A.; Du, T.; Read, J. A.; Jow, T. R.; Zheng, J. P. Hybrid Lithium-Ion Battery-Capacitor Energy Storage Device with Hybrid Composite Cathode Based on Activated Carbon / LiNi0.5Co0.2Mn0.3O2. *J. Power Sources* **2019**, *433* (May). https://doi.org/10.1016/j.jpowsour.2019.05.095.
(19) Khomenko, V.; Raymundo-Piñero, E.; Béguin, F. High-Energy Density Graphite/AC Capacitor in Organic Electrolyte. *J. Power Sources* **2008**, *177* (2), 643–651. https://doi.org/10.1016/j.jpowsour.2007.11.101.
(20) Sivakkumar, S. R.; Pandolfo, A. G. Evaluation of Lithium-Ion Capacitors Assembled with Pre-Lithiated Graphite Anode and Activated Carbon Cathode. *Electrochim. Acta* **2012**, *65*, 280–287. https://doi.org/10.1016/j.electacta.2012.01.076.
(21) Li, H.; Cheng, L.; Xia, Y. A Hybrid Electrochemical Supercapacitor Based on a 5 V Li-Ion Battery Cathode and Active Carbon. *Electrochem. Solid-State Lett.* **2005**, *8* (9), 4–8. https://doi.org/10.1149/1.1960007.
(22) Aravindan, V.; Gnanaraj, J.; Lee, Y. S.; Madhavi, S. Insertion-Type Electrodes for Nonaqueous Li-Ion Capacitors. *Chemical Reviews*. 2014. https://doi.org/10.1021/cr5000915.
(23) Krause, A.; Kossyrev, P.; Oljaca, M.; Passerini, S.; Winter, M.; Balducci, A. Electrochemical Double Layer Capacitor and Lithium-Ion Capacitor Based on Carbon Black. *J. Power Sources* **2011**, *196* (20), 8836–8842. https://doi.org/10.1016/j.jpowsour.2011.06.019.
(24) Amatucci, G. G.; Badway, F.; Du Pasquier, A.; Zheng, T. An Asymmetric Hybrid Nonaqueous Energy Storage Cell. *J. Electrochem. Soc.* **2001**. https://doi.org/10.1149/1.1383553.
(25) Cao, W. J.; Greenleaf, M.; Li, Y. X.; Adams, D.; Hagen, M.; Doung, T.; Zheng, J. P. The Effect of Lithium Loadings on Anode to the Voltage Drop during Charge and Discharge of Li-Ion Capacitors. *J. Power Sources* **2015**. https://doi.org/10.1016/j.jpowsour.2015.01.102.
(26) Hu, X.; Deng, Z.; Suo, J.; Pan, Z. A High Rate, High Capacity and Long Life (LiMn2O4 + AC)/Li4Ti5O12 Hybrid Battery-Supercapacitor. *J. Power Sources* **2009**. https://doi.org/10.1016/j.jpowsour.2008.11.033.
(27) Smith, P. H.; Tran, T. N.; Jiang, T. L.; Chung, J. Lithium-Ion Capacitors: Electrochemical Performance and Thermal Behavior. *J. Power Sources* **2013**. https://doi.org/10.1016/j.jpowsour.2013.06.012.
(28) Schroeder, M.; Winter, M.; Passerini, S.; Balducci, A. On the Use of Soft Carbon and Propylene Carbonate-Based Electrolytes in Lithium-Ion Capacitors. *J. Electrochem. Soc.* **2012**. https://doi.org/10.1149/2.050208jes.
(29) Hagen, M.; Cao, W. J.; Shellikeri, A.; Adams, D.; Chen, X. J.; Brandt, W.; Yturriaga, S. R.; Wu, Q.; Read, J. A.; Jow, T. R.; Zheng, J. P. Improving the Specific Energy of Li-Ion Capacitor Laminate Cell Using Hybrid Activated Carbon/LiNi0.5Co0.2Mn0.3O2 as Positive Electrodes. *J. Power Sources* **2018**, *379* (January), 212–218. https://doi.org/10.1016/j.jpowsour.2018.01.036.

(30) Puthusseri, D.; Aravindan, V.; Madhavi, S.; Ogale, S. Improving the Energy Density of Li-Ion Capacitors Using Polymer-Derived Porous Carbons as Cathode. *Electrochim. Acta* **2014**. https://doi.org/10.1016/j.electacta.2014.03.079.
(31) Ren, J. J.; Su, L. W.; Qin, X.; Yang, M.; Wei, J. P.; Zhou, Z.; Shen, P. W. Pre-Lithiated Graphene Nanosheets as Negative Electrode Materials for Li-Ion Capacitors with High Power and Energy Density. *J. Power Sources* **2014**. https://doi.org/10.1016/j.jpowsour.2014.04.076.
(32) Schroeder, M.; Menne, S.; Ségalini, J.; Saurel, D.; Casas-Cabanas, M.; Passerini, S.; Winter, M.; Balducci, A. Considerations about the Influence of the Structural and Electrochemical Properties of Carbonaceous Materials on the Behavior of Lithium-Ion Capacitors. *J. Power Sources* **2014**. https://doi.org/10.1016/j.jpowsour.2014.05.024.
(33) Gozin, M.; Weisman, A.; Ben-David, Y.; Milstein, D. Activation of a Carbon-Carbon Bond in Solution by Transition-Metal Insertion. *Nature* **1993**. https://doi.org/10.1038/364699a0.
(34) Abeykoon, N. C.; Bonso, J. S.; Ferraris, J. P. Supercapacitor Performance of Carbon Nanofiber Electrodes Derived from Immiscible PAN/PMMA Polymer Blends. *RSC Adv.* **2015**. https://doi.org/10.1039/c4ra16594b.
(35) Kobayashi, K.; Kitaura, R.; Kumai, Y.; Goto, Y.; Imagaki, S.; Shinohara, H. Fabrication of Single-Wall Carbon Nanotubes within the Channels of a Mesoporous Material by Catalyst-Supported Chemical Vapor Deposition. *Carbon N. Y.* **2009**. https://doi.org/10.1016/j.carbon.2008.11.011.
(36) Chen, H.; Wang, H.; Yang, L.; Xiao, Y.; Zheng, M.; Liu, Y.; Fu, H. High Specific Surface Area Rice Hull Based Porous Carbon Prepared for EDLCs. *Int. J. Electrochem. Sci.* **2012**, *7* (6), 4889–4897.
(37) Han, C.; Li, H.; Shi, R.; Xu, L.; Li, J.; Kang, F.; Li, B. Nanostructured Anode Materials for Non-Aqueous Lithium Ion Hybrid Capacitors. *Energy Environ. Mater.* **2018**. https://doi.org/10.1002/eem2.12009.
(38) Jagadale, A.; Zhou, X.; Xiong, R.; Dubal, D. P.; Xu, J.; Yang, S. Lithium Ion Capacitors (LICs): Development of the Materials. *Energy Storage Materials*. 2019. https://doi.org/10.1016/j.ensm.2019.02.031.
(39) Lang, J.; Zhang, X.; Liu, B.; Wang, R.; Chen, J.; Yan, X. The Roles of Graphene in Advanced Li-Ion Hybrid Supercapacitors. *Journal of Energy Chemistry*. 2018. https://doi.org/10.1016/j.jechem.2017.11.020.
(40) Marchal, J. C.; Krug, D. J.; McDonnell, P.; Sun, K.; Laine, R. M. A Low Cost, Low Energy Route to Solar Grade Silicon from Rice Hull Ash (RHA), a Sustainable Source. *Green Chem.* **2015**, *17* (7), 3931–3940. https://doi.org/10.1039/c5gc00622h.
(41) Pode, R. Potential Applications of Rice Husk Ash Waste from Rice Husk Biomass Power Plant. *Renew. Sustain. Energy Rev.* **2016**, *53*, 1468–1485. https://doi.org/10.1016/j.rser.2015.09.051.
(42) Liu, Y.; Guo, Y.; Zhu, Y.; An, D.; Gao, W.; Wang, Z.; Ma, Y.; Wang, Z. A Sustainable Route for the Preparation of Activated Carbon and Silica from Rice Husk Ash. *J. Hazard. Mater.* **2011**, *186* (2–3), 1314–1319. https://doi.org/10.1016/j.jhazmat.2010.12.007.
(43) Xu, H.; Gao, B.; Cao, H.; Chen, X.; Yu, L.; Wu, K.; Sun, L.; Peng, X.; Fu, J. Nanoporous Activated Carbon Derived from Rice Husk for High Performance Supercapacitor. *J. Nanomater.* **2014**, *2014*, 1–8. https://doi.org/10.1155/2014/714010.
(44) Laine, R. M.; Furgal, J. C.; Doan, P.; Pan, D.; Popova, V.; Zhang, X. Avoiding Carbothermal Reduction: Distillation of Alkoxysilanes from Biogenic, Green, and Sustainable Sources. *Angew. Chemie - Int. Ed.* **2016**. https://doi.org/10.1002/anie.201506838.

(45) Li, C. D.; Saeed, M. U.; Pan, N.; Chen, Z. F.; Xu, T. Z. Fabrication and Characterization of Low-Cost and Green Vacuum Insulation Panels with Fumed Silica/Rice Husk Ash Hybrid Core Material. *Mater. Des.* **2016**. https://doi.org/10.1016/j.matdes.2016.06.071.
(46) Guo, Y.; Qi, J.; Jiang, Y.; Yang, S.; Wang, Z.; Xu, H. Performance of Electrical Double Layer Capacitors with Porous Carbons Derived from Rice Husk. *Mater. Chem. Phys.* **2003**, *80* (3), 704–709. https://doi.org/10.1016/S0254-0584(03)00105-6.
(47) He, X.; Ling, P.; Yu, M.; Wang, X.; Zhang, X.; Zheng, M. Rice Husk-Derived Porous Carbons with High Capacitance by ZnCl2 Activation for Supercapacitors. *Electrochim. Acta* **2013**. https://doi.org/10.1016/j.electacta.2013.05.050.
(48) Liu, D.; Zhang, W.; Lin, H.; Li, Y.; Lu, H.; Wang, Y. A Green Technology for the Preparation of High Capacitance Rice Husk-Based Activated Carbon. *J. Clean. Prod.* **2016**. https://doi.org/10.1016/j.jclepro.2015.07.005.
(49) Isoda, N.; Rodrigues, R.; Silva, A.; Gonçalves, M.; Mandelli, D.; Figueiredo, F. C. A.; Carvalho, W. A. Optimization of Preparation Conditions of Activated Carbon from Agriculture Waste Utilizing Factorial Design. *Powder Technol.* **2014**. https://doi.org/10.1016/j.powtec.2014.02.029.
(50) Li, B.; Xiao, Z.; Chen, M.; Huang, Z.; Tie, X.; Zai, J.; Qian, X. Rice Husk-Derived Hybrid Lithium-Ion Capacitors with Ultra-High Energy. *J. Mater. Chem. A* **2017**. https://doi.org/10.1039/c7ta07088h.
(51) Kumagai, S.; Abe, Y.; Saito, T.; Eguchi, T.; Tomioka, M.; Kabir, M.; Tashima, D. Lithium-Ion Capacitor Using Rice Husk-Derived Cathode and Anode Active Materials Adapted to Uncontrolled Full-Pre-Lithiation. *J. Power Sources* **2019**. https://doi.org/10.1016/j.jpowsour.2019.226924.
(52) Guo, B.; Shu, J.; Wang, Z.; Yang, H.; Shi, L.; Liu, Y.; Chen, L. Electrochemical Reduction of Nano-SiO2 in Hard Carbon as Anode Material for Lithium Ion Batteries. *Electrochem. commun.* **2008**. https://doi.org/10.1016/j.elecom.2008.09.032.
(53) Prabunathan, P.; Sethuraman, K.; Alagar, M. MnO2-Doped, Polyaniline-Grafted Rice Husk Ash Nanocomposites and Their Electrochemical Capacitor Applications. *RSC Adv.* **2014**, *4* (88), 47726–47734. https://doi.org/10.1039/c4ra04633a.
(54) Hong, K. L.; Qie, L.; Zeng, R.; Yi, Z. Q.; Zhang, W.; Wang, D.; Yin, W.; Wu, C.; Fan, Q. J.; Zhang, W. X.; Huang, Y. H. Biomass Derived Hard Carbon Used as a High Performance Anode Material for Sodium Ion Batteries. *J. Mater. Chem. A* **2014**, *2* (32), 12733–12738. https://doi.org/10.1039/c4ta02068e.
(55) Chaudhary, D. S.; Jollands, M. C. Characterization of Rice Hull Ash. *J. Appl. Polym. Sci.* **2004**. https://doi.org/10.1002/app.20217.
(56) Hori, H.; Shikano, M.; Kobayashi, H.; Koike, S.; Sakaebe, H.; Saito, Y.; Tatsumi, K.; Yoshikawa, H.; Ikenaga, E. Analysis of Hard Carbon for Lithium-Ion Batteries by Hard X-Ray Photoelectron Spectroscopy. *J. Power Sources* **2013**. https://doi.org/10.1016/j.jpowsour.2013.05.160.
(57) Li, Y.; Han, J. T.; Wang, C. A.; Xie, H.; Goodenough, J. B. Optimizing Li^+ Conductivity in a Garnet Framework. *J. Mater. Chem.* **2012**. https://doi.org/10.1039/c2jm31413d.
(58) Pandolfo, A. G.; Hollenkamp, A. F. Carbon Properties and Their Role in Supercapacitors. *Journal of Power Sources*. 2006. https://doi.org/10.1016/j.jpowsour.2006.02.065.
(59) Kumagai, S.; Sato, M.; Tashima, D. Electrical Double-Layer Capacitance of Micro- and Mesoporous Activated Carbon Prepared from Rice Husk and Beet Sugar. *Electrochim. Acta* **2013**, *114*, 617–626. https://doi.org/10.1016/j.electacta.2013.10.060.

(60) Zhang, H.; Wang, J.; Chen, Y.; Wang, Z.; Wang, S. Long-Term Cycling Stability of Polyaniline on Graphite Electrodes Used for Supercapacitors. *Electrochim. Acta* **2013**. https://doi.org/10.1016/j.electacta.2013.04.114.
(61) Han, J.; Xu, G.; Ding, B.; Pan, J.; Dou, H.; MacFarlane, D. R. Porous Nitrogen-Doped Hollow Carbon Spheres Derived from Polyaniline for High Performance Supercapacitors. *J. Mater. Chem. A* **2014**. https://doi.org/10.1039/c3ta15271e.
(62) Sevilla, M.; Fuertes, A. B. Direct Synthesis of Highly Porous Interconnected Carbon Nanosheets and Their Application as High-Performance Supercapacitors. *ACS Nano* **2014**. https://doi.org/10.1021/nn501124h.
(63) Francke, R.; Cericola, D.; Kötz, R.; Weingarth, D.; Waldvogel, S. R. Novel Electrolytes for Electrochemical Double Layer Capacitors Based on 1,1,1,3,3,3-Hexafluoropropan-2-Ol. *Electrochim. Acta* **2012**, *62*, 372–380. https://doi.org/10.1016/j.electacta.2011.12.050.
(64) Jung, N.; Kwon, S.; Lee, D.; Yoon, D. M.; Park, Y. M.; Benayad, A.; Choi, J. Y.; Park, J. S. Synthesis of Chemically Bonded Graphene/Carbon Nanotube Composites and Their Application in Large Volumetric Capacitance Supercapacitors. *Adv. Mater.* **2013**. https://doi.org/10.1002/adma.201302788.
(65) Sun, X.; Zhang, X.; Zhang, H.; Xu, N.; Wang, K.; Ma, Y. High Performance Lithium-Ion Hybrid Capacitors with Pre-Lithiated Hard Carbon Anodes and Bifunctional Cathode Electrodes. *J. Power Sources* **2014**. https://doi.org/10.1016/j.jpowsour.2014.07.146.
(66) Zheng, H.; Qu, Q.; Zhang, L.; Liu, G.; Battaglia, V. S. Hard Carbon: A Promising Lithium-Ion Battery Anode for High Temperature Applications with Ionic Electrolyte. *RSC Adv.* **2012**. https://doi.org/10.1039/c2ra20536j.
(67) Buiel, E.; Dahn, J. R. Li-Insertion in Hard Carbon Anode Materials for Li-Ion Batteries. *Electrochim. Acta* **1999**. https://doi.org/10.1016/S0013-4686(99)00198-X.
(68) Kim, J. H.; Kim, J. S.; Lim, Y. G.; Lee, J. G.; Kim, Y. J. Effect of Carbon Types on the Electrochemical Properties of Negative Electrodes for Li-Ion Capacitors. *J. Power Sources* **2011**. https://doi.org/10.1016/j.jpowsour.2011.08.081.
(69) Sivakkumar, S. R.; Pandolfo, A. G. Carbon Nanotubes/Amorphous Carbon Composites as High-Power Negative Electrodes in Lithium Ion Capacitors. *J. Appl. Electrochem.* **2014**. https://doi.org/10.1007/s10800-013-0606-6.
(70) Shellikeri, A.; Yturriaga, S.; Zheng, J. S.; Cao, W.; Hagen, M.; Read, J. A.; Jow, T. R.; Zheng, J. P. Hybrid Lithium-Ion Capacitor with LiFePO4/AC Composite Cathode - Long Term Cycle Life Study, Rate Effect and Charge Sharing Analysis. *J. Power Sources* **2018**. https://doi.org/10.1016/j.jpowsour.2018.05.002.
(71) Ruan, D.; Huang, Y.; Li, L.; Yuan, J.; Qiao, Z. A Li4Ti5O12+AC/LiMn2O4+AC Hybrid Battery Capacitor with Good Cycle Performance. *J. Alloys Compd.* **2017**. https://doi.org/10.1016/j.jallcom.2016.10.318.
(72) Sun, X.; Zhang, X.; Huang, B.; Zhang, H.; Zhang, D.; Ma, Y. (LiNi0.5Co0.2Mn0.3O2 + AC)/Graphite Hybrid Energy Storage Device with High Specific Energy and High Rate Capability. *J. Power Sources* **2013**. https://doi.org/10.1016/j.jpowsour.2013.06.038.
(73) Cericola, D.; Novák, P.; Wokaun, A.; Kötz, R. Hybridization of Electrochemical Capacitors and Rechargeable Batteries: An Experimental Analysis of the Different Possible Approaches Utilizing Activated Carbon, Li4Ti5O12 and LiMn2O 4. *J. Power Sources* **2011**. https://doi.org/10.1016/j.jpowsour.2011.07.032.
(74) Hagen, M.; Cao, W. J.; Shellikeri, A.; Adams, D.; Chen, X. J.; Brandt, W.; Yturriaga, S. R.; Wu, Q.; Read, J. A.; Jow, T. R.; Zheng, J. P. Improving the Specific Energy of Li-Ion Capacitor

Laminate Cell Using Hybrid Activated Carbon/LiNi0.5Co0.2Mn0.3O2 as Positive Electrodes. *J. Power Sources* **2018**, *379* (November 2017), 212–218. https://doi.org/10.1016/j.jpowsour.2018.01.036.

Chapter 9

Electrochemical Performance of Li_xSiON Polymer Electrolytes

9.1 Introduction

Lithium ion batteries (LIBs) have been investigated intensively due to their high energy and power densities that enable applications ranging from portable electronics to vehicle electrification.[1–3] Unfortunately, the flammability of currently used liquid electrolytes and the thermal runaway of traditional LIBs remain as challenges regardless of significant advances in battery management systems (BMS).[4,5] Thus, solid electrolytes (SEs) are now highly sought due to their high thermal stability, reduced flammability and resistance to lithium dendrite penetration potentially enabling new battery designs and chemistries that can enhance both gravimetric and volumetric energy densities.[6–8] These objectives provide tremendous motivation to synthesize promising SEs with competitive ionic conductivities and wide electrochemical stabilities equal to or surpassing liquid electrolytes.[7,9,10]

The discovery of LISICON (Li^+ superionic conductors)[11,12] provided motivation to develop oxysalt Li_3PO_4-Li_4SiO_4 solid solutions targeting and realizing two order magnitude improvements in conductivity (10^{-6} S/cm) compared to single phased Li_3PO_4 electrolyte (10^{-8} S/cm).[13] This improvement is attributed to increases in Li interstitial site concentrations.[14] As P^{5+} is partially substituted by Si^{4+}, interstitial Li^+ is introduced to the Li_3PO_4 structure.[15] Molecular dynamic simulations of mixed Si/P compositions reveal the formation of a continuous 3D network of Li^+ conduction pathways with a cooperative-type interstitial mechanism.[13]

Moreover, studies show that N doping of the O site in Li_3PO_4 promotes faster Li diffusion and improves electrochemical stability attributed to introduction of disorder and decreases in electrostatic energy.[16,17] The room temperature ionic conductivity of amorphous LiPON ($\sim 3 \times 10^{-6}$) is 2 orders of magnitude greater than Li_3PO_4.[18,19] This enhancement is ascribed to the presence of N bridges at high Li^+ contents, which favor the mobility of Li and effectively renders P/O/N immobility.[17,20]

Thus, controlling nitrogen content is key to achieving higher ionic conductivity.[21,22] Both computational and experimental studies have demonstrated that amorphous rather than crystalline LiPON is a better Li^+ conductor attributed to increases in diffusion/conduction due to reduction of overall electrostatic interactions and higher disorder within the material.[17,20,21,23] Recently, we demonstrated that the introduction of Si into Li_xPON polymer electrolytes enhances ionic conductivity and lowers the activation energy of the polymer electrolyte (Li_xSiPON) by shortening the distance between Li^+ binding sites.[21,24] With this background, here we investigate the effect of N introduction into amphorous Li_4SiO_4 like polymer analogs.

The exploration of Li^+ containing oxynitride as electrolytes has been limited to thin-film batteries because of their low ionic conductivities (10^{-6} Scm^{-1}) at ambient.[4,22,25] In contrast, oxide-based SEs (LATP, LLZO, LLTO) offer optimal ionic conductivities (0.1-1 mS/cm) at ambient.[26–29] However, the integration of oxide SEs with high ionic conductivities into the current battery structures remains challenging mainly due to high resistivity at electrode/SE interfaces.[4,30,31]

Most oxide SEs must be sintered at elevated temperatures to fully densify, form target phases and reach optimal Li^+ diffusivities.[4,28,32] This limits the assembly of all solid-state-batteries (ASSBs) as co-sintering electrolyte with electrodes will result in unwanted interfacial layers/defects, phase changes, electrochemistries, and even mechanical properties.[4,31,33] In addition, the ceramic nature (brittleness and stiffness) of oxide-based SEs restrict both their fabrication and operation of ASSBs.[4] In contrast, amorphous electrolytes advantageously offer both isotropic Li^+ conduction and good interfacial contact with electrodes.[34]

The assembly of commercially viable ASSBs mandates careful management of both fabrication and material costs especially for SEs. McClosky et al[35] suggest that SE costs should be $\$10/m^2$ to compete with conventional LIBs. In this light, we recently developed a novel, amorphous polymer electrolyte, Li_xSiON, derived from rice hull ash (RHA), an agricultural waste product.[36]

Scheme **9.1** illustrates the extraction of silica from RHA by simple distillation of spirosiloxane, [SP = $(C_6H_{12}O_2)_2Si$]. Li_xSiON (x = 2, 4, and 6) polymers with varying Li and N contents can be synthesized simply by reacting SP with $xLiNH_2$, offering a low-cost, low-temperature, and green synthesis route.[36]

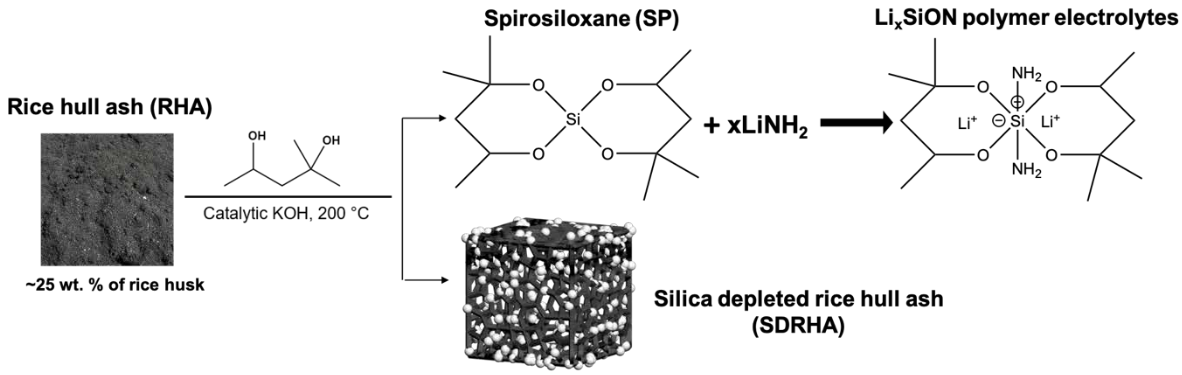

Scheme 9.1. Lithiation of SP to form Li_xSiON polymer electrolyte.

In this work, we characterize the physical and electrochemical properties of Li_xSiON polymer electrolytes by X-ray diffraction (XRD), X-ray photoelectron spectroscopy (XPS), Fourier-transform infrared spectroscopy (FTIR), and electrochemical impedance spectroscopy (EIS) studies. We also correlate compositional and structural changes as a function of nitrogen content and degree of lithiation with ionic conductivities.

Thereafter, we detail the electrochemical stabilities and diffusion kinetics of Li/Li_xSiON polymer electrolyte systems in symmetric cells. The Li_6SiON polymer electrolyte shows optimal ohmic stability at current densities as high as 3.75 $mAhcm^{-2}$. Coincidentally, we explored transference numbers and electrical conductivities of these polymer electrolytes. The compatibility of the polymer electrolyte with SPAN (sulfurized, carbonized polyacrylonitrile) cathode was also investigated.[37] The Li-SPAN[38] half-cell with the Li_6SiON polymer electrolyte delivered a specific capacity of ~725 mAh/g over 50 cycles.

9.2 Experimental section

9.2.1 Materials

RHA was provided by Wadham Energy LP (Williams, CA). To remove the impurities, RHA was milled in diluted hydrochloric acid (HCl) following the procedures described elsewhere.[39,40] The lithium amide ($LiNH_2$) and hexylene glycol (HG) were purchased from Acros Organics (Fair Lawn, NJ). The potassium hydroxide (KOH), lithium metal (~ 0.75 mm), HCl, tetrahydrofuran (THF), and N-methylpyrrolidone (NMP) were obtained from Sigma-Aldrich (St Louis, MO). Prior to use, the THF was distilled from sodium benzophenone ketyl/N_2. The coin cell parts and Celgard 2400 separator (~ 25 μm) were purchased from MTI Corporation (Richmond, CA).

9.2.2 Syntheses of Li_xSiON polymer electrolyte

Detailed discussion about the synthesis and structural composition of the Li_xSiON polymer electrolytes can be found elsewhere.[36] In brief, the SP was directly distilled out by reacting RHA with HG using catalytic base at 200 °C. The Li_xSiON polymer precursors were then synthesized by reacting SP with various $LiNH_2$ contents (Scheme **9.1)** to where the $LiNH_2$/SP mole ratio is in the range of ~ 2.1–6.6.[36] The analytical methods used in this work are provided as supporting information.

9.2.3 Cell fabrication

The electrochemical impedance spectroscopy (EIS), cyclic voltammetry (CV), and galvanostatic cycling tests were conducted using SP-300 potetntiostats/galvanostat (Bio-Logic Science Instruments, Knoxville, TN). The total ionic conductivities of the Li_xSiON electrolytes dissolved in THF (0.05 gml^{-1}) were measured by assembling symmetric cells using Celgard separator (18 mm x 25 µm) and stain less steel (SS) disks (ϕ = 8 mm). Prior to electrochemical characterization, the Li_xSiON polymer electrolyte, Celgard, Li metal, and SPAN electrode (ϕ = 6 mm) were stored in a glovebox (MBRAUN) filled with Ar. For EIS tests, an AC amplitude of 10 mV over a frequency range of 7 MHz-1Hz was used. The temperature-dependent ionic conductivities were performed between -15 ° to 85 °C. The electrochemical stability window of the Li_xSiON electrolyte was investigated by conducting cyclic voltammetry (CV) measurements at a scan rate of 1 mVs^{-1}.

Symmetric cells were assembled following the standard procedure described elsewhere.[21] To evaluate the stability and critical current density, the Li/Celagrd+Li_xSiON/Li symmetric cells were cycled between ±0.75-3.75 mA cm^{-2} current densities at room temperature. Detail electrode fabrication procedures for SPAN electrode can be found elsewhere.[37,41] The SPAN/Celgard + Li_6SiON/Li half-cell was assembled in 2032 coin cell and charge/discharge between 1- 3 V at 0.25 and 0.5 C rates.

The Li^+ transference number ($t_{Li}{}^+$) of the polymer electrolyte was calculated using *eq (1)* as suggested by Bruce et al.[42]

$$t_{Li}{}^+ = I_{SS}(U-Z_0*I_0)/I_0(U-Z_{SS}*I_{SS}) \qquad (1)$$

where I_0 and I_{ss} are the initial and steady-state current values obtained from chronoamperometry measurement, respectively. The initial and steady-state resistances obtained from EIS studies are represented by Z_0 and Z_{ss}, respectively. U represent the applied potential.

The electrical conductivities (σ_e) of the polymer electrolytes were determined by using *eq (2)*

$$\sigma_e = (t \times Iss)/(A \times U) \qquad (2)$$

Where the thickness of the Celgard is represented by t = 25 µm and A is the area of the electrode (ϕ = 8 mm).

9.3 Results and discussion

In this section, discussion focuses on the structural, surface, and morphological properties of the Li_xSiON polymer precursors as characterized by XRD, FTIR, and XPS analyses. The second part of the discussion entails the electrochemical performance of the Li_xSiON electrolytes assessed according to ionic conductivity, electrical conductivity, transference number, and the stability of the Li_xSiON electrolyte in symmetric and half-cell configurations.

9.3.1 Compositional characterization of Li_xSiON electrolytes

The Li_xSiON precursors were dried under vacuum/1 h/25 °C to evaporate the solvent (THF). The dried precursors were then compacted into pellets (ϕ = 13 mm) at 10 kpsi/25 °C. Figure **9.1a** shows XRDs of the Li_xSiON pellets with broad peaks centered ~ 20 ° 2θ, indicating an amorphous nature as also seen for amorphous Li_4SiO_4 thin films.[34,43] Nakagawa et al.[34] report that XRDs of pulsed laser deposited Li_4SiO_4 thin film also present a broad peak at 20 ° 2θ indicating a lack of crystallinity. Amorphous materials often provide improved charge carrier mobility in part by eliminating grain boundaries.[23]

The Figure **9.1b** FTIRs of the Li_xSiON precursors present broad peaks ~ 3400 cm^{-1} corresponding to νN-H, with N-H overtones at 1600 cm^{-1}.[36] The sharp peak ~ 1400 cm^{-1} is attributed to δ N-H/C-H. Peaks in the range 1000 -1200 cm^{-1} arise from νSi-O bands,[34] while peaks ~900-1000 cm^{-1} corresponds to νSi-O-Li.

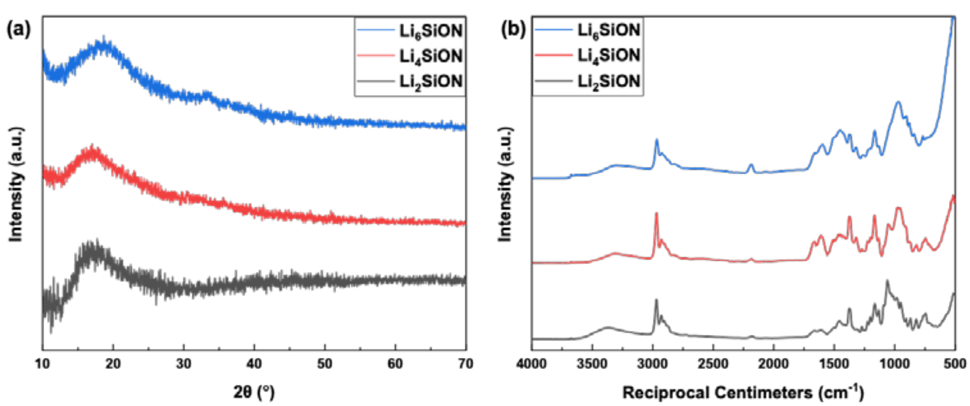

Figure 9.1. (a)XRD patterns and (b)FTIR spectra of Li_xSiON polymer electrolytes.

Figure **9.2a** shows XPS wide scan surveys revealing signature elements (Li, Si, O, and N). The C peak corresponds to the formation of LiOH/Li_2CO_3 due to brief air exposure. Table **9.1** lists the deduced atomic percentage of Li_xSiON precursors dried at RT/1 h/vacuum. The Li/Si and Si/N ratios increase with increasing $LiNH_2$ such that the Li_6SiON polymer electrolyte has the highest Li concentration. The N atomic percentage (0.7-0.8) at the surface is much lower than the calculated experimentally calculated values (5),[36] indicating the loss of N as NH_3 during vacuum treatments overnight prior to XPS studies. The N 1s core spectra (Figure **9.2b**) of Li_xSiON polymer electrolytes show shifts towards lower binding energies with increasing $LiNH_2$ contents. This is attributed to the presence of covalent N-H bonds that increase the electron density around the nitrogen atom.[44] The Li 1s peak ~ 52 eV corresponds to the presence of Li_2O[45] and it seems to increase with increasing $LiNH_2$ content (Figure **9.2c**).

Table 9.1. Atomic ratios of Li_xSiON polymer electrolytes based on XPS analyses.

Ratio	Li_2SiON	Li_4SiON	Li_6SiON
Li/Si	1.9	10.8	39.6
Si/N	8.4	3.3	0.85
C/O	2.4	1.3	1.6

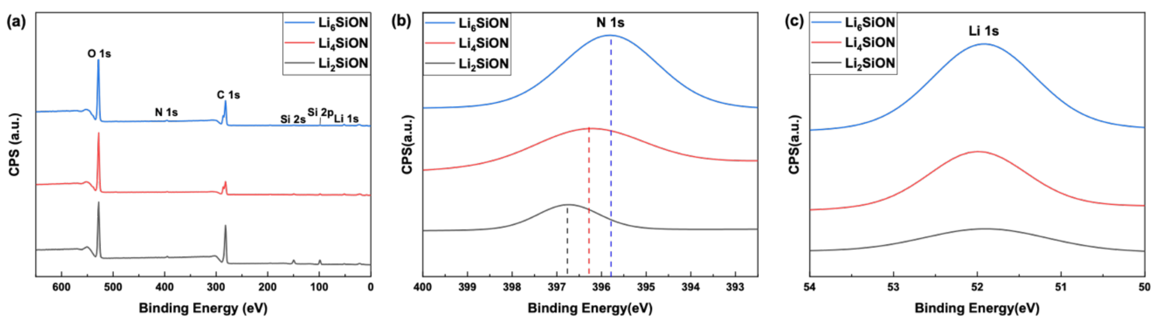

Figure 9.2. (a)Wide scan XPS spectra, (b) core N 1s (b), and core Li ls (c) plots of Li_xSiON polymer electrolytes.

9.3.2 Electrochemical characterization of Li_xSiON electrolytes

Figure **9.3a** presents Nyquist plots of SS/Celgard+Li_xSiON/SS symmetric cells. The total ionic conductivities are calculated similarly to conventional, liquid electrolytes-soaked separators. Detail procedures can be found elsewhere.[21] Table **9.2** lists the obtained total ionic conductivities of the polymer electrolytes. The Celgard+Li_6SiON polymer electrolyte showed the highest Li^+ conductivity of ~ 6.5 × 10^{-6} S/cm. The ionic conductivity was improved by an order of magnitude for Li_xSiON polymer electrolyte, suggesting that increasing the Li content does improve the conductivity. The ionic conductivity seems also to increase with increasing Li/S ratio.

Table 9.2. Total ambient ionic conductivities of Celgard+Li_xSiON polymer electrolytes.

Polymer electrolytes	Conductivity (S/cm)
Li_2SiON	$6.2 \pm 0.2 \times 10^{-7}$
Li_4SiON	$2.5 \pm 0.5 \times 10^{-6}$
Li_6SiON	$6.5 \pm 0.03 \times 10^{-6}$

Studies have shown that the ionic conductivity of Li_xSiPON electrolytes is higher than lithium silicophosphate, attributed to the introduction of N which presumably reduces electrostatic interactions.[21,46] However, typically N doped lithium silicophosphates and lithium phosphates are synthesized using gas phase deposition techniques, which are costly and require complicated steps to produce thin films, making them challenging for the assembly of ASSBs.[47–49] In contrast, here we demonstrate a facile polymer precursor route to Li_xSiON electrolytes impregnated on Celgard with optimal ionic conductivity at ambient. Furthermore, our materials derive from a plentiful Ag waste (RHA), making them attractive from both a cost and environment-friendly perspective.

One effective method of increasing the ionic conductivity of electrolytes is to increase the charge carrier density and mobility of the charged species. The former is difficult to attain using gas phase deposition methods, as previously reported by multiple groups,[50,51] as Li concentrations seems to approach an upper limit of 3 nearly irrespective of the deposition method. Nimisha et al[52] reports that the N_2 flow rate is a key process parameter in gas phase deposition techniques that governs the ionic conductivity of N doped thin films. However, increasing the N_2 flow (40 sccm) rate results in a reduction in sputtering rate and a decrease in ionic conductivity of LiPON thin film.[52] Here, we demonstrate that the ionic conductivity increases linearly with Li/Si ratio (Figure **9.3b**). The polymeric route allows control of Li^+ and N concentrations by adjusting initial $LiNH_2$ amounts.

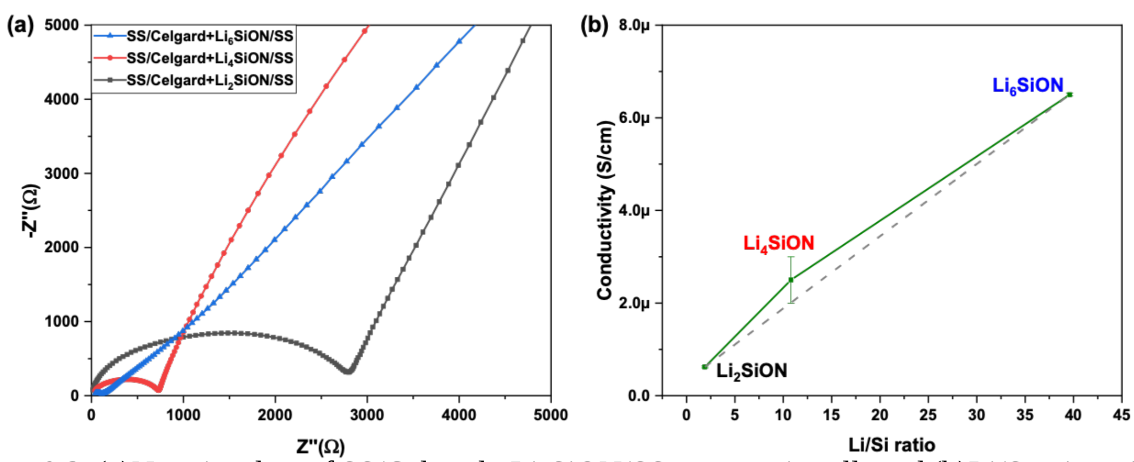

Figure 9.3. (a)Nyquist plots of SS/Celgard +Li_xSiON/SS symmetric cells and (b)Li/S ratio vs ionic conductivity at ambient.

In addition, the amorphous nature of the polymer electrolyte likely provides isotropic Li^+ conduction, eliminating grain boundary resistivities. Nakagawa et al[34] reports that the ionic conductivity of Li_4SiO_4 amorphous film deposited by PLD is ~ 4 x 10^{-7} S/cm at ambient. The N-doped Li_4SiO_4 polymer electrolyte on Celgard exhibits order of magnitude higher conductivity compared to the amorphous thin film fabricated by gas-phase deposition techniques.

Figure **9.4a** presents typical Nyquist plots for SS/Celgard+Li_6SiON/SS cells, where AC impedance measurements were performed from -15° to 85 °C. The linear fit to the Arrhenius plot permits calculating the activation energy (0.28 eV) for the Li_6SiON electrolyte. The reported activation energy of amorphous Li_4SiO_4 is 0.62 eV.[34]

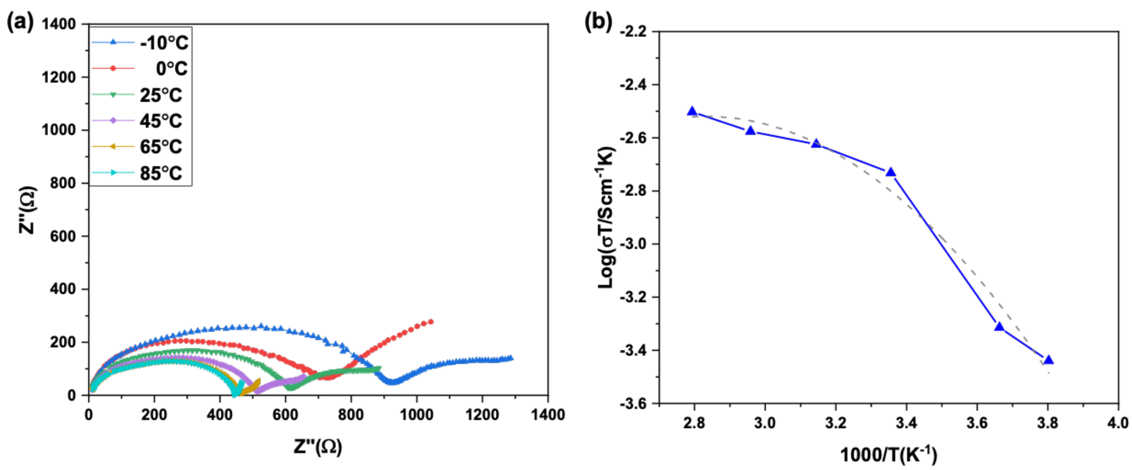

Figure 9.4. (a) Nyquist and (b) Arrhenius plots of SS/Celgard+Li_6SiON/SS.

In polymer electrolytes, the cations are typically responsible for ionic conductivity, thus cations forming liable bonds with polar groups of the host polymer promote conductivity. Figure **9.4b** shows the two regions for the ionic conductivity vs temperature (1000/T) plots, where the ionic conductivity gradually increases (< 25 °C) and the region where conductivity abruptly increases (> 25 °C). At high temperatures, the energy is large enough to overcome potential barriers, facilitating the mobility of ionic charge carriers.[53]

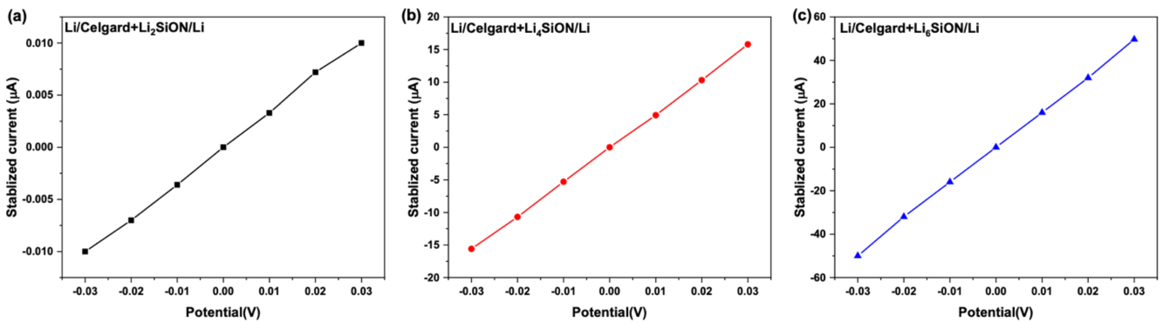

Figure 9.5. Stabilized current (*Iss*)-voltage (*U*) relations of Li symmetric cells with (a) Li_2SiON, (b) Li_4SiON, and (c) Li_6SiON electrolytes.

The representative *Iss-U* relations of Li/Li_xSiON/Li symmetric cells are shown in Figures **9.5(a-c)**. As expected from Ohms law, the *Iss* shows a linear increase with applied potential. The Li_2SiON, Li_4SiON, and Li_6SiON polymer electrolytes exhibit an average electrical conductivity of $2.7 \pm 1.4 \times 10^{-10}$, $6.4 \pm 0.4 \times 10^{-7}$, and $2 \pm 0.1 \times 10^{-6}$ S/cm respectively. The electrical conductivity appears to increase with increasing $LiNH_2$ content, supporting the XPS studies shown in Figure **9.2b**. The electron density seems to increase with increasing added $LiNH_2$ which results in a decrease in binding energy of N 1s.

In addition to the ionic and electrical conductivity, the transferences number (t_{Li^+}) is a key factor to evaluate the electrochemical performance of the polymer electrolyte.[54] Electrolytes with high t_{Li^+} enable fast charge-discharge capabilities regardless of relatively low ionic conductivities.[55] Furthermore, electrolytes with high t_{Li^+} are reported to suppress lithium dendrites and facilitate long cycling with metallic Li anodes.[56,57] The Nyquist plots of the Li/Celgard+Li_xSiON/Li symmetric cells before and after the chronoamperometry measurements at ambient are shown in Figures **9.6(a-c)**. The Nyquist plots show two semi-circles at high and low frequencies attributed to impedance of the polymer electrolytes and solid electrolyte interface (SEI)/charge-transfer resistance at the metallic Li electrode, respectively.

The impedance spectra show that the symmetric cells assembled with Li_2SiON and Li_4SiON electrolytes exhibit lower total resistivities after the steady-state current. However, the Li/Celgard+ Li_6SiON/Li symmetric cell show (Figure **9.6c**) slightly increased resistivity after the chronoamperometric measurements. This increase in resistivity is correlated with the formation of an SEI layer and charge-transfer resistance due to the high electrical conductivity of the Li_6SiON polymer electrolyte.

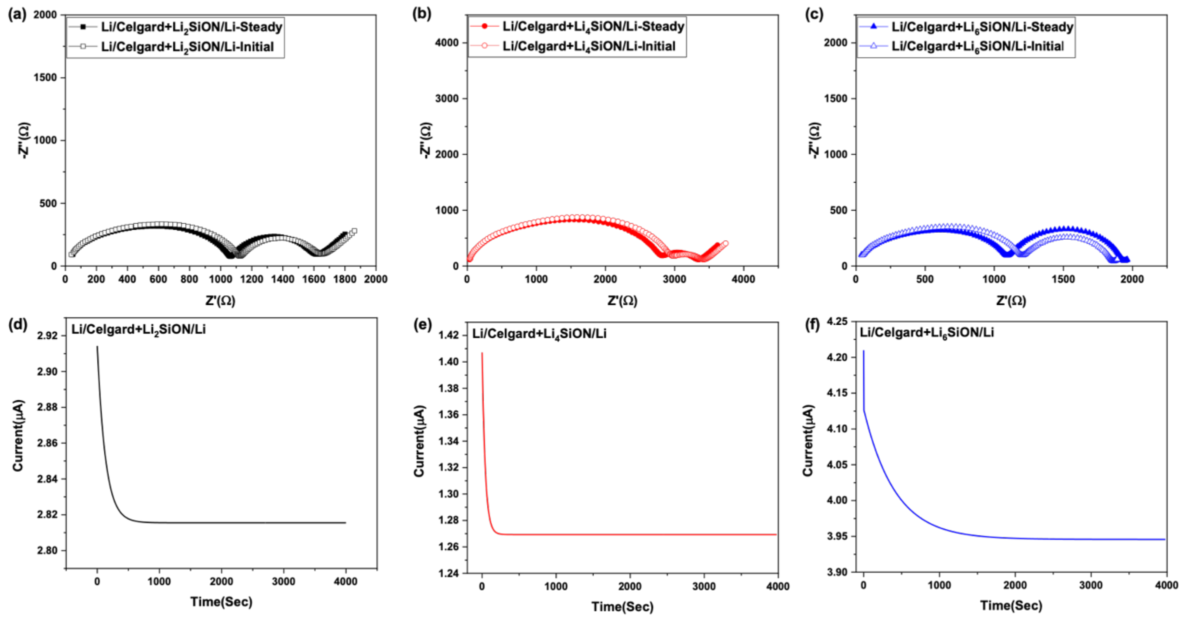

Figure 9.6. Nyquist (a-c) and Chronoamperometry(d-f) plots of Li/Celgard+Li_xSiON/Li cells.

Figure **9.6** (**d-f**) presents the chronoamperometry plots for the Li/Celgard+Li_6SiON/Li symmetric cells after stabilizing 1 h. Since the impedances of the polymer electrolytes were lower than the interfacial impedance, the steady-state method used in this work should be considered more of a qualitative than a quantitative study.

The t_{Li^+} values were further confirmed by using data from the DC polarization experiments per *eq (3)*.

$$t_{Li^+} = \sigma_{Li^+} / (\sigma_e + \sigma_{Li^+}) \qquad (3)$$

where σ_{Li^+} is the ionic conductivity of the polymer electrolytes deduced from the Nyquist plots shown in Figure **9.3a** and the σ_e represent the electrical conductivity obtained from the DC polarization studies (Figure **9.5**).

Table **9.3** summarizes the t_{Li^+} of the Li_xSiON polymer electrolytes calculated using *eq (1)* and *eq (3)*. The Li–SiON chemical interaction seems to facilitate higher Li^+ mobility as indicated by increased t_{Li^+} for the Li_xSiON polymer electrolytes. In traditional liquid electrolytes and dry solid polymer electrolytes, both the cations and anions are mobile species resulting in a decrease in the t_{Li^+}, which is generally < 0.5 due to the electro-polarization from anion buildup. The electro-polarization can lead to a decrease in the overall electrochemical performance due to high internal resistances, voltage losses, and dendrite growth. By anchoring anions to the polymeric backbone, the Li_xSiON polymer electrolytes with t_{Li}^+ (~0.75 -1) can overcome such challenges as faced by liquid electrolytes.

Table 9.3. Comparison of t_{Li}^+ calculated using *eq (1)* and *eq (3)*.

sample	tLi^+ from *eq (1)*	tLi^+ from *eq (3)*
Li_2SiON	0.9±0.03	1±0.02
Li_4SiON	0.8±0.06	0.79±0.04
Li_6SiON	0.73±0.08	0.76±0.06

The calculated t_{Li}^+ for the Li_xSiON electrolytes using both DC polarization and chronoamperometric studies are in good agreement (Table **9.3)**. The increase in electrical conductivity results in a relatively lower t_{Li}^+ for the Li_6SiON polymer electrolyte. Studies show that both structural design and material selection can significantly improve the t_{Li}^+ of electrolytes. The migration of anions in polymers can be reduced by anchoring the anions to the polymer backbone or by adding anion receptors that can favorably interact with anions.[58] The heterojunction and space charge region between the polymer electrolyte and metallic Li electrodes should be studied further to elucidate the ion conduction mechanism and anion mobility.

In addition to transference number measurements, the electrochemical stability window is an important parameter needed in evaluating the potential stability range for any polymer electrolyte. The electrochemical stability of the Li_xSiON polymer electrolyte was evaluated by assembling a three-electrode half-cell (Li/Celgard + Li_xSiON/SS), where metallic Li was used as both the reference and counter electrodes and SS was used as a working electrode. The electrochemical stability of the polymer electrolyte must be compatible with the operating potential of the electrodes to be considered for practical battery applications. The development of ASSB with high energy densities must rely strongly on the tolerance of the polymer electrolyte at high potentials.

Figure **9.7a** presents CV plots for the Li/Celgard+Li_6SiON/SS half-cells between potential ranges of -1 to 6 V at 1 mV/sec. The Li plating and stripping phenomena are demonstrated by the anodic and cathodic peaks ~ 0 V, indicating that the Li^+ ions diffuse through the polymer electrolyte and plate onto the working electrode. Good electrochemical stability is demonstrated by the quite small current response at high voltage (~ 4.5) vs Li/Li^+. The current response difference between the polymer electrolyte is attributed to variance in electronegativity of the framework. The increase in Li/Si ratio of the polymer precursor is postulated to decrease the covalency of Li-N framework, resulting in a decrease of the antibonding energy state.[41]

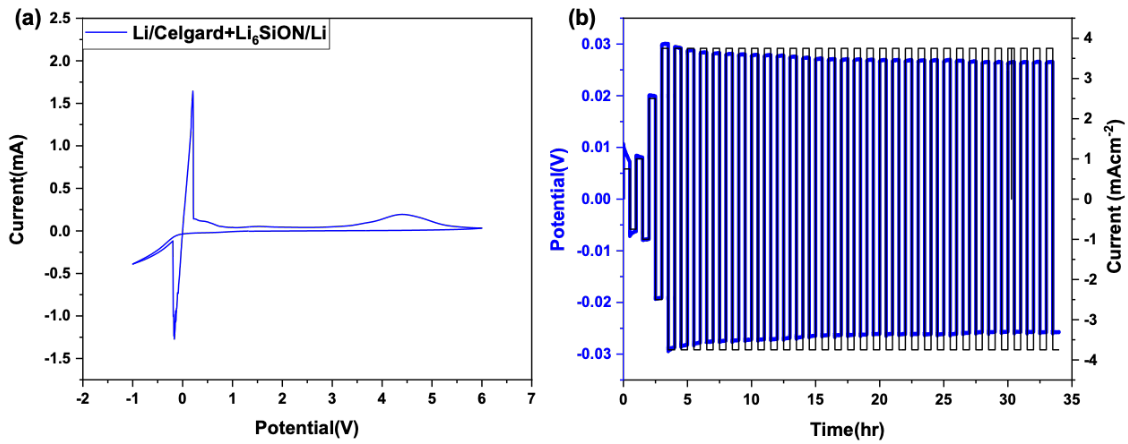

Figure 9.7. (a) CV plot of Li/Celgard+Li_6SiON/SS at sweep rate of 1 mV/sec and (b) galvanostatic cycling of Li/Celgard+Li_6SiON/Li symmetric cell at ambient.

After investigating the electrochemical stability and transference number of the polymer electrolyte, we now focus on the Li^+ plating/stripping behavior by charging/discharging the Li/Celgard + Li_6SiON/Li symmetric cells at ambient. Galvanostatic measurements with a constant current density of 0.75 – 3.75 mA cm^{-2} were used to determine the stability of the Li_6SiON polymer electrolyte and Li metal (Figure **9.7b**). The Li/Celgard + Li_6SiON/Li symmetric cell follows Ohmic behavior at both low and high critical current densities, delivering an average interfacial resistance of 8 $\Omega.cm^2$. The voltage response is stable at high current density of 3.75 mAh/cm^2, meeting the requirement of electrolytes to enable the assembly of ASSBs.[59,60]

The obtained critical current density for the polymer electrolyte is significantly higher than what is reported for inorganic solid electrolytes with higher ionic conductivities (0.1 mS/cm) at ambient. Irrespective of the use of numerous engineering processes, i.e., polishing, grinding, surface modification, and melting of metallic Li to bind with electrolyte surfaces, voids/pores, grain boundaries, and surface impurities exist in most oxide-based inorganic solid electrolytes.[4] These surface impurities provide pathways for Li dendrites to penetrate resulting in low critical current densities (< 0.5 mA cm^{-2}).[4]

During the past decade, Li-S batteries have drawn intense attention as candidates for next generation energy storage technologies owing to their high theoretical capacity (1672 mAh/g) and specific energy (2600 Wh/kg).[37] Part of the motivation comes from the fact that sulfur is low cost, abundant, and an environmentally friendly resource, making it a very promising cathode material.[61] Due to its structural framework, SPAN cathodes are known to suppress polysulfide shuttle effects and facilitate fast charging capabilities.

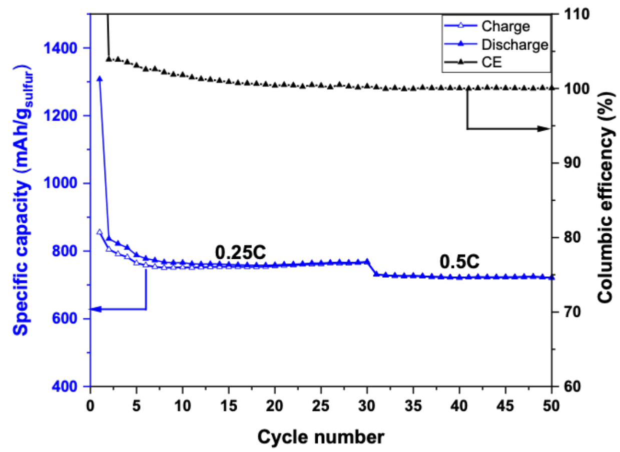

Figure 9.8. Cycle number vs specific capacity and columbic efficiency of SPAN/Celgard+Li6SiON/Li half-cell cycled between 1- 3 V at ambient.

Thus, we investigated the stability of the Li_6SiON electrolyte with SPAN cathode, metallic Li anode. The half-cell delivered an initial discharge capacity ~ 1300 mAh/g at ambient (Figure **9.8**). The reversible capacity was ~ 850 mAh/g at 0.25 C which gradually decreased to 765 mAh/g after 30 cycles. Fast cycling at 0.5C resulted in reversible capacity of 725 mAh/g for the rest of 20 cycles. This value is double the capacity attained for conventional Li-ion batteries with graphite anode and high voltage oxide cathode. The half-cell maintained high columbic efficiency of ~ 100% attributed to the high t_{Li}^+ and optimal ionic conductivity of the Li_6SiON polymer electrolyte.

9.4 Conclusions

We present detailed electrochemical performance of the Li_xSiON polymer electrolyte, derived from RHA, an agriculture waste product. XRD studies show the amorphous nature of Li_xSiON polymer electrolyte dried at ambient. The amorphous nature coupled with the high Li content and nitridation resulted in optimal conductivity of the Li_6SiON electrolyte (~ 6.5 x 10^{-6} S/cm) at ambient and low activation energy (0.28 eV). The Li_xSiON polymer electrolytes also exhibit a high Li^+ transference number (~0.7 -1) attributed to the polymer framework with low anion mobility. The wide electrochemical stability of the Li_xSiON polymer electrolyte makes it attractive for high energy density applications. Most importantly, the polymer electrolyte enabled the assembly of Li symmetric cells with high critical current density (3.75 mAh cm^{-2}), making it desirable for fast charging applications. Finally, we assembled half-cell using SPAN as the cathode, Celgard + Li_6SiON as the separator/electrolyte, and Li metal as the anode. The SPAN-Li half-cell delivered a reversible capacity of ~ 725 mAh/g at 0.5 C over 50 cycles.

References

(1) Lu, L.; Han, X.; Li, J.; Hua, J.; Ouyang, M. A Review on the Key Issues for Lithium-Ion Battery Management in Electric Vehicles. *Journal of Power Sources*. 2013. https://doi.org/10.1016/j.jpowsour.2012.10.060.

(2) Blomgren, G. E. The Development and Future of Lithium Ion Batteries. *J. Electrochem. Soc.* **2017**. https://doi.org/10.1149/2.0251701jes.

(3) Koga, S.; Krstic, M. Lithium-Ion Batteries. In *Systems and Control: Foundations and Applications*; 2020. https://doi.org/10.1007/978-3-030-58490-0_8.

(4) Wu, B.; Wang, S.; Evans, W. J.; Deng, D. Z.; Yang, J.; Xiao, J. Interfacial Behaviours between Lithium Ion Conductors and Electrode Materials in Various Battery Systems. *Journal of Materials Chemistry A*. 2016. https://doi.org/10.1039/c6ta05439k.

(5) Zhou, Q.; Dong, S.; Lv, Z.; Xu, G.; Huang, L.; Wang, Q.; Cui, Z.; Cui, G. A Temperature-Responsive Electrolyte Endowing Superior Safety Characteristic of Lithium Metal Batteries. *Adv. Energy Mater.* **2020**. https://doi.org/10.1002/aenm.201903441.

(6) Manthiram, A.; Yu, X.; Wang, S. Lithium Battery Chemistries Enabled by Solid-State Electrolytes. *Nature Reviews Materials*. 2017. https://doi.org/10.1038/natrevmats.2016.103.

(7) Takada, K. Progress and Prospective of Solid-State Lithium Batteries. *Acta Mater.* **2013**. https://doi.org/10.1016/j.actamat.2012.10.034.

(8) Chen, R.; Qu, W.; Guo, X.; Li, L.; Wu, F. The Pursuit of Solid-State Electrolytes for Lithium Batteries: From Comprehensive Insight to Emerging Horizons. *Materials Horizons*. 2016. https://doi.org/10.1039/C6MH00218H.

(9) Famprikis, T.; Canepa, P.; Dawson, J. A.; Islam, M. S.; Masquelier, C. Fundamentals of Inorganic Solid-State Electrolytes for Batteries. *Nature Materials*. 2019. https://doi.org/10.1038/s41563-019-0431-3.

(10) Zhang, B.; Tan, R.; Yang, L.; Zheng, J.; Zhang, K.; Mo, S.; Lin, Z.; Pan, F. Mechanisms and Properties of Ion-Transport in Inorganic Solid Electrolytes. *Energy Storage Materials*. 2018. https://doi.org/10.1016/j.ensm.2017.08.015.

(11) Alpen, U. v.; Bell, M. F.; Wichelhaus, W.; Cheung, K. Y.; Dudley, G. J. Ionic Conductivity of Li14Zn(GeO44 (Lisicon). *Electrochim. Acta* **1978**. https://doi.org/10.1016/0013-4686(78)80023-1.

(12) Bruce, P. G.; West, A. R. Ionic Conductivity of LISICON Solid Solutions, Li2+2xZn1-XGeO4. *J. Solid State Chem.* **1982**. https://doi.org/10.1016/0022-4596(82)90383-8.

(13) Deng, Y.; Eames, C.; Chotard, J. N.; Laleìre, F.; Seznec, V.; Emge, S.; Pecher, O.; Grey, C. P.; Masquelier, C.; Islam, M. S. Structural and Mechanistic Insights into Fast Lithium-Ion Conduction in Li4SiO4-Li3PO4 Solid Electrolytes. *J. Am. Chem. Soc.* **2015**. https://doi.org/10.1021/jacs.5b04444.

(14) Sakurai, Y.; Sakuda, A.; Hayashi, A.; Tatsumisago, M. Preparation of Amorphous Li4SiO4-Li 3PO4 Thin Films by Pulsed Laser Deposition for All-Solid-State Lithium Secondary Batteries. *Solid State Ionics* **2011**. https://doi.org/10.1016/j.ssi.2010.12.001.

(15) Bachman, J. C.; Muy, S.; Grimaud, A.; Chang, H. H.; Pour, N.; Lux, S. F.; Paschos, O.;

Maglia, F.; Lupart, S.; Lamp, P.; Giordano, L.; Shao-Horn, Y. Inorganic Solid-State Electrolytes for Lithium Batteries: Mechanisms and Properties Governing Ion Conduction. *Chemical Reviews*. 2016. https://doi.org/10.1021/acs.chemrev.5b00563.

(16) Yu, X.; Bates, J. B.; Jellison, G. E.; Hart, F. X. A Stable Thin-Film Lithium Electrolyte: Lithium Phosphorus Oxynitride. *J. Electrochem. Soc.* **1997**, *144*, 524–532. https://doi.org/10.1149/1.1837443.

(17) Li, J.; Lai, W. Structure and Ionic Conduction Study on Li3PO4 and LiPON (Lithium Phosphorous Oxynitride) with the Density-Functional Tight-Binding (DFTB) Method. *Solid State Ionics* **2020**. https://doi.org/10.1016/j.ssi.2020.115329.

(18) Albertus, P.; Babinec, S.; Litzelman, S.; Newman, A. Status and Challenges in Enabling the Lithium Metal Electrode for High-Energy and Low-Cost Rechargeable Batteries. *Nat. Energy* **2018**. https://doi.org/10.1038/s41560-017-0047-2.

(19) Bates, J. B.; Dudney, N. J.; Gruzalski, G. R.; Zuhr, R. A.; Choudhury, A.; Luck, C. F.; Robertson, J. D. Electrical Properties of Amorphous Lithium Electrolyte Thin Films. *Solid State Ionics* **1992**, *53*, 647–654. https://doi.org/10.1016/0167-2738(92)90442-R.

(20) Lacivita, V.; Westover, A. S.; Kercher, A.; Phillip, N. D.; Yang, G.; Veith, G.; Ceder, G.; Dudney, N. J. Resolving the Amorphous Structure of Lithium Phosphorus Oxynitride (Lipon). *J. Am. Chem. Soc.* **2018**. https://doi.org/10.1021/jacs.8b05192.

(21) Temeche, E.; Zhang, X.; Laine, R. M. Polymer Precursor Derived Li x PON Electrolytes : Toward Li − S Batteries. *ACS Appl. Mater. Interfaces* **2020**, *12*, 20548–20562. https://doi.org/10.1021/acsami.0c03341.

(22) Bates, J. B.; Dudney, N. J.; Gruzalski, G. R.; Zuhr, R. A.; Choudhury, A.; Luck, C. F.; Robertson, J. D. Fabrication and Characterization of Amorphous Lithium Electrolyte Thin Films and Rechargeable Thin-Film Batteries. *J. Power Sources* **1993**, *43–44*, 103–110. https://doi.org/10.1016/0378-7753(93)80106-Y.

(23) Lacivita, V.; Artrith, N.; Ceder, G. Structural and Compositional Factors That Control the Li-Ion Conductivity in LiPON Electrolytes. *Chem. Mater.* **2018**. https://doi.org/10.1021/acs.chemmater.8b02812.

(24) Zhang, X.; Temeche, E.; Richard, M. L. *Design, Synthesis and Characterization of Chemical Precursors to LixPON and LixSiPON Glasses. Materials That Enable All Solid-State Batteries.*; 2020.

(25) Bates, J. B.; Dudney, N. J.; Neudecker, B.; Ueda, A.; Evans, C. D. Thin-Film Lithium and Lithium-Ion Batteries. *Solid State Ionics* **2000**, *135* (1–4), 33–45. https://doi.org/10.1016/S0167-2738(00)00327-1.

(26) Yi, E.; Wang, W.; Mohanty, S.; Kieffer, J.; Tamaki, R.; Laine, R. M. Materials That Can Replace Liquid Electrolytes in Li Batteries: Superionic Conductivities in Li1.7Al0.3Ti1.7Si 0.4P2.6O12. Processing Combustion Synthesized Nanopowders to Free Standing Thin Films. *J. Power Sources* **2014**, *269*, 577–588. https://doi.org/10.1016/j.jpowsour.2014.07.029.

(27) Kwon, W. J.; Kim, H.; Jung, K. N.; Cho, W.; Kim, S. H.; Lee, J. W.; Park, M. S. Enhanced Li+ Conduction in Perovskite Li3XLa2/3-X□1/3-2xTiO3 Solid-Electrolytes via Microstructural Engineering. *J. Mater. Chem. A* **2017**. https://doi.org/10.1039/c7ta00196g.

(28) Yi, E.; Wang, W.; Kieffer, J.; Laine, R. M. Key Parameters Governing the Densification of Cubic-Li7La3Zr2O12 Li+ Conductors. *J. Power Sources* **2017**. https://doi.org/10.1016/j.jpowsour.2017.03.126.

(29) Jung, Y. S.; Oh, D. Y.; Nam, Y. J.; Park, K. H. Issues and Challenges for Bulk-Type All-

Solid-State Rechargeable Lithium Batteries Using Sulfide Solid Electrolytes. *Isr. J. Chem.* **2015**. https://doi.org/10.1002/ijch.201400112.
(30) Luntz, A. C.; Voss, J.; Reuter, K. Interfacial Challenges in Solid-State Li Ion Batteries. *Journal of Physical Chemistry Letters*. 2015. https://doi.org/10.1021/acs.jpclett.5b02352.
(31) Haruyama, J.; Sodeyama, K.; Han, L.; Takada, K.; Tateyama, Y. Space-Charge Layer Effect at Interface between Oxide Cathode and Sulfide Electrolyte in All-Solid-State Lithium-Ion Battery. *Chem. Mater.* **2014**. https://doi.org/10.1021/cm5016959.
(32) Sharafi, A.; Meyer, H. M.; Nanda, J.; Wolfenstine, J.; Sakamoto, J. Characterizing the Li-Li7La3Zr2O12 Interface Stability and Kinetics as a Function of Temperature and Current Density. *J. Power Sources* **2016**. https://doi.org/10.1016/j.jpowsour.2015.10.053.
(33) Takada, K.; Ohta, N.; Zhang, L.; Fukuda, K.; Sakaguchi, I.; Ma, R.; Osada, M.; Sasaki, T. Interfacial Modification for High-Power Solid-State Lithium Batteries. *Solid State Ionics* **2008**. https://doi.org/10.1016/j.ssi.2008.02.017.
(34) Nakagawa, A.; Kuwata, N.; Matsuda, Y.; Kawamura, J. Thin Film Lithium Battery Using Stable Solid Electrolyte Li 4 SiO 4 Fabricated by PLD . *ECS Trans.* **2019**. https://doi.org/10.1149/1.3393851.
(35) McCloskey, B. D. Attainable Gravimetric and Volumetric Energy Density of Li-S and Li Ion Battery Cells with Solid Separator-Protected Li Metal Anodes. *Journal of Physical Chemistry Letters*. 2015. https://doi.org/10.1021/acs.jpclett.5b01814.
(36) Zhang, X.; Temeche, E.; Laine, R. M. LixSiON (X= 2, 4, 6); A Novel Solid Electrolyte System Derived from Agricultural Waste. **2020**, 48–50. https://doi.org/10.1039/d0gc02580a.
(37) Warneke, S.; Zenn, R. K.; Lebherz, T.; Müller, K.; Hintennach, A.; Starke, U.; Dinnebier, R. E.; Buchmeiser, M. R. Hybrid Li/S Battery Based on Dimethyl Trisulfide and Sulfurized Poly(Acrylonitrile). *Adv. Sustain. Syst.* **2018**, *2* (2), 1700144. https://doi.org/10.1002/adsu.201700144.
(38) Temeche, E.; Zhang, X.; Richard, M. L. *Polymer Precursor Derived LixPON Electrolytes for Li-S Battery*; 2020.
(39) Marchal, J. C.; Krug, D. J.; McDonnell, P.; Sun, K.; Laine, R. M. A Low Cost, Low Energy Route to Solar Grade Silicon from Rice Hull Ash (RHA), a Sustainable Source. *Green Chem.* **2015**, *17* (7), 3931–3940. https://doi.org/10.1039/c5gc00622h.
(40) Temeche, E.; Yu, M.; Laine, R. M. Silica Depleted Rice Hull Ash (SDRHA), an Agricultural Waste, as a High-Performance Hybrid Lithium-Ion Capacitor. *Green Chem.* **2020**. https://doi.org/10.1039/d0gc01746a.
(41) Temeche, E.; Zhang, X.; Laine, R. M. Polymer Precursor Derived LiXPON Electrolytes: Toward Li-S Batteries. *ACS Appl. Mater. Interfaces* **2020**. https://doi.org/10.1021/acsami.0c03341.
(42) Evans, J.; Vincent, C. A.; Bruce, P. G. Electrochemical Measurement of Transference Numbers in Polymer Electrolytes. *Polymer (Guildf).* **1987**. https://doi.org/10.1016/0032-3861(87)90394-6.
(43) Nakagawa, A.; Kuwata, N.; Matsuda, Y.; Kawamura, J. Characterization of Stable Solid Electrolyte Lithium Silicate for Thin Film Lithium Battery. In *Journal of the Physical Society of Japan*; 2010. https://doi.org/10.1143/JPSJS.79SA.98.
(44) Matanovic, I.; Artyushkova, K.; Strand, M. B.; Dzara, M. J.; Pylypenko, S.; Atanassov, P. Core Level Shifts of Hydrogenated Pyridinic and Pyrrolic Nitrogen in the Nitrogen-Containing Graphene-Based Electrocatalysts: In-Plane vs Edge Defects. *J. Phys. Chem. C*

2016. https://doi.org/10.1021/acs.jpcc.6b09778.
(45) Radvanyi, E.; De Vito, E.; Porcher, W.; Jouanneau Si Larbi, S. An XPS/AES Comparative Study of the Surface Behaviour of Nano-Silicon Anodes for Li-Ion Batteries. In *Journal of Analytical Atomic Spectrometry*; 2014. https://doi.org/10.1039/c3ja50362c.
(46) Lee, S. J.; Bae, J. H.; Lee, H. W.; Baik, H. K.; Lee, S. M. Electrical Conductivity in Li-Si-P-O-N Oxynitride Thin-Films. *J. Power Sources* **2003**. https://doi.org/10.1016/S0378-7753(03)00457-9.
(47) Kim, Y. G.; Wadley, H. N. G. Lithium Phosphorous Oxynitride Films Synthesized by a Plasma-Assisted Directed Vapor Deposition Approach. *J. Vac. Sci. Technol. A Vacuum, Surfaces, Film.* **2008**. https://doi.org/10.1116/1.2823491.
(48) Zhao, S.; Fu, Z.; Qin, Q. A Solid-State Electrolyte Lithium Phosphorus Oxynitride Film Prepared by Pulsed Laser Deposition. *Thin Solid Films* **2002**, *415*, 108–113. https://doi.org/10.1016/S0040-6090(02)00543-6.
(49) Lee, S. J.; Baik, H. K.; Lee, S. M. An All-Solid-State Thin Film Battery Using LISIPON Electrolyte and Si-V Negative Electrode Films. *Electrochem. commun.* **2003**, *5*, 32–35. https://doi.org/10.1016/S1388-2481(02)00528-3.
(50) Meda, L.; Maxie, E. E. Lipon Thin Films Grown by Plasma-Enhanced Metalorganic Chemical Vapor Deposition in a N 2-H 2-Ar Gas Mixture. *Thin Solid Films* **2012**. https://doi.org/10.1016/j.tsf.2011.08.091.
(51) Hu, Z.; Li, D.; Xie, K. Influence of Radio Frequency Power on Structure and Ionic Conductivity of LiPON Thin Films. *Bull. Mater. Sci.* **2008**. https://doi.org/10.1007/s12034-008-0108-z.
(52) Nimisha, C. S.; Rao, K. Y.; Venkatesh, G.; Rao, G. M.; Munichandraiah, N. Sputter Deposited LiPON Thin Films from Powder Target as Electrolyte for Thin Film Battery Applications. *Thin Solid Films* **2011**, *519*, 3401–3406. https://doi.org/10.1016/j.tsf.2011.01.087.
(53) Aziz, S. B.; Woo, T. J.; Kadir, M. F. Z.; Ahmed, H. M. A Conceptual Review on Polymer Electrolytes and Ion Transport Models. *Journal of Science: Advanced Materials and Devices*. 2018. https://doi.org/10.1016/j.jsamd.2018.01.002.
(54) Zheng, Y.; Yao, Y.; Ou, J.; Li, M.; Luo, D.; Dou, H.; Li, Z.; Amine, K.; Yu, A.; Chen, Z. A Review of Composite Solid-State Electrolytes for Lithium Batteries: Fundamentals, Key Materials and Advanced Structures. *Chemical Society Reviews*. 2020. https://doi.org/10.1039/d0cs00305k.
(55) Kato, Y.; Hori, S.; Saito, T.; Suzuki, K.; Hirayama, M.; Mitsui, A.; Yonemura, M.; Iba, H.; Kanno, R. High-Power All-Solid-State Batteries Using Sulfide Superionic Conductors. *Nat. Energy* **2016**, *1* (4), 1–7. https://doi.org/10.1038/nenergy.2016.30.
(56) Shigenobu, K.; Dokko, K.; Watanabe, M.; Ueno, K. Solvent Effects on Li Ion Transference Number and Dynamic Ion Correlations in Glyme- And Sulfolane-Based Molten Li Salt Solvates. *Phys. Chem. Chem. Phys.* **2020**. https://doi.org/10.1039/d0cp02181d.
(57) Lee, Y. G.; Fujiki, S.; Jung, C.; Suzuki, N.; Yashiro, N.; Omoda, R.; Ko, D. S.; Shiratsuchi, T.; Sugimoto, T.; Ryu, S.; Ku, J. H.; Watanabe, T.; Park, Y.; Aihara, Y.; Im, D.; Han, I. T. High-Energy Long-Cycling All-Solid-State Lithium Metal Batteries Enabled by Silver–Carbon Composite Anodes. *Nat. Energy* **2020**. https://doi.org/10.1038/s41560-020-0575-z.
(58) Long, L.; Wang, S.; Xiao, M.; Meng, Y. Polymer Electrolytes for Lithium Polymer

Batteries. *Journal of Materials Chemistry A*. 2016. https://doi.org/10.1039/c6ta02621d.
(59) Raj, R.; Wolfenstine, J. Current Limit Diagrams for Dendrite Formation in Solid-State Electrolytes for Li-Ion Batteries. *J. Power Sources* **2017**. https://doi.org/10.1016/j.jpowsour.2017.01.037.
(60) Flatscher, F.; Philipp, M.; Ganschow, S.; Wilkening, H. M. R.; Rettenwander, D. The Natural Critical Current Density Limit for $Li_7La_3Zr_2O_{12}$ Garnets. *J. Mater. Chem. A* **2020**.
(61) Wang, H. C.; Cao, X.; Liu, W.; Sun, X. Research Progress of the Solid State Lithium-Sulfur Batteries. *Front. Energy Res.* **2019**, *7* (October), 1–20. https://doi.org/10.3389/fenrg.2019.00112.

Chapter 10

Electrically Conducting Calcium Aluminate ($12CaO{\cdot}7Al_2O_3$) Thin Films

10.1 Introduction

Abundant, traditional construction materials, CaO and Al_2O_3 form a variety of compounds of differing stoichiometric ratios including CA, C3A, CA6, C12A7 (C = CaO, A = Al_2O_3).[1-6] Of these, $12CaO{\cdot}7Al_2O_3$ (C12A7) is the subject of multiple studies for practical applications centered around the fact that it can be transparent and electrically conducting when properly processed. Among the many studies, perhaps the most significant are those demonstrating photo-induced electrical conduction and photoluminescence properties.[7-12]

C12A7 exhibits cubic morphology (I-43d space group) with a = 11:99 Å. The stoichiometry for this 118 atom unit cell (Z = 2) is $[Ca_{24}Al_{28}O_{64}]^{4+} + 2O^{2-}$. The two extra O^{2-} ions are trapped in Ca-Al-O cages.[1,2,13] The unit cell consists of 12 sub-nanometer-sized cages; The cage walls are composed of 8 tetrahedrally coordinated Al^{3+}, 16 bridging and non-bridging oxygens, and 6 Ca^{2+} ions.[14,15] The inner cage diameter is ~50 % larger than the diameter of O^{2-}, leading to loose coordination between the Ca^{2+} and O^{2-} ions.[15] Anionic substitutions are relatively facile in this structure because the mean effective charge per cage is 1/3 (4+ charges shared by 12 cages).[13] An approximately 0.1 nm channel permits ready ion exchange as the interionic distance between free O^{2-} and Ca^{2+}, is about 1.5x larger than the sum (0.24 nm) of their ionic radii.[1]

The electrical, chemical, and optical properties of C12A7 can be greatly altered by replacing some or all of the free O^{2-} ions with other elements.[1] Thus, multiple substitution analogs have been reported including OH^-, H^-, O^-, O_2^-, F^-, Cl^-, e^-, and Au^- for O^{2-}. Rare earth (Gd^{+3}, Er^{+3}, Ce^{+3}, Nd^{+3}, and Eu^{+3}) dopants can also be introduced into C12A7 nanocages with retention of the original structures.[16-20]

As synthesized, C12A7 is insulating; its optical band gap is ~ 5.8 eV. [14,21,22] However, electrical conductivity obtains simply by replacing O^{2-} with e^- via various chemical and/or physical processes forming C12A7:e^- (C12A7 electride).[2,13]

Transparent conducting oxides (TCOs) with high electrical conductivity are difficult to identify due their intrinsic band gaps.[1] Given the high cost of all In based materials; currently the most effective and extensively used commercial TCO; there have been intense efforts to discover alternate, lower cost TCOs especially environmentally friendly ones that permit mass production. Thus, C12A7 offers potentially significant cost advantages.

Hayashi *et al* have, in multiple publications, developed a number of new TCOs including C12A7 derivatives. They were able to transform C12A7 into a TCO like material by heating single crystals of C12A7 at 1300 °C for several hours in $20H_2/80N_2$ followed by irradiation with ultraviolet (UV) light.[13]

Multiple other approaches to C12A7 and its derivatives have been explored including solid-state reactions,[23,24] sol-gel processing,[15] pulsed laser deposition (PLD),[25] and floating zone (FZ) processing.[18] C12A7 solid-state syntheses are most common and start by heating 12:7 mixtures of $CaCO_3$ and Al_2O_3 in controlled atmospheres at ≥1000 ℃. [23,26-28] These techniques require multiple high temperature, and high cost process steps to produce single-phase, dense C12A7:e^- films.

The central goal of this study is to synthesize $12CaO{\cdot}7Al_2O_3$ NPs in a single step using liquid-feed flame spray pyrolysis (LF-FSP) and process C12A7 thin films, eliminating glass forming, crushing, and ball milling steps. The LF-FSP process also allows doping[29,30] and should provide access to C12A7 NPs with rare earth dopants (e.g Ce^{3+}, Er^{3+}, Nd^{3+}).[16,18,31-32] Rare earth doped C12A7 phosphors may offer potential applications in field emission devices.[16,20,33] In addition, NPs offer potential access to finer final grain sizes potentially crucial to obtaining transparent, dense and mechanically robust thin films.[1,34]

To facilitate developing materials for diverse applications, efficient fabrication methods are required for both bulk and thin film C12A7:e^-.[15,25,35] One of the simplest and lowest-cost routes to convert ceramic powders into free standing, dense monoliths is by casting–sintering as explored here.[26,34,37]

10.2 Experimental

10.2.1 Materials

Calcium propionate [$(CH_3CH_2CO_2)_2Ca$), 97%] was purchased from Alfa Aesar (Ward Hill, MA). Triethanolamine [$N(CH_2CH_2OH)_3$], polyacrylic acid [$(C_3H_4O_2)_n$, M_n 2000], and benzyl butyl phthalate {2-[$CH_3(CH_2)_3O_2C]C_6H_4CO_2CH_2C_6H_5$, 98%} were purchased from Sigma-Aldrich (Milwaukee, WI). Polyvinyl butyral [$(C_8H_{14}O_2)_n$, B-98, M_n 40,000-70,000] was purchased from Butvar (Avon, OH). Aluminum tri-sec-butoxide {$Al[OCH(CH_3)CH_2CH_3]_3$} was purchased from Chattem Chemicals (Chattanooga, TN), and absolute ethanol from Decon Labs (King of Prussia, PA).

10.2.2 C12A7 nanopowder synthesis

Calcium propionate and alumatrane at a molar ratio of 12 to 7 were dissolved in anhydrous ethanol and TEA (50 ml) to give a 3 wt. % ceramic yield solution. The precursor solution was aerosolized with oxygen into a chamber where it was ignited via methane/oxygen pilot torches and combusted in an oxygen rich environment. The resulting NPs were collected down-stream in rod-in-tube electrostatic precipitators (ESP) operated at 10 kV. The liquid-feed flame spray pyrolysis (LF-FSP) apparatus has been described previously.[29]

As discussed below, the recovered NPs when heated to produce C12A7, produced materials that contained a second phase ($CaAl_2O_4$) resulting from calcium loss as CaO during sintering. Thus, to compensate for CaO loss during sintering, 5 and 10 wt. % excess calcium propionate was added to the original precursor solution, hereafter referred to as C12A7+5% or C12A7+10% respectively. Table **10.1** shows the list of precursors used for each composition, which were dissolved in ethanol and TEA.

Table 10.1. Amount of precursors dissolved in ethanol (850 ml) and TEA (50 ml).

	$Ca(O_2CCH_2CH_3)_2$ (g)	$Al[OCH(CH_3)CH_2CH_3]_3$ (g)
C12A7	33.5	134.5
C12A7+5%	35.18	134.5
C12A7+10%	36.85	134.5

As-produced C12A7 NPs (6.5 g, 4.68 mmol) were first dispersed in anhydrous ethanol (300 ml) with 1 wt. % Bicine (65 mg, 400 μmol) dispersant, using an ultrasonic horn at 100 W for 10 min. The suspension was left to settle for overnight to allow larger particles to settle. Supernatant was decanted and the recovered solution was poured into a clean beaker and left to dry overnight in the oven (60 ℃). The dried powders were ground in an alumina mortar and pestle.

10.2.3 C12A7 thin film processing

A suspension was made by mixing collected nanopowder (0.7 g), benzyl butyl phthalate (0.13 g), as a plasticizer, poly acrylic acid (0.01g) as a dispersant, polyvinyl butyral (0.13 g) as a binder dissolved in anhydrous ethanol (0.9 ml) and acetone (0.9 ml). The mixture (2.39 g) was placed in a 20 ml vial and milled with spherical alumina beads (6 g) with 3 mm diameter media overnight to homogenize the suspension. Suspension was cast using a wire wound rod coater (Automatic

Film Applicator 1137, Sheen Instrument, Ltd). After solvent evaporation, dried green films were uniaxially pressed between stainless steel dies at 100 ℃ with a pressure of 50–70 MPa for 5 min using a heated bench (Carver, Inc) top press to improve packing density.[34]

Sintering studies Heat treatments were conducted in a high temperature vacuum/gas tube furnace (Richmond, CA). Green films of C12A7, C12A7+5%, and C12A7+10% were placed between alumina disks and sintered to 1300 ℃ for 3 h in O_2 (100 mL min^{-1}). The films are transparent and has a uniform thickness of < 50$\pm$2 μm. The polycrystalline films of C12A7+10% were heated at 1300 ℃ for 3 h in a mixing gas composed of 20%H_2/80% N_2 (150 mL min^{-1}). The films are transparent after the hydrogen treatment.

10.3 Results and discussion

In the following sections, we first characterize the LF-FSP C12A7 NPs by XRD, SEM, TGA, and FTIR. Thereafter we characterize the green and sintered thin films of C12A7, C12A7+5 %, and C12A7+10 %; the effects of sintering temperatures and added excess CaO were also studied. Finally, efforts to transform sintered thin films into transparent conducting films as assessed by impedance measurements are presented.

10.3.1 Characterization of as-produced NPs

Figure **10.1a** shows XRDs of as-produced C12A7, C12A7+5 %, and C12A7+10 % NPs. XRDs of the as-produced NPs are all very similar offering a broad amorphous hump around ~ 30° 2θ.

Figure **10.1b** provides an SEM of as-produced powders showing spherical morphologies typical of amorphous NPs with average particle sizes (APSs) < 100 nm. The specific surface areas (SSAs) and APSs for as-produced C12A7, C12A7+5 %, and C12A7+10 % NPs are listed in Table **10.2**.

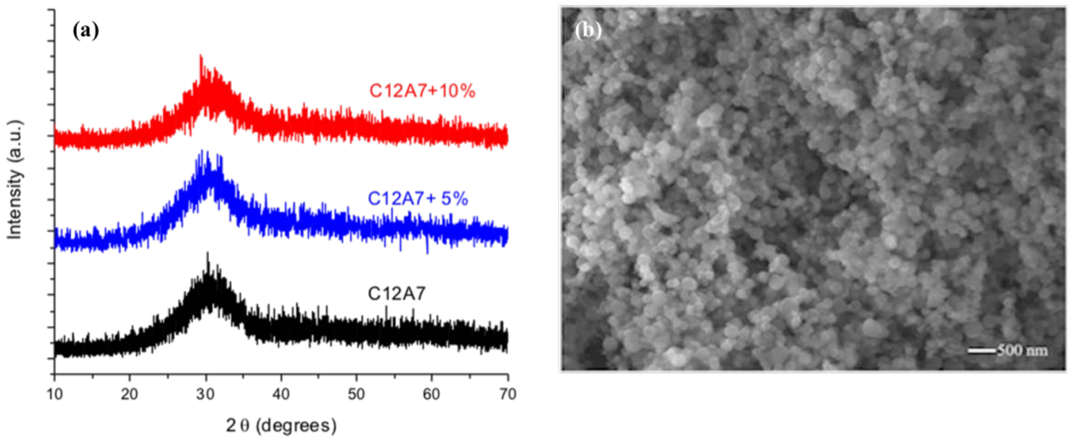

Figure 10.1. (a) NP XRDs of LF-FSP C12A7, C12A7+5 %, and (b) C12A7+ 10% and SEM of as-produced C12A7+ 10% NPs.

Table 10.2. SSAs and APSs of as-produced powders.

	SSAs (m^2g^{-1})	APSs (nm)
C12A7	23.4± 0.2	87
C12A7+5%	27.2 ± 0.4	75
C12A7+10%	28.5±0.4	72

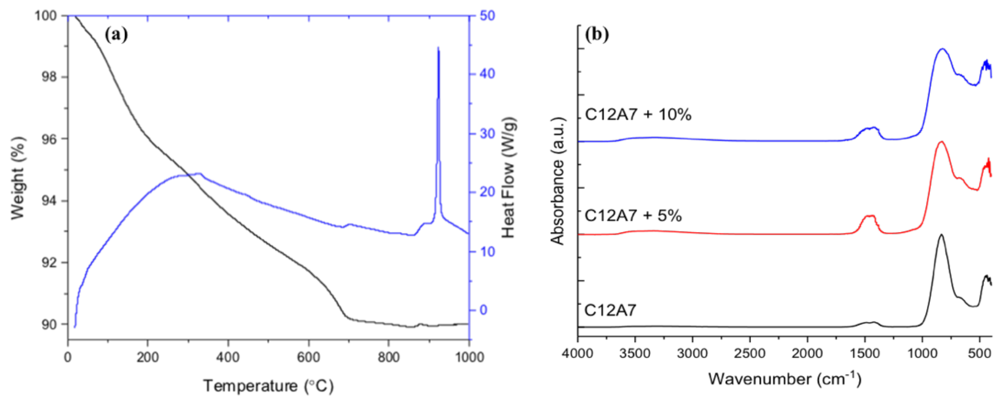

Figure 10.2. (a) TGA/DSC of as-produced C12A7+10% NPs and (b) FTIR of as-produced NPs.

Figure **10.2a** provides TGAs of as-produced NPs on heat treatment to 1000 °C/5 °C/min/air. Only one exotherm at ~ 950 °C is observed for each sample ascribed to crystallization of CaO, γ-Al_2O_3, and formation of α-Al_2O_3.[39] The mass loss is due to residual carbonate.

The Figure **10.2b** FTIR spectra show υC=O for carbonate (1400-1600 cm^{-1}) and υM−O (< 600 cm^{-1}) for as-produced NPs. The presence of carbonates is further confirmed by the TGA mass loss in the 200°- 300 °C region.

10.3.2 Thin film characterization

Figure **10.3a** shows the fracture surface SEM of C12A7+10% green film. The NPs appear well dispersed in the polyacrylic acid. The Figure **10.4b** TGA confirms the expected ceramic yield of green films matching the theoretical ceramic yield calculated as 85 wt. % (50 vol. %), excluding solvent as it evaporates on drying. The mass losses at intermediate temperatures arise as polymeric additives decompose.

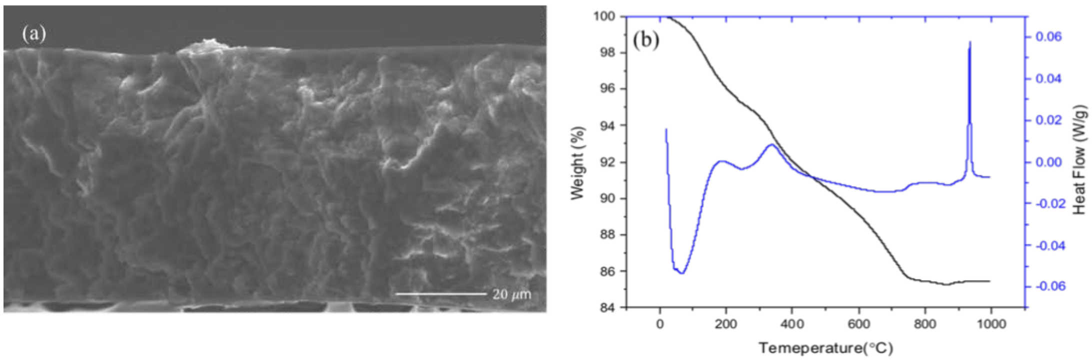

Figure 10.3. (a) C12A7 +10% green film SEM fracture surface image and (b) TGA of C12A7+10% green film.

Green C12A7 films were heated at 10 ℃/min/O_2 and sintered at 1050°, 1100°, 1200°, 1300 ℃ for 3 h. Figure **10.4** shows the XRDs of these sintered films. C12A7 with the secondary phase $CaAl_2O_4$ are observed. The sintering temperature was increased to achieve higher densities; however, it led to alumina rich phases arising due to calcium evaporation as shown in Table **10.3**. More CaO appears to be required to compensate for calcium loss and obtain higher densities.

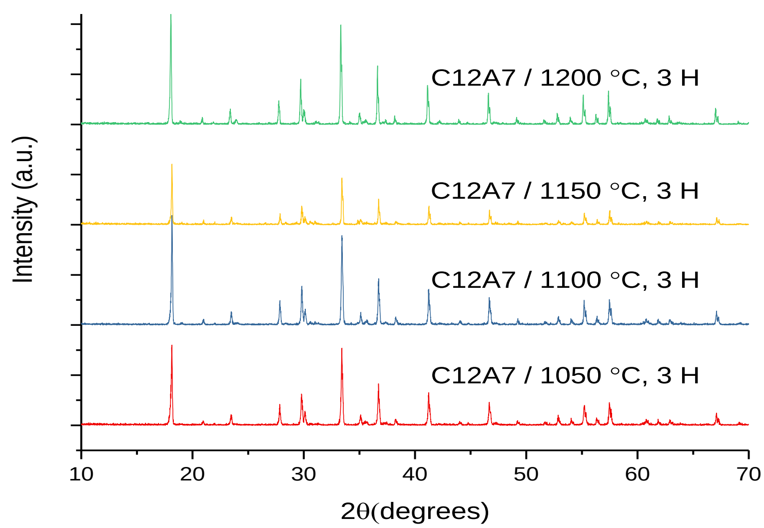

Figure 10.4. XRD patterns of C12A7 films heated at selected temperatures.

Table 10.3. Relative contents of phases in sintered C12A7 films.

Temperature (℃)/3 h	C12A7 (wt. %)	$CaAl_2O_4$ (wt. %)
1050	85.4	14.6
1100	84.6	15.4
1150	81.7	18.3
1200	80.9	19.1

The Figure **10.5** XRDs of C12A7, C12A7+5%, and C12A7+10% films sintered at 1300 ℃/3 h/O_2 shows mayenite (87.4 %) and $CaAl_2O_4$ (12.6 %), mayenite (92.3 %) and $CaAl_2O_4$ (7.7 %) and finally, single phase mayenite indicating that added CaO compensates for its loss during sintering. Thus, LF-FSP synthesis of NPs offers exceptional control of stoichiometry and phase purity.

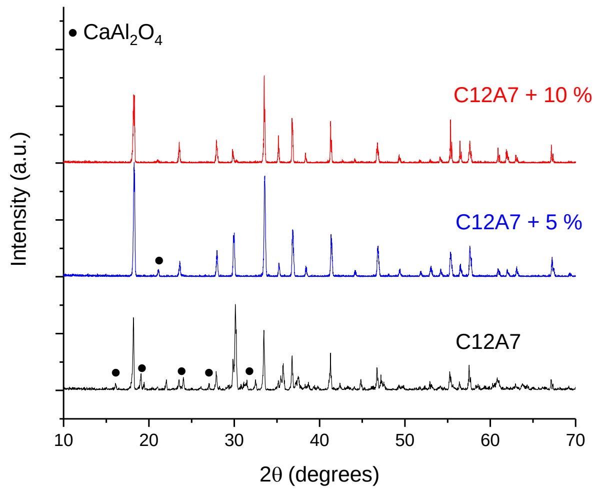

Figure 10.5. XRDs of C12A7 (black), C12A7+5 % (blue), and C12A7+ 10% (red) films sintered at 1300 ℃/ 3 h.

C12A7+ 10% sintered films were then treated in $20H_2/80N_2$ to 1050°, 1100°, and 1200 ℃ at 5 ℃ min^{-1} and held for 1 h in $20H_2/80N_2$. C12A7:H films were then illuminated under UV for 1 h causing the transparent film to change from colorless to light yellow, Figure **10.10**.

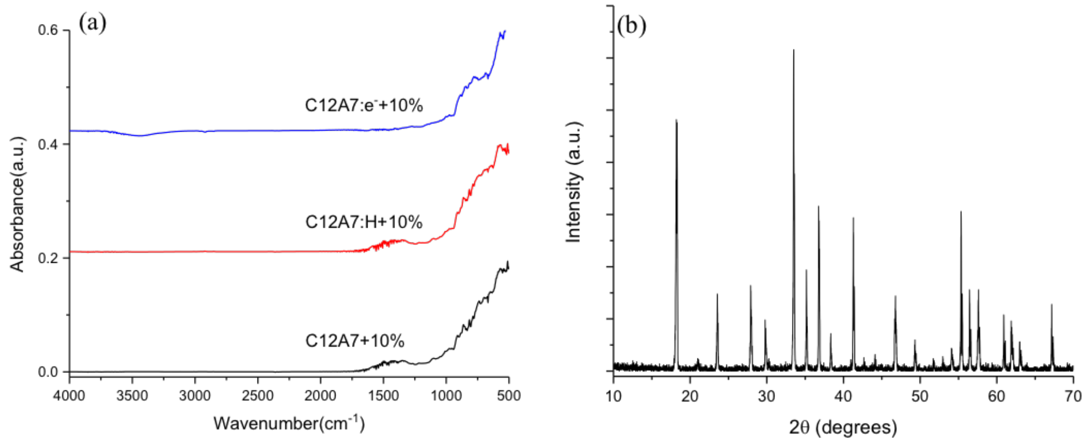

Figure 10.6. (a) FTIR spectra of C12A7+10% films sintered, and hydrogen treated followed by UV-irradiation. (b) XRDs of C12A7:H+10%.

Figure **10.6a** presents FTIR spectra of C12A7+10% films sintered to 1300 °C/3 h/O_2 followed by hydrogen treatment to 1100 °C/1 h and UV irradiation for 1 h. There is no significant difference in the spectra when comparing insulating, C12A7+10% films to electrically conducting, C12A7: e +10% films. Figure **10.6b** shows XRDs of C12A7:H+10% films confirming a single phase cubic C12A7 structure. There are no significant phase changes attributed to hydrogen treatment to replace the free O^{2-} in the cage of C12A7+10%.

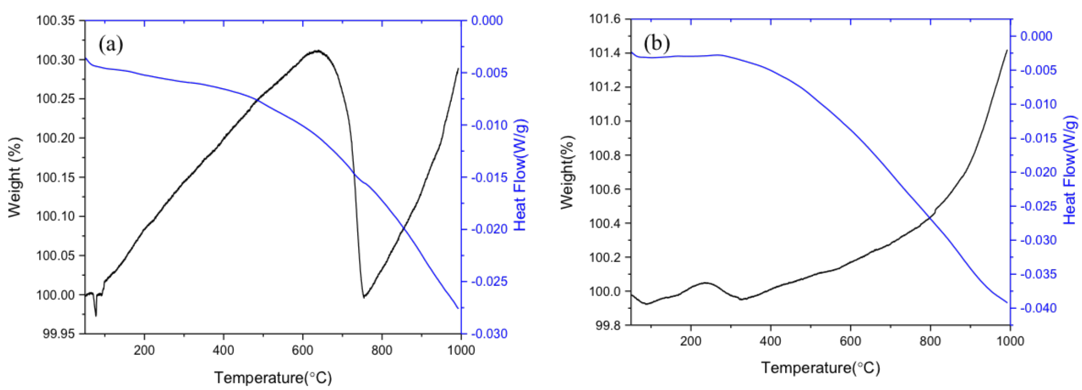

Figure 10.7. (a) Comparison TGA of C12A7+10% films hydrogen treated (b) UV-irradiation.

Figure **10.7(a-b)** present TGAs of C12A7:H+10% and C12A7:e+10% films heated to 1000 °C/N_2 respectively. The resulting mass gain for C12A7:H+10% films suggest that free oxygen ions were replaced by hydride ions. However, there is a mass loss at ~ 750 °C which might be ascribed to the loss of oxygen in partially filled cages. The TGA of C12A7:e +10% films shows a mass gain (~1.5 wt %) after 1000 °C heat treatment.

10.3.3 Microstructure and electronic conductivity

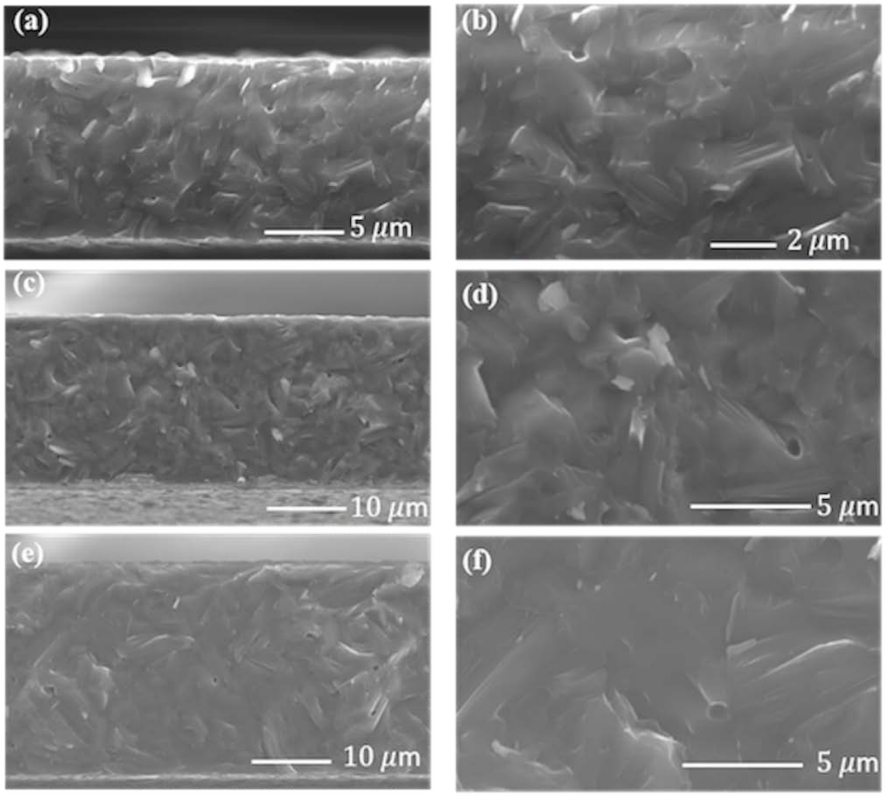

Figure 10.8. SEM fracture surface images of (a, b) C12A7, (c, d) C12A7+5 %, and (e, f) C12A7+ 10% films sintered at 1300 ℃/ 3 h.

Figure **10.8** shows microstructures of sintered C12A7, C12A7+5%, and C12A7+10% films. The nanoporous fracture surfaces look very dense with intergranular fracture modes. Final film densities were all ~ 98.8 %TD, per Archimedes method.

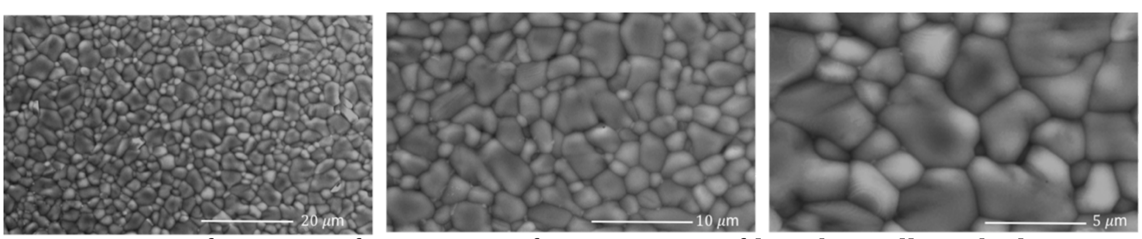

Figure 10.9. SEM fracture surface images of C12A7+ 10% films thermally etched to 1200 ℃/ 1 h at selected magnifications.

Figure **10.9** presents the microstructures for samples sintered to the highest densities. Thermal etching was conducted by fracturing and heating samples to 1200 ℃ for 1 h in O_2. Average grain sizes (AGSs) determined by the linear intercept method are 1.5 ± 0.2 μm and 2.3 ± 0.2 μm for C12A7, and C12A7+5 % respectively.

Figure **10.10** presents the microstructures of C12A7+10% films treated to 1100 ℃/1 h in $20H_2/80N_2$ atmosphere. The resulting C12A7:H+10% film looks very dense, nonporous. The SEMs also show smooth surfaces and uniform thicknesses. The optical images show the transformation of C12A7 from insulator to persistent conductor. The C12A7+10% films remain transparent after hydrogen treatment. However, they exhibit a greenish tint after UV treatment.

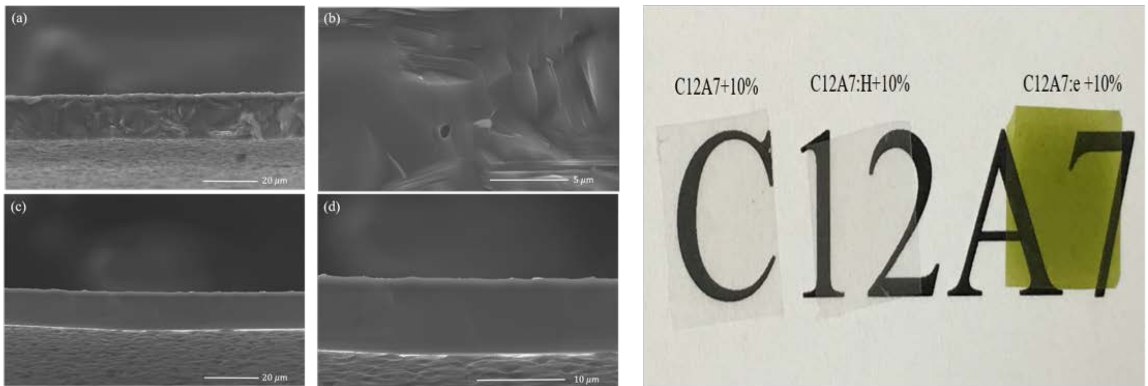

Figure 10.10. SEM fracture surface images of C12A7:H+10% (left) and optical images of C12A7+10% films treated in hydrogen followed by UV(right).

C12A7+10% films heated at selected temperatures (i.e. 1050°, 1100°, and 1200 ℃/1 h) in $20H_2/80N_2$ were exposed to UV-light for 1 h. Figure **10.11** presents a typical complex impedance spectrum of C12A7:e^- +10% films at 25 ℃. The resistance values at the intercept with real axis in the high frequency range were used to calculate conductivities. Table **10.4** presents the obtained total electronic conductivities at selected temperatures. The highest approximate electronic conductivity is 0.1 S cm^{-1}, which corresponds to the 1100 °C/1 h treated film at room temperature. By lowering hydrogen treatment temperature, the thermal activation process of replacing free O^{2-} ions with hydride ions increases; thus, providing higher conductivity. Rapid cooling to room temperature after hydrogen heat treatment is reported as a common condition of governing the cage with hydride ions.[13]

Table 10.4. Electronic conductivities of C12A7:e^- +10% films H_2 treated at selected temperatures.

H_2 heat treating T (℃)	σ(S cm^{-1})
1050/1 h	$5.6\pm0.2 \times 10^{-3}$
1100/1h	$3\pm0.6 \times 10^{-2}$
1200/1 h	$1.2\pm0.4 \times 10^{-2}$

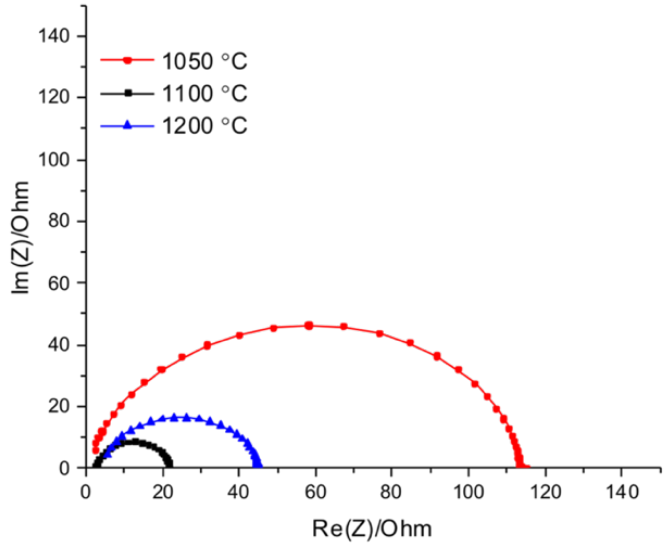

Figure 10.11. Nyquist plots of C12A7 +10 % films hydrogen treated to 1050° (red), 1100° (black), and 1200 ℃ (blue) for 1 h. C12A7:H +10% films illuminated by UV for 1 h before impedance measurement at 25 ℃.

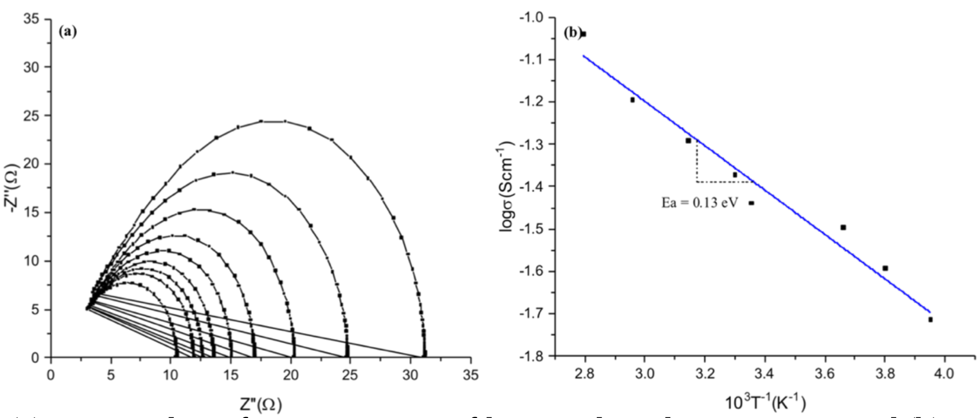

Figure 10.12. (a)Nyquist plots of C12A7:e$^-$ +10% films at selected temperatures and (b)Arrhenius plots of C12A7:e$^-$ +10%.

C12A7+10% films treated in H_2 to 1100 ℃/1 h and UV illuminated for 1 h were selected for electrical conductivity measurements at various temperatures. Figure **10.12a** presents a typical complex impedance spectrum of C12A7:e$^-$ +10% films where electrochemical impedance was collected in a frequency range of 10 MHz to 1 Hz at -20° to 85 ℃. Room temperature conductivities of 35 mS cm^{-1} and activation energies of 0.13 eV (12.5 kJ mol^{-1}) were obtained from the Arrhenius plot as shown in Figure **10.12b**.

Table **10.5** illustrates the total electrical conductivities of C12A7:e$^-$ +10% films at selected temperatures. Electrical conductivities of ~ 0.1 S cm^{-1} were obtained when films were heated to 85 ℃. Optimization of hydrogen and UV treatments to achieve higher room temperature electronic conductivities similar to what is reported in Table **10.6** remains as future work. The mechanical strength and flexibility will be measured as well.

Table 10.5. Total conductivities (σ_t) of C12A7:e$^-$ +10% samples at selected temperatures.

T (℃)	σ(S cm^{-1})
-20	2×10^{-2}
-10	2.5×10^{-2}
0	3.2×10^{-2}
25	3.7×10^{-2}
30	4.2×10^{-2}
45	5.1×10^{-2}
65	6.3×10^{-2}
85	9×10^{-2}

Table **10.6** compares thicknesses and room temperature electronic conductivities of C12A7:e$^-$ films reported in the literature. Note that some of the techniques used to achieve high electronic conductivities require a very expensive, and energy intensive processes. Despite the simplicity of solid-state reaction method, high sintering temperatures and longer dwell times are required to achieve dense, single phase, C12A7 samples; motivation for finding more effective mass production methods.[42]

Table 10.6. Reported room temperature conductivities for C12A7:e$^-$.

Sintering conditions (℃/h)	Processing Step	σ_t(S cm^{-1})	Thickness	Ref.
1300/3	LF-FSP/TC	3.5×10^{-2}	50 µm	-
1300/1	PLD	1.1	0.5 µm	[40]
1300/6	SSR/PLD	0.62	500 nm	[25]
1350/12	SSR/Fz	0.3	0.3 mm	[13]
1350/24	SM/DE	9×10^{-4}	13 mm	[41]
1600/1	MS/GC	1-10	-	[15]

GC = glass-ceramic, SSR = solid state reaction, SM = solution mixing, DE = direct evaporation, TC = tape casting, MS = melt solidification

10.4 Conclusions

Transparent and electronically conducting C12A7:e$^-$ films were synthesized by using LF-FSP NPs, then processed to thin(< 50 μm) films. Single cubic mayenite phase was achieved by introducing excess calcium precursor (10 wt. %) to compensate for its loss during sintering. C12A7 +10 % films after sintering to 1300 ℃/ 3 h have full densities and optimized phase purity thereby when hydrogen and UV treated, they show high electrical conductivities of 35 mS cm^{-1}. Films processed here show great density along with controllable thickness ascribed to the casting-sintering of nanoparticles synthesis. Further reduction in film thickness might result in improved electrical conductivity. The work presented here offers the potential to process low-cost TCOs at commercial scales providing simple processing routes to such materials can be developed.

References

(1) S. Liao, R. Yao, X. Chen, G. Wang, and F. Zheng, "Characteristics, Thermodynamics, and Preparation of Nanocaged $12CaO{\cdot}7Al_2O_3$ and Its Derivatives," *Int. J. Appl. Ceram. Technol.*, 13 [5] 844–855 (2016).

(2) S.W. Kim, S. Matsuishi, M. Miyakawa, K. Hayashi, M. Hirano, and H. Hosono, "Fabrication of room temperature-stable $12CaO{\cdot}7Al_2O_3$ electride: A review;" in *J. Mater. Sci. Mater. Electron.* 2007.

(3) K. Scrivener, "Calcium aluminate cements;" in *Adv. Concr. Technol.* 2003.

(4) J. Skibsted, E. Henderson, and H.J. Jakobsen, "Characterization of Calcium Aluminate Phases in Cements by 27Al MAS NMR Spectroscopy," *Inorg. Chem.*, (1993).

(5) K.L. Scrivener, J.L. Cabiron, and R. Letourneux, "High-performance concretes from calcium aluminate cements," *Cem. Concr. Res.*, (1999).

(6) D. a. Fumo, M.R. Morelli, and A.M. Segadães, "Combustion synthesis of calcium aluminates," *Mater. Res. Bull.*, (1996).

(7) H. Hosono and Y. Abe, "Occurrence of superoxide radical ion in crystalline calcium aluminate $12CaO.7Al_2O_3$ prepared via solid-state reactions," *Inorg. Chem.*, (1987).

(8) S. Yang, J.N. Kondo, K. Hayashi, M. Hirano, K. Domen, and H. Hosono, "Partial oxidation of methane to syngas over promoted C12A7," *Appl. Catal. A Gen.*, (2004).

(9) S. Watauchi, I. Tanaka, K. Hayashi, M. Hirano, and H. Hosono, "Crystal growth of $Ca_{12}Al_{14}O_{33}$ by the floating zone method," *J. Cryst. Growth*, (2002).

(10) K. Hayashi, S. Matsuishi, N. Ueda, M. Hirano, and H. Hosono, "Maximum incorporation of oxygen radicals, O^- and O2-, into $12CaO{\cdot}7Al_2O_3$ with a nanoporous structure," *Chem. Mater.*, (2003).

(11) K. Hayashi, N. Ueda, M. Hirano, and H. Hosono, "Effect of stability and diffusivity of extra-framework oxygen species on the formation of oxygen radicals in $12CaO\text{-}7Al_2O_3$;" in *Solid State Ionics*. 2004.

(12) T. Kamiya, S. Aiba, M. Miyakawa, K. Nomura, S. Matsuishi, K. Hayashi, K. Ueda, M. Hirano, *et al.*, "Field-induced current modulation in nanoporous semiconductor, electron-doped $12CaO{\cdot}7Al_2O_3$," *Chem. Mater.*, (2005).

(13) K. Hayashi, S. Matsuishi, T. Kamiya, M. Hirano, and H. Hosono, "Light-induced conversion of an insulating refractory oxide into a persistent electronic conductor," *Nature*, **419** [6906] 462–465 (2002).

(14) P. V. Sushko, A.L. Shluger, K. Hayashi, M. Hirano, and H. Hosono, "Hopping and optical absorption of electrons in nano-porous crystal $12CaO.7A_{l2}O_3$," *Thin Solid Films*, **445** [2] 161–167 (2003).

(15) H. Hosono, S.W. Kim, M. Miyakawa, S. Matsuishi, and T. Kamiya, "Thin film and bulk fabrication of room-temperature-stable electride C12A7:e- utilizing reduced amorphous $12CaO.7Al_2O_3$(C12A7)," *J. Non. Cryst. Solids*, **354** [19–25] 2772–2776 (2008).

(16) Y.X. Liu, L. Ma, D.T. Yan, H.C. Zhu, X.L. Liu, H.Y. Bian, H. Zhang, and X.J. Wang, "Effects of encaged anions on the optical and EPR spectroscopies of RE doped C12A7," *J. Lumin.*, **152**

28–32 (2014).
(17) X. Liu, Y. Liu, D. Yan, H. Zhu, C. Liu, W. Liu, C. Xu, Y. Liu, *et al.*, "A multiphase strategy for realizing green cathodoluminescence in 12CaO·7Al2O3–$CaCeAl_3O_7:Ce^{3+},Tb^{3+}$ conductive phosphor," *Dalt. Trans.*, **42** [46] 16311 (2013).
(18) M.M. Ali, M. Nagao, S. Watauchi, and I. Tanaka, "Floating Zone Growth and Characterization of $(Ca_{1-x}Nd_x)_{12}Al_{14}O_{33+6x}$($x \sim 0.001$) Single Crystals," *ACS Omega*, **1** [6] 1157–1163 (2016).
(19) M. Zhang, Y. Liu, J. Yang, H. Zhu, D. Yan, X. Zhang, C. Liu, C. Xu, *et al.*, "Enhanced emission of encaged-OH--free $Ca_{12(1-x)}Sr_{12x}Al_{14}O_{33}$:0.1%$Gd^{3+}$conductive phosphors via tuning the encaged-electron concentration for low-voltage FEDs," *Phys. Chem. Chem. Phys.*, (2017).
(20) R. Wang, Y. Zhang, J. Sun, L. Liu, and Y. Xu, "Up-conversion luminescence of Er^{3+}-doped and Yb^{3+}/Er^{3+} co-doped $12CaO.7Al_2O_3$ poly-crystals," *J. Rare Earths*, **29** [9] 826–829 (2011).
(21) H. Hosono, "Recent progress in transparent oxide semiconductors: Materials and device application," *Thin Solid Films*, **515** [15 SPEC. ISS.] 6000–6014 (2007).
(22) P. V. Sushko, A.L. Shluger, K. Hayashi, M. Hirano, and H. Hosono, "Electron Localization and a Confined Electron Gas in Nanoporous Inorganic Electrides," *Phys. Rev. Lett.*, **91** [12] 126401 (2003).
(23) S. Yang, J.N. Kondo, K. Hayashi, M. Hirano, K. Domen, and H. Hosono, "Formation and Desorption of Oxygen Species in Nanoporous Crystal 12CaO·7Al2O3," *Chem. Mater.*, **16** [1] 104–110 (2004).
(24) K. Hayashi, M. Hirano, S. Matsuishi, and H. Hosono, "Microporous crystal 12CaO·7Al2O3 encaging abundant O- radicals," *J. Am. Chem. Soc.*, **124** [5] 738–739 (2002).
(25) Y. Toda, M. Miyakawa, K. Hayashi, T. Kamiya, M. Hirano, and H. Hosono, "Thin film fabrication of nano-porous $12CaO\cdot7Al_2O_3$ crystal and its conversion into transparent conductive films by light illumination," *Thin Solid Films*, **445** [2] 309–312 (2003).
(26) T. Aitasalo, J. Hölsä, H. Jungner, M. Lastusaari, J. Niittykoski, M. Parkkinen, and R. Valtonen, "Eu^{2+}doped calcium aluminates prepared by alternative low temperature routes;" in *Opt. Mater. (Amst).* 2004.
(27) S. Liao, R. Yao, Y. Liu, X. Chen, X. Hu, and F. Zheng, "Green up-conversion of C12A7–Ho^{3+} prepared by co-precipitation method," *J. Alloys Compd.*, (2015).
(28) P.M. Chavhan, A. Sharma, R.K. Sharma, G. Singh, and N.K. Kaushik, "Dip coated $12CaO\cdot7Al_2O_3$ thin films through sol–gel process using metal alkoxide," *Thin Solid Films*, (2010).
(29) M. Kim and R.M. Laine, "Processing Research Liquid-feed flame spray pyrolysis (LF-FSP) for combinatorial processing of nanooxide powders along the $(ZrO_2)_{1-x} (Al_2O_3)_x$ tie-line . Phase segregation and the formation of core-shell nanoparticles," *Ceram. Process. Res.*, **8** [2] 129–136 (2007).
(30) R.M. Laine, J. Marchal, H. Sun, and X.Q. Pan, "A new Y3Al5O12 phase produced by liquid-feed flame spray pyrolysis (LF-FSP)," *Adv. Mater.*, **17** [7] 830–833 (2005).
(31) X. Liu, Y. Liu, D. Yan, H. Zhu, C. Liu, C. Xu, Y. Liu, and X. Wang, "Single-phased white-emitting $12CaO\cdot7Al_2O_3:Ce^{3+}$, Dy^{3+} phosphors with suitable electrical conductivity for field emission displays," *J. Mater. Chem.*, **22** [33] 16839 (2012).
(32) Lu, Q. Nie, T. Xu, S. Dai, X. Shen, and X. Zhang, "Up-conversion luminescence of $Er^{3+/}Yb^{3+}/Nd^{3+}$-codoped tellurite glasses," *J. Lumin.*, (2007).
(33) E. Tõldsepp, T. Avarmaa, V. Denks, E. Feldbach, M. Kirm, A. Maaroos, H. Mändar, and S. Vielhauer, "Synthesis and luminescence properties of Ce^{3+} doped nanoporous $12CaO\cdot7Al_2O_3$ powders and ceramics," *Opt. Mater. (Amst).*, **32** [8] 784–788 (2010).

(34) E. Yi, W. Wang, J. Kieffer, and R.M. Laine, "Flame made nanoparticles permit processing of dense, flexible, Li^+ conducting ceramic electrolyte thin films of cubic-$Li_7La_3Zr_2O_{12}$ (c-LLZO)," *J. Mater. Chem. A*, **4** [33] 12947–12954 (2016).
(35) M. Zahedi, A.K. Ray, and D.S. Barratt, "Preparation and crystallization of sol–gel C12A7 thin films," *J. Phys. D. Appl. Phys.*, **41** [3] 035404 (2008).
(36) E. Yi, W. Wang, S. Mohanty, J. Kieffer, R. Tamaki, and R.M. Laine, "Materials that can replace liquid electrolytes in Li batteries: Superionic conductivities in $Li_{1.7}Al_{0.3}Ti_{1.7}Si_{0.4}P_{2.6}O_{12}$. Processing combustion synthesized nanopowders to free standing thin films," *J. Power Sources*, **269** 577–588 (2014).
(37) E. Yi, E. Temeche, and R.M. Laine, "Superionically conducting β″-Al2O3thin films processed using flame synthesized nanopowders," *J. Mater. Chem. A*, (2018).
(38) S. Watauchi, I. Tanaka, K. Hayashi, M. Hirano, and H. Hosono, "Crystal growth of Ca12Al14O33 by the floating zone method," *J. Cryst. Growth*, **237–239** [1 4 I] 801–805 (2002).
(39) M. Gervais, "Crystallization of Amorphous Precursors in the Calcia – Alumina System : A Differential Scanning Calorimetry Study," *J. Am. Ceram. Soc.*, **83** [1] 70–76 (2000).
(40) M. Miyakawa, K. Hayashi, M. Hirano, Y. Toda, T. Kamiya, and H. Hosono, "Fabrication of highly conductive $12CaO{\cdot}7Al_2O_3$ thin films encaging hydride ions by proton implantation," *Adv. Mater.*, **15** [13] 1100–1103 (2003).
(41) M. Matsuda, Y. Inda, W. Hisamatsu, and T. Umegaki, "Conduction properties of oxide ion conductor $Ca_{12}AI_{14}0_{33}$ prepared with solution-synthesized powders," **15** 933–934 (1996).
(42) B. Matović, M. Prekajski, J. Pantić, T. Bräuniger, M. Rosić, D. Zagorac, and D. Milivojević, "Synthesis and densification of single-phase mayenite (C12A7)," *J. Eur. Ceram. Soc.*, **36** [16] 4237–4241 (2016).

Chapter 11

Conclusions and Future Work

11.1 Solid electrolytes

Current high-quality Li-ion battery cells and systems revolutionized many markets, especially mobile electronic devices with the transportation sector witnessing a similar experience. The trend is intentional, regulators as well as businesses are interested in sustainable clean transportation and thus sustainable businesses. One remaining challenge is battery cost, causing battery electric vehicles (BEVs) to still be more expensive than their combustion engine powered counterparts with similar range. With increasing demand for Li-ion batteries, even used in stationary storage systems, the cost is reduced through mass production, but material prices could go in the opposite direction. This is one reason to look into all solid-state batteries that promise to work without cost risk, and/or flammable, and toxic commodities. Another angle to consider is integration as part of automotive vehicle development. A battery supporting a ≥ 300-mile range requires ≥ 500 kg just in cell weight, counterproductive to all automotive industry efforts to increase range by reducing weight. The high weight comes with the requirement for structural elements that further reduce available volumes, valuable in automotive design.

Li-metal anodes, a high-capacity alternative to today’s graphite anodes, suffer from capacity losses during cycling, surface passivation due to the high chemical reactivity of Li-metal, and the tendency to grow dendrites on charging. One possible solution to these issues is the use of a solid-state electrolyte membrane that prevents liquid electrolyte from contacting the metal surface and prevents dendrites by a combination of mechanical blocking and control of Li-ion current density.

Different types of solid-state Li-ion conductors are increasingly available including polymers, ceramics, glass-ceramics, amorphous glasses, and composites thereof. All known solid-state electrolytes require further improvements in at least one of these parameters: conductivity at room temperature, chemical stability against Li-metal, stability against the electrochemical potential of the full cell, mechanical strength, wettability, porosity and manufacturability. An amorphous Li-ion conductor that stands out is LiPON. This material has been used in commercial thin-film lithium batteries for many years. Wetting of the electrolyte with Li-metal does not appear to be an issue for LiPON, as it is with otherwise highly promising $Li_7La_3Zr_2O_{12}$ (LLZO) garnet ceramics, which leads to large interface impedances. Due to LiPON's amorphous structure, an equal current density can be expected over the surface area, in contact with Li-metal.

The only problems with using LiPON are its low conductivity, compensated by application of very thin LiPON layers, and current, expensive methods of application. At present, LiPON can only be produced by sputtering in nitrogen atmosphere or atomic layer deposition (ALD) in nitrogen plasma. The main challenges of sputtering techniques is that it is difficult to fabricate a large target, slow deposition rates, high power requirements, and high cost of manufacturing. The thin layer cannot stand by itself since it must resist the mechanical stresses introduced by stripping and plating Li-metal.

Automotive applications mandate current density rates of multiple mA/cm^2. A combination of highly conductive LLZO or other ceramic electrolytes with very thin LiPON layers offers a viable option for a solid-state membrane with superior properties. We have demonstrated a completely different approach to the application of very thin LiPON films that avoids the costly methods currently extant through use of LiPON precursors applied via melt or solution processing at similar thicknesses but with much less capital equipment investment and using simple industry standard synthesis methods.

The Li-sulfur cathode is a good match for a Li-metal anode because both technologies have very high capacities, resulting in electrodes with similar thickness. A membrane, as described above, could resolve a series of issues for the sulfur-based cathode as well as the Li-metal anode. Intriguing is the new opportunity to design or select liquid electrolytes that specifically fit the sulfur electrode and not the Li-metal electrode, enabled by physical separation by a membrane.

Based on the design criteria for ceramic precursors discussed in Chapter 1, we have developed a set of polymer precursors that can be coated from solution onto thin film ceramic electrolytes and heated under mild conditions (< 600 °C) relative to the sintering temperatures needed to process dense, flexible ceramic thin films. The design and optimization of polymer precursors to glasses/ceramics and methods of processing them into a wide variety of thin films, binders, adhesives and ion conducting fillers offers a low energy/low-cost alternative to gas phase processing of LiPON-like materials.

In chapters 3-5, we demonstrated the utility of Li_xPON, Li_xSiON, and LiSiPHN polymer electrolytes as a coating on a Celgard membrane. These polymer electrolytes show high ohmic stability against Li metal at current densities of 0.375 – 3.75 $mAhcm^{-2}$. Furthermore, we have shown that the Celgard coated Li_6SiPON polymer electrolyte can be used to assemble a nearly all solid-state Li-S battery as described in chapter 3. Also, in these same engineering studies, our data demonstrate that polymer precursors can be used as active fillers in PEO matrices, resulting in a significant improvement in ambient ionic conductivity (2.8 mS/cm). If these PEO/polymer precursors can be melt cast onto cathodes and Li metal at the PEO melting point of 65−75 °C, it may be possible to replace the liquid electrolytes in traditional Li-ion batteries with melt cast mixtures of these materials eliminating fire hazards, reducing the extent of containment seals needed, and perhaps greatly simplifying the ASSB assembly. This would obviate the need to introduce both capital equipment and energy intensive new processes envisioned as necessary to assemble ASSBs that rely on ceramic electrolytes.

11.2 Cathode materials

Cathode materials used in LIBs attract extensive attention due to relatively high costs – usually the most expensive component in the cell.[1] In 2019 Wentker et al.[1] estimated that current cathodes can make up 30-50% of the total cost of the cell or 20-65 $/kWh. In a drive for global electrification, $/kWh is often used as a make or break metric. Dissecting this metric, gains can be accessed either via a decrease in the cost per energy or an increase in the energy per cost. Thus it is important to investigate high voltage oxides i.e. $LiNi_{0.5}Mn_{1.5}O_4$ (LMNO) and NMA ($LiNi_{0.883}Mn_{0.056}Al_{0.061}O_2$**)** as a low cost, high energy density cathode material. LMNO is currently one of the least expensive cathode materials on the market per kWh due to absence of cobalt.[2] The growing consenus to reduce cobalt use in LIB cathodes resulted in revitalized interest in LMNO. Another challenge is to increase the kWh per cost i.e. improve the performance of LMNO at the same affordable cost.

One trend observed in industry (BASF) and academia is particle size reduction for active materials in both the cathode and anode.[3,4] Particle size reduction results in three primary advantages focusing on interfaces and kinetics. First, nanoscale materials have higher SSAs than micron-scale materials increasing contact areas between the active material and electrolyte.[4,5] Increased interfacial contact area between active material and electrolyte means more Li^+ diffusion pathways and a higher chance Li^+ can diffuse more rapidly in and out of the active material. Kuppan et al.[6] report that realizing stable LMNO cathodes must be predicated on particle sizes below one micron, but such systems must counter increased surface reactions with increases in

SSA. The high NP SSAs should lead to superior charge transfer kinetics and shorter Li^+ diffusion paths on average. Characteristic migration times can be derived from Fick's law; Equation (1):[1]

$$\tau = \frac{L^2}{4\pi D^*} \qquad (1)$$

Where τ is the characteristic time (or in this scenario the Li^+ migration time), L is the diffusion length, and D^* is the chemical diffusion coefficient of Li^+ in the host lattice. The decrease in characteristic time from micro- to nanoparticles can be as much as 10. This greater access to Li^+ should in theory lead to higher capacity at higher C-rates and subsquently higher power.[1]

Despite compelling reasons to move to nanoscale cathodes, LMNO has one inherent disadvantage with increased SSAs. LMNO suffers from disproportionation of Mn^{3+} per Equation (2):[7]

$$2Mn^{3+} \rightarrow Mn^{4+} + Mn^{2+} \qquad (2)$$

Where the newly formed Mn^{2+} can easily dissolve into the elctrolyte, effectively accelerating cell aging and reducing capacity. This disproportionation reaction is triggered by the presence of acid such as HF, a common by product of electrolyte decompositon and SEI formation.[7]

Common solutions to this issue are coating particle surfaces, introducing electrolyte additives, and transtional metal doping.[8] Removing the cathode–liquid electrolyte interface altogether is another possibility to diminish Mn^{2+} dissolution. Reducing a major degradation mechanism is one rationale to couple high voltage LMNO with an all solid state cell. This is our eventual goal as discussed below.

LMNO can be synthesized using a variety of methods ranging from benchtop nanoreactors to industrial scale including but not limited to sol-gel, hydrothermal synthesis, spray pyrolysis, solution combustion, and organic co-precipitation.[9–11] Often these techniques are hindered by high cost, low yield, and complicated procedures and required capital equipment. Our group uses LF-FSP which benefits from controlled morphology, phase purity, high yield, and low cost. This technique has been proven to produce phase pure solid electrolyte and anode nanoparticles as discussed in Chapters 6 and 7, respectivley. By leveraging our expertise in nanoparticle synthesis, we believe we can produce LMNO materials that can be used directly in ASSBs taking advantage of improved kinetics while avoiding Mn^{2+} dissolution.

The future plan is to develop and optimize all solid-state lithium-ion batteries by using scalable polymer precursors to Li_xPON and Li_xSiON ike materials to coat, act as binder and/or adhesives for ceramic electrolytes and that offer potential to serve as interface buffer layers between electrolyte and electrodes (Scheme **11.1**). The target for the next 4 months is to use different cathodes that enable high specific energy batteries with performance goals of 500 Wh/kg and 1000 cycles. The high voltage cathodes such as LMNO and NMA will be investigated as proof-of-principle polymer coated ceramic electrolytes were found to offer wide electrochemical stability windows. The resulting technology aims to enable the commercialization of high performance, high energy, low-cost automotive battery that presents a potential path to achieving battery cost reduction, and US-based advanced manufacturing.

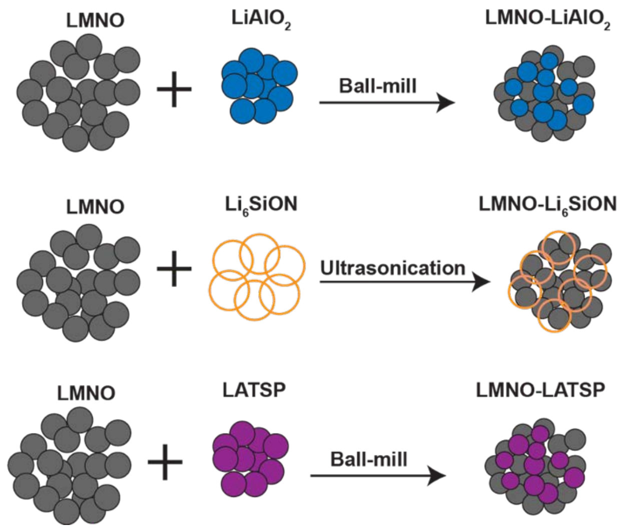

Scheme 11.1. LMNO catholyte synhesis.

11.3 Anode materials

Conventional lithium-ion batteries (LIBs) using graphite anodes cannot meet the increasing demands for power density, operational reliability, system integration, and safety in many applications. Replacing graphite (specific capacity 372 mAh g^{-1}) with higher energy density materials is a priority. Of the many potential LIB anodes, Si-based materials offer promise with high gravimetric/volumetric capacities (4200/9786 mAh g^{-1} Simet). Also, Si-based anodes offer low discharge potentials ~0.2-0.4 V reducing adverse lithium plating. Finally, Si is abundant, low cost, environmentally friendly, recyclable, non-toxic and easily isolated from SDRHA.

Unfortunately, Si anodes exhibit poor capacity retention due to severe volume changes during charge/discharge cycling. As alternatives, SiO_x and SiN_x films have received attention as they offer capacities of 1250-2300 mAh/g and capacity retention. SiC was previously regarded as an inactive anode material. However, recent studies of SiC anodes find high reversible capacity, 1200 mAh/g; <u>3x the theoretical capacity of graphite.</u> Some researchers suggest this process involves a conversion reaction of SiC with Li^+ via an alloying/dealloying reaction as shown in Equations (3 *and* 4).

$$SiC + 4Li^+ + 4e^- \leftrightarrow Li_4C + Si \qquad (3)$$

$$Si + 4.4Li^+ + 4.4e^- \leftrightarrow Li_{4.4}Si \qquad (4)$$

The suggested reaction mechanisms allow calculation of a 2288 mAh/g capacity, much larger than pristine silicon specific capacity (1200 mAh/g). However, the experimentally attainable capacity is < 1200 mAh/g. Hence, the actual lithiation mechanisms and the reversibility of the reaction seem to be unknown and should be carefully delineated to realize superior Ag waste SiC anodes, one proposed target.

Our lab proposed efforts center on using SP and SDRHA to access novel solid electrolyte and anode materials, respectively, as briefly detailed below (Scheme **11.2**). These low-cost, easily processed materials offer a unique opportunity to develop components for all-solid-state batteries (ASSBs) in a carbon neutral process that valorizes a plentiful Ag waste. One can envision using the same process technology to develop recycling methods at the end of battery life.

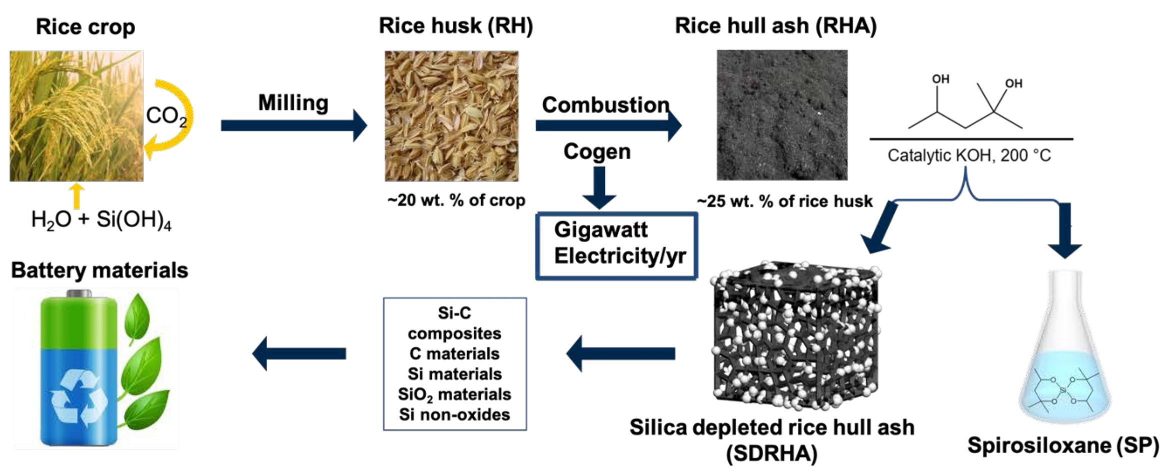

Scheme 11.2. Process steps toward battery materials from Ag waste.

Refernces

(1) Wentker, M.; Greenwood, M.; Leker, J. A Bottom-up Approach to Lithium-Ion Battery Cost Modeling with a Focus on Cathode Active Materials. *Energies* **2019**. https://doi.org/10.3390/en12030504.

(2) Li, W.; Lee, S.; Manthiram, A. High-Nickel NMA: A Cobalt-Free Alternative to NMC and NCA Cathodes for Lithium-Ion Batteries. *Adv. Mater.* **2020**. https://doi.org/10.1002/adma.202002718.

(3) Hu, M.; Pang, X.; Zhou, Z. Review Recent Progress in High-Voltage Lithium Ion Batteries. *J. Power Sources* **2013**, *237*, 2013. https://doi.org/10.1016/j.jpowsour.2013.03.024.

(4) Bazito, F. F. C.; Torresi, R. M. Cathodes for Lithium Ion Batteries: The Benefits of Using Nanostructured Materials. *Journal of the Brazilian Chemical Society*. 2006. https://doi.org/10.1590/S0103-50532006000400002.

(5) Tian, Q.; Zhang, Z.; Yang, L.; Xiang, Y. Improving the Lithium Storage Properties of Li4Ti5O12anodes by Facile Two-Phase Formation and Nanostructure Engineering Strategy. *J. Alloys Compd.* **2017**. https://doi.org/10.1016/j.jallcom.2017.02.175.

(6) Kuppan, S.; Xu, Y.; Liu, Y.; Chen, G. Phase Transformation Mechanism in Lithium Manganese Nickel Oxide Revealed by Single-Crystal Hard X-Ray Microscopy. *Nat. Commun.* **2017**. https://doi.org/10.1038/ncomms14309.

(7) Gabrielli, G.; Marinaro, M.; Mancini, M.; Axmann, P.; Wohlfahrt-Mehrens, M. A New Approach for Compensating the Irreversible Capacity Loss of High-Energy Si/C|LiNi0.5Mn1.5O4 Lithium-Ion Batteries. *J. Power Sources* **2017**. https://doi.org/10.1016/j.jpowsour.2017.03.051.

(8) Park, J. S.; Meng, X.; Elam, J. W.; Hao, S.; Wolverton, C.; Kim, C.; Cabana, J. Ultrathin Lithium-Ion Conducting Coatings for Increased Interfacial Stability in High Voltage Lithium-Ion Batteries. *Chem. Mater.* **2014**, *26* (10), 3128–3134. https://doi.org/10.1021/cm500512n.

(9) Duncan, H.; Hai, B.; Leskes, M.; Grey, C. P.; Chen, G. Relationships between Mn3+ Content, Structural Ordering, Phase Transformation, and Kinetic Properties in LiNixMn2-XO4 Cathode Materials. *Chem. Mater.* **2014**. https://doi.org/10.1021/cm502607v.

(10) Kebede, M. A.; Yannopoulos, S. N.; Sygellou, L.; Ozoemena, K. I. High-Voltage LiNi 0.5 Mn 1.5 O 4- δ Spinel Material Synthesized by Microwave-Assisted Thermo-Polymerization: Some Insights into the Microwave-Enhancing Physico-Chemistry . *J. Electrochem. Soc.* **2017**. https://doi.org/10.1149/2.1471713jes.

(11) Quispe, L.; Condoretty, M. A.; Kawasaki, H.; Tsuji, S.; Visbal, H.; Miki, H.; Nagashima, K.; Hirao, K. Synthesis of Spinel LiNi0.5Mn1.5O4 by a Wet Chemical Method and Characterization for Lithium-Ion Secondary Batteries. *J. Ceram. Soc. Japan* **2015**. https://doi.org/10.2109/jcersj2.123.38.